# Hyper-Fast NMR Imaging

by

**P.R.Harvey, B.Sc.**

Thesis submitted to the University of Nottingham for the degree of Doctor of Philosophy, October 1991

# Contents

# Abstract

The work presented in this thesis was carried out in the Physics Department at the University of Nottingham between October 1988 and October 1991. It is the original work of the author except where indicated by reference.

This thesis describes the continuation of the development of Echo Volumar Imaging (EVI) to facilitate snapshot imaging of a volume within the human body. Variants of the technique which have also been investigated include a spin echo version, SE-EVI, and a zoomed version ZEVI. All formats acquired data in a modulus fashion in times ranging from 64 ms to 120 ms. Hardware limitations have restricted the image matrix size to $64 \times 32 \times 8$ voxels and prompted the employment of more efficient gradient driver circuitry.

A multi-mode resonant gradient circuit is described for use in both Echo Planar Imaging (EPI) and EVI. The circuit behaves in an overall resonant manner but at a fixed number of discrete frequencies. By choosing the number of resonant modes, the circuit can be used to generate approximations to a square wave or trapezoidal waveform. Because of the energy conserving nature of the circuit design much faster current rise times can be achieved with a given amplifier and gradient coil.

The multi-mode gradient driver circuit was utilized both for planar imaging and to investigate the effect of rapidly modulated magnetic fields on the human body. A simple neural stimulation model is used to evaluate the stimulation threshold current density for a variety of magnetically induced waveforms and for sinusoidal stimulation as a function of frequency. Experimental results correlate well with the model showing that for short times, contrary to the widely held view, neural stimulation is independent of the magnetic field switching rate $dB/dt$, but depends on the final magnetic field value.

# Acknowledgements

The research work involved in this thesis would not have been possible without the financial assistance of the SERC, the MRC and the flexibility of the Department of Physics. In particular I would like to express my thanks to:

Professor P. Mansfield for his inspiring enthusiasm, insight and valuable tuition.

Professor R.J. Ordidge for his encouragement during my period on the microscope project.

Dr R.J. Coxon, Mr P.M. Glover and Mr J. Parramore for their valuable technical expertise.

Dr A.M. Blamire, Dr R.W. Bowtell, Dr G.D. Brown, Dr B. Chapman, Dr P. Gibbs, Dr P.A. Gowland, Dr D.N. Guilfoyle, Dr M.J. McJury, Dr J.C. Sharp, Dr M.K. Stehling, Mr M. Clemence, Mr B. Issa and Mr M.R. Symms for their support and enthusiasm both professionally and socially.

Mr T. Davies for his graphics expertise and particularly for some of the diagrams in chapter 6 and chapter 7.

Mr I. Thexton and the workshop staff for their experience and manufacturing skills.

My family for their continuous support and appreciation.

Dr R.S. Badar-Goffer and Adam for putting everything into perspective.

# Chapter 1: Introduction

## 1.1 A Brief History of NMR

The fundamentals to which the phenomenon of nuclear magnetic resonance (NMR) owes its origin were first implied in 1921 by Compton. He suggested that the electron, as well as possessing charge, also had angular momentum or spin. This idea was also proposed in 1925 by Goudsmit and Uhlenbeck and actually demonstrated in an experiment performed by Stern and Gerlach. In 1924 Pauli made a similar proposal for the nucleus in order to explain the hyperfine structure observed in certain atomic species and by 1928 his suggestion had been placed on a firm theoretical basis by Dirac.

The detection of nuclear magnetism in solid hydrogen was accomplished in the Soviet Union in 1937 by Lazarew and Schubnikow, while the existence of electronic magnetism was confirmed by Zavoisky in 1944 with the aid of resonance techniques.

In 1946 Bloch, Hansen and Packard [1] at Harvard and Purcell, Torrey and Pound [2] at Stanford announced, independently, the detection of NMR in samples of paraffin and water respectively. As a result of this work they were jointly awarded the Nobel Prize in 1952.

In 1949 Knight discovered that the resonant frequencies of nuclei in metal solids were dependent on the chemical form of the solid [3]. This was followed up in 1950 by Dickinson [4], Proctor and Yu's [5] discovery that, in liquids, the exact resonant frequency of a nucleus was dependent on its chemical environment. This effect, known as chemical shift, led to the first and arguably most important application of NMR, that is, in the field of spectroscopy. The first commercial spectrometer appeared in 1953 and proton NMR has since become virtually indispensable in the organic chemistry laboratory providing, along with $^{13}C$ spectroscopy, an extremely powerful tool with which to probe the structure of molecules.

Shortly after the discovery of NMR, Bloch inserted his finger into his equipment and observed a strong proton resonance signal. This observation, however, was not pursued. Hahn, who in 1950 discovered spin echoes [6], had little idea that his efforts would be of medical importance nor did Gabillard when he showed in 1951 that the introduction of magnetic field inhomogeneities could altered the shape of the free induction decay (FID) obtained from a homogeneous distribution of spins [7].

Odeblad in 1956 performed work on eye tissues and discovered that a decrease in water content may be correlated to an increase in linewidth and decrease in $T_1$ and $T_2$ values. Damadian in 1971 found that relaxation times

of tumours differ radically from those of normal tissue [8]. Following Hahn's theoretical analysis of diffusion on the NMR signal the Indian scientist Suryan published, in 1951, details of measurements on flowing solutions of ferric chloride. This work was adopted by Bowman and Kudravcev [9] who proceeded to demonstrate that magnetic field inhomogeneity could be used to localize a volume of interest and map the distribution of NMR susceptible nuclei in living tissue.

In 1972 Damadian submitted a patent application outlining the potential scope of NMR imaging. Later, in 1973, Abe *et al* submitted a patent in which a viable imaging method, similar to that proposed by Kudravcev, was described. He also mentioned the use of injected ferric powders for enhanced contrast.

The idea of obtaining spin density information by using magnetic field gradients to impose a linear relationship between spin position and resonant frequency was conceived in 1973 independently by Lauterbur [10] at Stony Brook, and Mansfield and Grannell [11] at Nottingham. Using a projection reconstruction technique, as in CT, Lauterbur succeeded in publishing the worlds first two dimensional NMR image of two water filled cylinders. In 1976 Mansfield and Maudlsey [12] produced the first biological image of a human finger and in 1978 Damadian produced the first whole-body image of the human thorax using, unbeknown to him, Kudravcevs concept of spatial localization by field inhomogeneity [13].

Much of the development of magnetic resonance imaging (MRI) took place in universities and in 1974 Garroway, Grannell and Mansfield at Nottingham conceived the idea of slice selection which used frequency selective pulses combined with a gradient to excite a thin slice of interest prior to imaging [14].

In 1975 Kumar *et al* proposed a new efficient method of imaging using two dimensional Fourier transformation (2D-FT) [15]. The consequent development of Spin-Warp imaging, at Aberdeen by Edelstein in 1980, alleviated some of the technical constraints required for the 2D-FT method [16]. Spin-Warp imaging is now the most popular technique used commercially. The basic 2D-FT method is rather slow, taking from tens of seconds to minutes to produce an image. It is for this reason that imaging of the heart and other moving organs within the body were initially very difficult to perform.

In 1977 the most efficient imaging technique to date was conceived by Mansfield [17]. Echo Planar Imaging (EPI) as it is called, acquires a complete image in less than 100 ms. The price to pay for this speed is a slight loss in spatial resolution and strenuous technical requirements. It is partly due to these reasons that EPI, up until recently, has not been implemented on commercial scanners. Recent improvements in EPI at Nottingham and Advanced NMR Systems in America show that it is capable of competing with the image quality produced by the slower 2D-FT hybrid techniques and is the class leader where rapid imaging is required.

Since the introduction of EPI other techniques hāve been developed to speed up imaging time. The most notable rival to EPI is the Fast Low Angle SHot technique or FLASH introduced in 1986 by Hasse *et al* [18]. FLASH is effectively a compression of the normal Spin-Warp technique using low flip angle radio frequency (RF) excitation pulses to avoid saturation of the sample magnetization. A FLASH experiment takes approximately 1 or 2 seconds to perform and more recently "Snapshot" or "Turbo" FLASH has been introduced which takes as little as 200 ms to perform. FLASH is generally perceived to be technically less demanding than EPI and this is partly the reason why it is more widely used on commercial scanners. It is, however, an inescapable fact that to perform FLASH at a speed comparable to EPI would require greater hardware demands and would result in an image of much lower signal/noise and contrast when compared to an EPI image of the same experimental duration and matrix size. Many other rapid imaging techniques have been developed over recent years all of which are hybrids of the three basic imaging modalities namely Projection Reconstruction, Spin-Warp and Echo Planar. All three have their advantages depending on the parameter under investigation.

## 1.2 Technical Innovation in MRI

In an NMR body scanner one of the pre-requisites for a good image is a homogeneous and stable main magnetic field. The magnets used today have evolved from room temperature electromagnets, providing field strengths of up to 0.15T, to superconducting magnets with fields strengths of 4T. The advancement in magnet technology was necessary to facilitate these higher field strengths. Some progress, by the Fonar Corporation, was made to introduce permanent whole-body magnets but for fields higher than about 0.3T the magnet becomes prohibitively large. Damadian himself produced the first whole-body image using a crude superconducting magnet. The main advantages of superconductive magnet technology are that high and homogeneous magnetic fields can be generated over a large bore with a relatively small magnet. For in-vivo spectroscopy good homogeneity and high field strength are essential. Superconductive magnet technology is also cheaper in the long term.

Gradient coil design is another area in which much progress has been made. From the simple use of Maxwell pairs and Golay type saddle coils has evolved the target field approach to gradient coil design [19]. In this technique the wire paths on the coil former can be precisely calculated to provide a specific magnetic field at any point within the imaging region. With the advent of rapid imaging techniques like EPI the gradient requirements had to be re-evaluated. The rapidly modulated transverse gradient used in the EPI technique can induce eddy currents in the main body of the magnet resulting in a grossly distorted image. The speed at which these gradients can be switched is, in most cases, limited by the maximum voltage available and the inductance of the field coils. The eddy current problem was solved by Mans-

field and Chapman in 1986 [20] with the introduction of actively screened gradient coils whereby a fraction of the current supplied to the gradient assembly is sent to an extra set, or in some cases two sets, of specially designed coils which surround the main field coils. These extra coils then act to actively screen the magnet body from induced eddy currents by cancelling any magnetic field beyond the main gradient coils. An approach similar to that used in the design of target field coils is used to overcome the problems of high inductance gradient coils. [21]

As rapid imaging techniques approach higher resolution the audible noise factor is becoming a notable problem. The gradient coil set acts effectively like a moving coil loudspeaker when a modulated current is supplied and the resultant tone can reach levels of above 105 dB depending on the frequency of operation. Work has taken place elsewhere to overcome this problem with a certain amount of success. However, further research is necessary in this area.

The RF coil is another key component in MRI and numerous designs have evolved in order to optimize its main requirements. The RF coil must have a reasonable Q but not too high as to make the pulse ring-down time excessively long. The coil must be able to generate a highly uniform RF field over the sample volume and the coil assembly must not be so large that its self resonant frequency becomes comparable with the operating frequency (the inductance of the coil increases in proportion to its linear dimension. If the coil and hence inductance become too large then there is a danger of the coil resonating with its own interturn capacitance).

Most coils today are used for both transmission and reception of the nuclear signal. The most popular choice is the saddle coil which can be tuned in either a series or parallel arrangement. This type of coil is relatively simple to build but suffers from inhomogeneity problems which become worse as the radius increases and particularly in the vicinity of the coil wires. The saddle coil becomes difficult to tune when the wavelength of the RF becomes smaller than the segments which make up the coil i.e. at high frequencies.

In 1979 Alderman and Grant [22] developed a head coil in which capacitance is distributed around the coil making the coil segments smaller. The resonant frequency increases accordingly. More recently Hayes *et al* [23] developed the birdcage coil which uses the idea of distributed capacitance to increase both the uniformity and frequency of the RF field. The coil consists of a rolled up ladder network comprising inductive strips and distributed capacitors. It can be considered as a parallel transmission line and, as current flows along the ladder there is a progressive phase change which is dependent on frequency. The ladder, however, is tied back to itself, and at the frequency at which the phase change is 360°, there is resonance. The resultant field is more homogeneous. The coil requires less power to drive and benefits the user with a $\sqrt{2}$ improvement in signal to noise over the saddle coil. The birdcage design can also operate at much higher frequencies [24]. Recent developments at Nottingham [25] include a miniature birdcage coil and cavity resonator

which operate at 500 MHz, and a half-birdcage design which is placed over the patient in the manner of a cheese dish cover. The use of a metal ground plate beneath the coil serves to mirror the RF field and greatly improves the homogeneity.

The improvement of computer hardware over the last ten years has greatly reduced the time taken to process images. Further to this, the increased flexibility that computers offer has eased the development of more sophisticated gradient and RF pulse sequences. To date it is possible, using EPI, to acquire, process and display a $128^2$ pixel image at a rate of 10 frames per second. Advantages offered by greater computing power on commercial scanners enable the user to choose a region of interest from a particular image and, under software control, zoom in on it from any angle. This is of particular use in brain surgery where the image provides a surgeons eye view of the tumour. The surgeon can plan the operation and target the tumour precisely thus minimizing unnecessary damage to healthy brain tissue.

## 1.3 Safety in MRI

A major advantage of MRI is the fact that it does not use any form of ionizing radiation. It is therefore considered to be an extremely safe diagnostic technique which can be used for long periods on a patient without the fear of harmful side effects. The long exposure times allowed in MRI enable more thorough investigations and, because ionizing radiation is not used, it is safe even for pregnant patients.

There are, however, minor hazards which need to be considered for the complete comfort and safety of the patient. These hazards fall into the three main categories of:

- RF irradiation.
- Exposure to static magnetic fields.
- Exposure to time varying magnetic fields.

The hazard from RF irradiation arises, at the frequencies currently used, from tissue heating through resistive loss. The RF pulses essential to an MRI experiment, if applied frequently enough and at a high enough power, can cause heating of the tissue. The NRPB guidelines therefore restrict the levels of RF that can be used in patient imaging experiments.

The effects of the static magnetic field on the human body are largely inconclusive. One magnetic interaction which is well documented is the magneto hydrodynamic effect, whereby an e.m.f. is generated across an electrically conductive fluid which is flowing in a magnetic field. Potentials due to this effect have been measured across the aortic arch in the hearts of monkeys subject to a static field of 10T. For humans the value of this potential, under the same conditions, has been estimated at 16 mV/T. Most commercial

body scanners operate at between 0.5 and 2T, that is, well below the field required to produce any hazardous effect by the afore mentioned mechanism. Less serious effects include nausea and magnetophosphenes (magnetically induced stimulation of the optic nerve) but these have only been experienced when the subject moves quickly in a high magnetic field. The only other notable hazards that exist are from the force exerted by the magnetic field on ferromagnetic implants such as surgical clips. Movement of these clips can be very dangerous particularly if they are close to the brain. Care has to be taken to screen any likely patients for such implants. Pacemakers are also vulnerable to high magnetic fields. For the most part, however, the static magnetic field is considered a very low level hazard.

Of more immediate concern are the effects of time varying magnetic fields on the patient. EPI and other similarly rapid techniques employ high amplitude, rapidly modulated, magnetic fields. Much debate has been sparked off recently concerning the safety of such fields following reports of magnetically induced peripheral nerve stimulation at gradient switching rates lower than predicted [26, 27]. An investigation into the causes and possible mechanisms of peripheral nerve stimulation by modulated magnetic fields is presented in chapter 7 of this thesis to which the reader is referred for further discussion.

# Chapter 2: Basic Theory of NMR

## 2.1 Introduction

This chapter is intended to provide a basic overview of the fundamental theory of NMR. For a more detailed description the reader is referred to the texts as listed in references [28, 29, 30, 31, 32, 33, 37].

The mechanisms involved in the phenomenon of NMR can be fully described with the aid of quantum mechanics by assuming the appropriate Hamiltonian in the Schrödinger equation. This approach, however, becomes very complicated when full interactions are taken into account.

For a basic understanding we may assume that the system under analysis is composed of non-interacting spins. In this case both classical and quantum mechanics may be used in juxtaposition.

## 2.2 NMR Sensitive Nuclei

It is appropriate at this point to introduce some of the nuclei which are able to undergo nuclear magnetic resonance. For nuclei other than a single proton, the magnitude of the nuclear spin is determined by three rules:

1. If the mass number A is odd, the spin is half-integral.
2. If A is even but the atomic number Z is odd, the spin is integral.
3. If both A and Z are even the spin is zero.

Most elements, as a result, have at least one naturally-occurring isotope which possesses a non-zero nuclear spin and is therefore observable by NMR. The more commonly observed nuclei are listed in table 2.1 together with their nuclear spin and magnetogyric ratio.

Quantum mechanics describes each component of the nucleus as having associated with it an angular momentum

$$\mathbf{J} = \mathbf{I}\hbar \tag{2.1}$$

where the corresponding eigenvalue equation for $\mathbf{I}$ is

$$\mathbf{I}|\psi\rangle = \sqrt{I(I+1)}|\psi\rangle \tag{2.2}$$

$I$ is the spin of the nucleon and for both proton and neutron is equal to $\frac{1}{2}$. These spins can add in a parallel or anti-parallel fashion and it is the vector sum of these additions which determines the overall spin of the nucleus.

| Species | Nuclear Spin ($I$) | Magnetogyric Ratio ($\gamma$) (MHz/T) |
|---|---|---|
| $^{1}H$ | $\frac{1}{2}$ | 42.573 |
| $^{13}C$ | $\frac{1}{2}$ | 10.705 |
| $^{31}P$ | $\frac{1}{2}$ | 17.237 |
| $^{19}F$ | $\frac{1}{2}$ | 40.052 |
| $^{23}Na$ | $\frac{3}{2}$ | 11.263 |

Table 2.1: Common NMR sensitive nuclei.

Also associated with the nucleus is a magnetic moment $\boldsymbol{\mu}$ which lies parallel to the angular momentum vector. The two are related by the magnetogyric ratio $\gamma$

$$\boldsymbol{\mu} = \gamma \mathbf{J} \tag{2.3}$$

Classically, the nucleus is seen as a sphere of radius $r$, mass $m$ and charge $e$ spinning on its axis. If this sphere is spinning with a period equal to $T$ then it will have an angular momentum defined as

$$J = \frac{2\pi m r^2}{T} \tag{2.4}$$

Additionally, its magnetic moment may also be defined

$$\mu = \frac{e\pi r^2}{T} \tag{2.5}$$

Equating (2.3), (2.4) and (2.5) gives

$$\gamma = \frac{e}{2m} \tag{2.6}$$

Thus the magnetogyric ratio is inversely proportional to the mass of the nucleus.

Since the frequency at which any species undergoes NMR is directly related to its magnetogyric ratio it follows intuitively that the lighter the nucleus the higher its resonant frequency. There are, however, exceptions to this rule, fluorine being an obvious example. $^{31}P$ also resonates at a higher frequency than $^{13}C$ despite being the heavier element.

## 2.3 The Nucleus in a Magnetic Field

The application of a magnetic field to the nucleus results in an interaction energy which may be represented by the Hamiltonian

$$\mathcal{H} = -\boldsymbol{\mu} \cdot \mathbf{B} \tag{2.7}$$

where $\mathbf{B}$ is the magnetic field vector. If $\mathbf{B}$ is confined along one axis only (usually defined as the z-axis) we may write

$$\mathbf{B} = B_o \hat{\mathbf{k}} \tag{2.8}$$

Generally $\mathbf{I}$ has eigenvalues given by

$$\mathbf{I}|\psi\rangle = m|\psi\rangle \tag{2.9}$$

where $m = -I, -I+1, \ldots, I-1, I$.

On application of the magnetic field the degeneracy of the energy levels in the nucleus is lifted and an axis of quantization, in this case the z-axis, is defined.

Under such conditions the interaction Hamiltonian can be represented by

$$\mathcal{H} = -\gamma \hbar B_o I_z \tag{2.10}$$

The energy eigenvalues allowed are therefore

$$E = -\gamma \hbar B_o m_z \tag{2.11}$$

where $m_z = -I, -I+1, \ldots, I-1, I$.

In the case of hydrogen $I = \frac{1}{2}$ giving just two energy levels. In order to excite a transition from a level of lower energy to one of higher energy (a net absorption of energy) it is necessary to supply a quantum of energy, in the form of electromagnetic radiation, where

$$\Delta E = \hbar \omega \tag{2.12}$$

and $\omega$ is the angular frequency of the applied radiation. Likewise, when a transition occurs from a higher energy level to a lower energy level the same quantum of energy is released. Combining equations (2.11) and (2.12) yields

$$\omega = \gamma B_o \tag{2.13}$$

It will be shown later that $\omega$, as intuition suggests, is equal to the Larmor frequency.

## 2.4 Resonance and the Rotating Frame of Reference

Classically, the equation of motion for a magnetic moment in a magnetic field is an expression of the torque exerted upon it by the field

$$\frac{d\mathbf{J}}{dt} = \boldsymbol{\mu} \times \mathbf{B} \tag{2.14}$$

The cross product implies a motion perpendicular to both $\boldsymbol{\mu}$ and $\mathbf{B}$ thus the magnetic moment precesses about the direction of the applied field.

Eliminating $\mathbf{J}$ using equation (2.3) gives

$$\frac{d\boldsymbol{\mu}}{dt} = \boldsymbol{\mu} \times \gamma\mathbf{B} \tag{2.15}$$

Using quantum mechanics it can be shown that the expectation value of the magnetic moment is described by an equation of the same form.

The vector which describes the magnetic moment can be represented in a coordinate frame of reference by

$$\boldsymbol{\mu} = \mu_x\hat{\mathbf{i}} + \mu_y\hat{\mathbf{j}} + \mu_z\hat{\mathbf{k}} \tag{2.16}$$

It is normal to think of $\hat{\mathbf{i}}$, $\hat{\mathbf{j}}$ and $\hat{\mathbf{k}}$ as being fixed with respect to time. However, this frame of reference can be specified as being able to rotate with an angular velocity $\Omega$ such that

$$\frac{d\hat{\mathbf{i}}}{dt} = \Omega \times \hat{\mathbf{i}} \tag{2.17}$$

In this case

$$\frac{d\boldsymbol{\mu}}{dt} = \frac{\partial\boldsymbol{\mu}}{\partial t} + \Omega \times \boldsymbol{\mu} \tag{2.18}$$

where $\frac{\partial\boldsymbol{\mu}}{\partial t}$ is the rate of change of $\boldsymbol{\mu}$ with respect to the coordinate system.

Equating (2.15) and (2.18) gives

$$\frac{\partial\boldsymbol{\mu}}{\partial t} = \boldsymbol{\mu} \times (\gamma\mathbf{B} + \Omega) \tag{2.19}$$

This is similar in form to equation (2.15) and may be expressed likewise

$$\frac{\partial\boldsymbol{\mu}}{\partial t} = \boldsymbol{\mu} \times \gamma\mathbf{B_e} \tag{2.20}$$

where $\mathbf{B_e} = \mathbf{B} + \frac{\Omega}{\gamma}$

Thus the motion of $\boldsymbol{\mu}$ in the coordinate system obeys the same equation of motion as in the laboratory system provided the magnetic field $\mathbf{B}$ is replaced by the effective field $\mathbf{B_e}$.

If $\Omega = \omega_o$ is chosen such that $\mathbf{B_e} = 0$ and the static magnetic field $B_o$, as defined in equation (2.8), is applied

$$\omega_o = -\gamma B_o \tag{2.21}$$

Here the rotation of $\boldsymbol{\mu}$ with respect to the coordinate system is zero but the coordinate system itself is rotating at $\omega_o$, the Larmor frequency. This is called Larmor precession and $\omega_o$ is equal in magnitude to the angular frequency required to produce magnetic resonance absorption (see equation (2.13) ).

## 2.5 Bulk Magnetization and Static Susceptibility

The symbol $\boldsymbol{\mu}$ refers to the magnetic moment of only one nuclear spin. A macroscopic sample, however, contains an ensemble of many spins which are distributed in such a way as to describe the precessional cone as shown in figure (2.1 (a)). It can be assumed that the sample consists of many identical molecules, each with one nucleus of spin $I = \frac{1}{2}$. The allowable energy states, either $m_z = \frac{1}{2}$ or $m_z = -\frac{1}{2}$, can be represented using Boltzmanns equation.

At normal temperatures the energy difference, $\Delta E = \gamma\hbar B_o$, between the two states is much less than the thermal energy $kT$ and the population difference is

$$n_L - n_U = \Delta n_o = \frac{N\Delta E}{2kT} \tag{2.22}$$

where $n_L$ and $n_U$ represent the populations of the lower and upper energy states respectively. $N$ is the total number of nuclei in the sample and $\Delta n_o$ refers to the equilibrium population of states. For $^1H$ at room temperature in a field of 2.35T, $\Delta n_o = 8 \times 10^{-6}$ indicating that $\Delta n_o$ is extremely small. This accounts, in part, for the poor sensitivity of NMR over other spectroscopic techniques.

The total magnetic moment for the sample, $\mathbf{M}$, is the resultant of the individual magnetic moments, $\boldsymbol{\mu}$, and when considering macroscopic properties may be suitably substituted. It is sometimes referred to as the "bulk magnetization".

At equilibrium $\mathbf{M}$ points along the direction of the static magnetic field, see figure (2.1 (b)), and has a magnitude

$$M_o = n_L\mu_{zL} + n_U\mu_{zU} = \Delta n_o\mu_{zL} = \frac{1}{2}\gamma\hbar\Delta n_o \tag{2.23}$$

since $\mu_{zU} = -\mu_{zL}$. Substituting for $\Delta n_o$ gives

$$M_o = \frac{N\gamma\hbar\Delta E}{4kT} = \frac{N(\gamma\hbar)^2 B_o}{4kT} \tag{2.24}$$

which is analogous to the Curie equation. This equation may be compressed further to the form

$$M_o = \chi_o B_o \tag{2.25}$$

where $\chi_o = \frac{N(\gamma\hbar)^2}{4kT}$ and is termed the "static nuclear susceptibility".

It can be seen from this expression that the sensitivity of an NMR experiment may be improved by decreasing the temperature, $T$, of the sample or increasing the static magnetic field strength $B_o$.

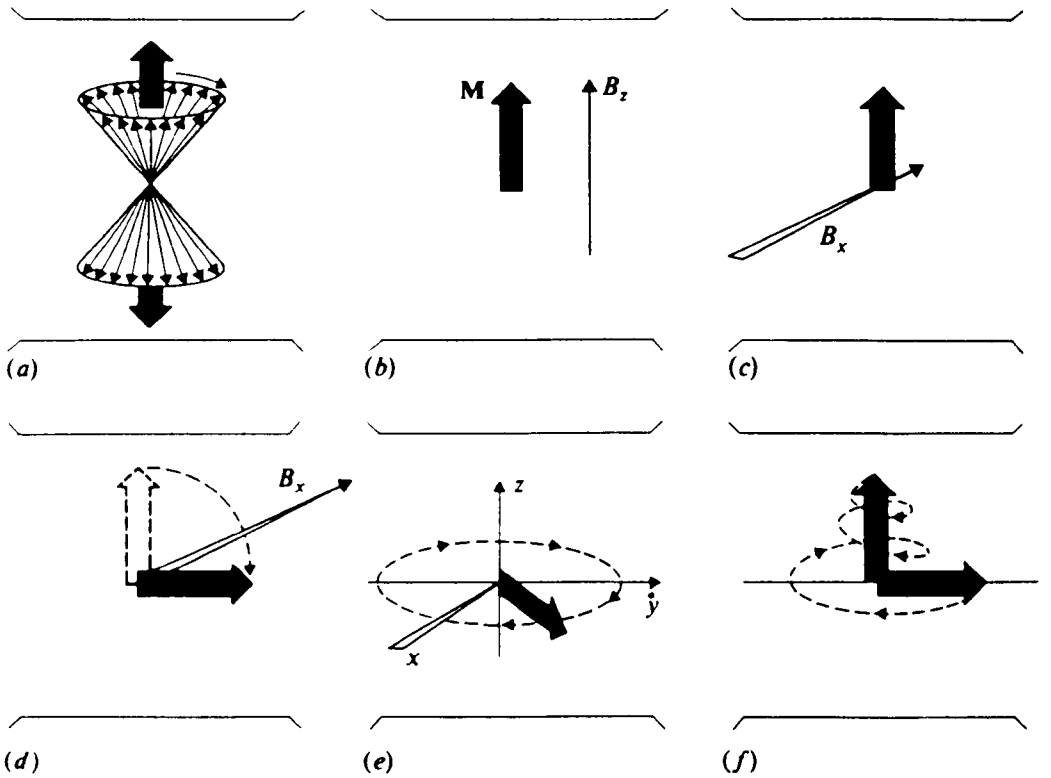


Figure 2.1: (a) the precessional "cone" of a group of spinning nuclei; (b) the resulting bulk magnetic moment vector, M; (c) the application of a 90° pulse along the x-axis; (d) the precession of M through 90° about the x-axis; (e) the additional precession of M about the main field axis; (f) relaxation and the FID: Diagram ref. [37].

## 2.6 Ensemble Response to an Alternating Magnetic Field

It is the application of an alternating magnetic (RF) field perpendicular to $B_o$ which makes resonance observable. This alternating field may be considered as a combination of two oppositely rotating fields of magnitude $B_1$ namely, $B_1(\hat{\mathbf{i}}cos\omega t + \hat{\mathbf{j}}sin\omega t)$ and $B_1(\hat{\mathbf{i}}cos\omega t - \hat{\mathbf{j}}sin\omega t)$. Near resonance, however, the component which is rotating in the opposite sense to the direction of precession of $\mathbf{M}$ may be neglected. In the general case

$$\mathbf{B_1} = B_1[\hat{\mathbf{i}}cos\omega_z t + \hat{\mathbf{j}}sin\omega_z t] \tag{2.26}$$

where $\omega_z$ is the z-axis component of $\omega$.

The equation of motion of $\mathbf{M}$ incorporating both static and alternating magnetic fields is given by

$$\frac{d\mathbf{M}}{dt} = \mathbf{M} \times \gamma(\mathbf{B} + \mathbf{B_1}(t)) \tag{2.27}$$

The time dependence of $\mathbf{B_1}$ is removed when transposed into a frame of reference which is rotating at the frequency $\omega_z$. Setting $\omega_z = -\omega$ and expanding equation (2.27) yields

$$\begin{aligned} \frac{\partial \mathbf{M}}{\partial t} &= \mathbf{M} \times \gamma \left[ \hat{\mathbf{k}} \left( B_o - \frac{\omega}{\gamma} \right) + \hat{\mathbf{i}} B_1 \right] \\ &= \mathbf{M} \times \gamma \mathbf{B_{eff}} \end{aligned} \tag{2.28}$$

where $\mathbf{B_{eff}} = \hat{\mathbf{k}}(B_o - \frac{\omega}{\gamma}) + \hat{\mathbf{i}}B_1$.

Thus if $\mathbf{M}$ was initially aligned along the z-direction it will periodically return there during its precession around the effective field $\mathbf{B_{eff}}$, as shown in figure (2.2).

## 2.7 RF Pulses and Free Induction Decay

When the resonance condition is fulfilled exactly ($\omega = \gamma B_o$) the effective field is simply $\hat{\mathbf{i}}B_1$ and the equation of motion for $\mathbf{M}$ becomes

$$\frac{\partial \mathbf{M}}{\partial t} = \mathbf{M} \times \gamma \hat{\mathbf{i}} B_1 \tag{2.29}$$

$\mathbf{M}$ now precesses about $B_1$ and is periodically in alignment against $B_o$.

If $B_1$ is pulsed for a short time only $\mathbf{M}$ precesses through an angle $\theta$ determined by

$$\theta = \gamma B_1 \tau_p \tag{2.30}$$

where $\tau_p$ is the duration of the pulse.

If $\tau_p$ is chosen such that $\theta = \pi$, then $\mathbf{M}$ is simply inverted to point in the opposite direction to that of $B_o$. Such a pulse is referred to as a "180 degree

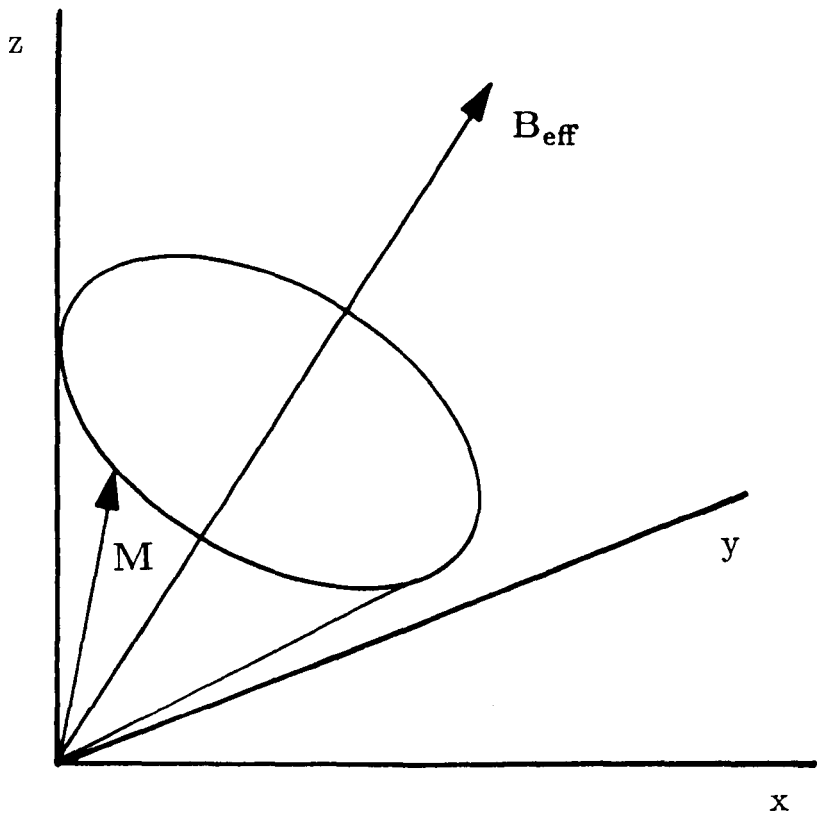


Figure 2.2: Precession of the magnetic vector **M** around the effective field $\mathbf{B_{eff}}$.

pulse". If $\theta = \frac{\pi}{2}$ then the pulse is called a "90 degree pulse" and **M** is turned from the z-direction to the y-direction (assuming $B_1$ is applied along the x-direction).

Magnetic resonance may be observed by placing the chosen sample in a coil the axis of which lies perpendicular to $B_o$. The sample is allowed to reach a state of thermal equilibrium i.e. when the magnetization has relaxed to point along the direction of $B_o$. A 90 degree pulse, when applied, tips **M** into the transverse (x,y) plane about which it precesses at the resonant frequency. The precession of **M** produces an alternating flux through the coil which induces an observable e.m.f. This e.m.f. does not continue indefinitely but decays away due to relaxation processes (see section 2.9) as the individual spins interact with each other and with their surroundings. This decaying e.m.f. is called the "Free Induction Decay" or FID and is illustrated in figure (2.1).

## 2.8 The Bloch Equations

The theoretical model used so far to describe the dynamics of the sample magnetization does not include terms to account for the interactions which result in the return of **M** to its equilibrium value following RF excitation.

Energy lost between spins and their surroundings is characterized by the relaxation time $T_1$ called the "spin-lattice relaxation time". Energy exchanged between spins is characterized by $T_2$, the "spin-spin relaxation time".

Bloch modified the equation of motion for **M** with the introduction of these constants. The full Bloch equations are therefore

$$\begin{aligned} \frac{dM_x}{dt} &= \gamma(\mathbf{M} \times \mathbf{B})_x - \frac{M_x}{T_2} \\ \frac{dM_y}{dt} &= \gamma(\mathbf{M} \times \mathbf{B})_y - \frac{M_y}{T_2} \\ \frac{dM_z}{dt} &= \gamma(\mathbf{M} \times \mathbf{B})_z + \frac{M_o - M_z}{T_1} \end{aligned} \tag{2.31}$$

where $\mathbf{B} = B_o + B_1(t)$

The Bloch equations are mostly used to model the dynamics of the individual components (x,y,z) of sample magnetization following any interactions with the spin system.

## 2.9 Relaxation Mechanisms

### 2.9.1 Spin-lattice Relaxation

Integrating the term which contains the $T_1$ dependence as given by the Bloch equations yields

$$M_z = M_o(1 - e^{-\frac{t}{T_1}}) \tag{2.32}$$

Therefore if $M_z$ is the z-component of the bulk magnetization it will achieve a maximum value equal to $M_o$ after a time $T_1$ measured from when the initially unmagnetized sample is placed in a magnetic field.

$T_1$ is thus a measure of the time taken for the sample to become magnetized and the sample is said to be magnetized when **M** is aligned with $B_o$.

Equation (2.32) also describes the relaxation, following an RF pulse, of **M** *along* the axis of the static magnetic field. This process of realignment of the nuclear spins is a return of the system to a state of lowest energy. In this state more spins are aligned with the static field than against, the proportions of which are described by the Boltzmann distribution (see equation (2.24)). The alignment process involves the transfer of energy to and from the reservoir or lattice in which the molecules associated with the spins are contained, hence the term spin-lattice relaxation. Because this effect occurs along the axis of the main magnetic field it is sometimes called "longitudinal relaxation".

$T_1$ may be measured in a sample by first applying a $180^o$ pulse as shown in figure (2.3). This inverts **M** such that it points along the $-$z-direction. **M** can then be interrogated by the application of $90^o$ pulses at successive time intervals. Each time a $90^o$ pulse is applied **M** is tipped into the xy-plane where it is now able to induce an e.m.f. in the receiver coil. The intensity of the signal received immediately after the $90^o$ pulse is directly proportional to the magnitude of **M** at the time of that pulse.

The spin-lattice relaxation is effectively "frozen" at various times following the initial inversion pulse. The intensity of each measured signal when plotted against a time axis follows an exponential decay similar to that described in equation (2.32). See also figure (2.3).

### 2.9.2 Spin-spin Relaxation

Spin-spin relaxation, characterized by the constant $T_2$, is the process in which the net magnetization in the xy-plane, following an RF pulse, is destroyed. On application of a $90^o$ pulse **M** is tipped into the xy- (transverse) plane. From this point onwards the total observed magnetization decays at a rate much quicker, in some materials, than can be described by the processes associated with longitudinal relaxation.

When **M** is initially placed in the transverse plane all the spins are in phase. The spins themselves, being effectively small magnets, can add or subtract from the main magnetic field, $B_o$, depending on their orientation. This has the effect of changing the local magnetic field that the spin, or spins in close proximity, see. As a result the spins begin to precess at slightly different frequencies and phase coherence is lost. The spins eventually fan out around the transverse plane and the net magnetization averages to zero.

Random spin-spin interactions are not the only mechanism by which spin coherence is lost. Clearly the magnitude of the spin-spin interactions is very

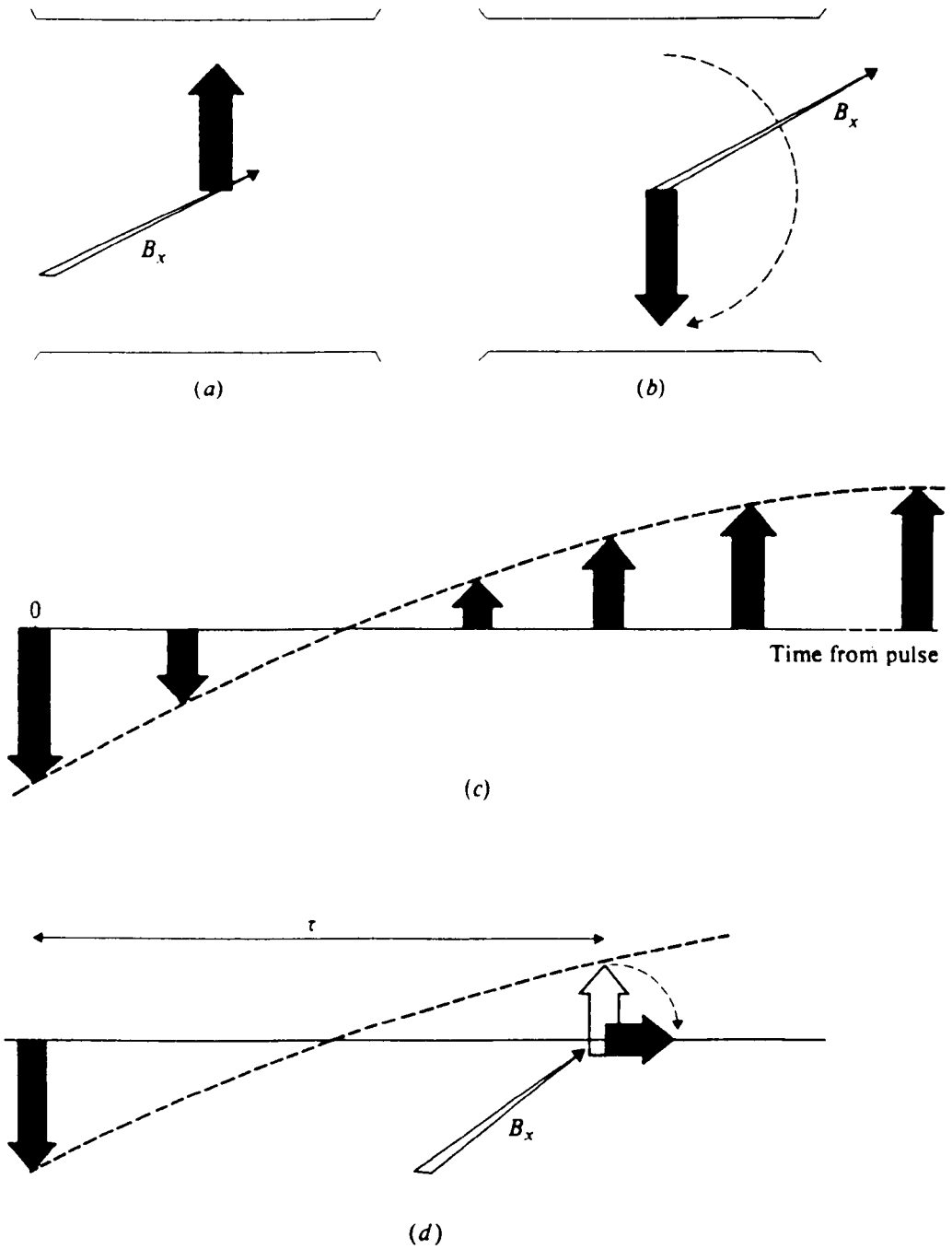


Figure 2.3: A $180^o - \tau - 90^o$ pulse sequence and its effect on M. (a) Application of a $180^o$ pulse; (b) rotation of M to face along $-z$-axis; (c) relaxation of M to equilibrium value; (d) interrogation of M after time $\tau$ using a $90^o$ pulse: Diagram ref. [37].

small indeed and main field fluctuations occur on a larger scale due to inherent imperfections in the magnet. These magnetic field inhomogeneities produce a similar effect which tends to mask the smaller spin-spin interactions resulting in a faster transverse relaxation than predicted by purely random processes.

The transverse relaxation time therefore consists of two components. If $T_2$ is the component associated with the random spin-spin interactions and $(\gamma \Delta B_o)/2$ the component associated with the main field inhomogeneities, the observed resonance linewidth is given by

$$\Delta f_{1/2} = \frac{1}{\pi T_2^*} \tag{2.33}$$

where $\frac{1}{T_2^*} = \frac{1}{T_2} + \frac{\gamma \Delta B_o}{2}$

## 2.10 Spin Echoes

The dephasing of spins which occurs in the transverse plane due to main field inhomogeneities can be reversed by the application of a $180^o$ pulse following the initial $90^o$ pulse. The way in which this can be visualized is shown in figure (2.4).

Once in the transverse plane the magnetization begins to fan out as the individual spins lose coherence. The application of a $180^o$ pulse at a time $\tau$ flips the spins about the x-axis from the y-axis to the $-$y-axis. The spins that were fanning out are now travelling in the opposite sense and the magnetization is re-phased along the $-$y-axis at a time $2\tau$ from the initial $90^o$ pulse. The re-phasing and subsequent dephasing process appears as an echo of the initial FID.

### 2.10.1 Measurement of $T_2$

The phenomenon described above is used in the measurement of $T_2$ and the sequence is called a $90^o - \tau - 180^o$ sequence (see figure (2.5)).

The $90^o$ pulse is applied followed by a $180^o$ pulse at time $\tau$. The signal reaches a maximum at $2\tau$ and begins to decay again. At $3\tau$ another $180^o$ pulse is applied and the signal builds up to a maximum again at $4\tau$. This new maximum will be lower in amplitude than the previous one due to spin-spin interactions which are not refocused by the pulse. The $180^o$ pulse can be applied repeatedly at intervals of $\tau, 3\tau, 5\tau$ etc. The signal intensities measured at $2\tau, 4\tau, 6\tau$ follow an exponential decay with a time constant determined by $T_2$.

## 2.11 Gradient Echoes

Following RF excitation, the application of a magnetic field gradient across the sample (essential to all imaging techniques) is, in effect, the same as

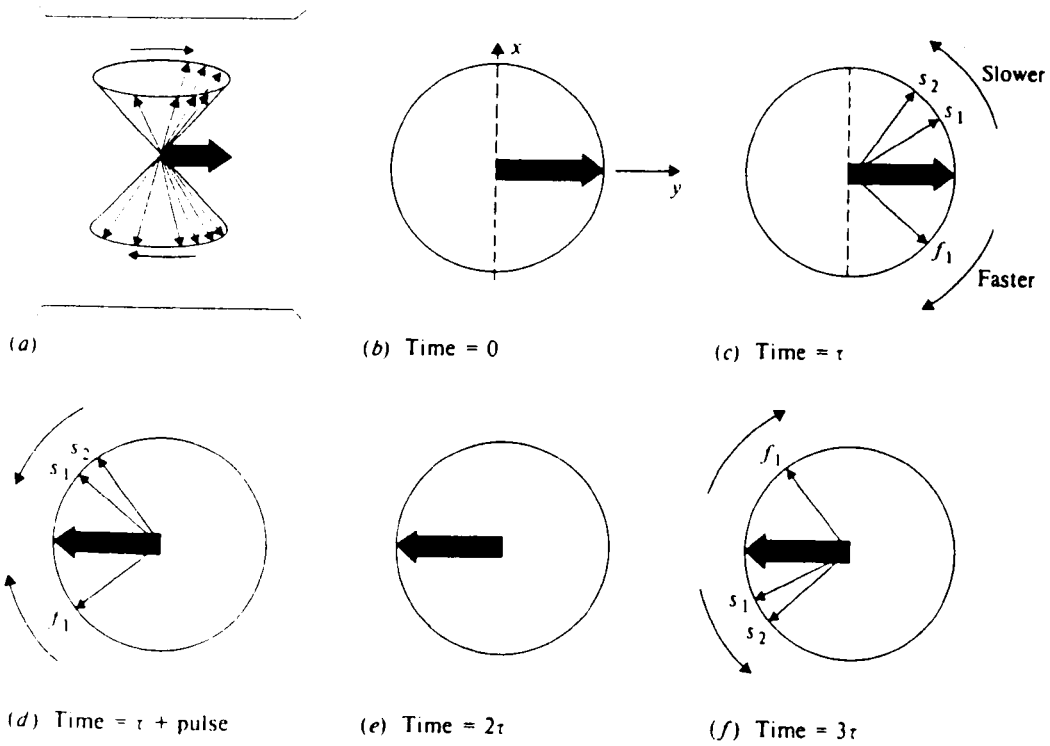


Figure 2.4: The bunching of nuclear spins after a 90° pulse and the effect of a subsequent 180° pulse. (a) Bunching of nuclear spins; (b) total magnetic vector; (c) loss of spin phase coherence (de-phasing); (d) spins begin to re-phase following 180° pulse; (e) magnetic vector re-phased at time $2\tau$; (f) de-phasing begins again: Diagram ref. [37].

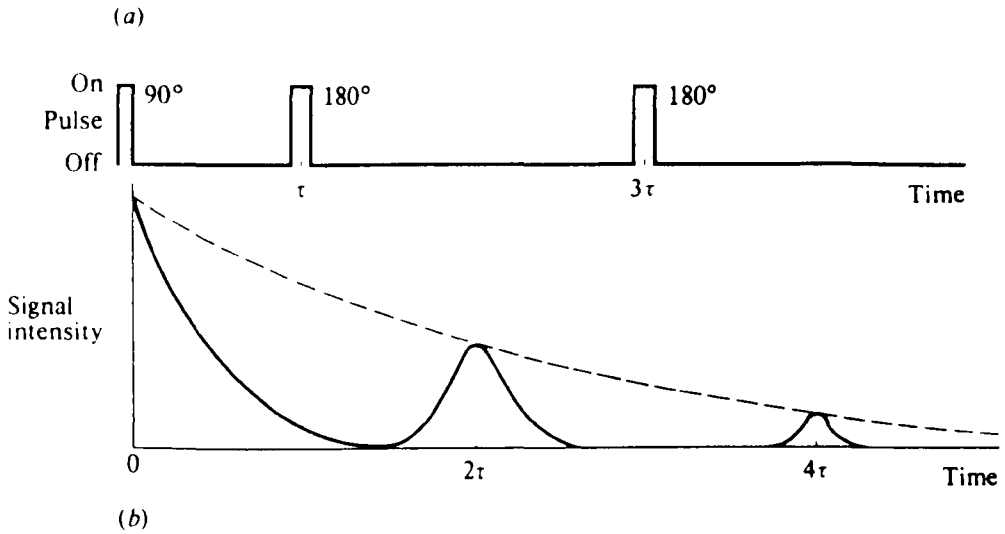


Figure 2.5: (a) the pulse timing diagram of a $90^o - \tau - 180^o$ sequence for the measurement of $T_2$ and (b) the resultant spin echoes: Diagram ref. [37].

making the main magnetic field inhomogeneous for a short time (albeit in a controlled manner). The magnetization therefore dephases more quickly under a gradient since all the spins see a different magnetic field dependent upon their position within the sample. If the gradient is left on for long enough the magnetization becomes completely dephased in a time much less than the natural $T_2$ of the sample. This ploy is often used to "spoil" unwanted magnetization at the end of or even during an imaging experiment. If, however, the gradient is first applied for a specific duration and then reversed in amplitude for twice this duration a "Gradient echo" is formed whereby the magnetization which was dephased under the negative gradient lobe is re-phased again under the positive lobe. The gradient echo does not refocus the dephasing due to the inherent magnet inhomogeneities or sample susceptibilities thus the amplitudes of successive echoes decrease at a faster rate than would be observed in the case of spin echoes.

Echo Planar Imaging (EPI) acquires a complete image from a train of gradient echoes although spin echoes may just as easily be used.

## 2.12 Chemical Shift

All nuclei in atoms and molecules have associated with them a number of orbital electrons. When placed in a magnetic field these surrounding electron clouds tend to circulate in such a direction as to produce a field *opposing* that applied. The total field experienced by the nucleus is

$$B_{effective} = B_o - B_{induced} \tag{2.34}$$

and, since the induced field is directly proportional to the applied field

$$B_{induced} = \sigma B_o \tag{2.35}$$

where $\sigma$ is the shielding constant. Substitution yields

$$B_{effective} = B_o(1 - \sigma) \tag{2.36}$$

Thus the nucleus is said to be shielded from the applied field by diamagnetic electronic circulation. The extent of this shielding is constant for a given atom in isolation but varies with the electron density about an atom in a molecule. Depending on the physical structure of a molecule some nuclei may experience a higher $B_{effective}$ than the applied field. These nuclei are said to be de-shielded.

The effect of these chemically associated field perturbations results in a shift of the resonant frequency for nuclei in different chemical environments and it is this phenomenon which is exploited in NMR spectroscopy. The effect is called chemical shift and may be expressed as

$$\delta = \left( \frac{f - f_{TMS}}{f_{TMS}} \right) 10^6 \tag{2.37}$$

where $\delta$ is the chemical shift in parts per million (p.p.m.) of the sample. $f$ is the resonant frequency of the species of interest and $f_{TMS}$ is the resonant frequency of a reference sample, usually TMS (tetramethylsilane).

The chemical shift effect can be observed in images where more than one chemical species are present. In the human body the effect is most noticeable between fat and water. The fat image is seen shifted slightly from the water image and can be cause for confusion. The problem, however, is usually eliminated in the slice selection stage of the imaging process (see chapter 3).

## 2.13 Bulk Susceptibility

In addition to the chemical shift effect minor perturbations in the static field arise due to the overall magnetic properties of the environment containing the resonant species. This further effect is termed the "bulk susceptibility" effect and is usually less than 1 p.p.m.. It occurs mainly at boundaries within the sample. In the human body, for example, going from fat to liver causes $B_o$ to change a little, simply because of the change in physical structure. The effect is noticeable in images by the loss of signal and distortion which can occur at distinct structural interfaces.

## 2.14 Continuous Wave (CW) NMR

A continuous wave NMR experiment may be performed in two ways. Using a fixed main field the sample is subject to electromagnetic radiation which is scanned through the frequency range of interest. Alternatively, the RF field can be applied at a fixed frequency and the magnetic field swept to bring successive nuclei into resonance.

The steady state solution for the Bloch equations in a low amplitude $B_1$ field are given by

$$\chi' = \frac{\chi_o \omega_o T_2}{2} \left( \frac{(\omega_o - \omega) T_2}{1 + (\omega - \omega_o)^2 T_2^2} \right) \tag{2.38}$$

$$\chi'' = \frac{\chi_o \omega_o T_2}{2} \left( \frac{1}{1 + (\omega - \omega_o)^2 T_2^2} \right) \tag{2.39}$$

where $\omega_o$ is the resonant frequency of the sample, $\omega$ is the frequency of the applied RF field and $\chi_o$ is the static susceptibility. $\chi'$ and $\chi''$ represent the complex susceptibility of the sample and can be expressed

$$\chi_o = \chi' + i\chi'' \tag{2.40}$$

$\chi'$ is the signal derived from the component of magnetization along the direction of the rotating $B_1$ field and is known as the dispersion mode signal. $\chi''$ is 90 degrees out of phase with $\chi'$ and represents the absorption mode signal, see figure (2.6).

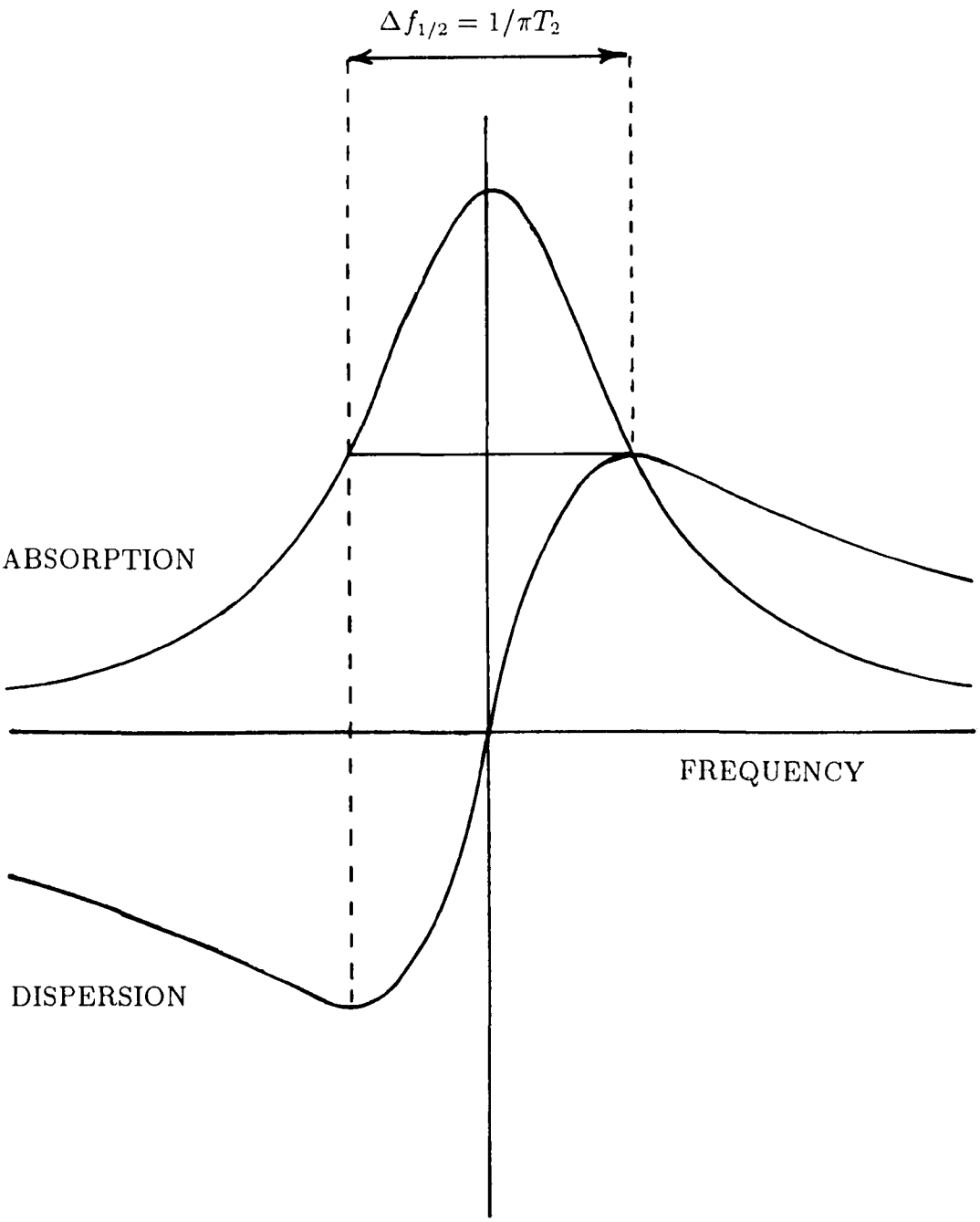


Figure 2.6: The Lorentzian lineshapes observed in an NMR experiment.

## 2.15 Fourier Transform (FT) NMR

Fourier transform NMR is the preferred mode of operation of most of the state-of-the-art spectrometers in use today. It gained popularity in the 1960's replacing CW techniques for most applications.

The technique of FT NMR involves irradiating the sample with a wide band of frequencies achieved by applying a short intense RF pulse (the bandwidth of which is inversely proportional to pulse duration). The signal induced in the receiver coil is the sum of responses from all the resonant species present. The individual frequency components are separated upon Fourier transformation of the recorded time data (FID).

The advantage of the FT approach is the saving in time it offers since the flow of data/unit time is much greater than in CW techniques. Transmission of the RF field and reception of the nuclear signal are two separate functions in time in FT NMR therefore only one RF coil is required.

# Chapter 3: Imaging Principles and Modalities

## 3.1 Introduction

In this chapter the basic concepts of NMR imaging (MRI) are introduced with the main emphasis being placed on the more popular techniques such as 2D-FT, FLASH and EPI. Also included is a brief description of 3D imaging. A more detailed treatment of the latter, in application to Echo Volumar Imaging (EVI), is left until chapter 5.

Full reviews covering all aspects of the historical and scientific development of MRI are given elsewhere [28, 33].

## 3.2 Magnetic Field Gradients

The basis of all imaging techniques is the response of the spin system, following RF excitation, to applied magnetic field gradients. In a static, non-spatially varying magnetic field all the spins in a sample will undergo resonance at approximately the same Larmor frequency. This situation offers no means of gaining information about the spatial variation of spin density.

If the static field is made to vary spatially however, each spin within the sample will resonate at a Larmor frequency which is dependent on its position in the magnetic field. This can be illustrated by considering a uniform magnetic field gradient

$$G_x = \frac{\partial B_z}{\partial x} \tag{3.1}$$

which produces a net magnetic field in the z-direction given by

$$B_z = B_o + xG_x \tag{3.2}$$

The angular frequency of precession of spins lying at a position $x$ in the gradient is thus

$$\omega(x) = \gamma(B_o + xG_x) \tag{3.3}$$

There is clearly a spatial dependence of the angular frequency which is the same for all spins lying in the plane normal to the x-direction.

The FID following a $90^o$ pulse, excluding relaxation mechanisms is given by

$$S(t) = \int_{\infty}^{-\infty} \int_{\infty}^{-\infty} \rho(x,y) e^{i\gamma G_x x t} dx dy \tag{3.4}$$

where $\rho(x,y)$ is the spin density distribution of the sample. Fourier transformation of this signal yields the one-dimensional projection of spin density in the direction normal to the applied gradient.

## 3.3 Selective Excitation

In most imaging experiments it is preferable to limit sample excitation and hence signal emission to the region of interest only. This is performed using selective excitation in which only a thin slice of the extended sample is excited, see figure (3.1). The idea was first introduced in 1974 [14] and is now employed in all commercial imaging systems.

To illustrate how selective excitation works it is instructive to think of the excited slice of comprising a number of equally spaced discrete frequency pulsed oscillators each producing an RF signal of given phase and amplitude. Figure (3.2 (a)) represents such a set of oscillators of common phase and amplitude with frequency separation $\Delta\omega$.

The RF envelope required to produce the above spectral distribution is shown in figure (3.2 (b)). If an RF pulse modulated in such a fashion is applied, in the presence of a uniform magnetic field gradient, for a time $T$ and then switched off, each of the spins contained within the bandwidth defined by the pulse and gradient will be excited and resonate at its own frequency.

The introduction of the gradient during RF excitation means that the spread of Larmor frequencies along the axis to which it is applied will be much greater than the RF pulse bandwidth and thus only a very narrow slot of spins will be excited. The slice thickness may be adjusted by increasing or decreasing the gradient, the higher the gradient the narrower the selected slice. In addition, the bandwidth of the RF pulse must be sufficiently wide enough to include the high frequency modulations required to define as sharp a profile as possible.

Each discrete frequency in the slot produces a non-equilibrium magnetization distribution, $(m_x, m_y)$, which has a spatially integrated net $M_y$ component but a zero net $M_x$ component. For all the discrete frequencies approximating the rectangular slice profile $M_y$ evolves as shown in figure (3.2 (b)). The final spatial distribution of magnetization $m_x$, $m_y$ at turn-off is summarized in the phase plot, $m_y$ versus $m_x$, of figure (3.2 (c)). As is shown the net $M_y \neq 0$ but $M_x = 0$. The lobe however is not very directional.

The directionality of the lobe can be improved by changing the temporal phase of the RF pulse such that it starts and ends at zero amplitude as shown in figure (3.3 (a)). This corresponds to the oscillators being initially alternately in antiphase. The effect of this is to place half of the net $M_y$ magnetization along the y-axis and half along the $-$y-axis. This may at first seem counter productive. However, if the selection gradient is reversed without RF for a time $T/2$ the precessional angle $\Delta\omega T/2\pi$ is exactly right to bring spins along $-m_y$ into phase along $+m_y$ in the extra time interval $T/2$. Components of magnetization already along $+m_y$ will remain there and residual components along $\pm m_x$ will also be brought partially into phase. Thus the net effect of gradient reversal is a focusing of magnetization to give more directionality to the phase lobe, see figure (3.3 (b)).

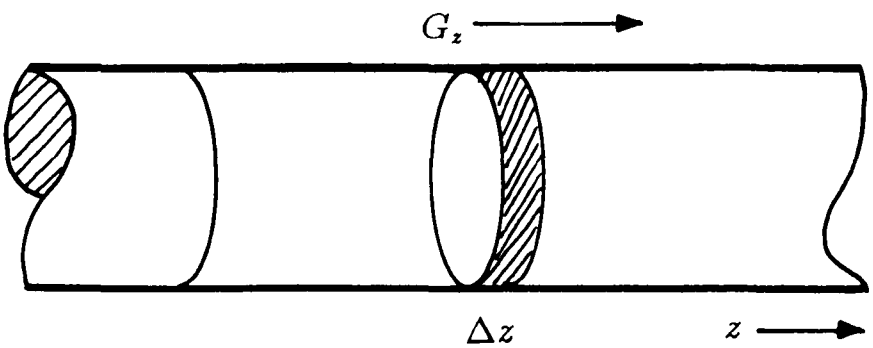


Figure 3.1: Slice selection from an extended object in a gradient.

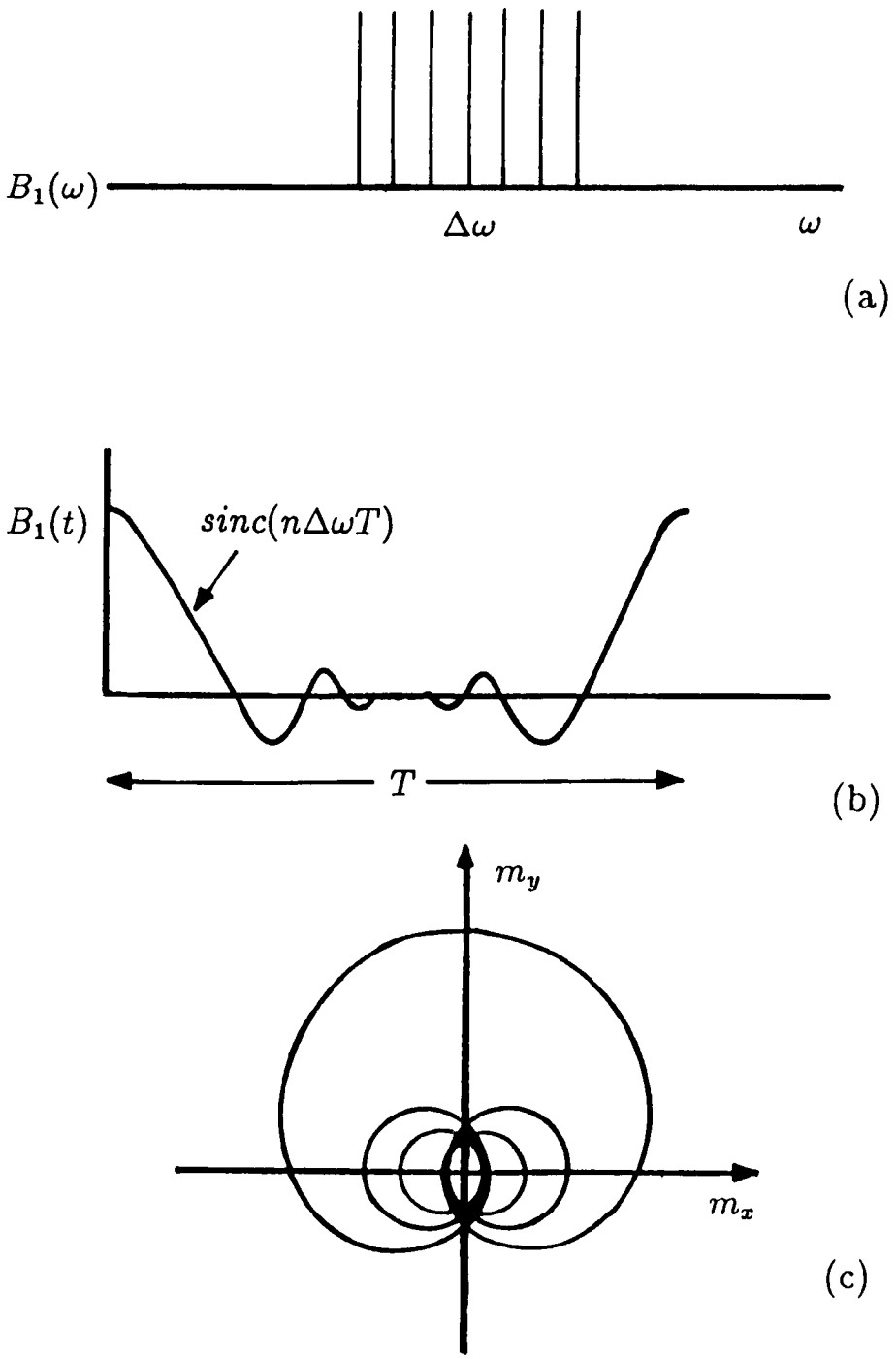


Figure 3.2: Selective pulse details. (a) Spectral distribution function for a selective pulse composed of seven discrete-frequency oscillators with equal amplitude. (b) Time evolution of RF envelope over one period. (c) Phase diagram for spins in selected slice following RF switch-off at time $T$.

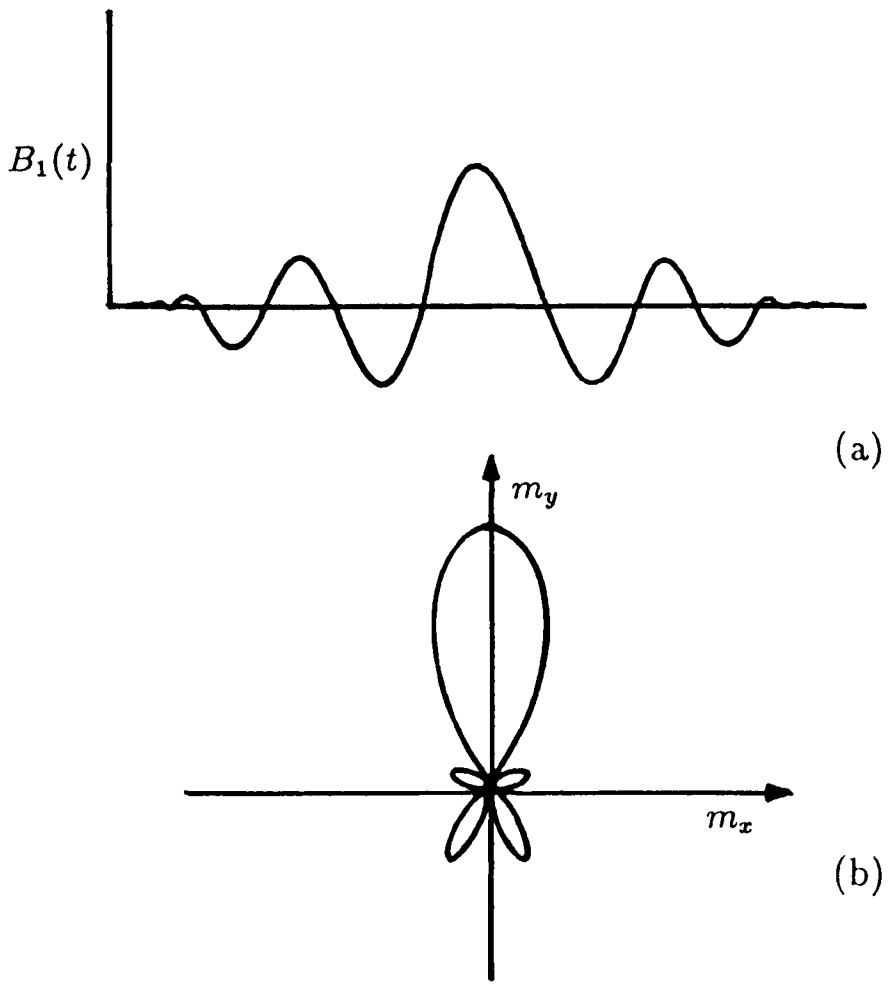


Figure 3.3: (a) Re-ordered selective pulse envelope. (b) Typical phase lobe of spin magnetization in a selected slice using pulse envelope as in (a) together with gradient reversal.

The complete slice selection procedure is shown in figure (3.4).

More recently the procedure of slice selection has been refined such that selection may be done without the need to reverse the gradient lobe. These "self refocusing pulses" rely on being able to predict the behaviour of the magnetization using the Bloch equations [35].

## 3.4 The Concept of k-space

Reciprocal lattice, or "k-space", is used frequently in Fourier optics where k has the units of *1/distance* and represents a spatial frequency. As such, the intrinsic resolution of an image can be quantified in terms of the maximum spatial frequency (value of k) present in the diffraction pattern which is formed upon Fourier transformation of the image (optical or digital).

Mansfield and Grannell [11] introduced the k-space concept to MRI when they realized the analogy between the expression for the signal recorded in an imaging experiment to that which describes plane wave scattering. Essentially, the time signal recorded in the MRI experiment represents the diffraction pattern of the object being imaged. All the rules which apply to the optical case are similarly applicable in the MRI case. Indeed, optical reconstruction from MRI diffraction patterns has been attempted [34].

The signal following a $90^o$ pulse, excluding relaxation, can be represented by

$$S(t) = \int \rho(\mathbf{r}) e^{i\gamma \int_0^t \mathbf{r}.\mathbf{G}(t')dt'} d\mathbf{r} \tag{3.5}$$

This is identical to equation (3.4) except for a more general approach the letter $\mathbf{r}$ has been substituted to represent position. Thus $\rho(\mathbf{r})$ is the spin density at position $\mathbf{r}$.

Equation (3.5) may be written differently by introducing the reciprocal space wave vector $\mathbf{k}$ where

$$\mathbf{k} = \int_0^t \gamma \mathbf{G}(t')dt' \tag{3.6}$$

Substitution into equation (3.5) yields

$$S(\mathbf{k}) = \int \rho(\mathbf{r}) e^{i\mathbf{k}.\mathbf{r}} d\mathbf{r} \tag{3.7}$$

Equation (3.7) is analogous to that which describes scattering of a plane wave. The wave in this case is fictitious but does have a wavelength given by

$$\lambda = \frac{2\pi}{|\mathbf{k}|} \tag{3.8}$$

As mentioned previously the maximum value of $\mathbf{k}$ attainable determines the resolution in the image.

The resolution in the x-direction, for example, is given by

$$\Delta x = \frac{2\pi}{k_{max}} \tag{3.9}$$

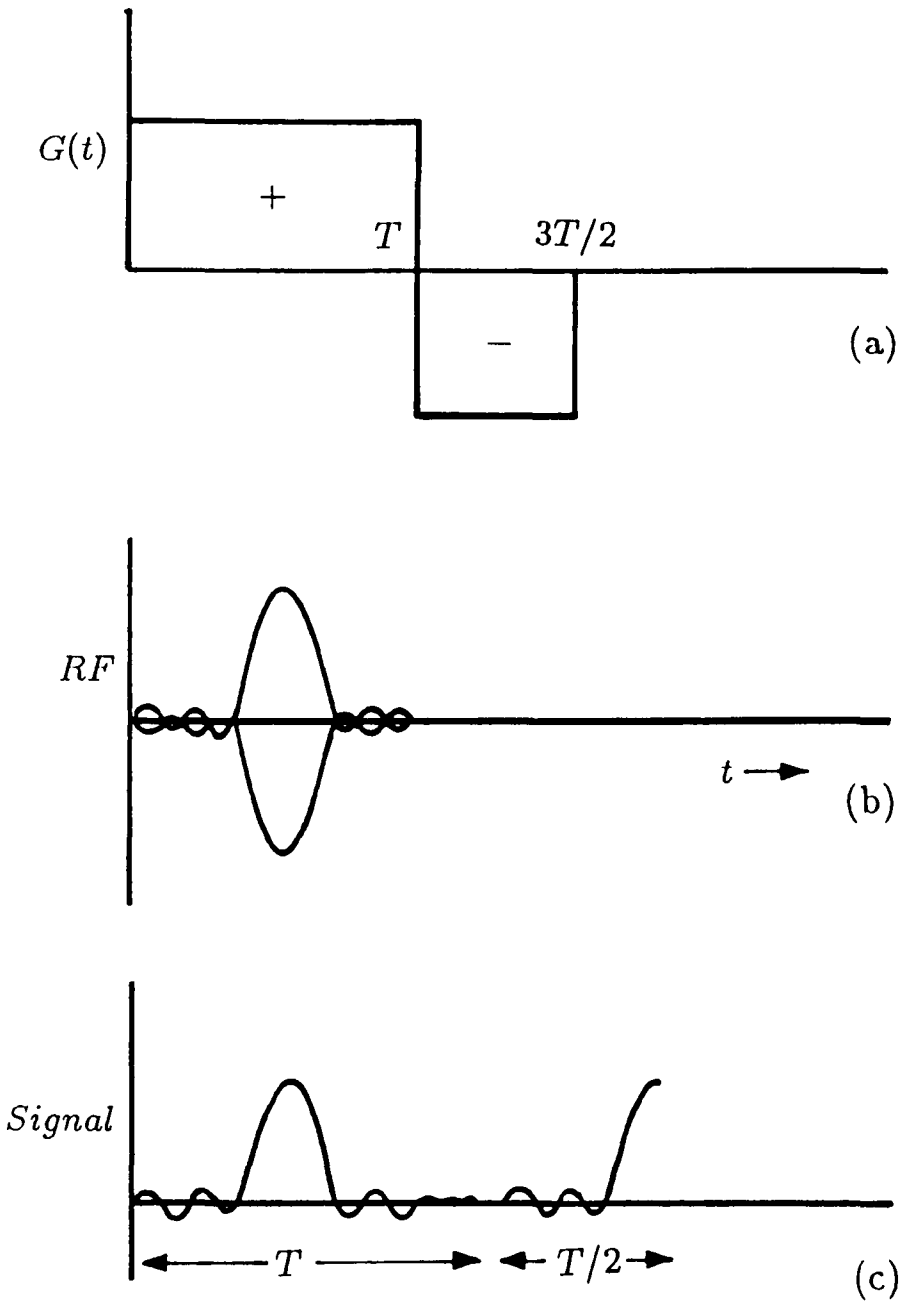


Figure 3.4: Complete slice selection: (a) Gradient waveform. (b) RF pulse envelope. (c) Signal magnetization during and after RF pulse switch-off.

For a time independent gradient the above equation may be written

$$k_{max} = \gamma G T_{dur} \tag{3.10}$$

where $T_{dur}$ is the duration of the applied gradient.

Clearly, for high resolution it is necessary to increase either $G$, the gradient amplitude or $T_{dur}$ the gradient duration.

It was pointed out by Ljunggren [36] that the way in which k-space is scanned offers a convenient way of categorizing the many different imaging sequences available. Some examples are shown in figure (3.5).

## 3.5 Standard Imaging Methods

### 3.5.1 General Imaging Regimes

Once a plane is selectively excited, a gradient can be applied along the x-axis during signal acquisition. The presence of this gradient, as described earlier, imparts a spatial dependence to the frequencies at which the spins resonate. The Fourier transform of the signal obtained is the one-dimensional projection of the object onto the x-axis. If the process is repeated with the direction of the gradient rotated by $1^o$ a new projection of the object is obtained. If the process is repeated 180 times, a reconstruction of the object from its projections can be obtained using one of the many conventional back-projection algorithms [28, 33]. This is the projection reconstruction method which Lauterbur [10] used to demonstrate MRI. Figure (3.6) shows the RF and gradient timing diagram.

At the time Lauterbur produced the first image, projection reconstruction was the obvious technique to use. Only one year before, the EMI CT scanner had been released which used X-ray projection reconstruction to produce high quality transaxial images, initially of the head and subsequently of the body. The first generation of commercial MR scanners used this technique but later generations use mainly Fourier based techniques which sample the spin density (k-space) in a more uniform manner. The projection reconstruction method is particularly susceptible to static magnetic field inhomogeneities, which give rise to streak artefacts in the image, the problem being particularly acute at high fields.

Other early imaging techniques include FONAR which stands for Field fOcused Nuclear mAgnetic Resonance. This was adopted by Damadian et al [13] in 1976 to produce the first whole body MR image.

FONAR relies on the use of shaped magnetic fields and RF pulses to isolate a small resonance aperture within the sample. Inside the aperture the magnetic field is homogeneous and produces the signal during resonance. Outside the aperture the signal dies away rapidly. After recording the signal from one position of the aperture it can be moved to a new position, a signal recorded, and so on until an image is built up. It was found easier to move

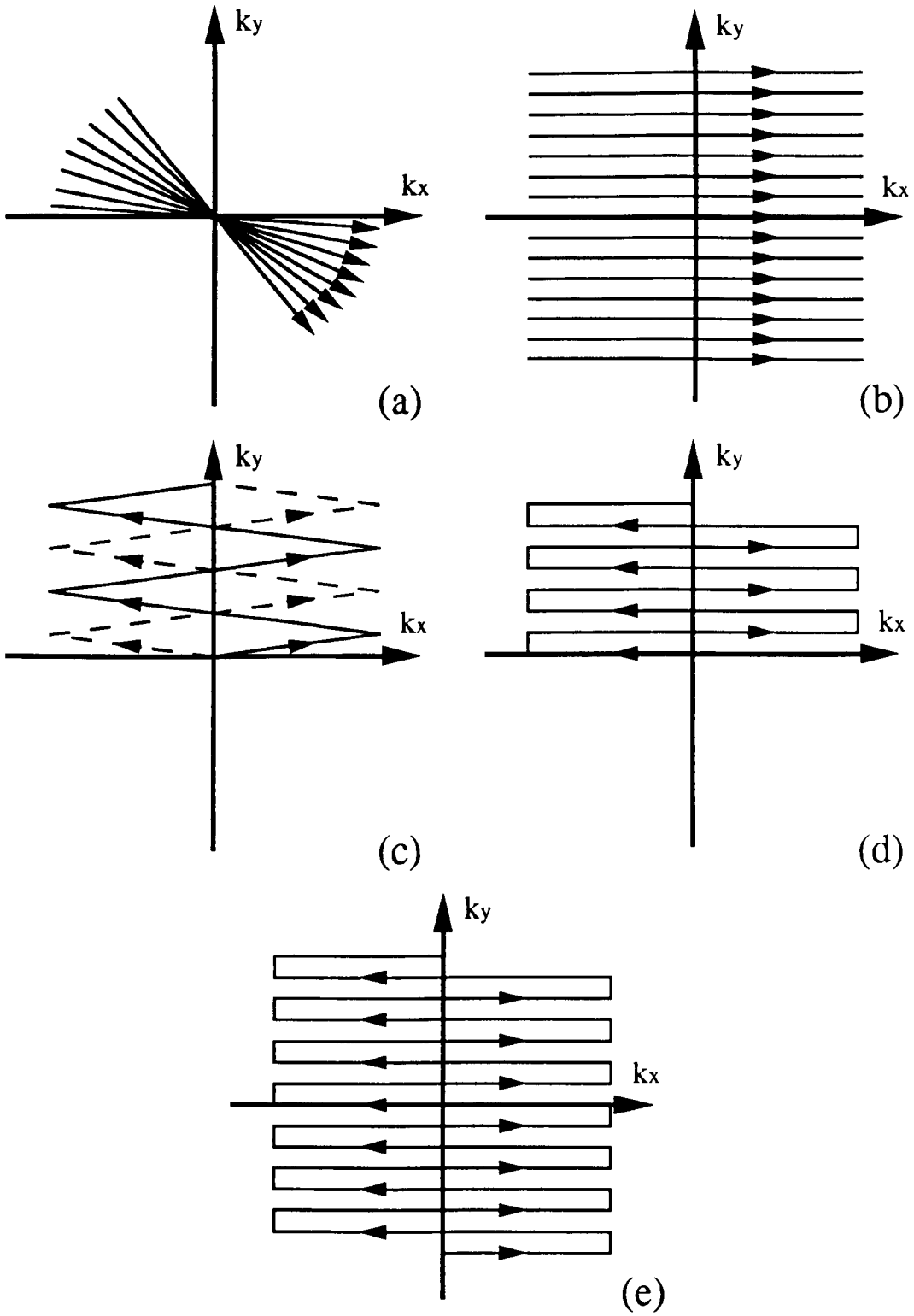


Figure 3.5: k-space trajectories, (a) Projection Reconstruction (PR). (b) Two-dimensional Fourier Transform (2DFT). (c) Double Echo Planar (DEPI), Fast Low angle Excitation EPI (FLEET). (d) Blipped EPI (BEPI), (BEST). (e) Modulus Blipped EPI (MBEST).

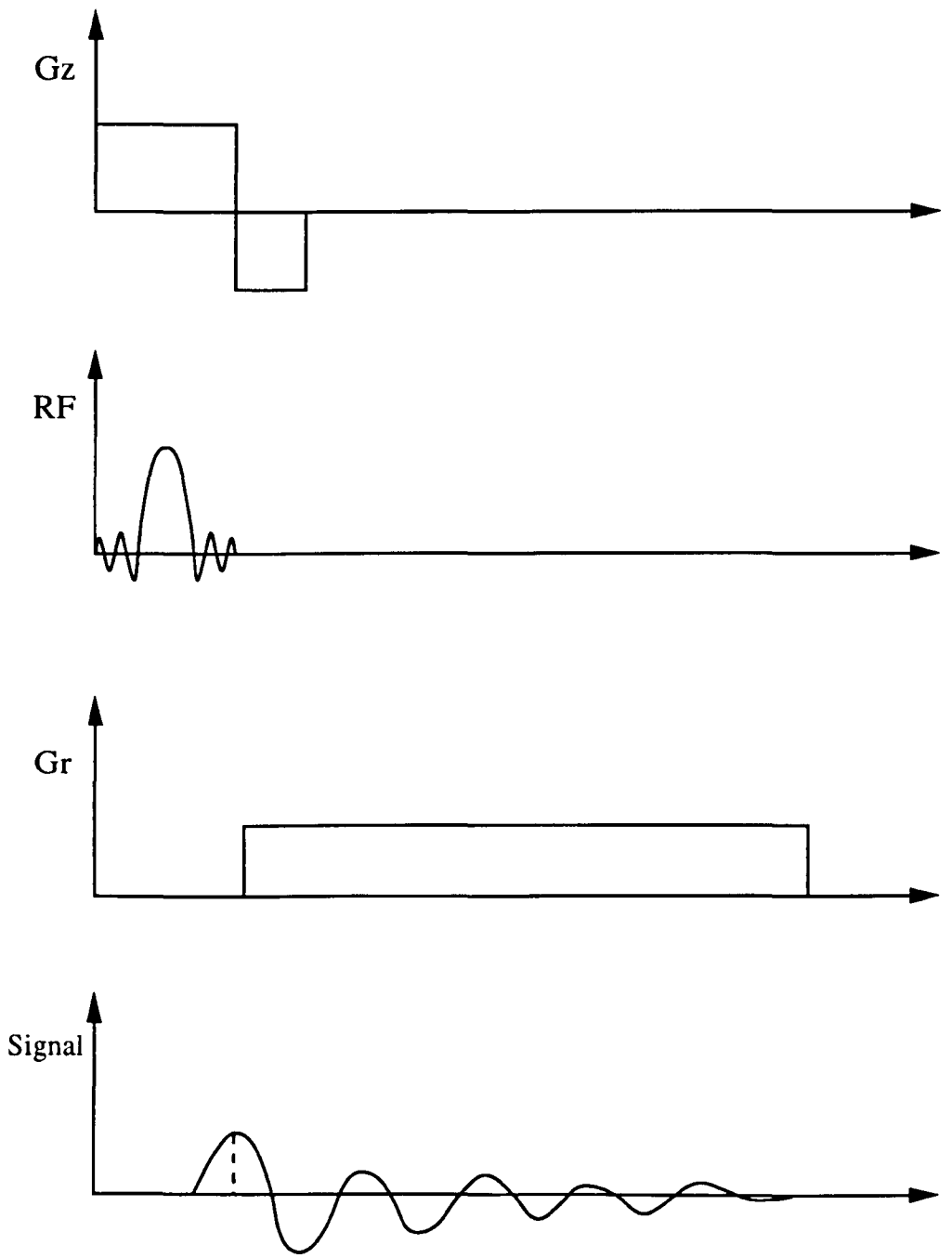


Figure 3.6: Projection reconstruction (PR) gradient and RF timing diagram.

the patient relative to the aperture rather than vice versa, however, this had the drawback of being very time consuming requiring up to 4 hours per image. Because of the nature of this technique the images produced were very crude.

A technique not unlike FONAR was the sensitive point method first introduced by Hinshaw [39] in which three mutually orthogonal oscillating field gradients are used to define a point (at their intersection) where the field is time invariant. The signal emitted from this point, following excitation, is extracted using a narrow band filter. By altering the current balance in the gradient coils the sensitive point can be steered around the sample to build up an image. Some advantages of this technique are that localized $T_1$ and high-resolution spectrum measurements can be performed without having to build up an image.

### 3.5.2 Two Dimensional Fourier Transform Imaging (2D-FT)

The most popular method used to form images and the one which is standard on most commercial MR scanners is the two dimensional Fourier transform technique (2D-FT) [15, 16]. The timing diagram is shown in figure (3.7).

Firstly, a selective excitation is performed to define the plane to be imaged. This is then followed by a phase encoding gradient $G_y$ of either stepped height or duration. A projection is then obtained along the x-axis under the "read" (frequency encoding) gradient just as in projection reconstruction. For complete coverage of k-space this sequence must be repeated the same number of times as the number of lines required in the final image. The phase encoding gradient is increased incrementally (usually from full negative to full positive for Spin-Warp) each time.

The effect of stepping $G_y$ is to make the spins lose coherence. The spins along the centre line of the xy-plane see no gradient at all, and those further away see progressively stronger gradients. If $G_y$ is very weak the loss of coherence is very gradual along the y-axis of the plane, and cancellation of signal occurs between wide bands in the object. The stronger the gradient, the more such bands are produced, until, for a 128-line image, the last projection generates 128 bands among which cancellation of signal occurs. This process encodes y-axis spatial distribution in a form which is mathematically identical to the form in which the time domain signal encodes x-axis information. The information along both axes can be decoded using the Fourier transform which has to be performed twice, once along each direction, hence the name 2D-FT.

The phase accumulated along the y-direction during the time, $t_y$, that $G_y$ is on can be represented by

$$\phi_y = \gamma y \int_0^{t_y} G_y(t)dt \tag{3.11}$$

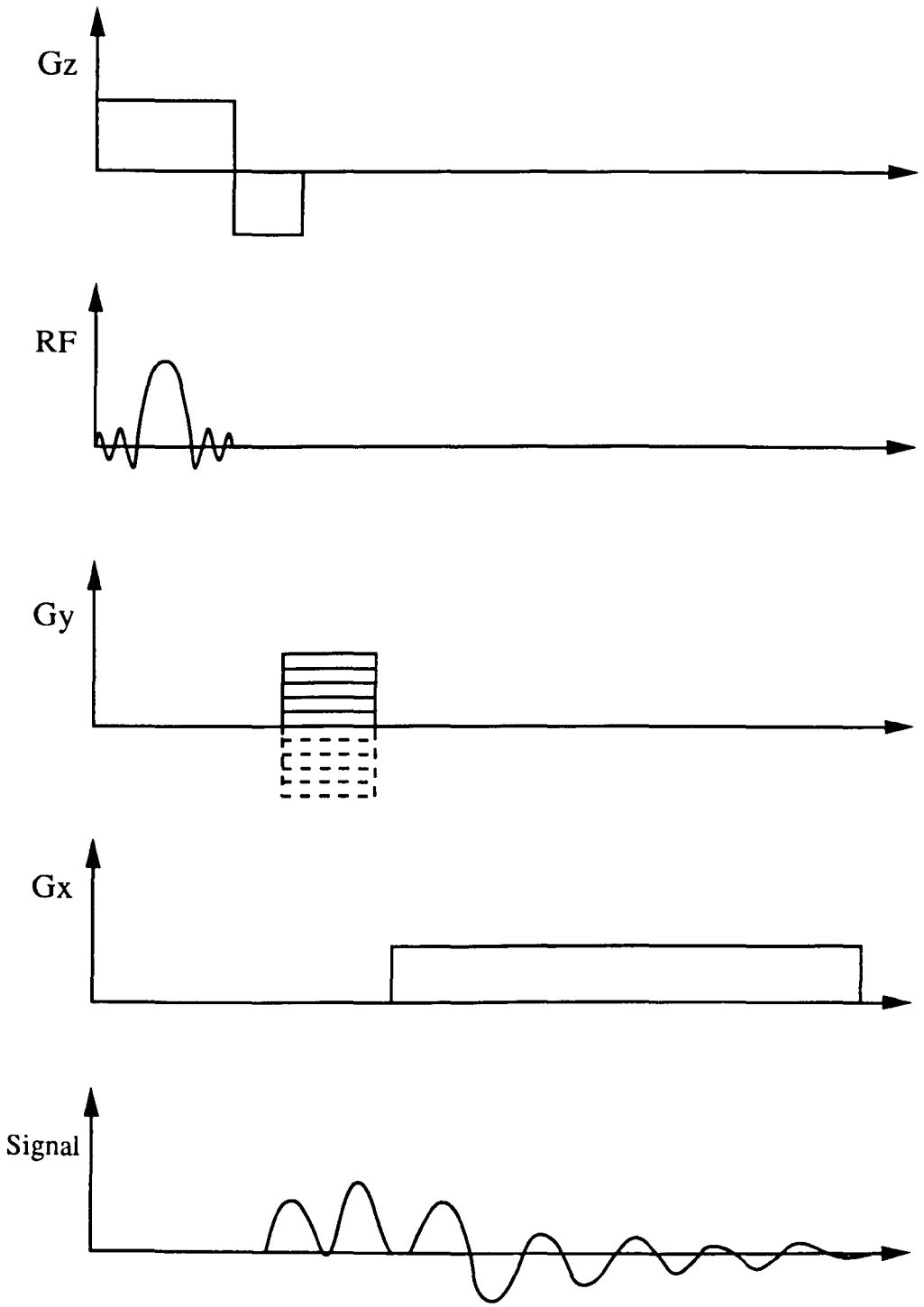


Figure 3.7: Two dimensional Fourier transform (2D-FT) gradient and RF timing diagram.

The signal in the $n$th acquisition is

$$S_n(t) = \int \rho e^{in\phi_y} e^{i\gamma G_x x T_{acq}} dx dy \tag{3.12}$$

where $n = 0, 1, 2, \ldots, N$ and $N$ is the total number of lines required in the final image.

Two extreme cases exist:

1. $G_y$ may be kept constant and $t_y$ incremented [15].
2. $t_y$ is fixed and $G_y$ incremented [16].

The latter case is the more popular technique and is often referred to as the Spin-Warp technique.

The inclusion of a $180^o$ pulse between the phase encoding step and sampling allows signal acquisition under a spin echo. This has certain advantages in that effects due to field inhomogeneities during slice selection and phase encoding are refocused. This version is referred to as Spin-Echo (SE) imaging.

### 3.5.3 Full Fourier and Partial Fourier Imaging

The appropriate k-space map for the 2D-FT technique has been shown earlier (figure (3.5)) and it is clear to see that phase and frequency encoding corresponds to scanning k-space along the $k_y$ and $k_x$ axes respectively.

When all four quadrants of k-space are scanned this is referred to as "full Fourier" imaging. After FT the data consists of real and imaginary signals for each pixel (since the signal is received in quadrature). Ideally all the data would be contained in the real image but imperfections in the MR scanner and in-vivo effects, such as flow, cause the signal to be distributed between the real and imaginary images. Taking the modulus of the two images eliminates these phase error problems.

In the ideal case the bottom half of k-space (the diffraction pattern) is the complex conjugate of the top half. In theory, given only half the data, the other half can be synthesized mathematically. All that is required then is to calculate the complex conjugate for each of the acquired data points and FT the complete data set to yield a real image. This approach is suitable only if the acquired portion of k-space is correctly phased. In reality this is very rarely the case. Various methods have been developed which estimate and correct for the phase errors [40] but these are only approximate solutions.

Partial Fourier imaging requires only just over half the normal number of phase encoding steps for a given image size. This reduces the imaging time by a half. The drawback of this technique is a reduced S/N ratio and a slight reduction in resolution if the phase of the image is not completely corrected. Gross phase errors are quite easy to correct but the higher order ones which contribute to the "sharpness" of the image are a greater problem.

### 3.5.4 Contrast in 2D-FT Imaging

In the 2D-FT sequence the length of each echo acquisition is short compared to the $T_1$ and $T_2$ of the sample. If a $90^o$ excitation pulse is used then the length of time between successive excitations is usually required to be greater than the longest $T_1$ in the sample to avoid saturation of the magnetization. If the signal is acquired immediately following slice selection the resultant image contains little contrast as the decay of the transverse magnetization has not been allowed to progress very far.

$T_2$ contrast may be introduced by increasing the time between slice selection and data acquisition. In SE imaging this involves a simple time delay between the slice selection and $180^o$ pulse. This delay is usually referred to as the echo time ($T_E$). Since the echo is sampled at a later time, spins with short $T_2$'s will contribute less signal to the image and will show up darker.

An alternative method of introducing contrast is to consider the expression for the steady state transverse magnetization produced when the spin system is subjected to a repetitive chain of pulses of flip angle $\alpha^o$, spaced $T_R$ apart.

$$M_x = \frac{M_o sin\alpha(1 - e^{\frac{-T_R}{T_1}})e^{\frac{-t}{T_2}}}{1 - cos\alpha e^{\frac{-T_R}{T_1}}} \tag{3.13}$$

Equation (3.13), given by Ernst and Morgan [41], assumes that the FID decays to zero or is spoilt prior to the next pulse. By adjusting $T_R$ between successive pulses the sample will become partially saturated as long as $T_R < T_1$. The degree of saturation depends on the $T_1$ of each spin, thus species with $T_1 \ll T_R$ will become more saturated and appear darker in the image.

The advantages of the 2D-FT type techniques are shown in their ability to produce high resolution images with good S/N ratio. The price to pay for this quality is shown in the time required to produce each image. For an $N$ lined image the sample has to undergo $N$ RF excitations complete with slice selection and phase encoding. As a consequence of this requirement there is a lot of "dead time" inherent in the technique with only a very small proportion of the imaging time involved in data acquisition. $T_R$ values can range from $0.5-3.5$ seconds and $T_E$'s from $30-90$ milliseconds. A $256^2$ image of the brain can take anything from $4-20$ minutes depending on the contrast required. In the body, objects which move during this time (i.e. heart, intestines, motion due to breathing) result in gross artefacts and blurring in the image. The temporal resolution for 2D-FT imaging is therefore very low.

## 3.6 Rapid Imaging Techniques

### 3.6.1 FLASH Imaging

Fast-Low-Angle-SHot (FLASH) imaging was introduced in 1985 [18] and in its basic form is simply the gradient echo version of 2D-FT imaging with a

very short repetition rate ($T_R$). To avoid saturation, low flip angle RF excitation pulses are used during slice selection. The optimum angle for maximum signal is generally referred to as the Ernst angle. A FLASH experiment can take between 1 and 6 seconds to perform and is an attempt to improve the temporal resolution of the 2D-FT/Spin-Warp technique.

The sequence as it stands has inherent problems. The S/N ratio can be very low and decreases as the imaging time is reduced. When very short $T_R$ is used such that $T_R < T_2$, the formation of transverse coherences is encountered leading to a bright stripe artefact in the image. Contrast is also very poor unless preceded by a spin conditioning pulse (i.e. inversion recovery).

### 3.6.2 "Snapshot/Turbo" FLASH

More recently the FLASH sequence has been condensed to allow sub-second imaging. This faster version is identical to FLASH and is sometimes referred to as "snapshot" or "turbo" FLASH. The reduced imaging time (still an order of magnitude slower than EPI) takes a further toll on the S/N ratio [42] and to be comparable with EPI in speed would incur even greater hardware demands. A very low flip angle is required to avoid image artefacts.

### 3.6.3 GRASS Imaging

GRASS stands for Gradient Recalled Acquisition in the Steady State. It is also known by other names including; refocused-FLASH, FAST, FISP, SSFP and FFE. The sequence is almost identical to FLASH except for an additional phase encoding gradient which is applied after the sampling period. This "rewinder" gradient is of equal amplitude but opposite polarity to the normal phase encoding gradient and serves to re-phase the transverse coherences which are encountered in standard FLASH. The net effect is an increase in S/N ratio and removal of coherence artefacts from the image.

## 3.7 Echo Planar Imaging

Echo Planar Imaging (EPI) was introduced by Mansfield in 1977 [17] and is a true snapshot technique which enables the formation of a complete image in $10 - 131$ ms.

The rapid nature of this technique is due to the fact that only one RF excitation is required per image. This feature, in addition, enables rapid repetition of the imaging sequence at rates approaching 10 frames per second thus enabling real time motional studies.

Following slice selection the signal is sampled in the presence of two orthogonal magnetic field gradients. One, the x-gradient ($G_x$), is modulated rapidly to form a series of gradient echoes which constitute the frequency encoding part of the experiment. The other gradient, the y-gradient ($G_y$) is applied either continuously or blipped (between $G_x$ reversal) during this period and performs the phase encoding part of the experiment. The effect

of applying a $G_y$ blip between $G_x$ reversals serves to encode each gradient echo with a different degree of phase evolution. The train of echoes is then Fourier transformed using a 1D Fourier transform although, after suitable data re-ordering, a 2D Fourier transform may just as easily be used. To form a $128^2$ image (modulus), 128 gradient echoes are required with each echo being sampled using 128 data points.

EPI has passed through many stages of development:

1. In early experiments the trajectory through k-space started at the origin (half Fourier). 32 $G_x$ echoes were acquired in approximately 32 ms in the presence of constant $G_y$. In this way only half of k-space was acquired so the data set had to be "zero filled" before Fourier transformation. To build up one image two experiments were required each one corresponding to either a positive or negative starting phase of $G_x$. The data sets were then edited by splicing together all echoes formed in a wholly positive or wholly negative gradient. Two images were produced, one of which is the left-to-right mirror image of the other. These two images, after suitable re-registration, could then be co-added to yield a $\sqrt{2}$ improvement in S/N ratio. To minimize the time between the two experiments low flip angles ($45^o - 90^o$) were used. These original forms of EPI were called Double Echo Planar Imaging (DEPI) and Fast Low angle Excitation Echo Planar Technique (FLEET) [45, 46].

2. The constant $G_y$ was replaced with blips which are applied at the spaces between echoes (i.e. on the $G_x$ switch). With a constant $G_y$ each gradient echo is continually evolving along the phase encoding direction and thus k-space is scanned in a zig-zag fashion as shown in figure (3.5 (c)). Two experiments are required such that alternate lines in k-space can be interleaved so that all echoes are seen to evolve in the same direction for correct Fourier transformation.

   Blipping $G_y$ modifies the trajectory through which k-space is scanned. No phase evolution occurs during the gradient echo thus movement in k-space occurs along the $k_x$ direction only. Movement along the $k_y$ direction occurs at the end of each echo when the blip is applied. The resulting trajectory through k-space is thus a "square raster" scan. Since all $k_x$ lines lie parallel to each other and normal to the $k_y$ axis, two experiments are no longer required and the correct time evolution can be achieved by simply reversing the data which makes up every alternate echo prior to FT. The scan still starts at the k-space origin and zero filling is still required.

   These "single shot" versions of EPI are known as Blipped-EPI (BEPI) or Blipped Echo Planar Single pulse Technique (BEST) [43, 44]. The "half-Fourier" nature of BEST makes it particularly susceptible to magnetic field inhomogeneity induced phase errors. It is therefore important, if phase correction is not used, to ensure that the transverse magnetization is completely in phase at the start of the experiment. Practi-

cally, this involves the use of a 180° pulse which is applied immediately following slice selection. Data acquisition is then initiated at the point of maximum signal, when the magnetization is fully refocused.

3. The technique currently used at Nottingham is the MBEST (Modulus-BEST) technique [47, 48, 49]. This is essentially identical to BEST except for the addition of a large negative $G_y$ blip prior to data acquisition. This blip moves the starting point of the scan to a negative point on the $k_y$ axis which enables a symmetric scan of k-space with the origin occurring usually in the centre of the data acquisition window. In this case a full scan of k-space is performed and FT of the time data yields a modulus image which is considerably more robust and less susceptible to phase errors. The MBEST timing diagram is shown in figure (3.8).

Throughout the stages mentioned above, the image matrix size, hence data acquisition window, has increased from $32^2$ in approximately 32 ms through $64 \times 128$ in just over 65 ms to $128^2$ in 131 ms (Note: In order to integerize the definition of the non-linear sample pattern, the modulated gradient half-period is set to 1024 $\mu$s as opposed to 1000 $\mu$s. The total acquisition time for 128 echoes is therefore 131 ms). Recent reports from ANMR in America describe $128^2$ image acquisition in approximately 50 ms [79]. At Nottingham, using multi-mode resonant gradient drive, the MBEST acquisition time has also recently been reduced to approximately 80 ms although, at time of writing, this is not standard procedure.

### 3.7.1 Technique Related Problems in EPI

Rapid Gradient Modulation

As mentioned previously, the two factors which determine image resolution are gradient amplitude and duration. In EPI, individual echoes are sampled over a period of time ranging from 360 $\mu$s to 1024 $\mu$s as compared to the $3 - 7$ ms taken in most conventional imaging techniques. For comparable resolution, the $G_x$ amplitude is required to be 7 to 20 times higher in EPI than in the conventional case. These high amplitudes must be achieved and reversed rapidly thus placing tremendous demands on gradient coil circuitry.

The ideal gradient waveform is a square wave although in practice a trapezoidal waveform is used. Until recently, generation of such waveforms, with adequate amplitude, has been limited by power supply voltage and finite gradient coil inductance. An alternative approach incorporates the gradient coil as the inductor in a resonant circuit thereby reducing amplifier power requirements. The waveform in this case is a sinusoid and is required to be $\pi/2$ higher in amplitude than a square wave of the same duration.

Multi-mode resonant gradient driver circuitry is a new technique which uses a filter network to simultaneously produce gradient coil resonance at the

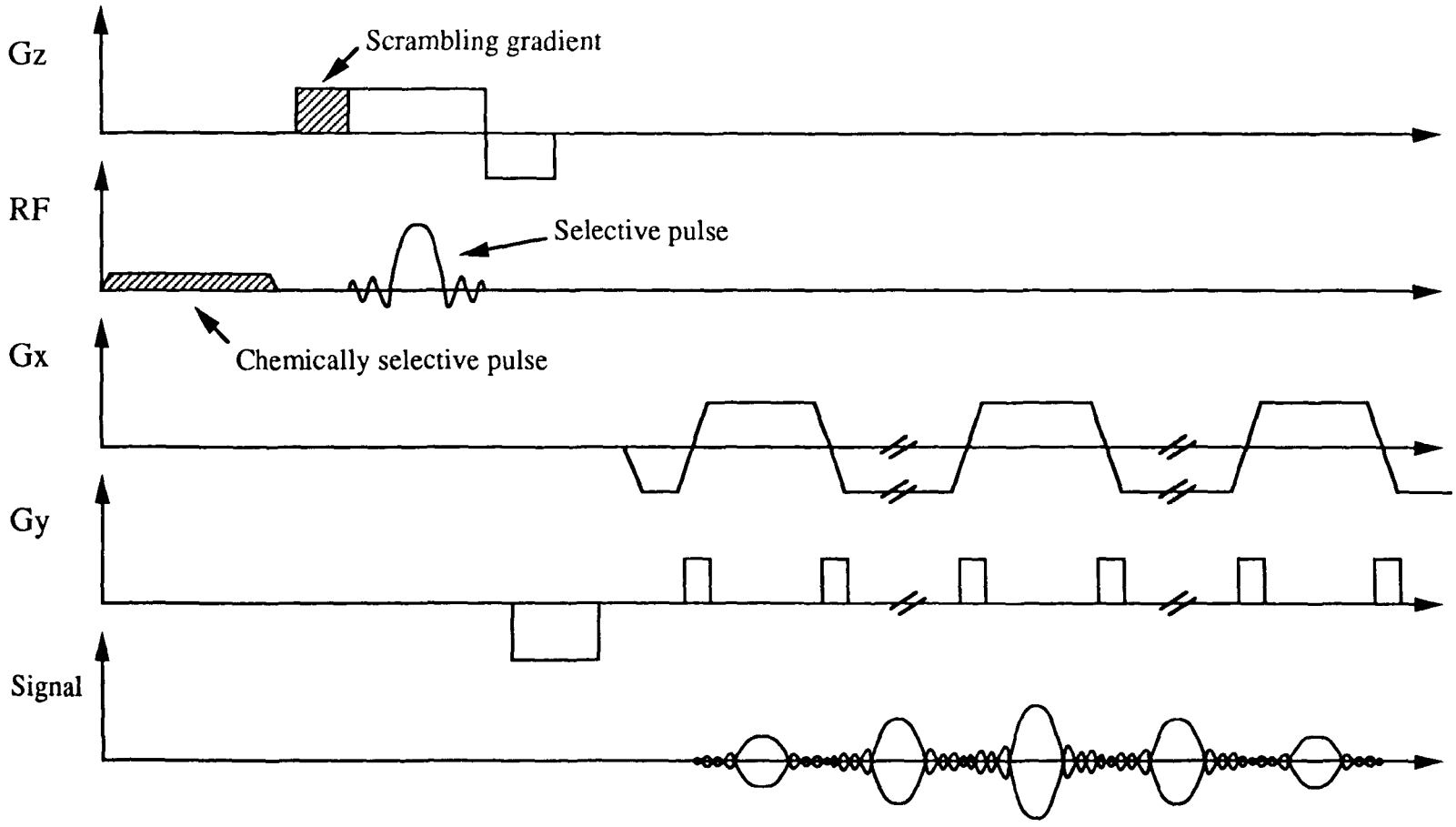


Figure 3.8: MBEST gradient and RF timing diagram (fat supression included).

harmonics required to synthesize a trapezoidal waveform. This combined approach offers the advantages of lower absolute gradient amplitude requirements and the low power requirements associated with a resonant circuit (see chapter 6).

Active Magnetic Shielding

When magnetic fields vary in time they induce eddy currents in any metallic structures which are in close proximity. These currents in turn produce their own magnetic fields which reflect back in upon the original field, distorting it in some complex time-dependent manner. Overdriving the gradient coil is commonly used to compensate for this but in turn causes even higher local eddy currents which produce still further problems. In the case of superconductive magnets, eddy currents in the magnet body cause heating and an increase in cryogen boil off rate with the risk of a quench. High currents induced in the room temperature shims also risk damaging shim power supplies.

Mansfield and Chapman [20] overcame these problems with the introduction of active magnetic screening. An active screen is in effect a second coil surrounding the primary coil, connected in series in such a way as to nullify the magnetic field from the primary coil beyond the screens radius. A double active screen works in a similar manner but uses two screens surrounding the primary. In this way the return lines of the magnetic flux are forced to lie between the two screens which, effectively, completely absorb the primary field beyond the inner screen.

Alternate Echo Reversal

If the signal from an EPI experiment were Fourier transformed directly, two mirror images would result, one superimposed upon the other. This occurs because every alternate echo evolves under a gradient of opposite polarity to the previous one (k-space is traversed in the opposite direction). Two images are formed upon Fourier transformation, one from the echoes acquired in a positive gradient and one from the echoes acquired in a negative gradient.

The initial approach in overcoming this problem was to perform two experiments end to end (FLEET, DEPI), the second experiment starting with the opposite $G_x$ polarity to the first. Alternate echoes from each data set were then spliced and two images produced which could be processed and co-added with a $\sqrt{2}$ improvement in S/N ratio. With the introduction of blips the experiment was reduced to a "single-shot" and the need to splice data removed. All that is required instead is time reversal of the signal from each alternate echo prior to FT. This is achieved by extracting the data points for each alternate echo, reversing the order, and re-inserting them.

### Non-Linear Sampling

Non-linear sampling was introduced in 1985 [50] in application to sinusoidal gradient modulation and is applicable to all non-square waveforms. When linearly sampling under a perfectly square gradient shape, the signal evolution between sample points is the same because the gradient amplitude remains constant during this time. The k-space trajectory therefore evolves in a linear fashion.

In the trapezoidal case the gradient amplitude is not constant during the ramp to maximum field and the use of linear sampling results in a ripple artefact in the image. The signal evolution between sample points acquired during the ramp is non-linear since the amplitude-duration product is changing each time. The trajectory in k-space appears non-linear with the lower spatial frequencies undersampled and the higher spatial frequencies oversampled.

Sampling in a non-linear fashion involves placing the sample points in such a way that the amplitude-duration product is the same between each point. For a trapezoid the sample points are more widely spaced during the ramp and more closely spaced during the plateau. The effect this has results in a linear signal evolution/trajectory in k-space. A slightly higher bandwidth is usually required to account for the non-linear spacing of sample points.

### Zero Filling

The process of zero filling involves padding out the acquired data set with as many zero's as there are data points thereby doubling the array size. It is a technique usually employed in half-Fourier techniques (BEST) where half the data is missing anyway [51].

Fourier transformation of the padded data set yields an image with twice the field of view allowing image size, hence resolution, to be increased whilst avoiding wrap around artefacts. The disadvantage of this approach is that only a real image can be formed since the imaginary channel data is convoluted with a broadening function which results from the discontinuity introduced by the zero's. The condition that the real image remains undistorted is that all pixel magnetizations are in phase at the beginning of the experiment.

### One-dimensional Fourier Transformation

A 1D Fourier transform can be performed more quickly than a 2D Fourier transform since very little re-ordering of data is required in EPI. There is, however, a slight difference between the two. The visible effect of performing a 1D Fourier transform on EPI data is a spatial rotation of the image by an angle $tan^{-1}(\Delta x/N\Delta y)$, where $\Delta x$ and $\Delta y$ are the spatial resolutions along the x and y axes and $N$ is the size of the image matrix along the y-axis [47].

Pixel Bandwidth

The frequency bandwidth assigned to each pixel in an EPI image is determined by the total sample time. For a $128^2$ image acquired in 131 ms, the pixel bandwidth (also termed "frequency per point") is given by

$$\Delta f_{PIXEL} = \frac{1}{T_{acq}} = 7.6Hz \tag{3.14}$$

This is an order of magnitude lower than the frequency per point in standard imaging procedures based on the 2D-FT technique.

The net spatial resolution in EPI is therefore limited by magnetic field homogeneity, $T_2$ characteristics of the sample and off-resonance effects [52, 53]. The point spread function (PSF) in an image characterizes the accuracy to which a single frequency can be isolated. Large static field inhomogeneities, short $T_2$ values and off-resonance effects such as magnetic susceptibility and chemical shift all serve to broaden the PSF. In order to avoid signal spread between pixels, and hence loss of intrinsic resolution, the PSF width must be narrower than the pixel bandwidth. As an example, at 0.52T the proton resonant frequency is 22.03 MHz and the static field homogeneity may be specified to 0.1 p.p.m. over the imaging plane. If an EPI experiment is performed in 131 ms the pixel bandwidth, in p.p.m., is 0.34 p.p.m., thus the degree of homogeneity can be tolerated with little or no spread of signal between pixels. Similarly, a sample with $T_2 = 50$ Hz will have a PSF bandwidth given by

$$\Delta f_{1/2} = \frac{\Delta\omega_{1/2}}{2\pi} = \frac{1}{\pi T_2} = 6.4Hz \tag{3.15}$$

which is still less than the pixel bandwidth.

The chemical shift between the protons in fat and those in water is approximately 3.3 p.p.m., or 72 Hz at 0.52T. This results in a displacement of 9 pixels in the image (see below).

Fat Suppression

A standard EPI experiment on the human body yields an image which contains both a water component and a fat component. The fat component appears shifted by a number of pixels and is, in the most part, undesirable. Selective imaging of either the water or the fat signal can be performed using a variety of techniques which either excite or suppress the required species before data acquisition [48].

The preferred method of chemical shift selection for MBEST relies upon the removal of the unwanted signal component with a chemically selective prepulse. The simplest approach is to excite the unwanted signal component with a $90^o$ pulse and then destroy all transverse magnetization by cancellation using a suitable combination of scrambling gradients. This can be immediately followed by a standard MBEST sequence to obtain an image of

the unperturbed component as shown in figure (3.8). A suitable $90^o$ selective pulse shape is a simple rectangle of duration $T$. A pulse length of 13.8 ms will effectively excite on-resonance nuclei, but will not affect nuclei which are off-resonance by $\pm 72$ Hz and will have very little effect on nuclei in the immediate vicinity of this frequency offset. This is a consequence of the sinc-shaped excitation frequency spectrum associated with a rectangular pulse, the width of the sinc being inversely proportional to the duration of the rectangular pulse. If the peak of the sinc is positioned on the fat resonance then this will be removed in the image, likewise with the water resonance.

### 3.7.2 Contrast In MBEST Imaging

The advantage of MBEST images over BEST images are their inherent soft tissue contrast. The overall image intensity is derived from the signal intensity of the lower spatial frequency components which occur close to the k-space origin. In BEST, sampling starts at the k-space origin where the signal contributions from all $T_2$ components is at a similar level since no decay has been allowed to occur. The resultant image contains little contrast. In MBEST the k-space origin occurs in the middle of the experiment after some 64 ms. During this time various $T_2$ components will have decayed away and the point of maximum signal (k-space origin) will contain contributions from $T_2$ components in a ratio dictated by their relative amplitudes at that point. Some components will have decayed all together and disappear from the image.

When referring to $T_2$ contrast in EPI it is more correct to use the $T_2^*$ term which includes static field inhomogeneity effects. It is clear to see that after 64 ms a good deal of the available signal will have been lost. It is therefore the $T_2^*$ of the sample which determines the maximum allowable duration of an EPI experiment.

### 3.7.3 Echo Planar Variants

EPI, being a compact technique, is adaptable as an imaging module which can be simply tagged onto the end of any suitable spin preparation experiment.

Inversion Recovery EPI

$T_1$ weighted images can be produced by preceding the MBEST module with a $180^o$ pulse. The time elapsed between this pulse and the data acquisition determines the level of $T_1$ contrast in the image [54].

Spin Echo EPI

If the selective pulse is followed by a $180^o$ pulse the gradient echo train may be acquired under a spin echo envelope. Magnetization lost due to $T_2^*$ effects

is refocused at the centre of the experiment. Variable contrast is performed by moving the position of the spin echo [55].

Zoomed EPI

This variant uses two selective pulses to excite a strip within the sample. The gradient amplitude along the transverse direction of the strip may be increased to fill out the image field of view (FOV) whilst avoiding wrap around. The FOV in the longitudinal direction of the strip is limited by the bandwidth of the receiver. Strip selection usually involves a selective $90^o$ pulse to select a slice. The signal is then allowed to decay away in a gradient applied along the phase encoding direction. Whilst this gradient remains switched on a selective $180^o$ pulse is applied which defines the zoomed strip within the image. Only these spins within the zoom strip will refocus in a spin echo, at which point the image is acquired [56].

## 3.8 Three Dimensional MRI

### 3.8.1 Fourier Techniques

The two common ways to image a volume using Fourier techniques are multislicing and three-dimensional Fourier imaging (3D-FT).

3D-FT Imaging

In 3D-FT imaging the 2D-FT process is repeated $s$ times without slice selection ($s$ is the number of slices desired) each time with a different value of z-gradient applied prior to signal readout. This process encodes z-axis information in exactly the same way as it is encoded along the y-axis. Reconstruction is by a 3D Fourier transform, where the FT is applied sequentially three times. The total imaging time is given by

$$T_{3D} = (nNs)T_R \tag{3.16}$$

where $n$ is the number of averages and $N$ the number of lines in the image.

Multislicing

Multislicing involves cycling through slices of the object during the interval $T_R$. The actual time spent acquiring data is small (approx 5% of the imaging time) and 95% of the time is spent waiting for $T_1$ recovery of magnetization ($T_R$). During the $T_R$ interval a different slice can be selected and imaged, and so on, until $T_R$ is used up. In this way if, for example, it takes 100 ms to acquire data for one slice with a $T_R$ of 1.5 s, 15 slices can be imaged, 14 of which are sampled in a time span that would otherwise be lost. Multislicing produces images of different sections of the object in the time it would take to image just one, without sacrificing image quality.

### 3.8.2 Echo Planar Techniques

Multislice EPI

This is not unlike the Fourier technique in principle except that in the time between each slice selection a complete image is acquired. This enables up to 10 different slices to be imaged in a period of 1 second. When coupled with an inversion recovery sequence, each slice contains a different amount of $T_1$ weighting. The slice selection order can be cycled round and $T_1$ maps of each slice produced.

Phase Encoded Volumar Imaging (PEVI)

This involves selection of a thick slice and stepping of the z-gradient between a series of MBEST experiments. PEVI is a hybrid technique and differs from the 3D-FT methods in that a complete planes worth of data is acquired between z-axis phase encoding steps as opposed to just one line. After suitable re-ordering the PEVI data is processed using a 3D Fourier transform. A large saving on total imaging time is made enabling a complete 3D image, with isotropic resolution along all axes, to be acquired in just over a minute (using low flip angle RF pulses) [57].

Echo Volumar Imaging (EVI)

Echo Volumar Imaging is the natural extension of EPI to three dimensions [58, 51, 59]. Following thick slice selection, the signal is sampled in the presence of all three gradients. Two of these gradients are modulated whilst the third remains constant in polarity. In this way a complete three-dimensional scan of k-space is performed and a 3D image data set acquired in just over 100 ms. In keeping with EPI, EVI is very much more technically demanding which, in part, has limited the image matrix sizes, hence resolution, achievable. A more detailed description of EVI complete with applications and discussion is left until chapter 5.

Chemical Shift Imaging

In addition to mapping spatial information, EPI may be used as the basis for chemical shift imaging. EPSM [61], a pre-cursor to EVI, is a 3D experiment in which the third axis is used to map chemical shift in the sample. Other hybrid techniques include PEEP and PREP which combine, respectively, 2D-FT and PR with EPI.

EPI Flow Mapping

Suitable spin preparation prior to MBEST data acquisition can make the image flow sensitive. Such a technique is used in this laboratory to study the flow of fluid through porous media and represents a further unique application of EPI to an area other than medical imaging.

# Chapter 4: Instrumentation

## 4.1 Introduction

The imaging system used at Nottingham has evolved over a number of years. Imaging was originally carried out on a water cooled resistive magnet which, in recent years, has been replaced by a superconducting magnet. Most of the associated hardware has been designed and built in-house with any commercial hardware being built to specification.

The author has had no part in the manufacture of the imaging system although, for certain work presented in this thesis, additional hardware was necessary. In all cases this extra hardware was designed by the author and built in conjunction with the department workshops.

More recently the computer control and processing hardware has been replaced by a SUN workstation coupled to an AT & T pixel machine. For the experiments performed by the author however, the Data General Eclipse S140 (DG) was used (except where otherwise stated).

## 4.2 General System Overview

The Nottingham imaging system in 1991 is based around an Oxford Magnet Technology (OMT) 0.52T superconducting magnet which corresponds to a proton resonance of 22.03 MHz. The bore of the magnet contains shims for homogeneity correction and within the shim set lie the screened gradient coils. A single RF coil is used for both transmission and reception and the imaging diameter available within this coil is 48 cm.

Computer control is performed by a Data General Eclipse S140 which runs in Fortran 5 and assembler. Real-time program interaction is available via 64 on-off "sense switches" and 32 16-bit "parameter switches". Hardware control and coordination is performed by a home built waveform controller (WC) which is programmed via the DG. The waveform controller provides triggers for RF amplifier gating and ADC initiation as well as waveforms for all three gradient drivers and RF modulation.

The frequency synthesizer can be programmed from the DG and provides stable reference for both the single sideband modulator (SSB) transmitter and phase sensitive detector receiver systems. RF transmission to the coil is via a 2 kW linear RF amplifier which takes its input from the SSB modulator via an attenuator and separate matching network.

The received signal is phase sensitively detected producing quadrature outputs. Aliasing is prevented by 8-pole Butterworth low-pass filters installed between the receiver and ADC's.

Two 16-Bit ADC's sample the demodulated and filtered signal under control of the WC. The digitized signal is sent directly to the AP500 array processor where it is stored and processed under instruction from the DG.

Image display is by a Ramtek 9351 display system which can display $512^2$ pixel images using an 8-bit grey scale. Additional 1D display of the raw sampled signal is available using the home built digital display buffer connected to an oscilloscope.

Program and image storage is performed using a Fujitsu 2284n 160 Mb winchester disc system. Permanent file storage is also available using the DG 6231 1/4 inch cartridge and tape sub-system.

A general schematic layout is shown in figure (4.1).

## 4.3 The Magnet

The magnet is an OMT 0.52T, horizontal bore, superconducting magnet. The internal diameter is 1.1 m which is reduced to 97 cm upon insertion of the shim set. The cryostat consists of two concentric stainless steel reservoirs, housed in the outer vacuum vessel. An enthalpy cooled shield and multilayer superinsulation are employed between metal surfaces.

The magnet windings are to a 6 coil design and are contained in the central liquid helium reservoir. The average helium boil off rate is 0.35 litres/hour. The helium vessel is contained within a liquid nitrogen jacket which itself has a boil off rate of approximately 1.15 litres/hour. Nitrogen replenishment is performed once a week from a Statebourne Cryogenics, self pressurizing, 300 litre, stainless steel dewar. Helium replenishment is performed once every three weeks from a similar 200 litre dewar.

RF screening of the bore is performed by earthed aluminium mesh cages fitted to each end of the magnet. All electrical connections are filtered where they enter the cage and where screened cable is used, the screen is connected to the cage.

## 4.4 Shims

The resistive shim set allows an homogeneity of 3 p.p.m. over a 30 cm sphere or 1 p.p.m. over a 50 cm transverse plane at the magnet axis.

The 13 shim coils are wound on a rigid fibre-glass former, the constant current power supplies for each coil being provided by an OMT 2313 shim power supply. LC filters provide protection from extraneous RF transmission into the imaging environment and these are contained within a box which is bolted to the cage top.

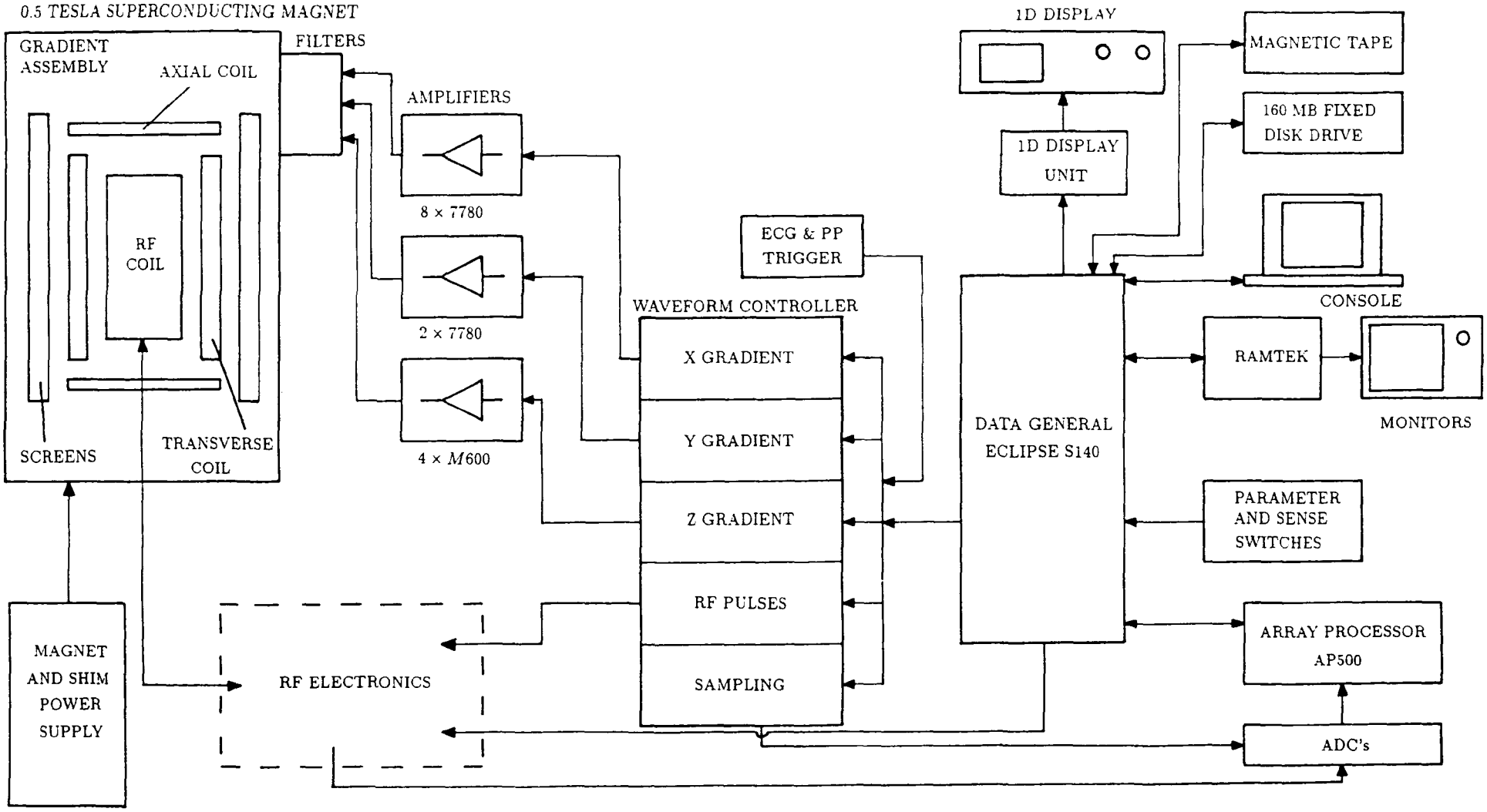


Figure 4.1: Block diagram of Echo-Planar Imaging system.

The shim power supply is sensitive to voltage spikes as might occur from switched gradient coupling. Protection is afforded using a set of chokes, bi-filar wound on a laminated iron core and connected in opposition such that steady current does not saturate the iron cores. Induced currents see an inductance of 0.1 $H$ and the peak voltages developed at the power supply are reduced by several orders of magnitude, see figure (4.2).

## 4.5 Gradient Coils

The gradient set consists of three concentric fibre-glass formers with a radial spacing of approximately 8 cm. The inner cylinder has an internal diameter of 54 cm and contains the three primary gradient coils. The two outer cylinders form the double active screens and serve to contain stray fields and prevent eddy current induction in the shim coils and magnet body. The gradient set was manufactured by OMT and are designed to be of low inductance to facilitate rapid gradient modulation.

The transverse (X,Y) gradients are generated by saddle coil pairs connected in opposition. Two pairs are required for each gradient with one set simply rotated through $90^o$ to provide orthogonal gradients.

The axial gradient (Z) is generated by a Maxwell pair which is also doubly screened.

The transverse gradients are designed to use half the primary current in each of the screens whilst the axial gradient carries the full primary current, see figure (4.3).

Each gradient connection is filtered at the cage boundary using tuned T filters, see figure (4.4). L1/C1 form band reject filters tuned to 22 MHz. L2/C2 bypass residual RF to earth via the cage and R lowers the Q to give a bandwidth of approximately 1 MHz. The inductors used must take the full current and have values of approximately 5 $\mu$H each. The total gradient coil inductances measured at the terminals are:

- $X = 103\ \mu H$
- $Y = 110\ \mu H$
- $Z = 5\ mH$

With resistances of 0.13, 0.13 and 7 Ohms respectively.

## 4.6 Gradient Drivers

### 4.6.1 X Gradient

X gradient drive capability is provided by 8 Techron 7790, 3 phase, 415 V linear power amplifiers. The total current available is 700 Amps at a peak voltage of $\pm$320 Volts.

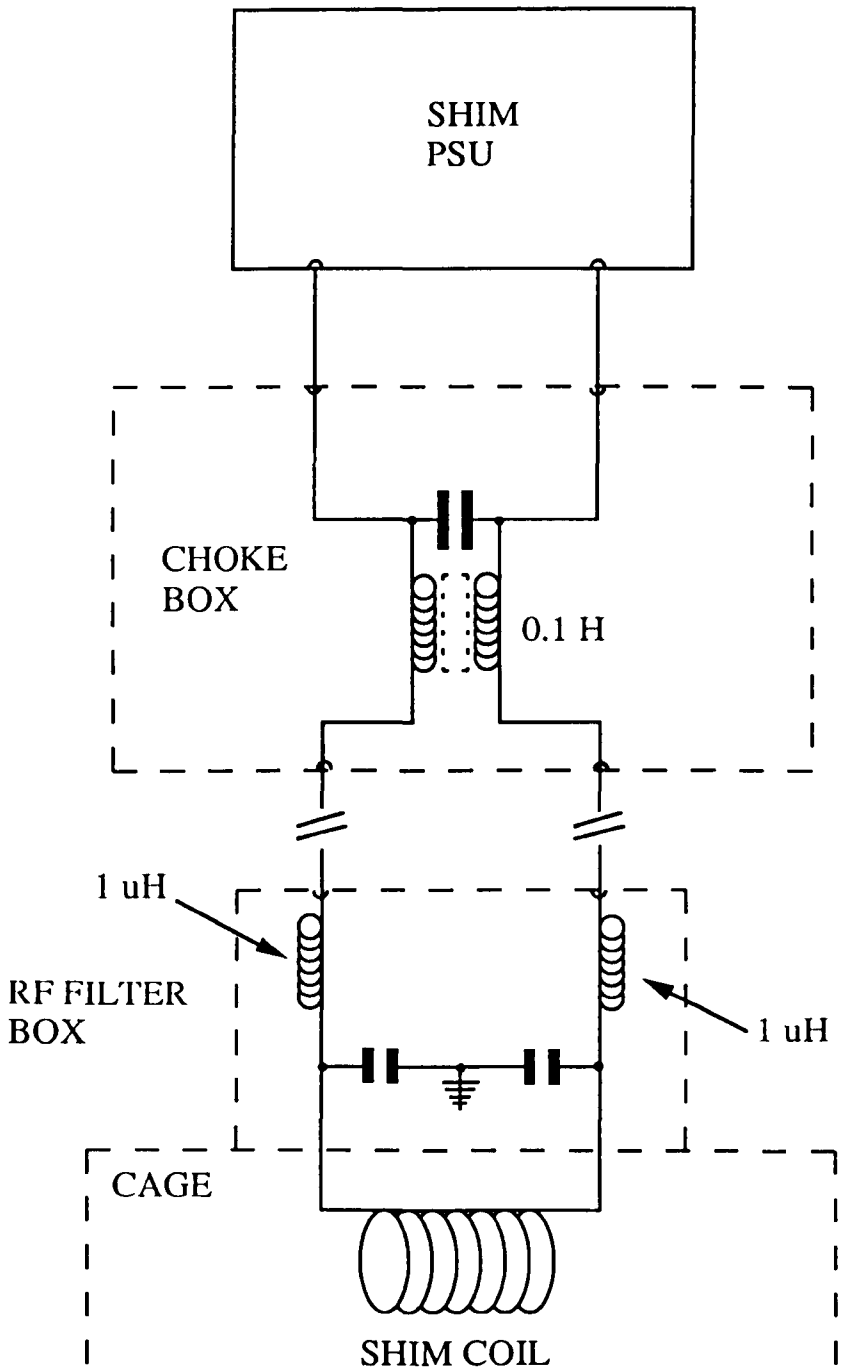


Figure 4.2: Shim coil protection circuitry.

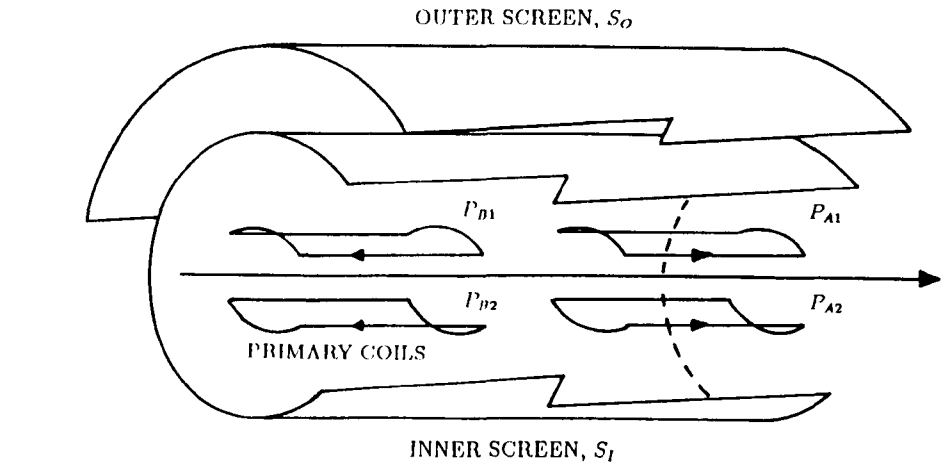


(a)

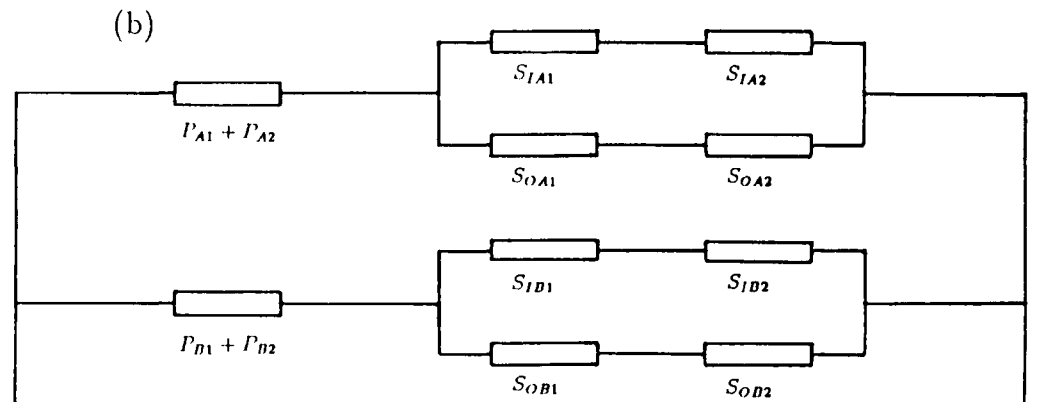


(b)

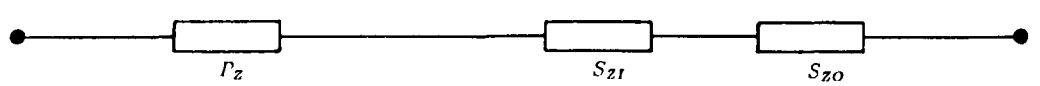


(c)

Figure 4.3: (a) Geometry of screened transverse gradient coil system. (b) Wiring arrangement for screened gradient coils - transverse gradients. Subscripts O and I denote outer and inner respectively. (c) Wiring arrangement for axial coils.

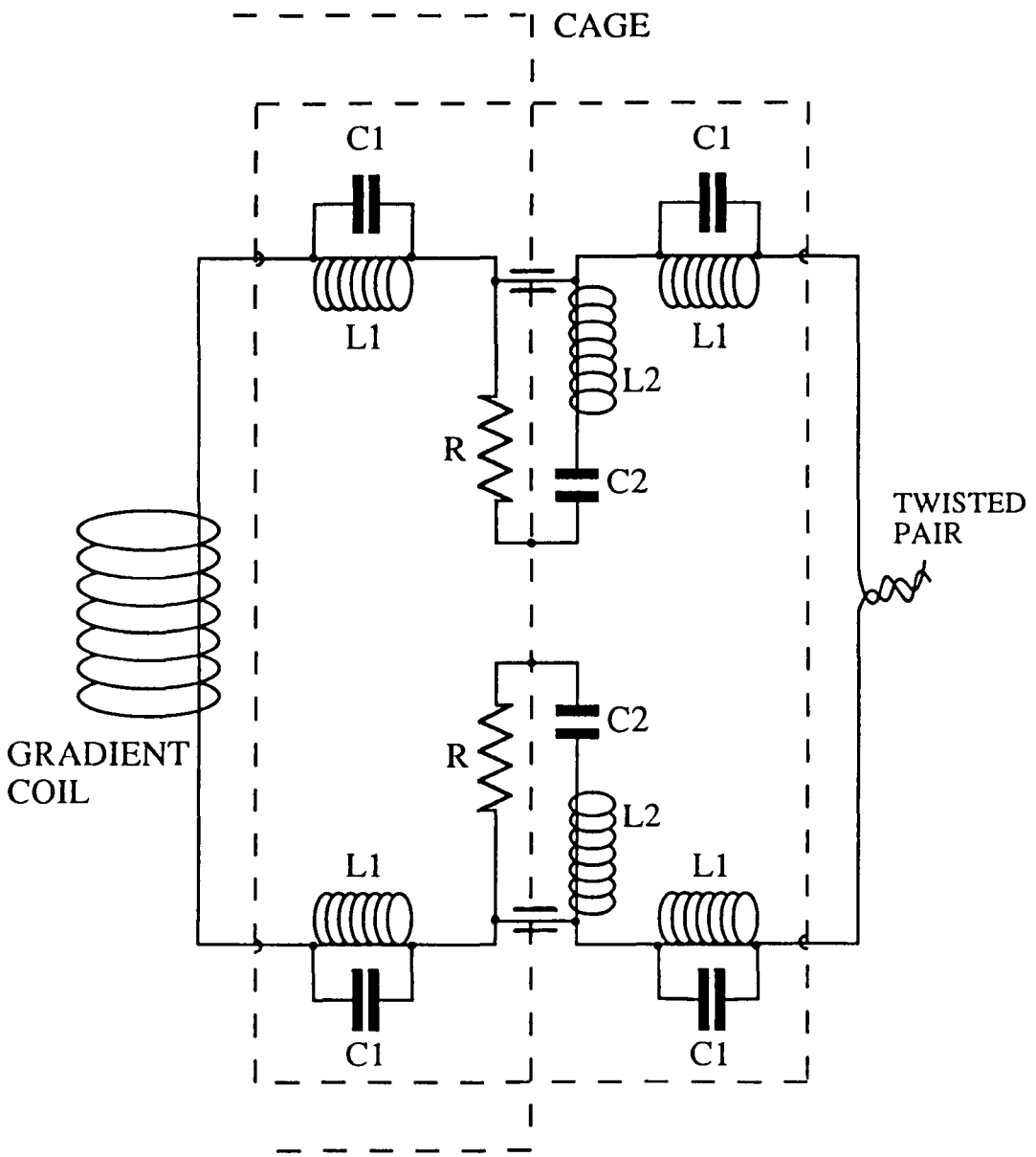


Figure 4.4: Gradient coil RF filter circuit.

The eight amplifiers are connected in four pairs with each pair connected in series opposition to provide double the voltage capability. Master/slave operation is employed with current controlled feedback (constant current mode). It is necessary to balance the outputs of each pair to avoid circulating currents so each amplifier is fitted with a fine gain and trim control for this purpose. Connection to the field coils is by four twisted pairs which mimic current sharing resistors and aid balancing. The length of each pair is 15m providing a resistance of 50 m$\Omega$.

The master amplifier is driven via opto-isolators which are used to avoid ground loops and provide independent amplitude and slew rate control. Slew rate limitation is necessary to prevent saturation of the output devices which occurs when the input voltage changes more rapidly than the output current can follow. This effect results in the superposition of mains ripple onto the gradient waveform and is detrimental to the image.

### 4.6.2 Y Gradient

Y gradient drive is provided by two Techron amplifiers in series opposition providing a total current of 160 Amps at $\pm$320 Volts. Master/slave and constant current mode are used as for the X gradient drivers. Signal injection is also via an opto-isolator control box. The large voltage capability is necessary to enable the generation of the short blips as required for MBEST.

### 4.6.3 Z Gradient

For the Z gradient, two pairs of Amcron M600 amplifiers are used connected in a series parallel arrangement. Each unit is a single phase 220 V unit capable of producing 22 Amps at $\pm$100 Volts. The bank of four are operated in voltage mode and connected to the field coil via 1$\Omega$ discrete current sharing resistors.

A differential amplifier is fitted to the input of the master amplifier to eliminate ground loops whilst voltage offsets are prevented from reaching the field coil by a series diode pair which only conduct above 0.6 Volts.

The whole arrangement provides 45 Amps at $\pm$200 Volts.

## 4.7 RF System

### 4.7.1 RF Coil

A single coil is used for both transmission and reception. The design is of a birdcage type [23] and incorporates a slotted screen. The purpose of the screen is to limit coupling of the coil with the transverse gradient coils and shims therefore allowing them to be placed in close proximity to each other. The slots prevent eddy current induction from the switched gradient but allow the RF current circulation necessary for the screening action. The whole arrangement is driven between the screen and coil.

The unloaded Q of the coil is approximately 120 whilst the loaded Q falls to 33. Impedance matching is performed within the cage using a $\pi$-network matching box, see figure (4.5).

The pre-amp is isolated from the transmitter during transmission by use of a $\lambda/4$ line and crossed diodes D1. Diodes D2 isolate the transmitter during reception. An additional $\lambda/4$ line at 52 MHz is included as a bandstop filter for this frequency and serves to improve the S/N ratio.

### 4.7.2 RF Transmitter

The required 10 MHz reference for the Wavetek 5130A phase continuous frequency synthesizer is provided by a Darlington off-air frequency standard. Frequency hopping (as required in multislice imaging) is provided by 4 programmable registers which are controlled from the WC.

SSB modulation is performed by a home built modulator and amplified to 2 kW peak pulse by an Eddystone Radio H1301 linear RF amplifier which is also gated from the WC.

Variable attenuation 0-20 dB is provided on the output and phase shifts in $90^o$ steps can be performed utilizing the spares outputs from the WC.

### 4.7.3 RF Receiver

A Trontech W110F 50$\Omega$ pre-amp provides the first stage of amplification. The amplified signal is then phase sensitively detected by a Picker International receiver which uses a 15 MHz intermediate frequency. The RF synthesizer must therefore be set 15 MHz higher at 37 MHz.

The quadrature outputs from the receiver pass through a set of 8-pole Butterworth filters which limit aliasing effects in the ADC. The bandwidths available are 16, 32, 64, 128 and 256 kHz.

The filtered signal is then sampled using two Analogic 16-bit ADC's which download their data directly to the AP500 array processor.

## 4.8 Computer Hardware

### 4.8.1 The Data General Eclipse S140

The Data General Eclipse S140 is a 16-bit machine with 64k of addressable memory. It uses the real time disc operating system (RDOS) with programs being stored on and executed from a 160 Mb Winchester hard disc.

The advantage of such a system is that the device drivers are resident in the computer RAM thus communication to and between external devices is very fast allowing real time processing and user interaction.

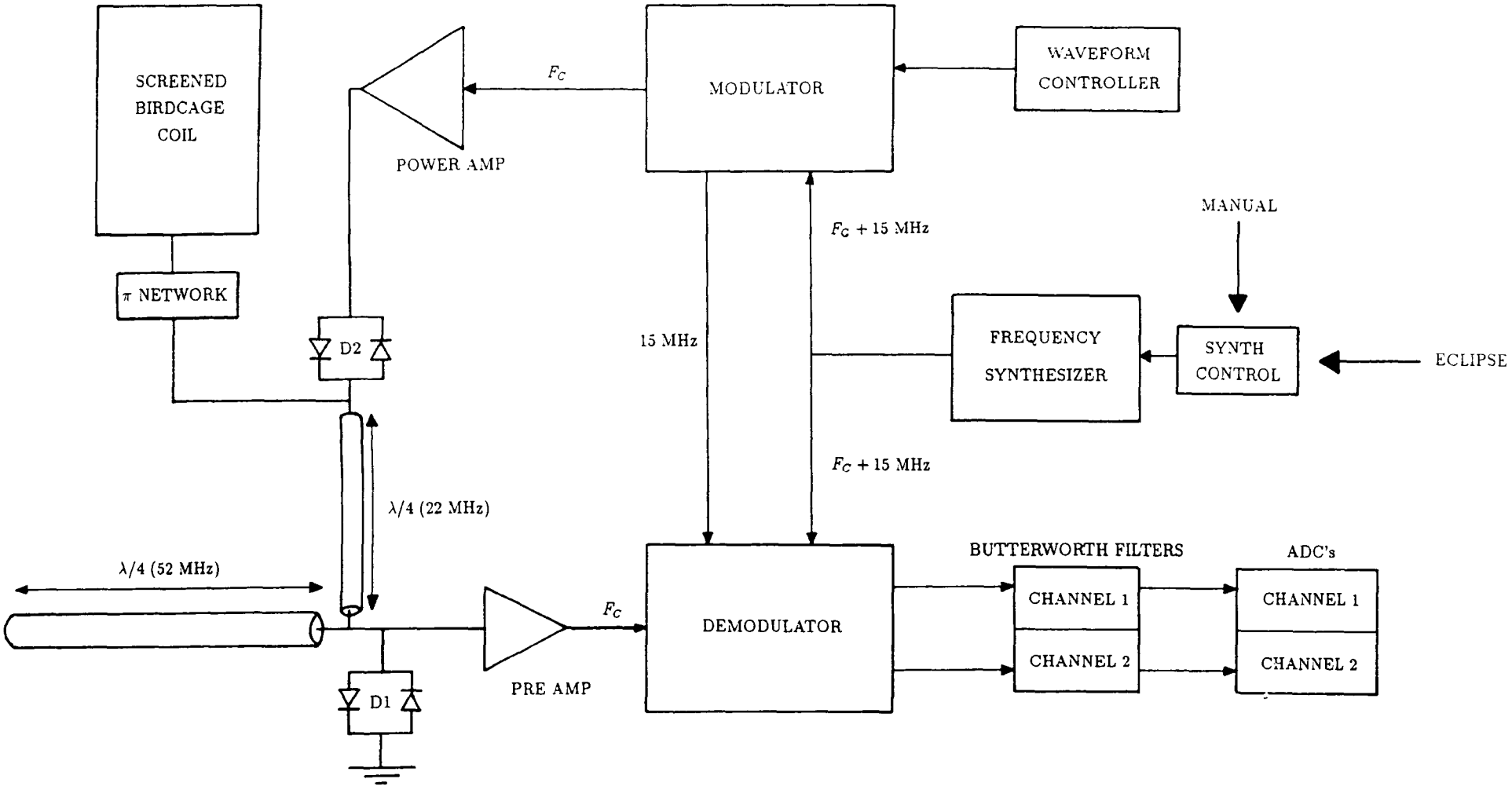


Figure 4.5: Block diagram of 22 MHz RF electronics.

### 4.8.2 Analogic AP500 Array Processor

The AP500 is a 32-bit dedicated array processor containing 4 Mb of addressable memory. Resident in the device is a library of functions which facilitate rapid data handling enabling a $128^2 \times 2$ fast Fourier transform (FFT) to be performed in 100 ms. Memory allocation and partitioning is controlled by the DG.

### 4.8.3 Waveform Controller

The waveform controller was designed and built in-house by Coxon [60]. It comprises a master unit and six other channels. Each channel is under control of its own CPU. The waveforms required for each gradient and the RF channel are downloaded each to a separate channel. A software start (SWS) command, issued in Fortran, activates the WC. The master unit then triggers the other six units and synchronization is maintained by its on board clock. The ADC's are triggered by a series of pulses, positionable to an accuracy of 62.5 ns with a minimum spacing of 1 $\mu$s. These are issued from the sample channel.

Waveforms are defined using 256 levels (8-bit) and analogue output is provided by a DAC on each unit. The output levels of the DAC's are adjustable as are the + and − levels and the zero's. Each channel has, in addition, 4-bit spares which are used for gradient polarity assignment and phase assignment of RF pulses as well as triggers for other peripheral monitoring devices such as an oscilloscope.

A cross assembler has been written by Coxon [60] which allows high level programming of the WC. It contains sixteen instructions which are entered in a menu as well as duration, amplitude and phase data. On running the experimental program, the menu is complied each time prior to execution.

## 4.9 General Technical Requirements

Various monitoring facilities are available with which to fine tune each experiment. A current monitor facility is available on the opto-isolator control box connected to each amplifier bank. Using these, the current in the gradient coils may be checked for distortion during each image acquisition. The conversion factor at the monitor jack is 20 Amps/Volt per amplifier pair. For the X gradient set (4 pairs) this sums to 80 Amps/Volt.

The standard MBEST experiment, at time of writing, acquires data for a $128^2$ image in approximately 131 ms. This corresponds to a $G_x$ trapezoidal modulation of 488 Hz with a rise time of 300 $\mu$s (Pk - Pk). The duration of each $G_y$ blip is 256 $\mu$s. For 10 mm slice selection, $G_z$ is set at 4 mT/m. The gradient strength requirements for 3 mm and 1.5 mm resolution are shown in table 4.1.

| Gradient | 3 mm Resolution | | 1.5 mm Resolution | |
|---|---|---|---|---|
| | mT/m | Amps (Pk) | mT/m | Amps (Pk) |
| $G_x$ | 9.00 | 190 | 18.00 | 380 |
| $G_y$ | 2.14 | 45 | 4.29 | 90 |

Table 4.1: Gradient strength requirements for 131 ms MBEST.

# Chapter 5: Hyper-Fast Volumetric Imaging

## 5.1 Introduction

Object motion either intrinsic or due to respiration, is a major problem when performing MRI on any part of the body other than the head or limbs. In recent years snapshot imaging techniques like EPI have evolved which enable a 2D planar image to be acquired in as little as 20 ms with resolution approaching 1.5 mm. To a certain extent these ultra-fast techniques have alleviated the image degradation caused by sample movement.

In most cases however, motion is not restricted to any one direction. During a heart beat, for example, the whole heart expands and contracts along three directions. Two-dimensional imaging techniques, however fast, are unable to follow motion in and out of the plane. Furthermore, techniques such as FLASH, which acquire a single image using multiple RF excitations, run the risk of exciting a slightly different slice for each echo acquired. The plane from which the complete image is taken is then derived from an average of all these slices and hence resolution is compromised. EPI on the other hand, uses only one RF excitation so the recorded signal originates from a single well-defined slice.

Few options exist for a full three-dimensional study of the thorax or indeed, any other dynamic processes within the body (e.g. gastro-intestinal (GI) tract). Commercial Fourier techniques are simply too slow. 3D FLASH has dramatically reduced volumetric imaging time for the brain but is unsuitable for objects which move rapidly and aperiodically. EPI hybrid techniques like PEVI involve performing a series of EPI experiments separated by a stepped phase encoding gradient along the third axis. $64^3$ voxel images of the brain have been achieved which take just over 1 minute to acquire. This technique, whilst fast, would still require cardiac triggered acquisition for thoracic studies and is unsuitable for the study of non-periodic motion. Multislice EPI is another option which also requires cardiac triggering.

Echo Volumar Imaging (EVI) [58] is the only true snapshot 3D technique. The problems inherent in its implementation were addressed, from a general standpoint, in the first paper on EPI. A pre-cursor, and somewhat similar technique to EVI is Echo Planar Shift Mapping (EPSM) which is a four-pass technique and uses two modulated orthogonal gradients to provide two dimensions of spatial information with chemical shift providing signal evolution along the third direction [61].

Work on EVI prior to that presented here, resulted in the first images of the brain of a human volunteer. This data set was acquired using a two-pass

modulus experiment resulting in an image matrix size of $16^3$ voxels. The in-plane (x,y) resolution was 1.28 cm by 1.27 cm with a z-direction resolution of 1.16 cm [59]. Whilst very coarse, the images provided delineation of grey and white matter and very crude structural information spanning the whole volume of the head. Image acquisition and display was achieved using two separate programs thereby removing further the true real-time-interaction aspect of the technique.

Improvements undertaken by the author, and presented in this chapter, involved extensive software and pulse sequence modification to enable single-pass (snapshot) modulus-EVI experiments to be performed with real-time display and user interaction. The largest image matrix size achieved to date is $64 \times 32 \times 8$ (x,y,z) voxels, acquired in a single experiment lasting between $80 - 102$ ms. This matrix size represents the limit of the present hardware performance. Also presented here are the first, real-time, modulus-EVI images of the human thorax and mid-body as well as the first zoomed-EVI images of the brain of a volunteer.

## 5.2 Modulus Echo Volumar Imaging

No modification to the existing hardware was made and all EVI experiments were performed using the whole-body gradient set and birdcage coil, as for EPI (see chapter 4).

EVI is the natural extension of EPI to three dimensions. In a similar manner it has evolved from a multi-pass technique to the single-pass experiment used for this work. The basic concepts however, are the same for all versions. The trajectory in k-space is extended to three dimensions which are covered, as in EPI, in a continuous raster fashion, see figure (5.1 (b)).

In modulus-EVI a volume or thick slice is selectively excited within the sample and the signal from this region is recorded in the presence of modulated gradients along two orthogonal spatial axes with either a continuous or blipped gradient along the third spatial axis. Figure (5.1 (a)) shows the RF and gradient pulse sequence for the basic (four-pass) modulus experiment.

As shown, $G_x$ is modulated rapidly to provide a train of gradient echoes as in EPI. Simultaneously, $G_y$ is modulated at a slower frequency, the half period of which is set to enclose a specific number of $G_x$ echoes. The slower modulation results in a train of larger $G_y$ echoes which have nested within them the $G_x$ echoes. Previous to $G_x$ and $G_y$ modulation a negative $G_z$ blip is applied which moves the start of the experiment to a negative point on the $k_z$ axis (necessary for modulus acquisition). During data sampling $G_z$ is switched positive and applied at a low level throughout the experiment. A $G_z$ echo is thus formed which peaks in the centre of the data sampling window and contains, nested within it, the $G_y$ echoes and nested within them the $G_x$ echoes. In effect then, the $G_y$ echo peaks form the "sample points" for the $G_z$ envelope, the $G_x$ echo peaks form the "sample points" for each $G_y$ echo

and the digital data points sample each $G_x$ echo.

If, for example, 8 $G_y$ echoes are formed under the $G_z$ envelope and within each of these echoes are formed 32 $G_x$ echoes with each $G_x$ echo sampled using 64 data points, the final image matrix size will be $64 \times 32 \times 8$ voxels. The total number of $G_x$ switches required is 256 and the total number of $G_y$ switches is 8 during the same total time interval. EVI is essentially a tree of nested EPI experiments where any two axes form the basis of a planar experiment.

As in EPI, the amplitude of each gradient in EVI is determined by its duration and the resolution required along that direction. Clearly, for any useful matrix size, many $G_x$ switches are required in the allotted acquisition time. For example, a modulus image matrix size of $64 \times 64 \times 16$ voxels with 3 mm resolution along all axes, acquired in 128 ms, would require a total of 1024 $G_x$ switches. This is equivalent to performing $128^2$ MBEST in 16 ms and would require a $G_x$ amplitude 8 times larger than that currently used.

### 5.2.1 Four-Pass EVI

The RF and gradient pulse sequence and k-space trajectory for four-pass modulus-EVI are shown in figure (5.1). Thick slice selection is performed in a similar manner to MBEST. The dotted gradient waveforms represent the alternative phases for $G_x$ and $G_y$. As in DEPI, it is necessary to perform experiments such that a spliced data set can be formed which contains data obtained in the presence of either a wholly positive or wholly negative gradient. In EVI this applies to both $G_x$ and $G_y$ therefore four experiments are required with $G_x$ and $G_y$ starting phases $++$, $+-$, $-+$, $--$. Splicing provides four complete data sets which, after Fourier transformation, can be suitably re-ordered and co-added.

### 5.2.2 Two-Pass EVI

By applying blips on $G_y$, as shown in figure (5.2), EVI is reduced to a two-pass experiment where only the starting phase of $G_y$ needs to be alternated. Every alternate $G_x$ echo can be reversed, just as in MBEST, in order to provide consistent coverage of k-space.

### 5.2.3 Single-Pass EVI

The single-pass version is shown in figure (5.3). It is identical to the two-pass version except that the constant $G_z$ has been replaced with blips at the $G_y$ switches. In addition to alternate echo reversal, alternate k-plane reversal is required before Fourier transformation. This is done by reversing the order of the $G_x$ echoes contained within each alternate $G_y$ echo envelope.

The single-pass experiment performed by the author was slightly different to that described above. Whilst blips were applied on $G_y$, a constant $G_z$ was used during z-direction phase encoding as in the two-pass version (figure

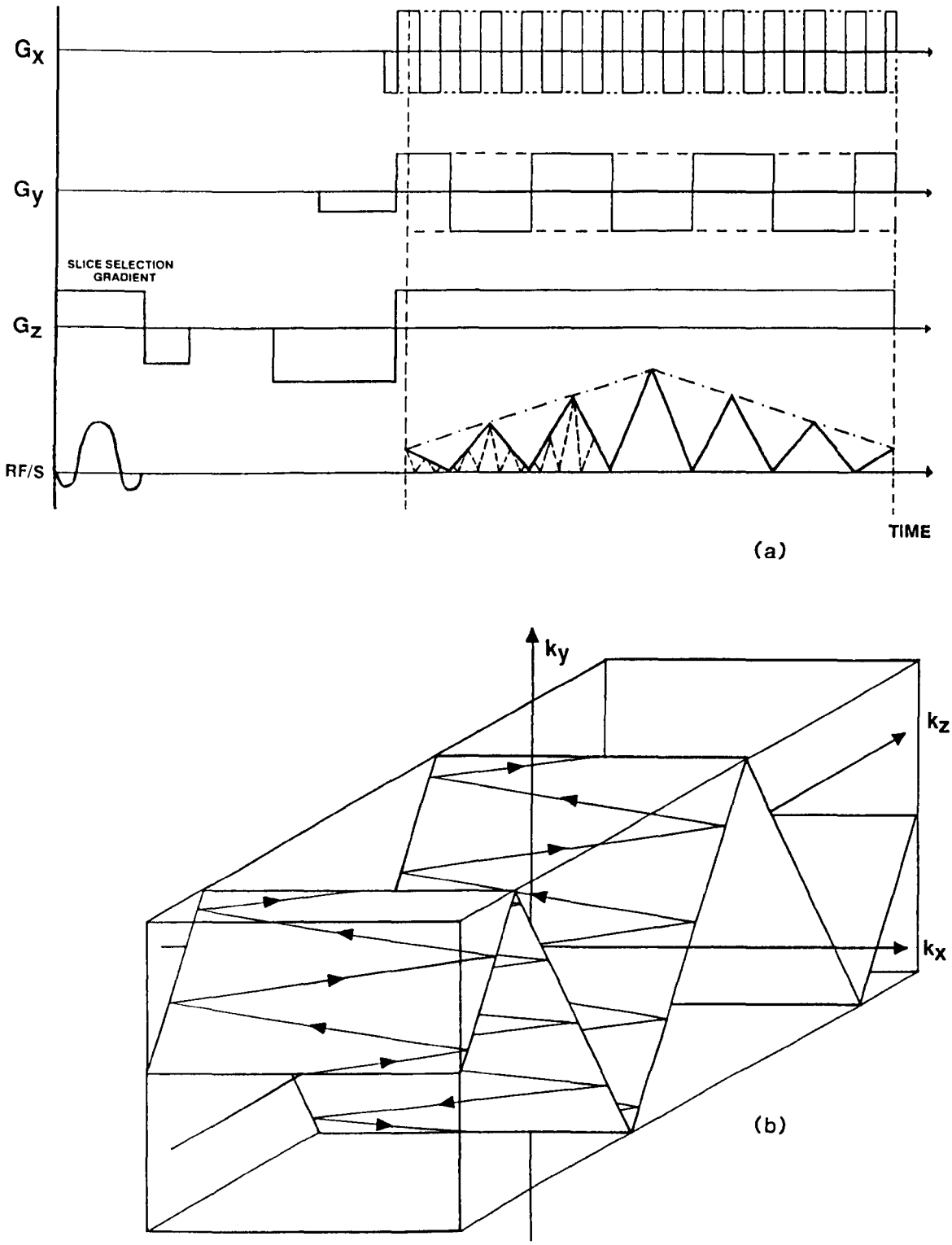


Figure 5.1: (a) Schematic diagram of 4-pass modulus-EVI (dotted lines on gradient waveforms indicate alternate starting polarities). (b) k-space trajectory for a typical (a)-type experiment.

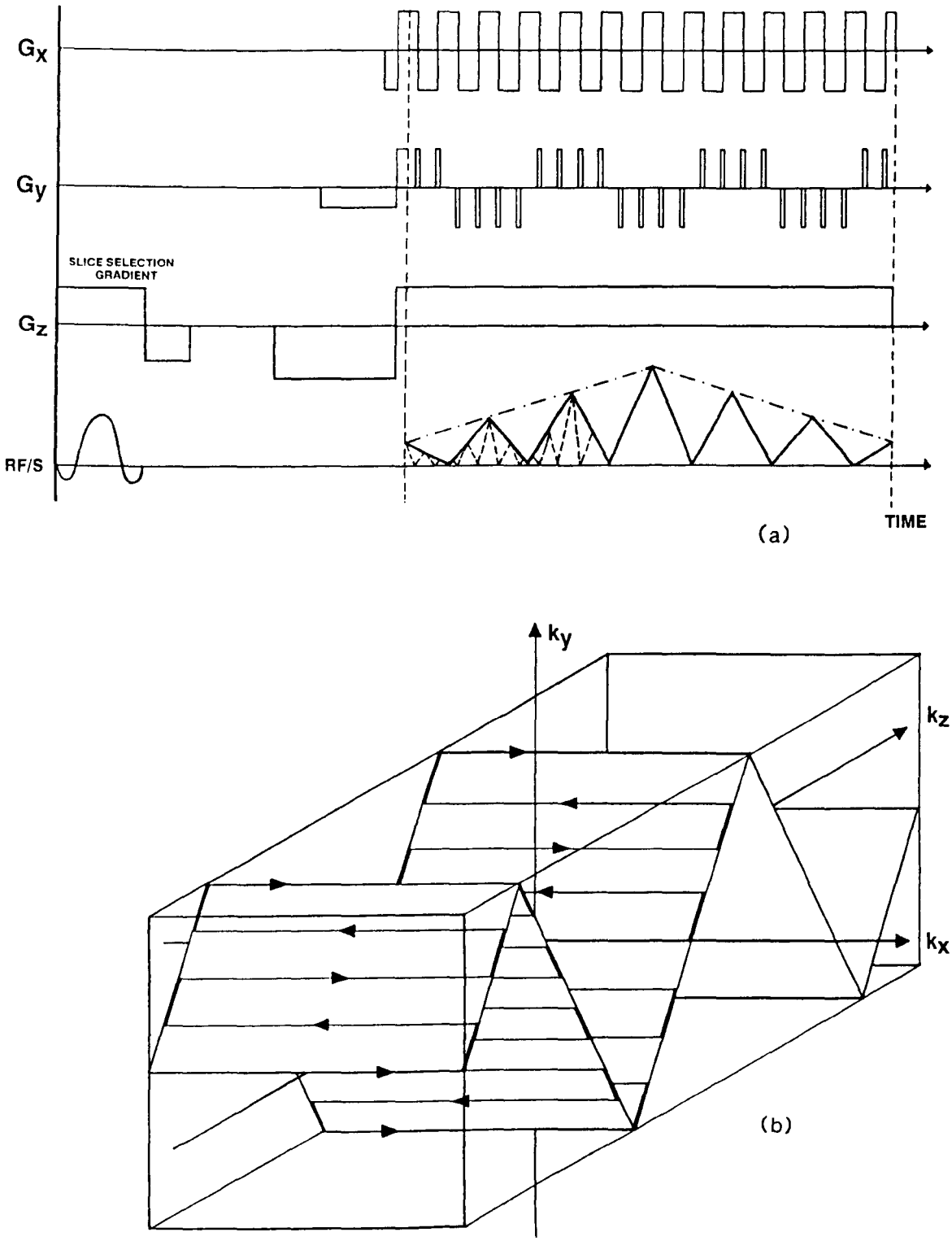


Figure 5.2: (a) Schematic diagram of 2-pass modulus-EVI. Note: This version was used here for single-pass modulus-EVI, see text. (b) k-space trajectory for a typical (a)-type experiment.

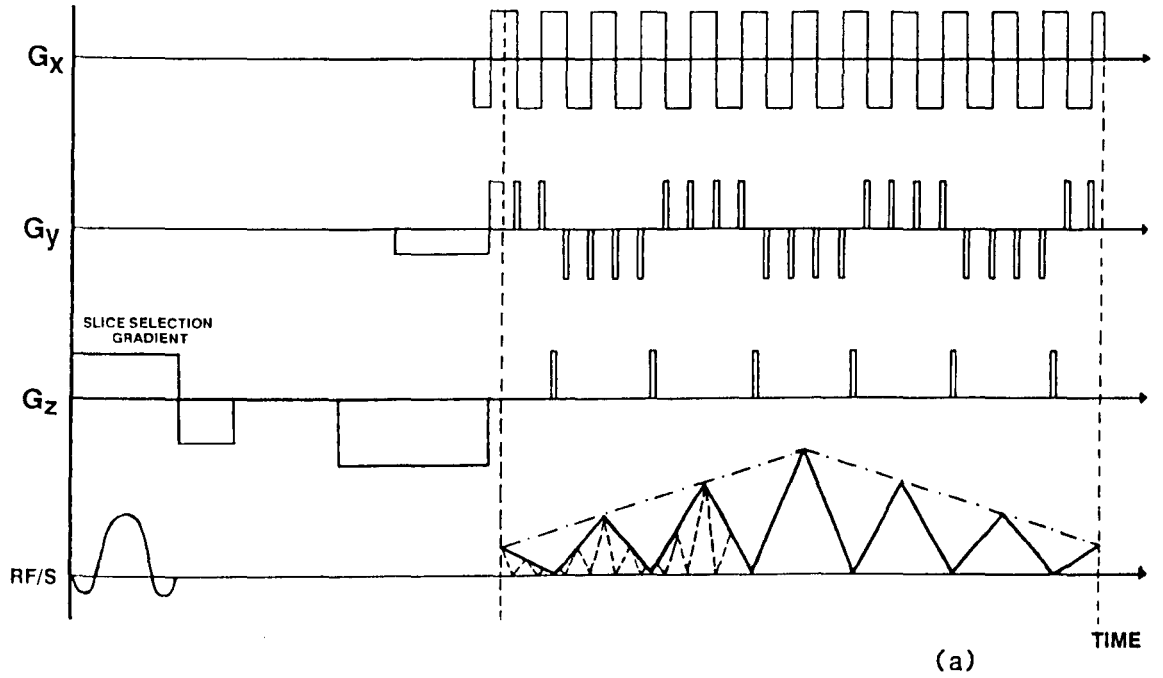


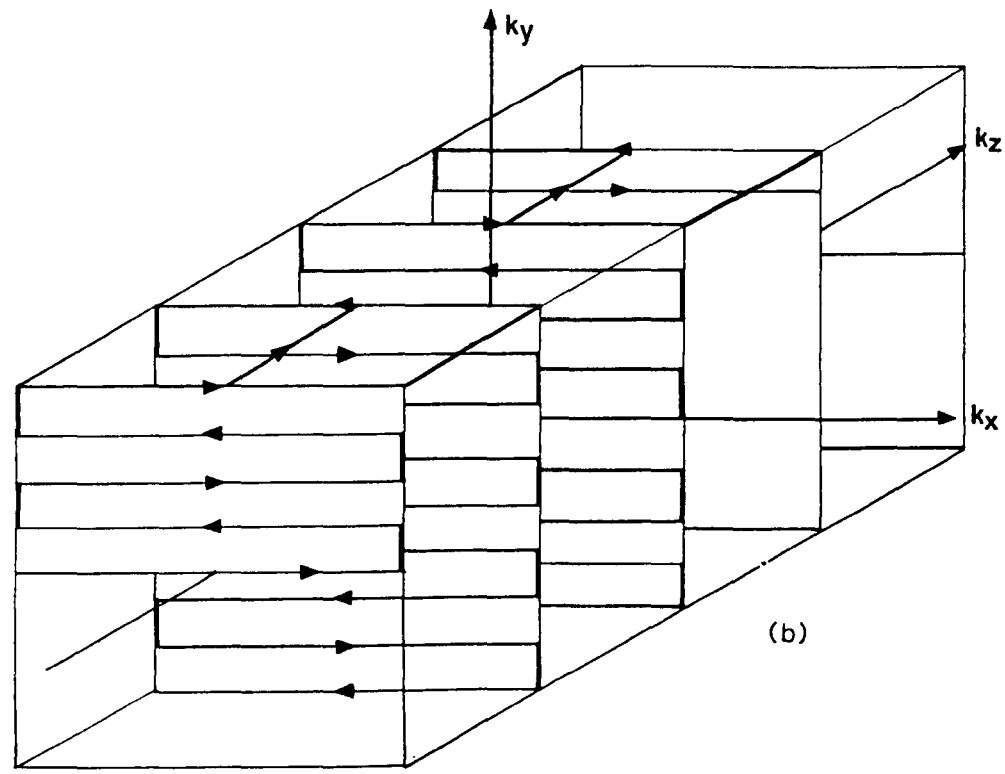


Figure 5.3: (a) Schematic diagram of true "Snapshot" modulus-EVI. (b) k-space trajectory for a typical (a)-type experiment.

(5.2)). This was necessary due to the prohibitively high inductance of the $G_z$ field coil, making short blips impossible to produce with the voltage available. Comparison between MBEST and Single Echo Planar Imaging (SEPI) [51] showed a minimal loss of resolution when a constant gradient is used instead of blips. Comparison of phantom results obtained in preliminary two-pass EVI experiments and those obtained using the single-pass experiment with constant $G_z$-phase encoding showed insignificant differences at such small matrix sizes. The single-pass experiments were processed as described for the fully blipped version.

## 5.3 The Theory of EVI

The analysis used here is an extension, to three dimensions, of that used by Johnson and Hutchison [53] to describe the frequency spectrum yielded upon Fourier transformation of the signal acquired in an MBEST experiment.

The 3D extension of this analysis assumes a correctly ordered set of data, uniformly spaced on a rectangular grid, as would be acquired in a single-pass fully blipped experiment.

The image matrix size may be represented by three integers which, whilst describing the relative dimensions of the image set, indicate also the number of echoes, nested echoes and data points per echo required in the experiment.

- L = The number of sample points per $G_x$ echo.
- M = The number of $G_x$ echoes per $G_y$ echo (i.e. $G_x$ reversals per $G_y$ reversal).
- N = The number of $G_y$ echoes in the experiment. (i.e. $G_y$ reversals).

The total data acquisition time, $T_E$, can be expressed in terms of L, M, N and the various gradient half-periods.

$$T_E = LMN\tau = MNT_x = NT_y \tag{5.1}$$

Where $\tau$ is the sample time, $T_x$ is the $G_x$ half-period and $T_y$ the $G_y$ half period.

The phase of a voxel at position $z$ due to $G_z$ where $\frac{-N}{2} + 1 < n < \frac{N}{2}$ and $n$ is an integer is given by $\phi_z$ where

$$\phi_z = |n|\gamma z \int G_z dt \tag{5.2}$$

The $|n|$ takes account of the refocusing and de-focusing portions of the $G_z$ echo envelope in the modulus-EVI experiment and the integral is performed over a single blip.

For the $G_y$, where $\frac{-M}{2} + 1 < m < \frac{M}{2}$ is the number of a blip from the beginning of a $G_y$ lobe, $\phi_y$ is given by

$$\phi_y = |m|\gamma y \int G_y dt \tag{5.3}$$

If the blips on both $G_y$ and $G_z$ are rectangular and of known duration, $t_y$ and $t_z$ respectively then

$$\begin{aligned} \int G_y dt &= G_y t_y = A_y \\ \int G_z dt &= G_z t_z = A_z \end{aligned} \tag{5.4}$$

The signal component arising from the volume element $dxdydz$ at position (x,y,z) at the $l$th sample point ($\frac{-L}{2} < l < \frac{L}{2}$) of the $m$th $G_x$ echo nested within the $n$th $G_y$ echo is given by

$$ds(l,m,n) = \rho(x,y,z)e^{[i(|l|\tau\gamma x G_x + \phi_y + \phi_z)]}dxdydz \tag{5.5}$$

Expressing this as a sampled function of continuous frequencies $k_x$, $k_y$ and $k_z$ whilst assuming the spins are all in phase when $l = m = n = 0$

$$\begin{aligned} ds(l,m,n) &= \rho(x,y,z)e^{[i(xk_x + yk_y + zk_z)]}dxdydz \\ &\times \delta(k_x - l\Delta k_x)\delta(k_y - m\Delta k_y)\delta(k_z - n\Delta k_z) \end{aligned} \tag{5.6}$$

where

$$\begin{aligned} \Delta k_x &= \frac{\gamma G_x \tau}{2\pi} \\ \Delta k_y &= \frac{\gamma A_y}{2\pi} \\ \Delta k_z &= \frac{\gamma A_z}{2\pi} \end{aligned} \tag{5.7}$$

The signal derived from the whole sample is obtained by integrating equation (5.6) over the whole volume to give the expression

$$\begin{aligned} S(k_x,k_y,k_z) &= \int\int\int \rho(x,y,z)e^{[i(xk_x + yk_y + zk_z)]}dxdydz \\ &\times {}^3III\left(\frac{k_x}{\Delta k_x}, \frac{k_y}{\Delta k_y}, \frac{k_z}{\Delta k_z}\right) \\ &\times {}^3II\left(\frac{k_x}{L\Delta k_x}, \frac{k_y}{M\Delta k_y}, \frac{k_z}{N\Delta k_z}\right) \end{aligned} \tag{5.8}$$

Here the nomenclature follows that of Bracewell [38] where

$${}^3III(u,v,w) = \sum_{a=-\infty}^{\infty} \delta(u-a) \sum_{b=-\infty}^{\infty} \delta(v-b) \sum_{c=-\infty}^{\infty} \delta(w-c)$$

and represents the three-dimensional sampling function and

$${}^3II(p,q,r) = \begin{cases} 1 & \text{when } p, q \text{ and } r < \frac{1}{2} \\ 0 & \text{when } p, q \text{ and } r > \frac{1}{2} \end{cases}$$

and represents the three-dimensional window function.

Equation (5.8) may be transformed using the convolution theorem and the Fourier transforms of ${}^3III$ and ${}^3II$ to yield $\rho'(x,y,z)$, an approximation to the true spin density distribution.

$$\begin{aligned}\rho'(x,y,z) &= \rho(x,y,z) \otimes {}^3III(x\Delta k_x, y\Delta k_y, z\Delta k_z) \\ &\otimes\ L\Delta k_x M\Delta k_y N\Delta k_z\ {}^3sinc(Lx\Delta k_x, My\Delta k_y, Nz\Delta k_z)\end{aligned} \tag{5.9}$$

where ${}^3sinc$ represents the three-dimensional *sinc* function.

The use of a discrete Fourier transform to obtain the image imposes sampling and windowing, in x, y and z space, on the continuous function $\rho'(x,y,z)$. If the Fourier transform is arranged such that the point of zero net phase evolution is brought to the centre of the image, the image is then given by

$$I(x,y,z) = \rho'(x,y,z)\,{}^3III\left(\frac{x}{\Delta x}, \frac{y}{\Delta y}, \frac{z}{\Delta z}\right)\,{}^3II\left(\frac{x}{L\Delta x}, \frac{y}{M\Delta y}, \frac{z}{N\Delta z}\right) \tag{5.10}$$

The ${}^3III$ function determines the spatial extent of the image. To avoid aliasing, convolutions of $\rho(x,y,z)$ about adjacent delta functions of ${}^3III$ should not overlap. The spacing of these delta functions is $1/\Delta k_x$, $1/\Delta k_y$ and $1/\Delta k_z$ along the x, y and z-directions respectively. If the dimensions of the volume to be imaged are $L_x \times L_y \times L_z$ then, to avoid aliasing in the image

$$L_x \leq \frac{1}{\Delta k_x} \quad L_y \leq \frac{1}{\Delta k_y} \quad L_z \leq \frac{1}{\Delta k_z} \tag{5.11}$$

or

$$L_x \leq \frac{2\pi}{\gamma G_x \tau} \quad L_y \leq \frac{2\pi}{\gamma A_y} \quad L_z \leq \frac{2\pi}{\gamma A_z} \tag{5.12}$$

To derive conditions for the required gradient strengths for a specific resolution, it is more convenient to express the blipped gradients as continuous gradients of a lower amplitude and duration equal to the half-period, $T_y$, in the case of $G_y$ and the data acquisition time, $T_E$, in the case of $G_z$. If $G'_y$ and $G'_z$ represent the continuous gradient amplitudes then, for equivalent resolution

$$\begin{aligned}G'_y T_y &= A_y M \\ G'_z T_E &= A_z N\end{aligned} \tag{5.13}$$

must be satisfied.

The voxel bandwidths along each axis are given by

$$\Delta\omega_x = \frac{2\pi}{T_x} \quad \Delta\omega_y = \frac{2\pi}{T_y} \quad \Delta\omega_z = \frac{2\pi}{T_E} \tag{5.14}$$

From equation (5.1)

$$T_x = \frac{T_E}{MN} \quad T_y = \frac{T_E}{N} \tag{5.15}$$

| Matrix size | $T_E$ (ms) | No. of Reversals | | Gradient amplitude for 3 mm resolution (mT/m) | | |
|---|---|---|---|---|---|---|
| | | X | Y | $G_x$ | $G'_y$ | $G'_z$ |
| 16 × 16 × 16 | 64 | 256 | 16 | 31.47 | 1.97 | 0.12 |
| 16 × 16 × 16 | 128 | 256 | 16 | 15.74 | 0.98 | 0.06 |
| 32 × 32 × 8 | 128 | 256 | 8 | 15.74 | 0.49 | 0.06 |
| 32 × 32 × 16 | 128 | 512 | 16 | 31.47 | 0.98 | 0.06 |
| 64 × 32 × 8 | 128 | 256 | 8 | 15.74 | 0.49 | 0.06 |
| 64 × 32 × 16 | 128 | 512 | 16 | 31.47 | 0.98 | 0.06 |
| 64 × 64 × 8 | 128 | 512 | 8 | 31.47 | 0.49 | 0.06 |
| 64 × 64 × 16 | 128 | 1024 | 16 | 62.94 | 0.98 | 0.06 |

Table 5.1: Modulus-EVI parameters for various experimental configurations.

Substitution of the above equation into equation (5.14) yields

$$\Delta\omega_x = \frac{2\pi MN}{T_E} \quad \Delta\omega_y = \frac{2\pi N}{T_E} \quad \Delta\omega_z = \frac{2\pi}{T_E} \tag{5.16}$$

In the general case, by equation (3.3)

$$\Delta\omega = \gamma G \Delta r \tag{5.17}$$

where $\Delta r$ represents a sampling interval which, in this application, corresponds to the physical resolution along the direction of $r$.

Combining equations (5.17) and (5.16) for the non-blipped case, and rearranging. The gradient amplitudes along each axis are given by

$$G_x = \frac{2\pi MN}{\gamma T_E \Delta x} \quad G'_y = \frac{2\pi N}{\gamma T_E \Delta y} \quad G'_z = \frac{2\pi}{\gamma T_E \Delta z} \tag{5.18}$$

For equal resolution along all axes ($\Delta x = \Delta y = \Delta z$) then

$$G_x T_x = G'_y T_y = G'_z T_E \tag{5.19}$$

Table (5.1) lists a summary of various modulus-EVI image matrix sizes, acquisition times and appropriate gradient strengths for 3 mm isotropic resolution. All values refer to square wave gradient modulations.

## 5.4 Data Processing and Image Reconstruction

The procedure, following data acquisition from a single-pass modulus-EVI experiment, prior to FT is as follows:

For illustration it is assumed a time data matrix consisting of $4 \times 4 \times 4$ complex points has been acquired and throughout this description, reference to a single time data point refers always to a complex pair. The physical size of the time data set is therefore twice that of the image data set with data points stored as contiguous complex pairs in a one-dimensional array within the AP500. Here, they can be processed using customized commands which account for their complex nature.

Figure (5.4 (a)) shows a schematic of the nature of the sampled time data following acquisition. Each small triangle represents a $G_x$ echo ($k_x$ line) and each triangle in which they are contained, a $G_y$ echo (($k_x, k_y$) plane). It is worth noting that acquisition begins on half an echo and ends on half an echo in both $G_x$ and $G_y$. In this way the k-space origin occurs in the centre of the sample window making the data set symmetric. For such a data set, a 1D Fourier transform must be used since a 3D Fourier transform would require the asymmetric acquisition as shown figure (5.4 (b)). In all the experiments described here, symmetric acquisition was used.

The first stage of pre-FT processing involves swapping the two halves of the time data in the manner shown by the schematic and k-space diagram of figure (5.5 (a)). This ensures that the FT starts with the DC intensity components and correctly assigns the two halves of the image.

The second stage requires that each alternate $k_x$ line be reversed. This is achieved by reversing every alternate $G_x$ echo as described in chapter 3. The data set afterwards resembles that shown in figure (5.5 (b)). It should be pointed out that alternate $G_x$ echo reversal begins with the first "full" echo. In this way the half echoes at the edge of each $G_y$ echo (($k_x, k_y$) plane) remain untouched. Reversal of these half echo pairs would result in data being swapped between consecutive ($k_x, k_y$) planes and leads to errors in the image.

The final stage prior to FT is alternate ($k_x, k_y$) plane reversal and is a two part process. The first part, figure (5.6 (a)) is achieved in a similar manner to alternate $k_x$ line reversal except, for plane reversal the data corresponding to one complete $G_y$ echo is reversed as compared to a single $G_x$ echo. Unfortunately, the $k_x$ lines within each alternate plane, although now in the correct position with respect to the plane, are all time reversed again. The second part of the process is therefore individual reversal of each of these $k_x$ lines to restore them to correct time orientation, figure (5.6 (b)).

A problem arises with the half $k_x$ lines at the edges of each plane. On the first reversal of the data set they were placed in the correct position w.r.t. the plane but are the wrong way round w.r.t. time evolution and the half $k_x$ lines in the previous and following planes. Individual reversal of these half lines is also incorrect since it creates a discontinuity in the data set. However, the discontinuity is not so great because the $G_x$ half echoes corresponding to these half lines always occur during the $G_y$ switch, when the amplitude of the $G_y$ echo envelope is very low (i.e. at the very edge of the plane). The $k_x$

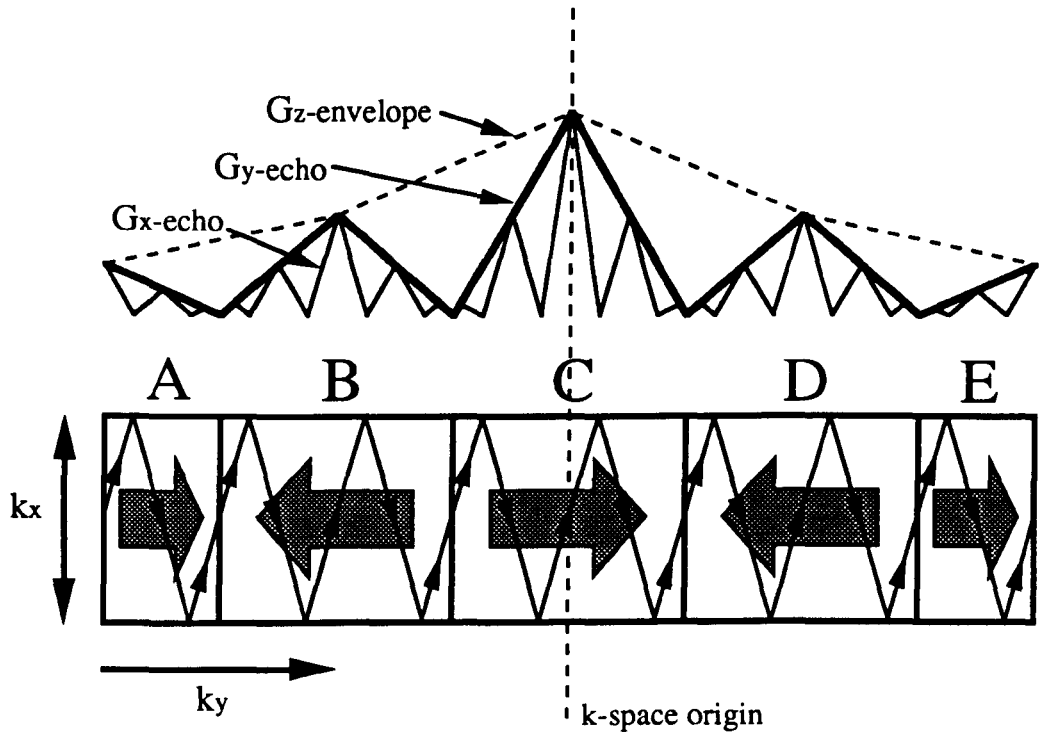


Figure 5.4 (a): Symmetric data acquisition. Time direction from left to right. Large arrows represent Gy polarity i.e. effective time direction for plane.

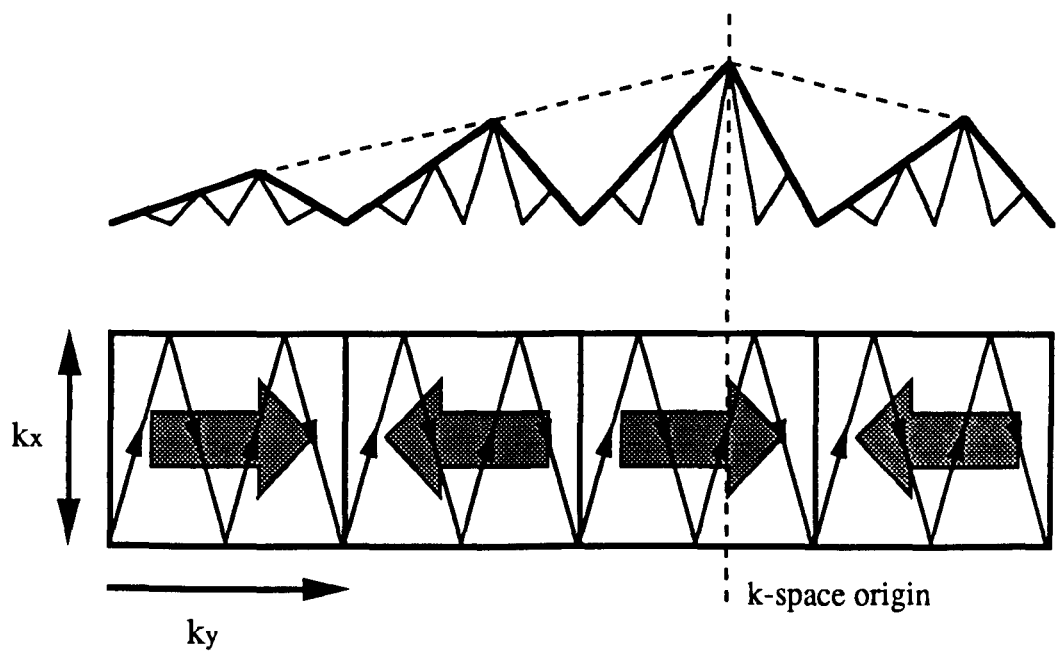


Figure 5.4 (b): Asymmetric time data acquisition involving the same number of echoes as above.

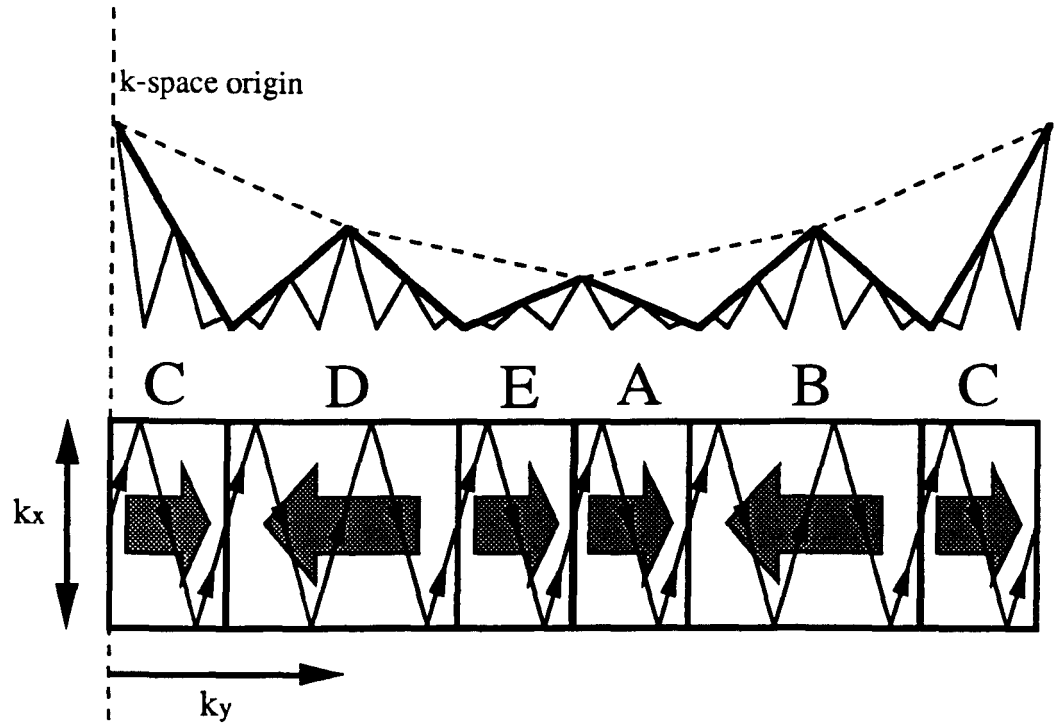


Figure 5.5 (a): Swapping halves of data set.

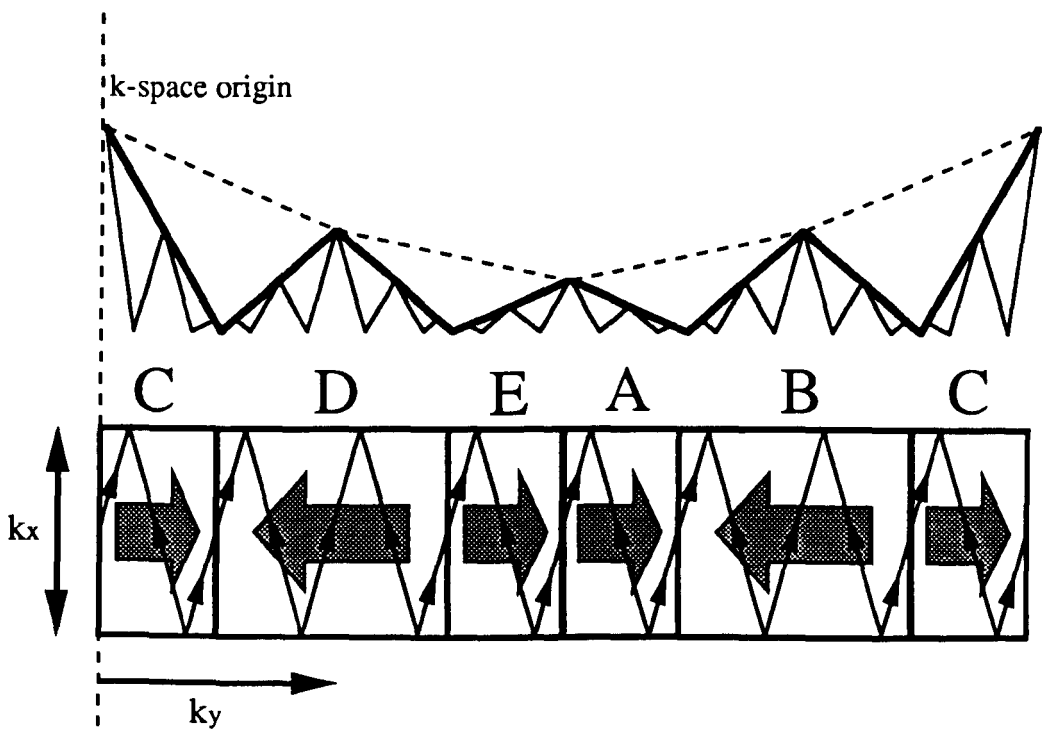


Figure 5.5 (b): Reversal of alternate kx lines within each plane. Reversal begins with first full line (echo).

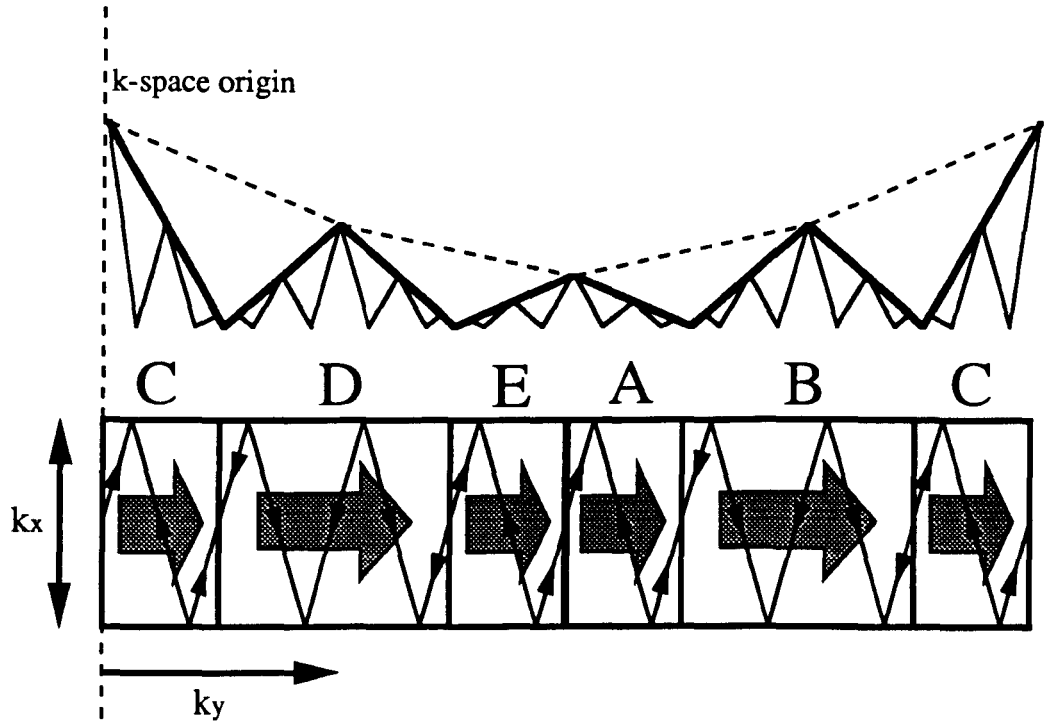


Figure 5.6 (a): Complete reversal of alternate planes D and B.

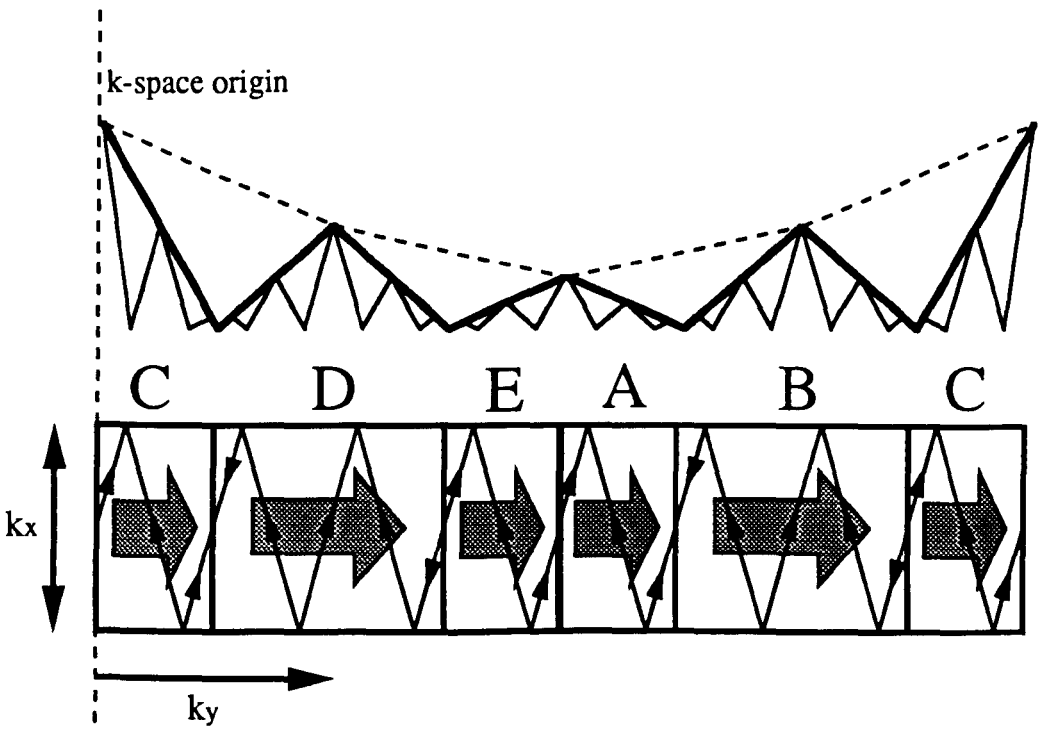


Figure 5.6 (b): Reversal of each full kx line in planes D and B. Note: non-reversal of half lines at edge of each reversed plane.

half lines therefore occur at the extremities of k-space and contribute very little signal to the final image. In asymmetric data acquisition (figure (5.4 (b))) this is not a problem.

Fourier transformation is performed using a 1D complex to complex FFT. As mentioned in chapter 3, use of a 1D FT imparts a slight tilt on the 2D image. In this case, where three dimensional information is present, the tilt manifests itself as a skew through the image data set. Consequently each consecutive image plane, whether viewed transaxially (as a series of stacked XY-planes), coronally (as a series of XZ-planes) or sagittally (as a series of ZY-planes), contains an increasing degree of tilt.

The image spectrum acquired upon FT is shown in figure (5.7 (a)). For the $4 \times 4 \times 4$ example used each single data point is separated by a frequency equal to the pixel bandwidth along the z-direction, $\Delta\omega_z$. Every fifth point is separated by $\Delta\omega_y$ and every seventeenth point by $\Delta\omega_x$. The first 16 points therefore relate to the first $ZY$ plane at $X_0$. The next 16 points to the next $ZY$ plane at $X_1$ and so on to $X_3$. Suitable manipulation, figure (5.7 (b)), in the AP500, allows the image points to be re-ordered into a series of $XY$ image planes stepping from $Z_0$ to $Z_3$. The order can therefore be manipulated to display transaxial, coronal or sagittal views of the object.

Also apparent from figure (5.7 (a)), is that chemical shift and inhomogeneity effects, depending upon their magnitude, can appear not only shifted by pixels in the planar images, but by complete planes. This is not too unreasonable since EPSM, effectively EVI without $G_z$-phase encoding, uses the axis with the lowest pixel bandwidth as the chemical shift axis. Species with different chemical shifts therefore appear in different planes when the data set is viewed as a series of transaxial images.

## 5.5 Experimental Details

### 5.5.1 Software and General Details

For data acquisition and real time display the general purpose program MEVIXP was written. The basic skeleton of the program was provided by EVIMEXP [59].

With the memory available in the AP500, image matrix sizes were restricted to a maximum of $64 \times 32 \times 8$ voxels. The inherent flexibility of MEVIXP allowed both two- and single-pass experiments to be performed using any desired acquisition time. Splicing/plane reversal, data re-ordering, FFT and display all being performed within the processing subroutine. The time from data acquisition to display is about 1 second. Subroutines were added to enable variable display format and either block or smooth image interpolation. All volumar images were displayed as a series of consecutive planar images of transaxial, coronal or sagittal view where appropriate.

On running MEVIXP the operator is asked for details of the number of

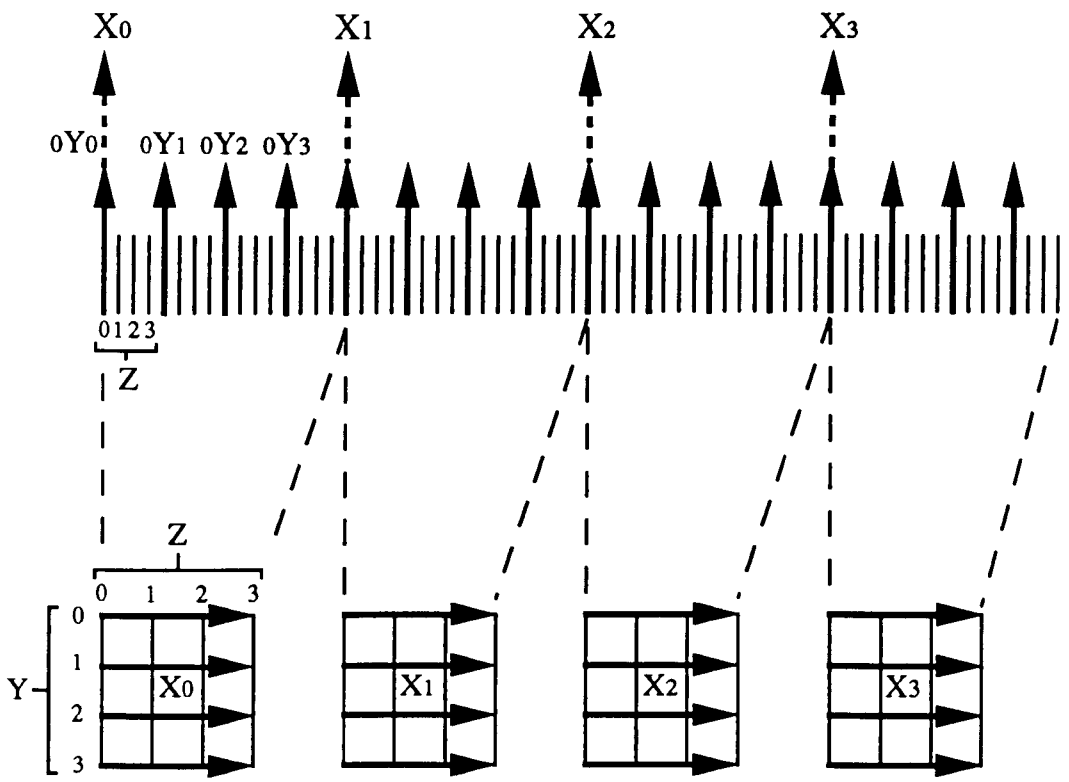


Figure 5.7 (a): Image spectrum acquired upon Fourier transform of the re-ordered time data. The spectrum data points relate to planar images as shown by the dashed lines. See text for further details.

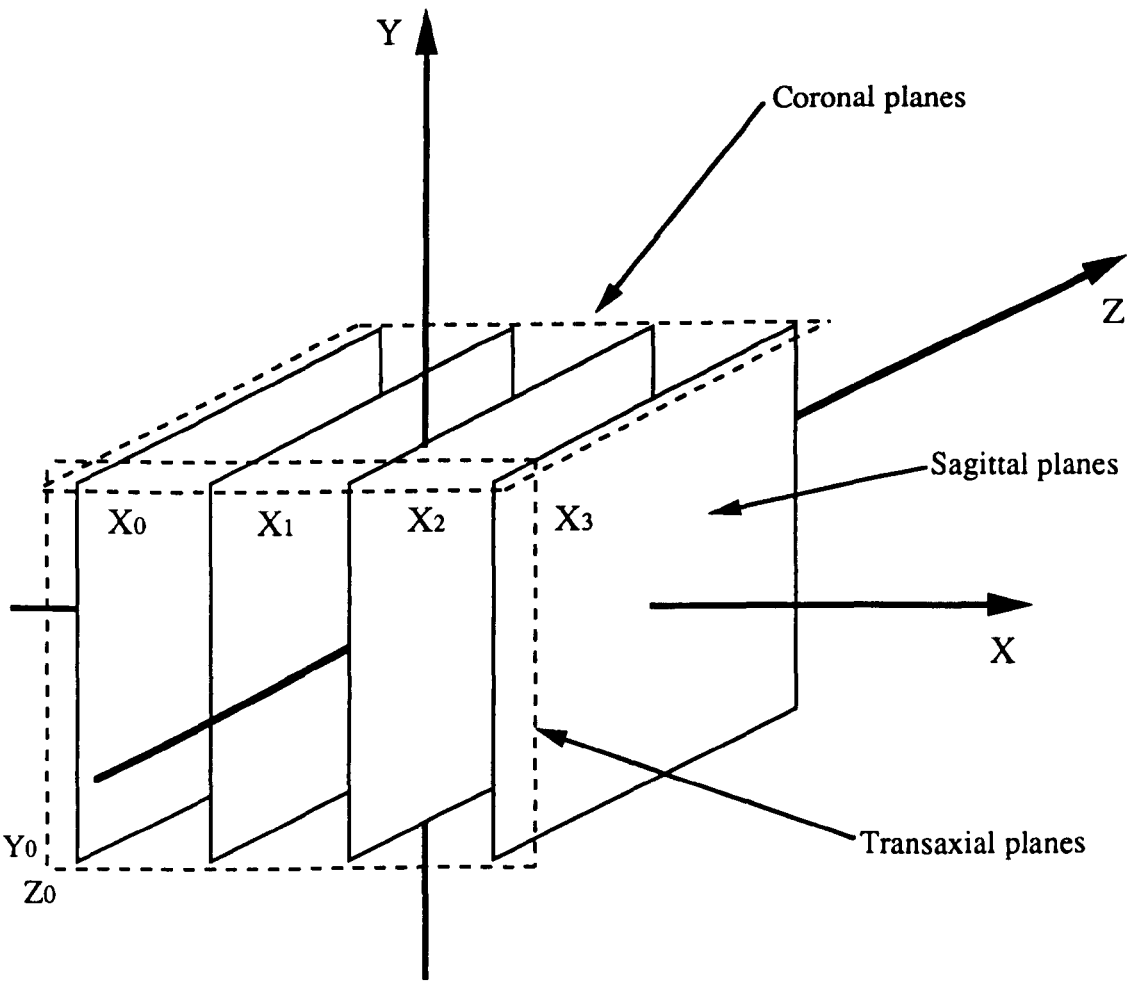


Figure 5.7 (b): Image data organization for transaxial, coronal or sagittal view.

reversals required on each gradient, whether a single- or two-pass experiment is required and whether blips are to be used. MEVIXP then prompts for a WC menu program which contains waveform definitions for each channel of the WC. This menu program may be edited whilst the main program is running and enables quick modification to gradient and RF pulse sequences.

The data acquisition time is determined at run time by setting the appropriate parameter switch to $T_x$, the duration of the $G_x$ half-period. This value and the value entered for the number of $G_x$ switches required, determines the total data acquisition time. Non-linear sampling was used throughout and was set up in the normal way using the program SAMPLEM (which also determines the number of sample points per $G_x$ echo).

The option to store either time data or image data was available and storage was performed using the disc space allocated specially for this purpose.

### 5.5.2 Calibration of Thick Slice Profile

For the purpose of slice profile calibration two WC menu programs were used, PROF1 and EVIPROF. Both of these are run from the EPI experimental program MMEXP.

PROF1 configures the WC to run an experimental pulse sequence consisting of a non-selective $90^o$ RF pulse followed by a $180^o$ pulse at time $\tau$. The spin echo thus formed is sampled in the presence of a constant $G_z$ using 128 sample points. Fourier transformation of the recorded signal yields the z-axis profile of the object being imaged. The use of a $180^o$ pulse serves to refocus any susceptibility effects.

EVIPROF is similar to PROF1 but employs a selective $90^o$ pulse and allows for software adjustment of $G_z$ during slice selection and separately during the spin echo acquisition.

Calibration for an 80 mm slice was undertaken using two phantoms. The first phantom consisted of a perspex water filled rectangular box of height 50 mm, length 160 mm and width 80 mm. This phantom was placed in the central imaging plane of the whole-body birdcage coil with its width (80 mm) parallel to the z-axis. Padding was necessary to raise the phantom such that it lay in the centre of the magnet bore with respect to the x and y axes. PROF1 was executed and the z-profile of the phantom displayed on the 1D display. This profile, obtained without slice selection, represents the full width of the box i.e. 80 mm. $G_z$, the "read" gradient, was adjusted, at the amplifier, until the phantom profile filled out the 1D display. The width of the profile on the display was noted and the display itself calibrated.

The rectangular phantom was replaced by an extended phantom (longer than 80 mm) which consisted of a water filled plastic bottle of diameter 120 mm and length approximately 240 mm. The bottle was placed such that its circular cross-section was concentric with the magnet bore (i.e. the bottle extended 120 mm either side of the central imaging plane). EVIPROF was

loaded into the WC and executed. The $G_z$ read gradient was set as for PROF1 and the $G_z$ slice selection adjusted under software control until the z-profile of the slice selected from the bottle was as wide, when displayed on the 1D display, as that recorded for the rectangular phantom without slice selection. The selected slice width was now 80 mm. The read gradient was switched off (in software) and just the slice selection gradient applied. The needle positions on the front of the Amcron amplifiers which drive $G_z$ were carefully noted. Having calibrated the 1D display previously it was possible to determine absolute $G_z$ slice selection levels for slices of thickness 100 and 160 mm in the same manner. Figure (5.8) summarizes the amplifier levels for each of the four amplifiers required for various slice thicknesses.

MEVIXP incorporates the variable slice selection facility. For modulus-EVI a large $G_z$ pre-acquisition blip is required to initiate imaging at the correct position in k-space. It is preferable therefore to use the full dynamic range of the amplifiers so that this pre-pulse is as short as possible. In order to set up the required slice thickness, the $G_z$ amplifiers are set to a high level and the imaging sequence executed with the $G_z$ phase encoding portion of the experiment set to zero. In this way only the $G_z$ slice selection part of the experiment is input to the amplifiers. The parameter switch which controls slice selection gradient amplitude is then adjusted until the amplifier levels compare with those shown in Figure (5.8) for whatever slice thickness is required.

The response of the whole-body coil and non-linearities in the RF amplification mean that the spins at the ends of the slice do not receive a full $90^o$ selection pulse therefore the signal intensity drops off in these regions. The volumar slice profile, when measured as above, was found to be more trapezoidal than rectangular in shape. In practice, the slice thickness was set such that the length of the plateau region of the profile was equal to 80 or 160 mm. The $G_z$-phase encoding, during image acquisition, was adjusted until each transaxial image (when set up on the bottle phantom) contained the same level of intensity. If figure (5.9) represents the volumar slice profile then this is the point where the net phase accumulation between C and D does not exceed $2\pi$. This ensures approximately equal signal contribution to all XY planes within the image data set. However, as is apparent, the spins in the two regions at either end of the slice have phase accumulations in excess of $2\pi$ therefore wrap-around between the extreme planes of the slice is unavoidable. The signal level, however, is small and the effect is therefore not too severe. An alternative approach to this problem would be to throw away the image planes at each end of the transaxial image data set. Other solutions are discussed later.

### 5.5.3 Setting Up and Fine Adjustment

For EVI the isolated inputs to both the $G_x$ and $G_y$ control boxes were used. This allowed independent adjustment of slew rates and zero levels by manner of the miniature potentiometers on the front panel of each control box.

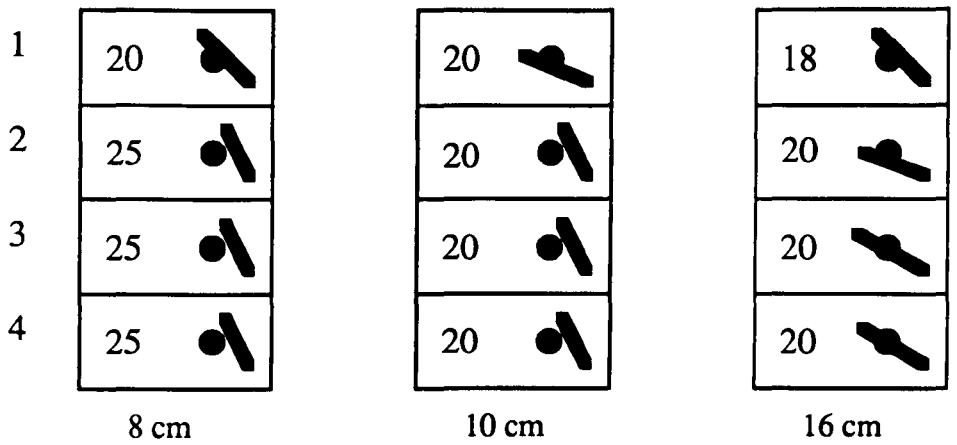


Figure 5.8: Amcron needle positions for slice thicknesses of 8, 10 and 16 cm.

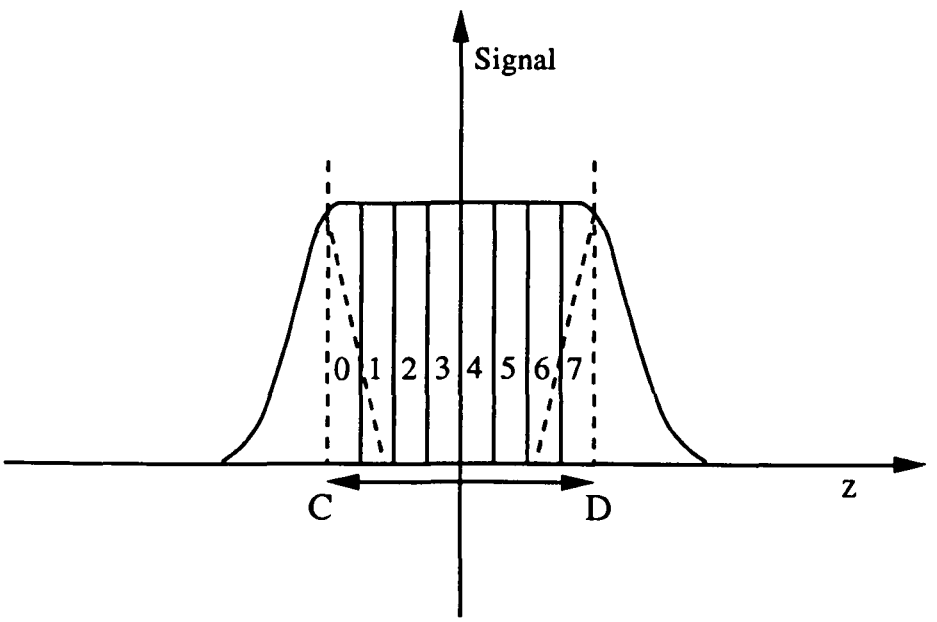


Figure 5.9: Typical thick slice profile. Diagram demonstrates signal wrap around between end slices.

A WC program named EVIB was written which was designed to perform single-pass modulus-EVI using constant $G_z$ and blipped $G_y$-phase encoding. This was loaded into MEVIXP which was previously set up for the required matrix size and acquisition time.

MEVIXP was set in "free run" mode with the $G_x$ and $G_y$ amplifiers and $G_z$-phase encoding switched off. A conical flask of maximum diameter 125 mm and length greater than 80 mm was filled with water and a perspex rod of diameter 25.4 mm inserted. The flask was then sealed and laid in the central imaging plane with its circular cross-section concentric with the magnet bore and the perspex insert parallel to the z-axis. Thick slice selection was set up and shimming performed to maximize the sample FID (displayed using a digital storage oscilloscope (DSO) connected to the imaginary channel of the receiver). Following this, the $G_x$ amplifier was switched into "standby" and left in "mute" mode. This way the amplifier is connected to the field coils but the input is switched off. Any zero offsets on the amplifier at this point result in a field offset across the sample and dephasing of the FID. As expected, the FID was seen to distort but was re-maximized by adjusting the "zero" potentiometer on the amplifier control box. This procedure was repeated for $G_y$ until both sets of gradient amplifiers were correctly zeroed.

With the experiment still in "free run" mode, the $G_x$ amplifier was switched on (out of mute) and a series of gradient echoes monitored on the DSO. For the matrix sizes used, the number of $G_x$ echoes required was 256 in all cases. The pre-acquisition $G_x$ blip, commonly referred to as "FQUAD" was then adjusted to evenly space the first few echo's. Leaving this parameter set, the last few echo's were checked for even spacing. If not, adjustment was performed using the $+ve$ and $-ve$ amplitude fine controls on the amplifier control box. All $G_x$ echoes were then checked for even spacing and the procedure repeated as required.

With the echoes evenly spaced the transaxial plane images were monitored and pre-sample delay (PSD) adjusted until a horizontal streak was produced in the central image plane of the 3D data set. At this point the gradient amplitude and slew rate were adjusted to give the required resolution (streak width), without ghosting, along the x-direction of the image. Careful adjustment was required to confine the streak to one plane only. Having achieved this, $G_x$ was then switched off and the same procedure, including echo spacing, repeated for $G_y$ using the assigned parameter switches and monitoring a vertical streak in the image. The blipped nature of $G_y$ means that the echoes appear as discrete phase encoding steps. This, however, is not a problem when setting up.

With $G_z$-phase encoding still off, $G_x$ and $G_y$ were switched on simultaneously. On doing this, a 2D cross-sectional image of the flask (representing all the transaxial planes collapsed onto the central plane) was displayed. Signal was not confined to just the central plane, as required, and meticulous adjustment of both $G_x$ and $G_y$ $+ve$ and $-ve$ amplitudes was necessary in order to make this the case. Initially, confining all the signal to the central plane was very

difficult–since modulation of $G_x$, by its very nature, produces a component of magnetic field along the z-direction [62]. This pseudo phase encoding gradient was a likely cause of signal spread into planes adjacent to the central plane. It was found, however, that this effect could be minimized by careful shimming.

Once $G_x$ and $G_y$ were set up, $G_z$-phase encoding was applied at the level required for the desired resolution. This level was determined by linearly scaling, under software control, the $G_z$ amplitude required for 80 mm slice thickness. Once set, the pre-acquisition $G_z$ blip was adjusted to position the $G_z$ echo envelope in the centre of the acquisition window. At this point the image was seen to expand throughout all the transaxial planes displayed, representing the full 3D data set.

## 5.6 Spin Echo EVI (SE-EVI)

Magnetic field inhomogeneity and gradient imperfections, encompassed by $T_2^*$, are of concern in EPI. In EVI these effects are a much greater problem because of the inherently low voxel bandwidth along the z-direction. The consequent broadening of the PSF along this axis, leads to a spread of signal between transaxial image planes. To minimize such problems, the experimental pulse sequence shown in figure (5.10) was employed to enable data acquisition under a spin echo. In this way, $T_2^*$ effects are refocused in the centre of the acquisition window and the inter-plane spread reduced

All pre-acquisition, spin conditioning, blips occur before the $180^o$ pulse so that any effects due to gradient imperfection are refocused. The price to pay for the introduction of the $180^o$ pulse is a reduction in image contrast. If the data is to be acquired in a modulus fashion then it must be sampled under a complete spin echo. If, for example, the acquisition window is of duration 100 ms then the spin echo must peak 50 ms after sampling begins. In order for this to occur the $180^o$ pulse must be applied, at least, 50 ms after slice selection. During this period of "dead time" spin components with short $T_2$ values will have decayed away and therefore do not appear in the image. Additionally, flowing material, such as blood, having been selected by the $90^o$ pulse, may well have flowed out of the slice by the time the $180^o$ pulse is applied. Rapidly flowing blood, such as in the heart, appears dark in the image. These problems are reduced if a shorter $T_E$ is used.

## 5.7 Zoomed EVI (ZEVI)

Zoomed EVI (ZEVI) [56, 58] offers the greatest potential for localized volume studies of the heart. Image matrix sizes can remain relatively small, thereby reducing hardware requirements, whilst still maintaining a high resolution over the restricted field of view. In cardiovascular studies the region of interest is usually restricted to the heart mass only. The surrounding body need not be imaged, reducing the required FOV by at least a half.

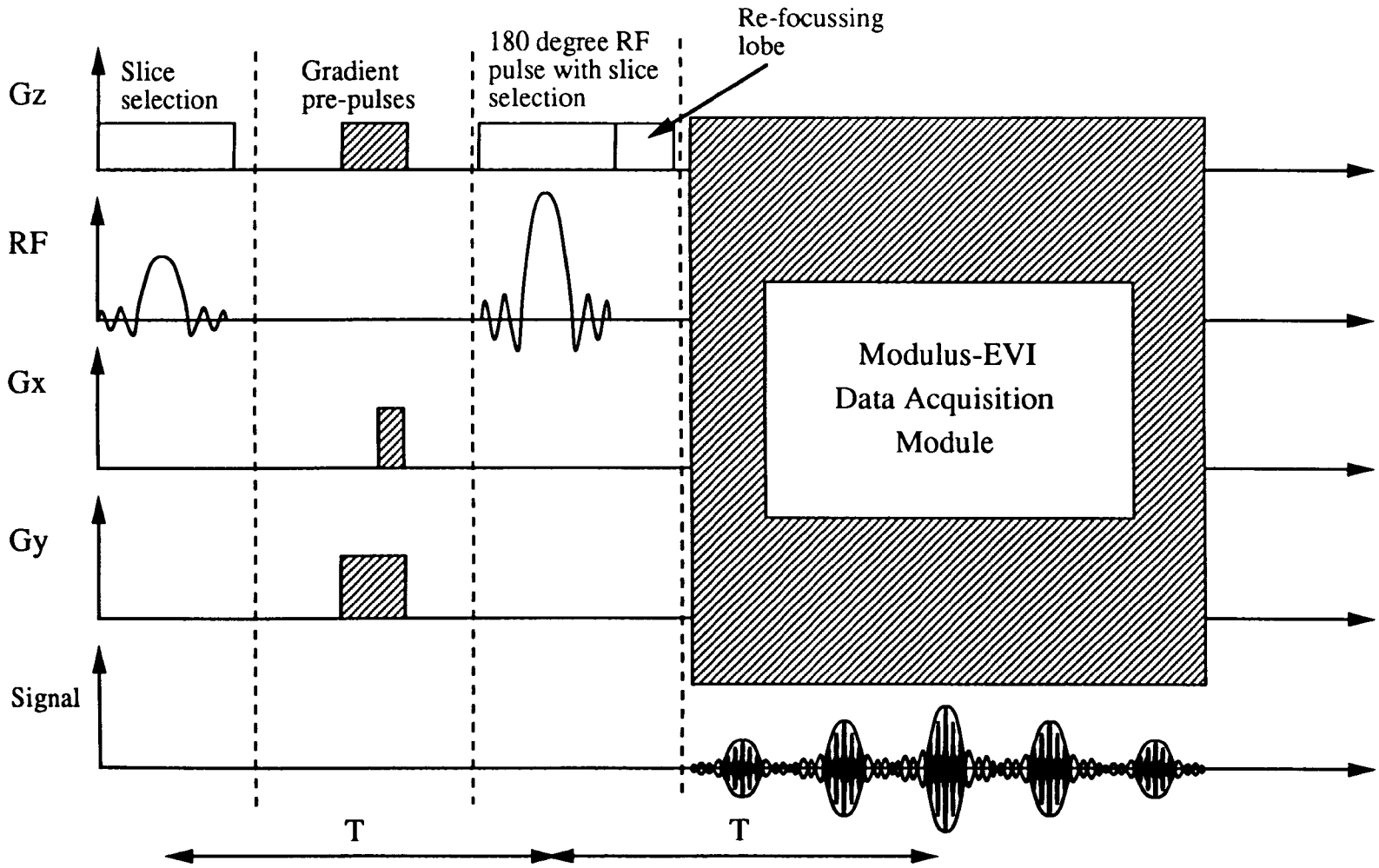


Figure 5.10: Spin echo EVI (SE-EVI) gradient and RF timing diagram.

The ZEVI results presented here were acquired with the intention of demonstrating that the zooming procedure is feasible. However, hardware limitations prevented the author from expanding the zoomed regions to fill the matrix size available, the gradient amplitudes being limited by their slew rate.

The zooming procedure itself is not unlike SE-EVI, the only difference being that $G_y$ is applied during the selective 180° pulse instead of $G_z$. In this way the volume of interest is defined along the two axes z and y. The extent along the x-axis is defined by the receiver bandwidth. The pulse sequence for ZEVI is shown in figure (5.11). Following thick slice selection the signal is allowed to decay to zero in the presence of $G_y$. While this is still switched on, a selective 180° pulse is applied which defines the zoomed strip within the image. Only those spins within the zoom strip are refocused into a spin echo. As with SE-EVI, a delay (for modulus acquisition) is inherent in the technique.

## 5.8 General Results Using Modulus-EVI

All the results presented in this section were acquired using the pulse sequence for the single-pass modulus experiment detailed in figure (5.3).

### 5.8.1 $16 \times 16 \times 16$ Voxel Results

Conical Flask Phantom

Figure (5.12) shows 16 transaxial and sagittal sections of a water phantom consisting of a conical flask of base diameter 125 mm. Contained within the flask was a perspex insert of 25.4 mm in diameter. The total, or volumar, slice thickness was 80 mm and data acquisition took 122.88 ms. The $G_x$ waveform used was a trapezoid of half-period duration 480 $\mu$s and zero to peak rise time of 150 $\mu$s. The z-direction resolution is approximately 5 mm and the transaxial plane resolution approximately 7 mm, corresponding to a peak $G_x$ amplitude of 10 mT/m (corrected for trapezoidal waveform). Non-linear sampling was used throughout.

Slight ghost artefacts can be seen in the images which represent each end of the thick slice. These are due, in part, to the non-linear spatial response of the RF coil (see profile calibration) along its axial direction. In practice the image display was set to sagittal view and $G_z$-phase encoding adjusted until the sagittal sections filled out the image FOV. The intensity in each plane is therefore the same. In dealing with the problem of poor slice profile, consideration of the RF coil response may be taken into account during the design stage of the selective pulse.

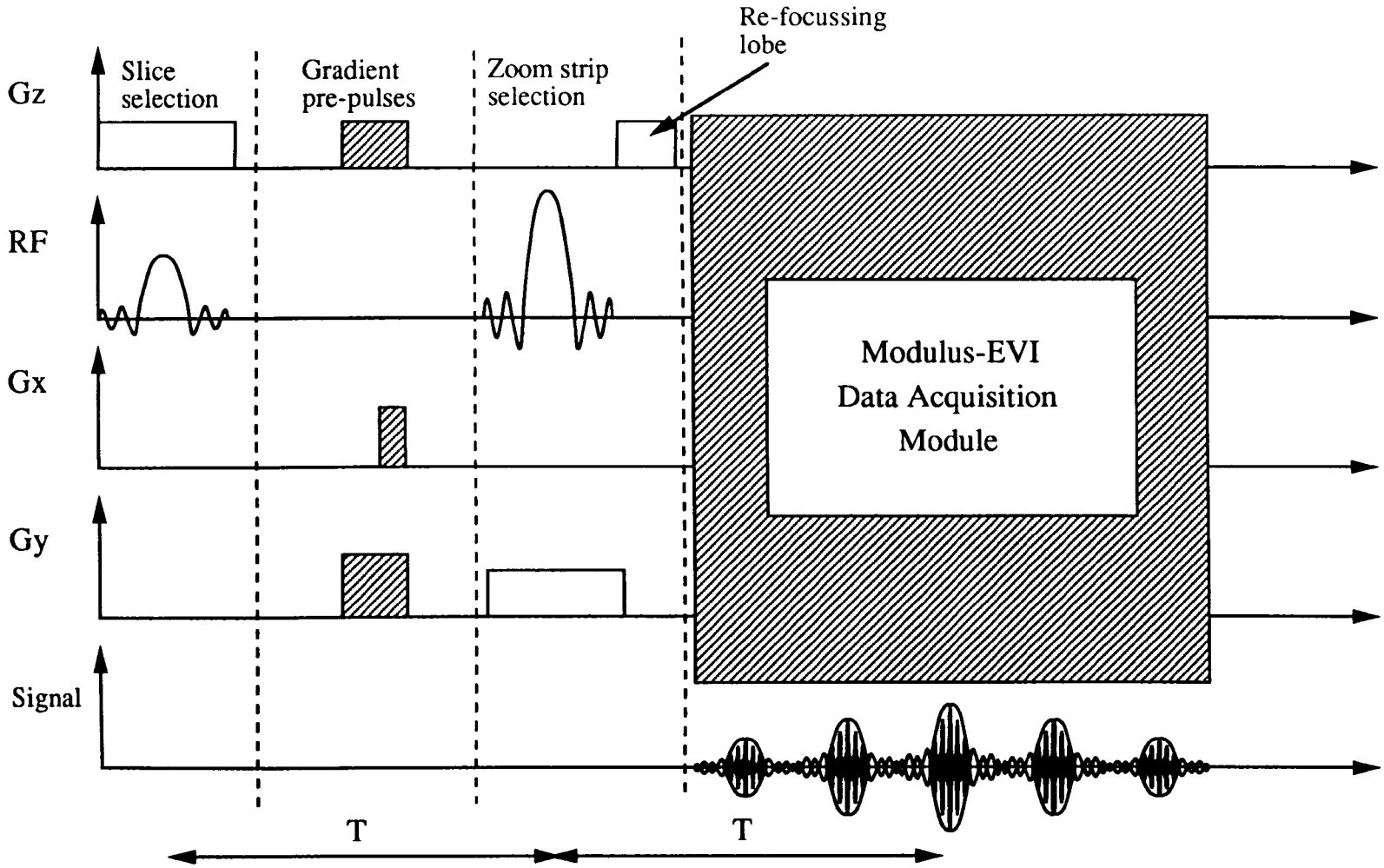


Figure 5.11: Zoomed EVI (ZEVI) gradient and RF timing diagram.

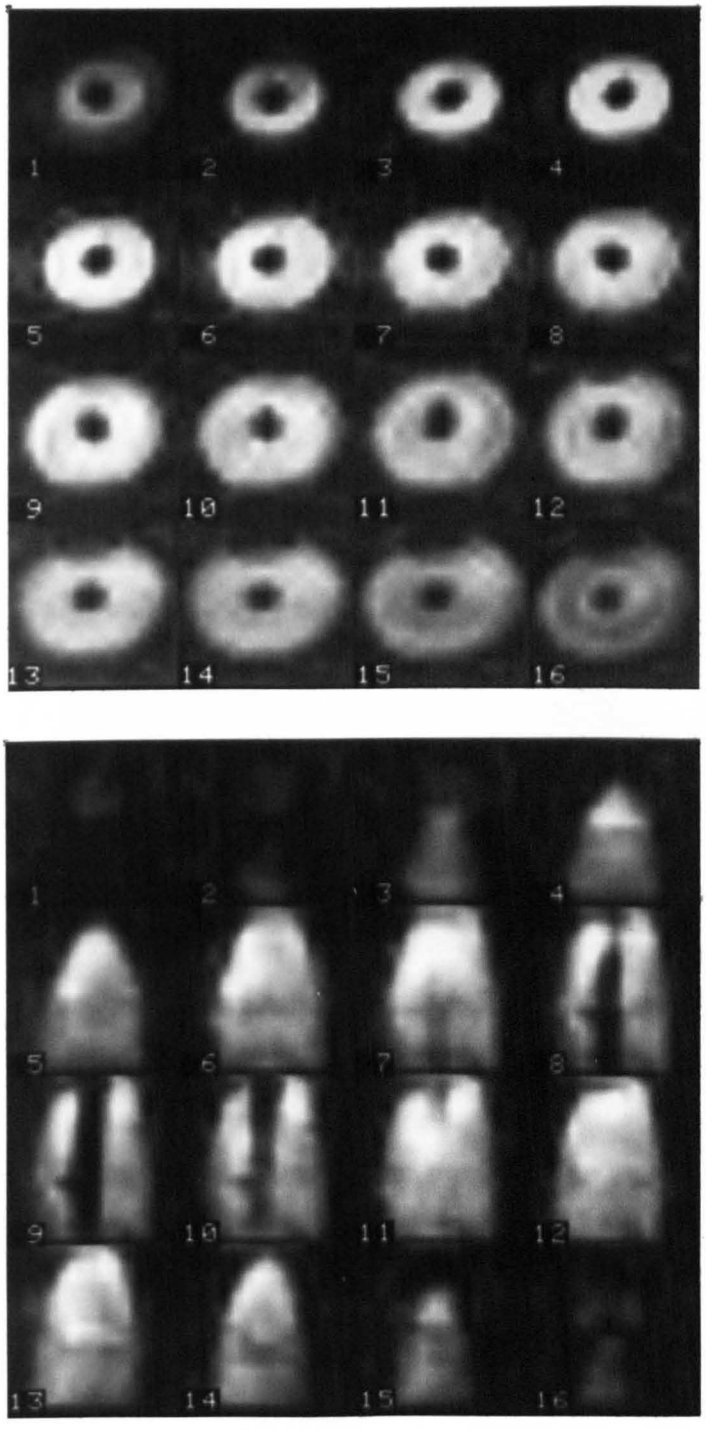


Figure 5.12: Transaxial and sagittal sections of a water filled conical flask. Each data set consists of 16 16 $\times$ 16 pixel images. Data linearly interpolated to fill screen.

### 5.8.2 $32 \times 32 \times 8$ Voxel Results

Conical Flask Phantom

Keeping the data acquisition time the same as for the previous section, the experiment was re-configured for a $32 \times 32 \times 8$ voxel image. Figure (5.13 (a)) shows images obtained with $G_z$-phase encoding off. As was expected most of the signal is concentrated in one plane only (the central plane). There is a slight bleeding of signal into surrounding planes which is indicative of the pseudo phase encoding caused by the z component of the modulated $G_x$. $+ve$ and $-ve$ amplitude adjustment for both $G_x$ and $G_y$ was meticulous in order to achieve this image.

Figure (5.13 (b)) shows the full volume transaxial data set with $G_z$-phase encoding switched on. The volumar slice thickness was 80 mm and the corresponding axial resolution approximately 10 mm. The in-plane resolution is approximately 5 mm by 5 mm corresponding to a peak $G_x$ amplitude of 14 mT/m. During these phantom experiments certain hardware limitations of the present gradient drivers were reached. The slew rate of the gradient amplifiers limited practical $G_x$ rise times to approximately 116 $\mu$s (0 - Pk). In addition, the slew rate limited the usable area of gradient available since the waveform became more triangular in shape with increasing amplitude. Additional problems with the accuracy of the non-linear sample pattern definition also prevented the use of very fast gradient rise times.

Volunteer Head Results

Figure (5.14) shows results obtained on the head of a volunteer. These images were acquired in two separate snapshot experiments by moving the patient through the imaging region, by approximately 80 mm, between each experiment. Data acquisition took 122.88 ms and the in-plane resolution is 5 mm by 5 mm. Slight aliasing has occurred in the extreme planes as expected but there is a notable difference in structure between individual planes. Differentiation between grey and white matter is apparent as are the fluid filled ventricles, figure (5.14 (a)). Further down in the head the fluid filled orbits can be seen and even further still, the cerebellum. The signal voids in regions around the mouth and upper jaw may be due to the changes in susceptibility encountered here. Susceptibility artefacts introduced by the ear cavities are also present in planes 6 and 7 figure (5.14 (b)).

### 5.8.3 $64 \times 32 \times 8$ Voxel Results

Thorax Results

Figure (5.15) shows the results obtained from the thorax of a healthy volunteer. For these experiments, the number of sample points per $G_x$ echo was doubled from 32 to 64. The acquisition time was 102.4 ms which corresponds to a $G_x$ half-period of 400 $\mu$s. This shortened sample window was possible since the whole of the thorax, could be made to fill out the image matrix

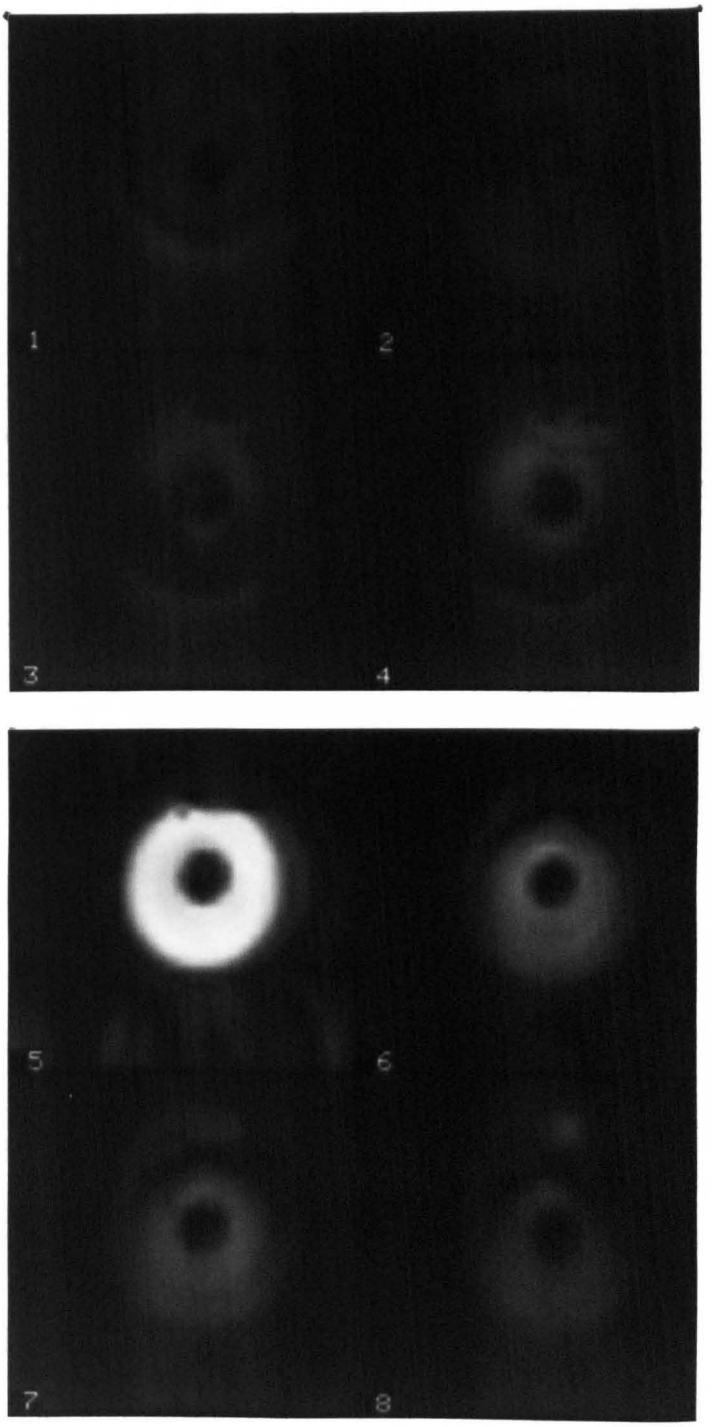


Figure 5.13 (a): Transaxial $32 \times 32 \times 8$ voxel images of conical flask phantom. No $G_z$ on.

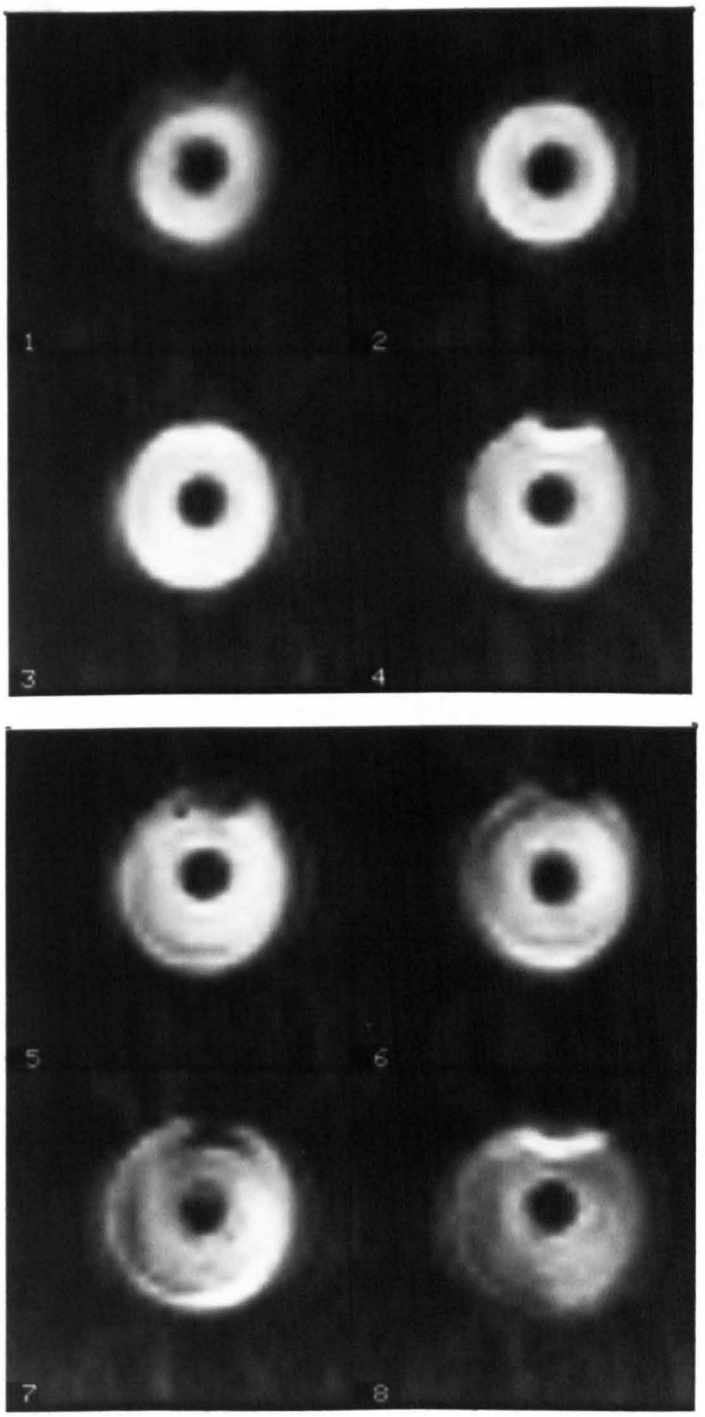


Figure 5.13 (b): As (a) with $G_z$ on.

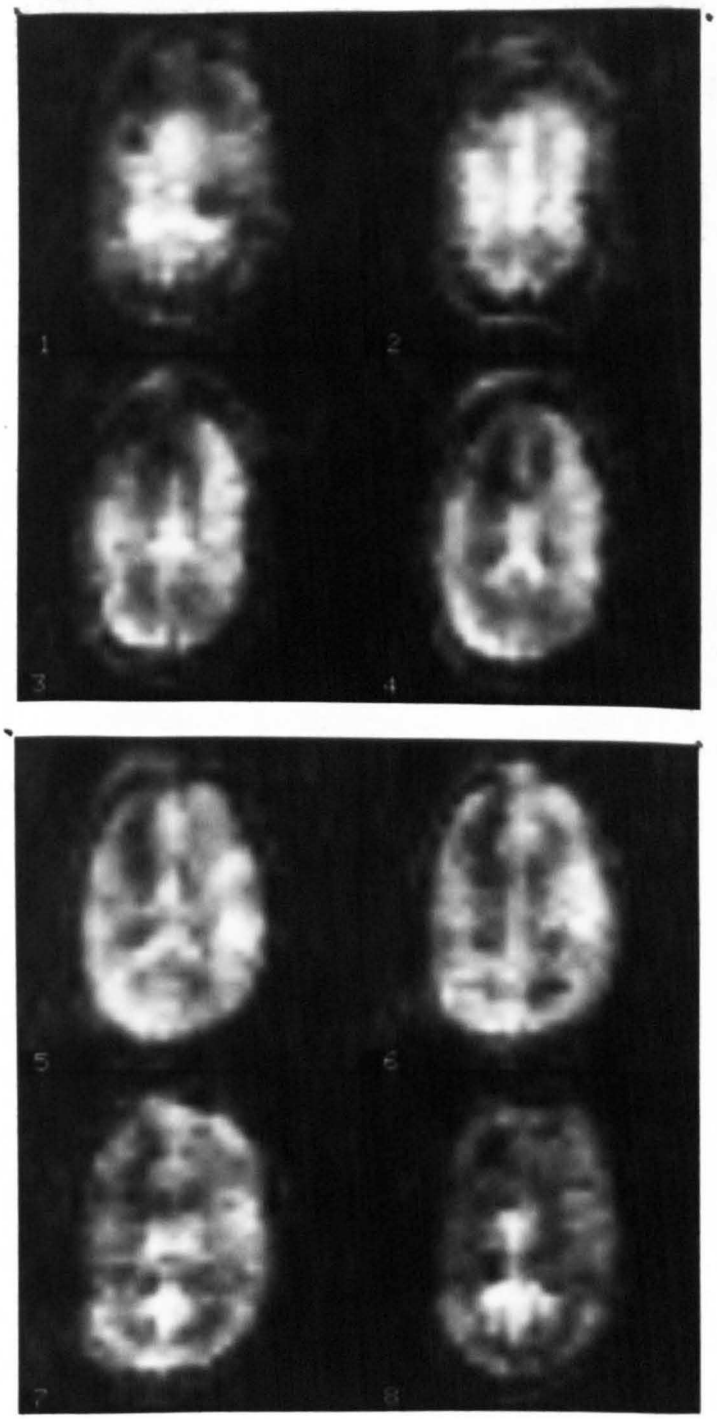


Figure 5.14 (a): $32 \times 32 \times 8$ volunteer head images - upper section showing ventricles.

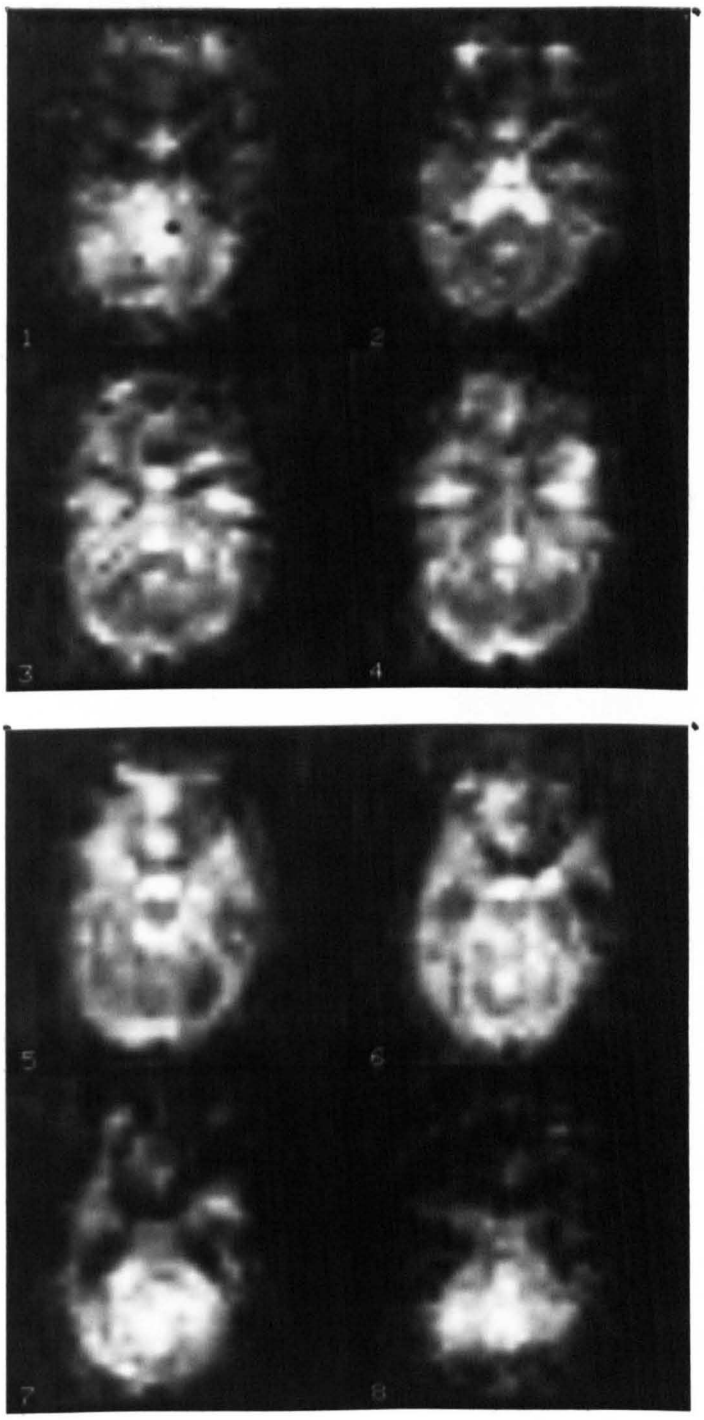


Figure 5.14 (b): $32 \times 32 \times 8$ volunteer head images - lower section showing orbits. Susceptibility artefacts in planes 6 and 7.

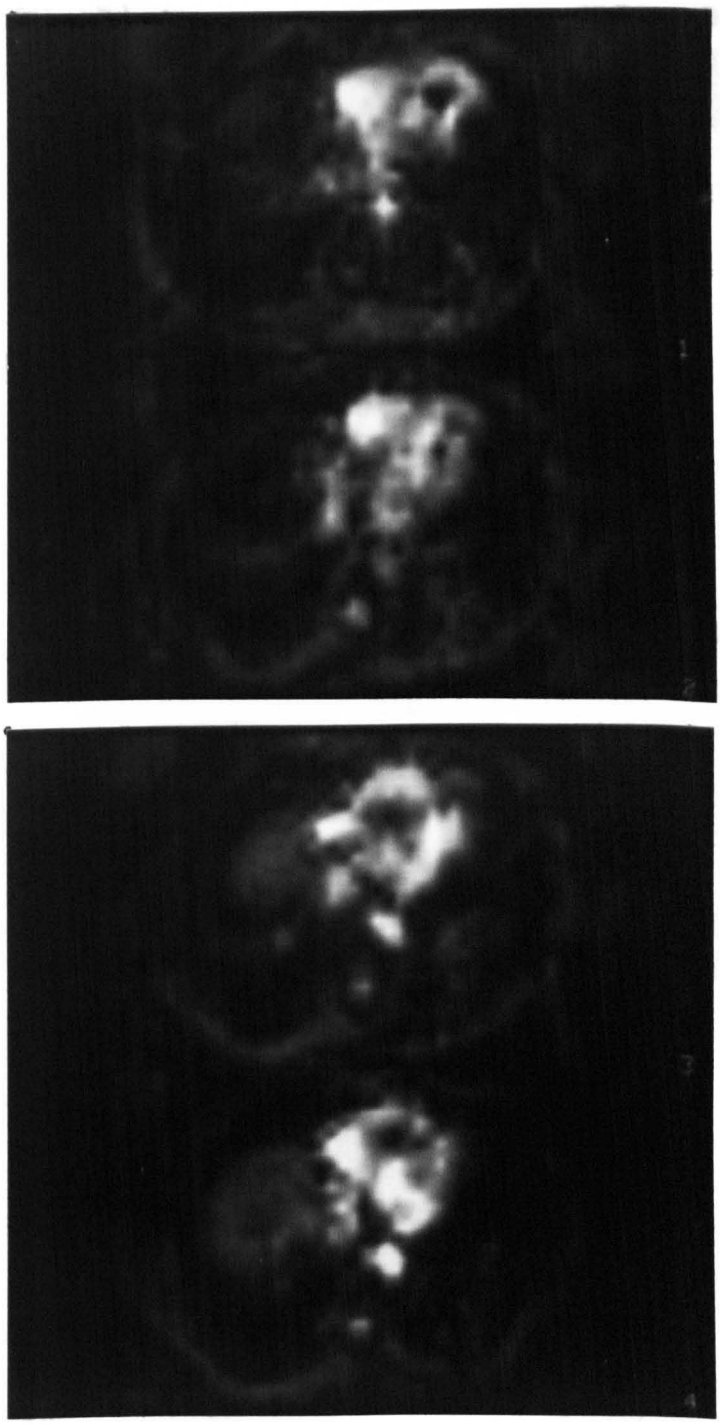

Figure 5.15: $64 \times 32 \times 8$ Voxel results obtained from the thorax of a healthy volunteer.

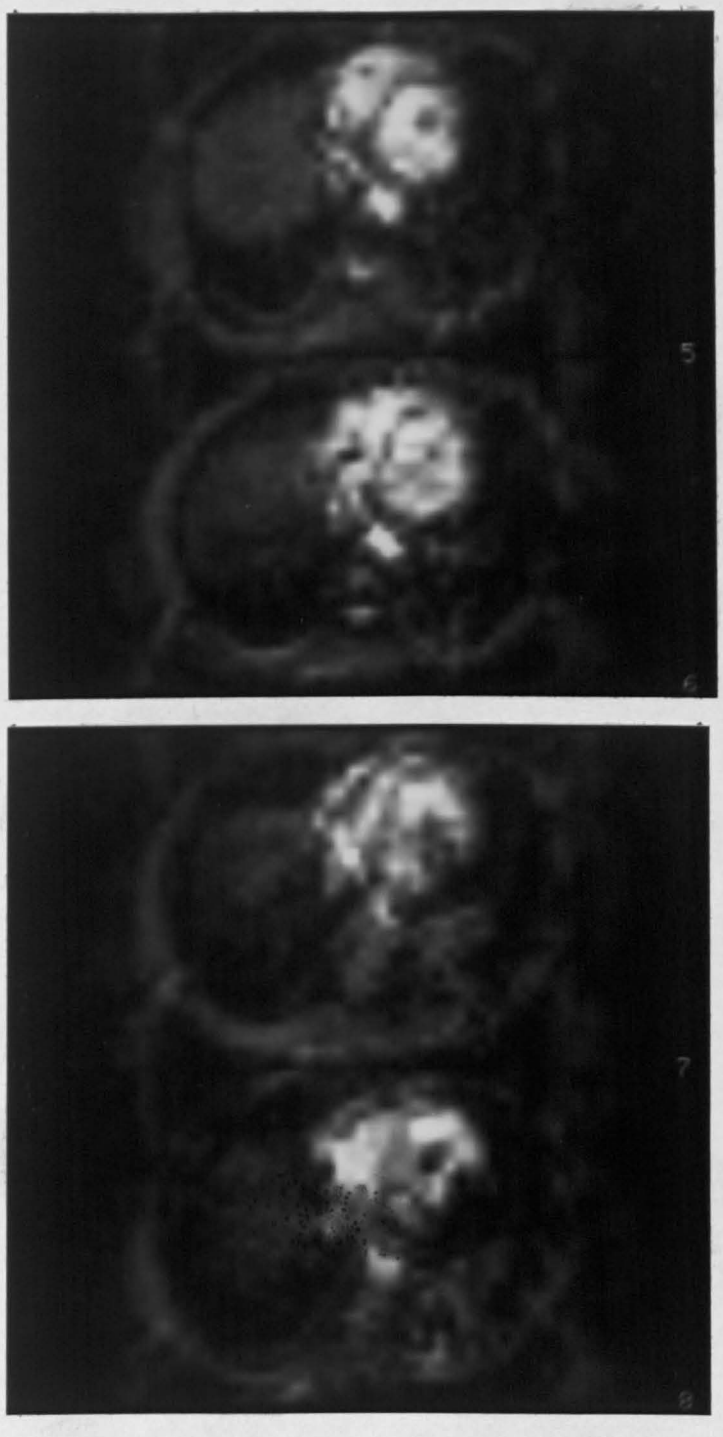


Figure 5.15: CONTINUED.

with the limited gradient amplitude available. The images depict 8 transaxial planes from a thick slice of approximately 80 mm. The axial resolution is 10 mm with an in-plane resolution of 6 mm by 4 mm. Although crude, much detail can be seen. The aorta is visible as are the septum and the chambers of the heart. In the lower most planes, the top of the liver can also be seen. Susceptibility artefacts from the surrounding lungs are not too severe, however, the short $T_2$ of the heart muscle is responsible for slight through-plane signal spread.

Mid-Body Results

Figure (5.16) shows the images obtained from the mid-body of the same volunteer. Starting at the level of the liver and moving down, CSF in the spine is shown and details of the hepatic veins are visible. The stomach is empty and does not appear in these images. Moving further down, the kidneys come into view and details of the renal pelvis in the left kidney are apparent. In the lower image planes the spleen and the intestines can also be seen. Through-plane signal spread seems very low in these images and wrap around between the end slices is also minimal. These qualities may be by virtue of the fact that the trunk represents a homogeneous sample containing long $T_2$ components and few susceptibility problems.

## 5.9 Spin Echo EVI (SE-EVI) Results

### 5.9.1 $32 \times 32 \times 8$ Voxel - Head Results

Figure (5.17) shows the results obtained from the head of a volunteer using the SE-EVI pulse sequence. Data acquisition took 79.9 ms for a $G_z$ half-period of 312 $\mu$s. The rise time used here was 116 $\mu$s (0 - Pk) and represents the hardware limit. The spin echo peak occurred approximately 80 ms after slice selection. The image contrast is therefore fairly poor. Through-plane signal spread is greatly reduced with the use of a 180° RF pulse resulting in clear distinction between individual transaxial planes. Slice thickness is 80 mm and in-plane resolution approximately 7 mm by 5 mm corresponding to a $G_x$ amplitude of 15 mT/m.

### 5.9.2 $64 \times 32 \times 8$ Voxel - Moving Tube Phantom

This experiment was designed to test the degree of signal confinement between transaxial planes. The phantom used consisted of two 15 mm diameter water filled test tubes mounted side by side and upright on a wooden board, figure (5.18 (a)). This board was then placed on the patient bed and pushed through the imaging volume (through planes $Z_0 - Z_7$) in increments of 10 mm, figure (5.18 (b)). The imaging sequence was as in the previous section but with 64 as opposed to 32 data points per $G_x$ echo. The slice thickness was 80 mm.

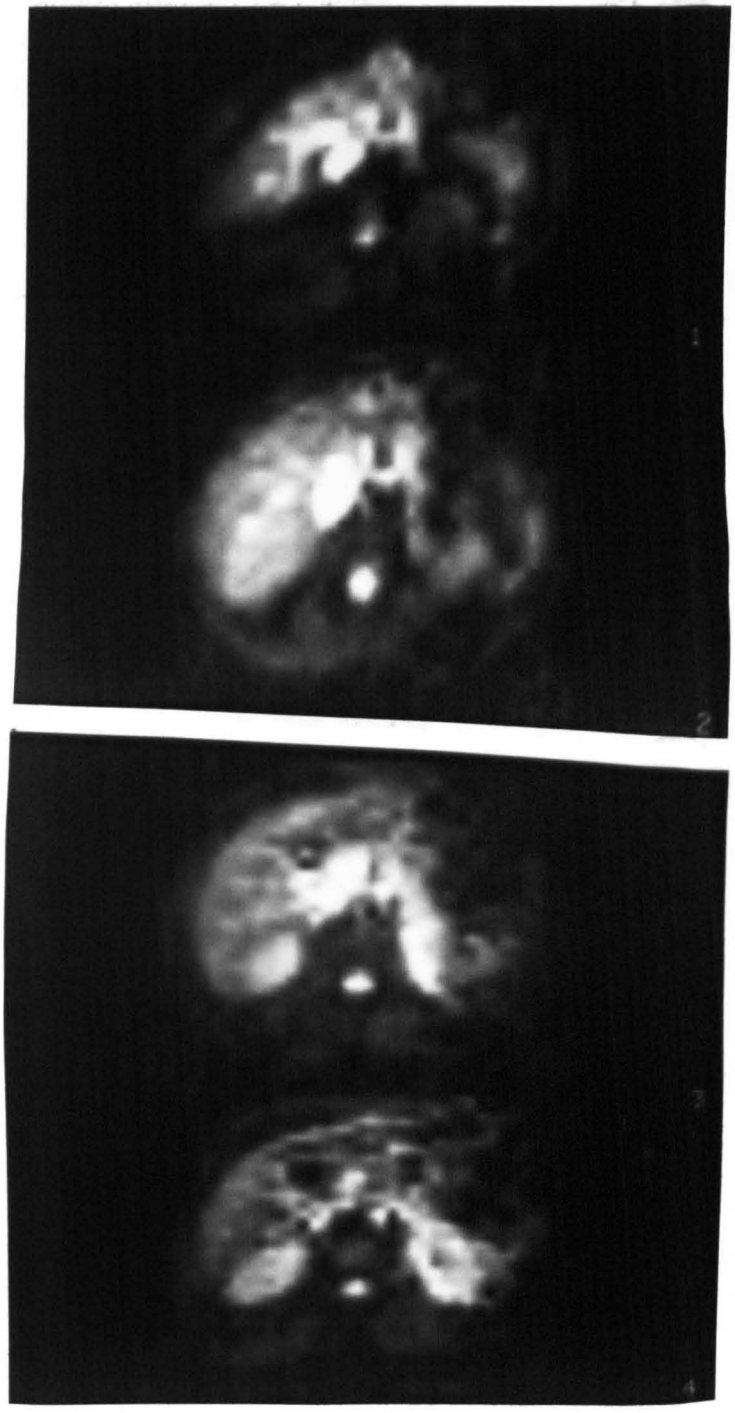

Figure 5.16: $64 \times 32 \times 8$ Voxel results obtained from the mid-body of a volunteer.

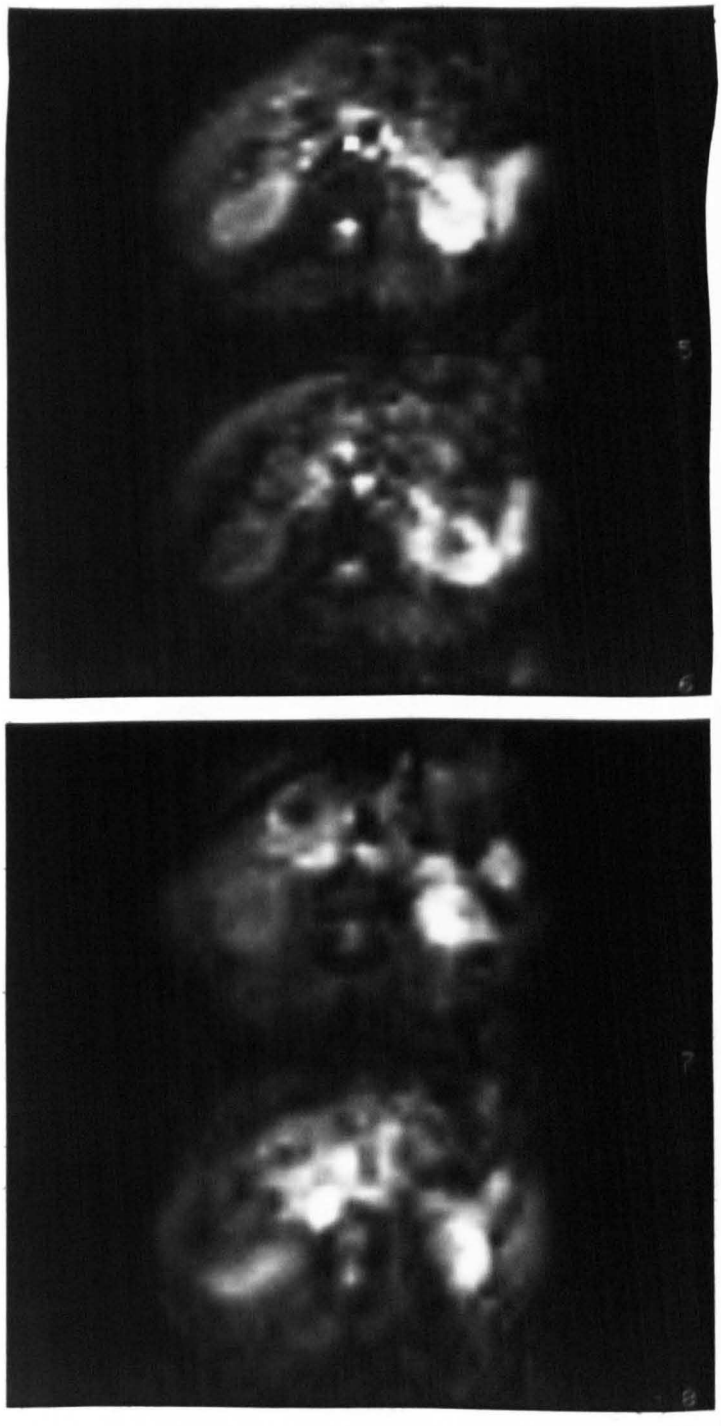

Figure 5.16: CONTINUED.

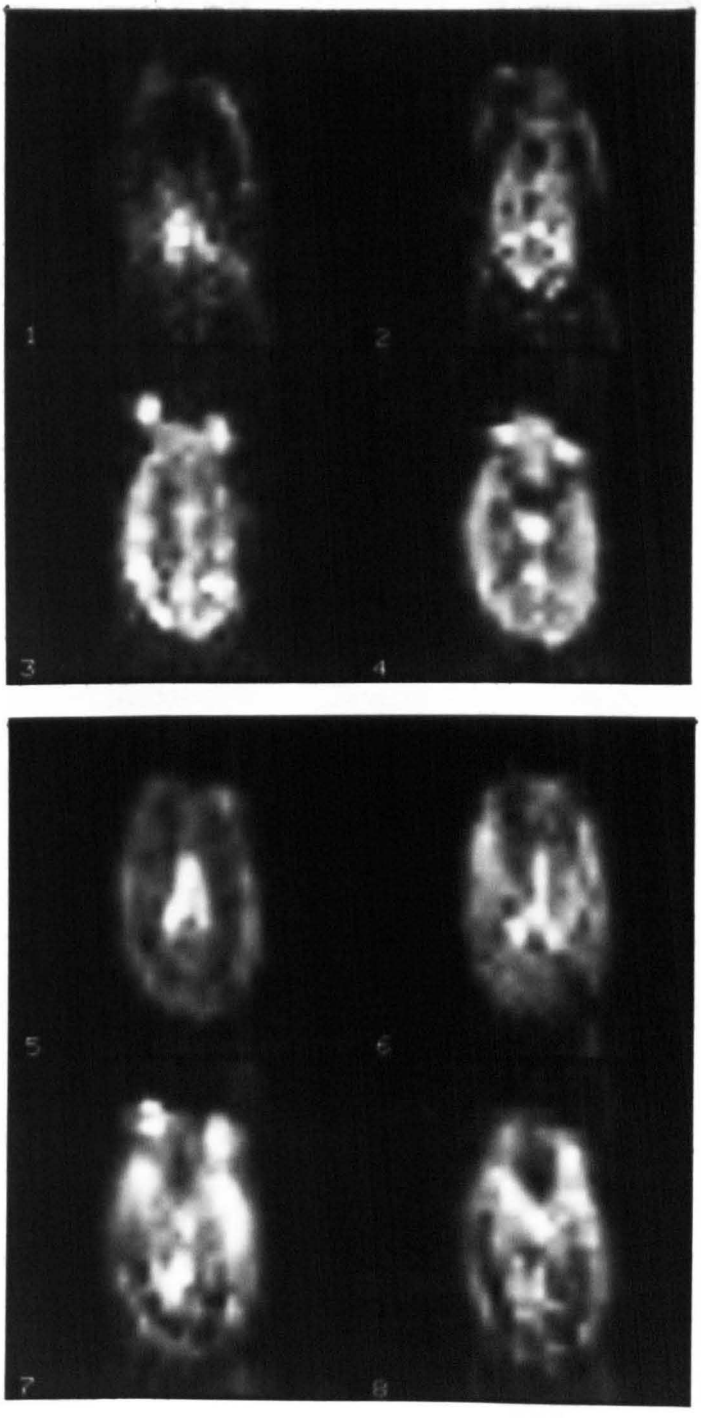


Figure 5.17: $32 \times 32 \times 8$ SE-EVI images of the head of a volunteer. Images exhibit less inter-plane signal spread but lower contrast.

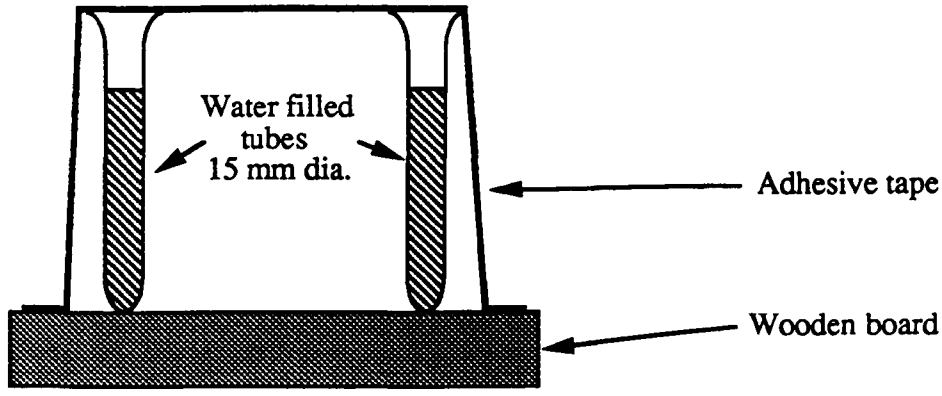


Figure 5.18 (a): Moving test tube phantom.

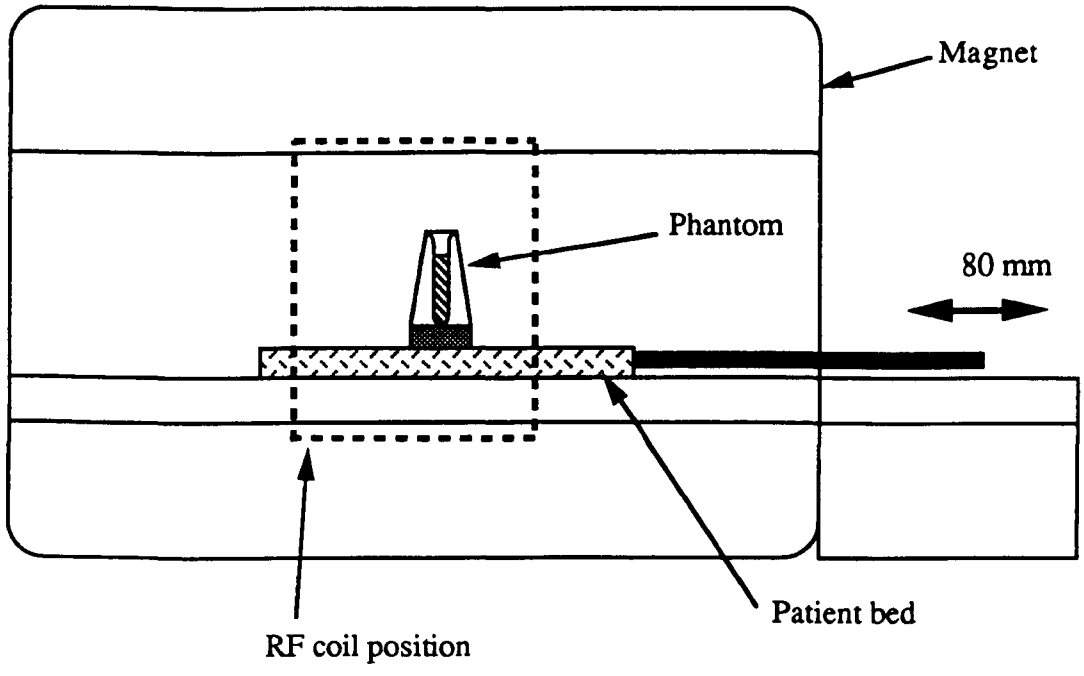


Figure 5.18 (b): Position of tube phantom within magnet body.

For the image in figure (5.19 (a)) the tubes were positioned 20 mm into the slice therefore most of the signal appears between planes 2 and 3 of the 8 transaxial planes, as expected. Signal appears in plane 3 because the tubes are actually wider than the z-direction resolution of 10 mm per plane. The image in figure (5.19 (b)) was obtained after pushing the tubes 40 mm into the slice. This time signal appears between planes 4 and 5 confirming a correctly calibrated slice thickness and demonstrating good in-plane signal confinement.

## 5.10 Zoomed EVI (ZEVI) Results

### 5.10.1 $32 \times 32 \times 8$ Voxel ZEVI

Data acquisition using ZEVI took 79.9 ms. The pulse sequence used was very similar to SE-EVI but with slice selection performed along $G_y$ during the $180^o$ pulse. The spin echo peak occurred 80 ms after $G_z$ slice selection.

Spherical Phantom Results

Figure (5.20) shows the results obtained from a water filled glass sphere phantom of diameter 220 mm. In these images ZEVI was used with $G_y$, during zoom strip selection, set to a low level so that the volume of interest is not yet restricted along the y-direction. In this way the whole phantom can be seen. There is a pronounced tilt in these images which results directly from the use of 1D Fourier transform.

Figure (5.21) shows results obtained when $G_y$ was set to restrict the volume of interest along the y-direction (zoom strip selection). Unfortunately, the gradient strength was not available to expand the image out to fill the available FOV.

Figure (5.22) shows results obtained when both zoom strip selection and bandwidth limitation (along $G_x$) are employed. As can be seen, the volume of interest is restricted entirely to the centre of the sphere. As before the gradient strength was not available to expand the images, however, the principles of ZEVI are clearly demonstrated.

Zoomed Head Results

Figure (5.23) shows the results obtained when the phantom was replaced with the head of a volunteer. Zooming has restricted signal emission from a strip through the centre of the brain. For these images bandwidth limitation was not used.

With bandwidth limitation and higher gradient strengths, the images could have been expanded out to fill the full image data set. Such a technique would be useful for localized, dynamic, 3D imaging of tumours during the uptake of a contrast agent.

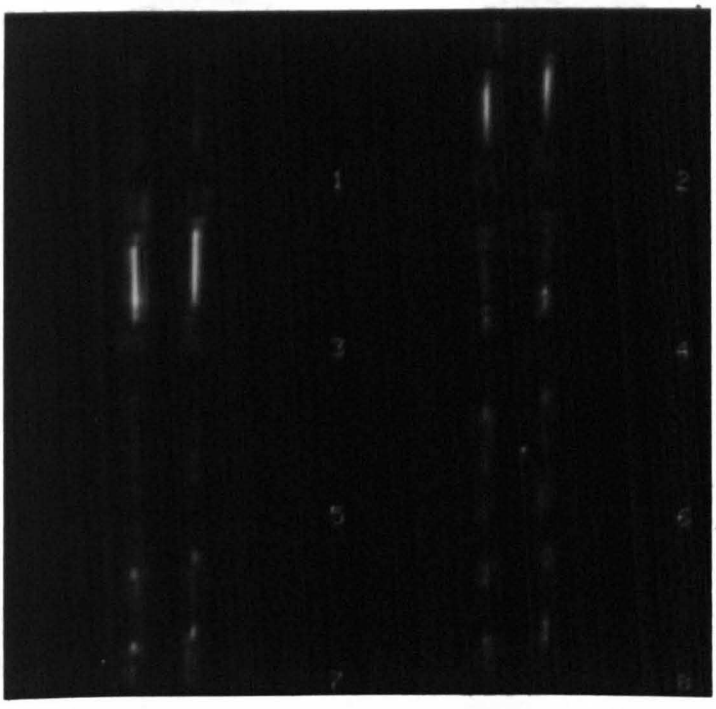

(a)

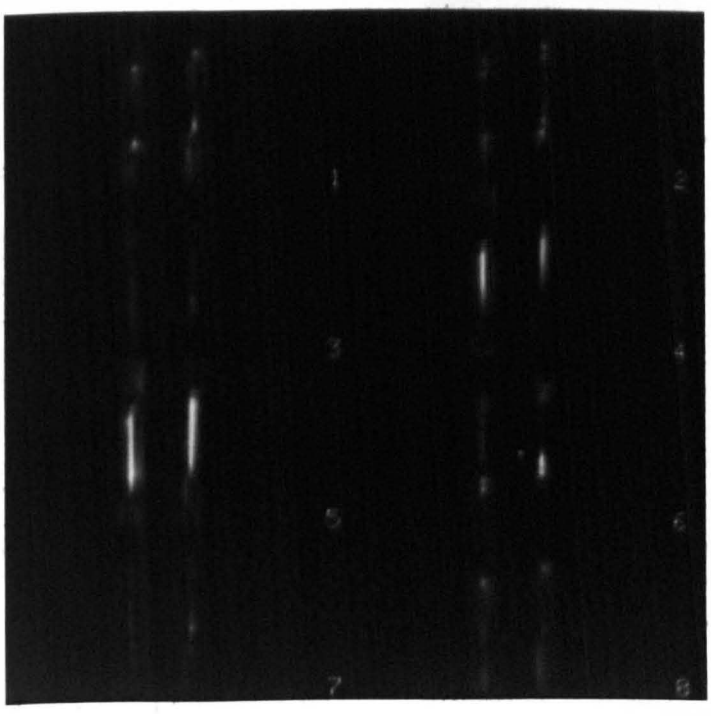

(b)

Figure 5.19: $64 \times 32 \times 8$ voxel images of moving tube phantom positioned (a) 20 mm into slice. (b) 40 mm into slice.

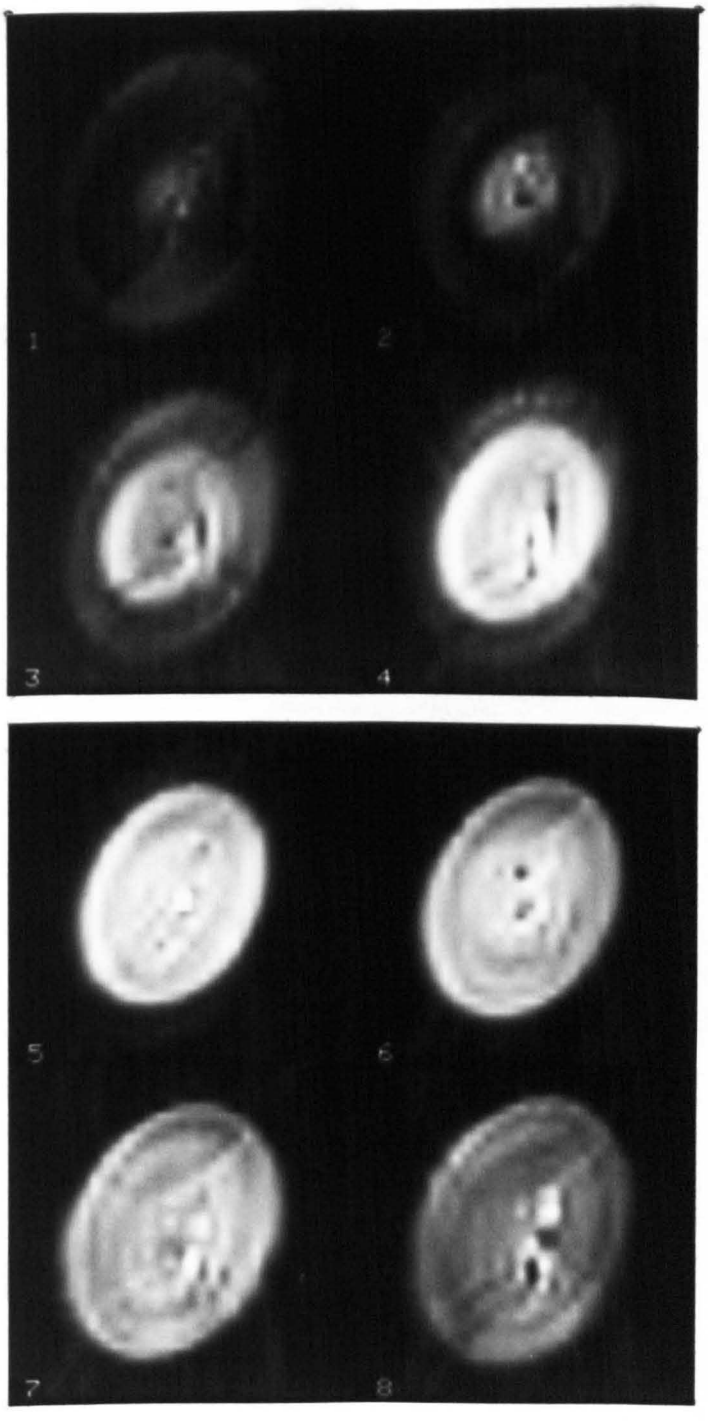


Figure 5.20: $32 \times 32 \times 8$ ZEVI results obtained on a water filled glass sphere. No zoom strip selection.

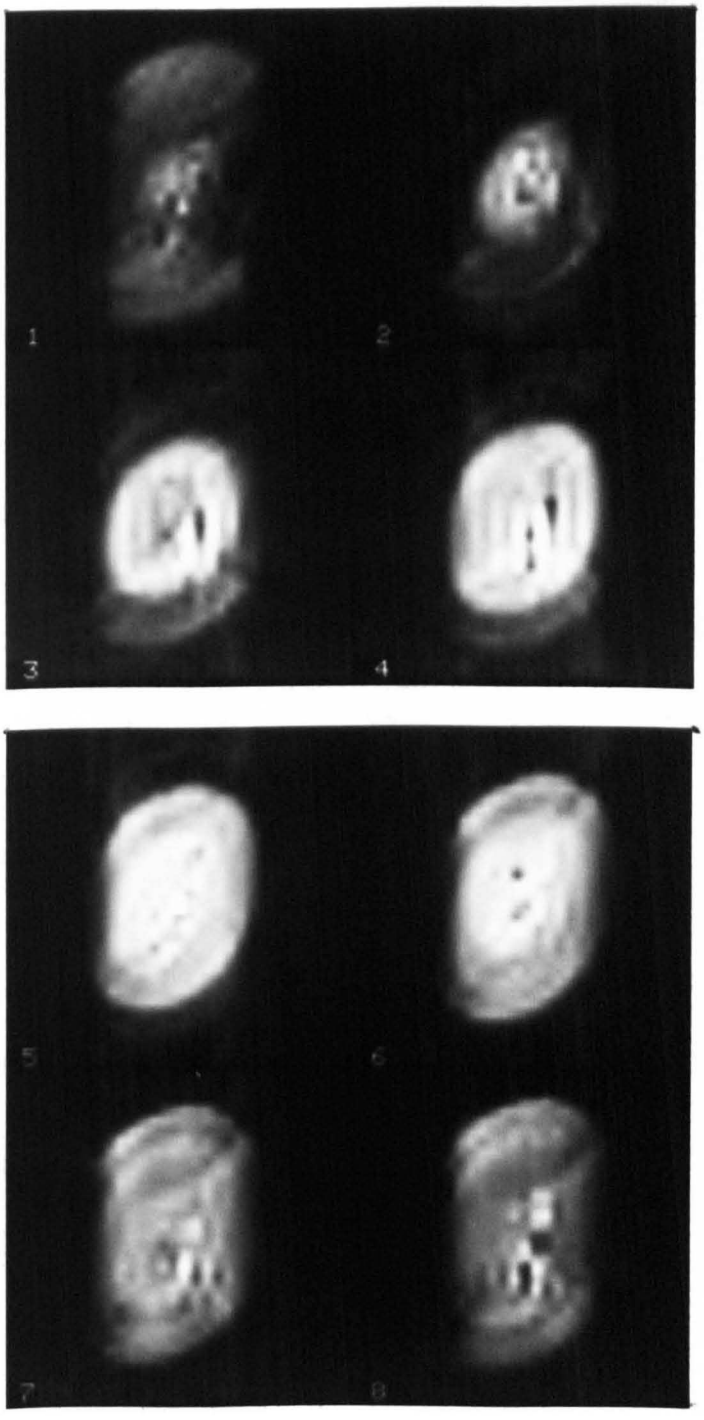


Figure 5.21: As figure (5.20) with zoom strip selection confining signal along one axis.

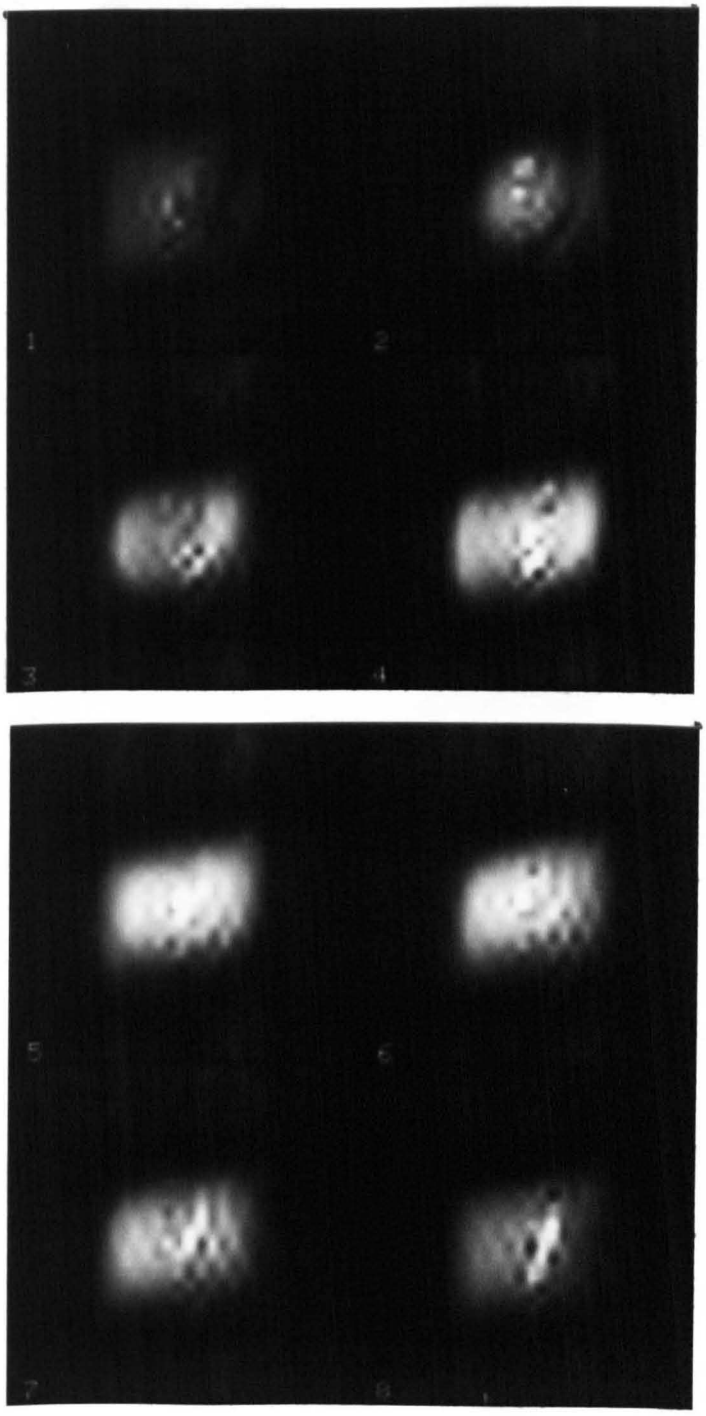

Figure 5.22: As figure (5.21) with bandwidth limitation. Signal restricted to central region of phantom.

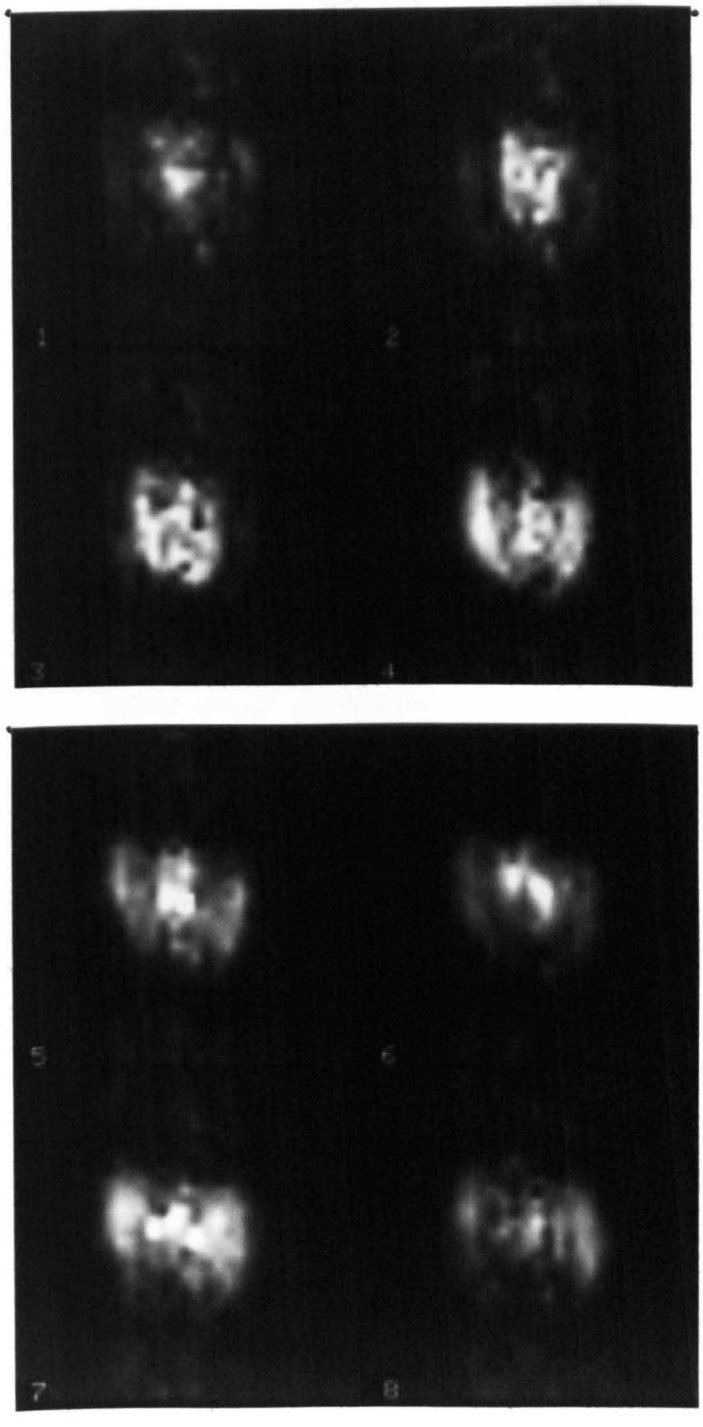


Figure 5.23: $32 \times 32 \times 8$ ZEVI head results. Signal restricted to central portion of brain only.

Attempts were made to perform the zoom experiment on the thorax. Unfortunately, as with SE-EVI also, the acquisition time is just too long. The spin echo in both cases peaks after 80 ms. This is far too late if detail of the myocardium is required, since it has a very short $T_2$ and contributes very little signal in such a long experiment. In addition, the blood which was excited with the 90° pulse has usually passed out of the heart by the time the 180° pulse is applied therefore its signal is also lost. Suggestions for overcoming these problems are discussed later.

## 5.11 Image Artefacts In EVI

Many of the problems encountered in EVI owe their origin to the usual error mechanisms associated with EPI. Incorrect sample patterns and sample point positioning leads to ghosting in the image. Incorrect positioning of the k-space origin leads to gross phase errors across the image. The nested nature, and temporal compression, of data in an EVI experiment therefore puts greater demands on the accuracy with which the data must be acquired, leaving a very small margin for error. Before the routine implementation of EVI can take place, some fundamental physical constraints need to be addressed.

### 5.11.1 Chemical Shift and Main Field Inhomogeneity

If EVI is performed without the $G_z$-phase encoding, this is the basis of an EPSM experiment in which the z-direction becomes the chemical shift axis. By nature of the way in which the experiment is performed, the voxel bandwidth along this direction is very low (i.e. 8 Hz for 128 ms $32 \times 32 \times 8$ voxel experiment) thus making it very sensitive to chemical shift and magnetic field inhomogeneities.

If the sample being imaged contains a chemical species with a shift greater than the voxel bandwidth then it will appear shifted by possibly a few transaxial planes. If the shift does not correspond to an integer number of planes exactly then the signal from that species will appear shifted vertically in addition to its plane shift. For example, fat has a shift of about 72 Hz at 0.52T which, for the $32 \times 32 \times 8$ voxel experiment described above, corresponds to a shift of 9 planes. Since there are only 8 planes available the signal wraps around and appears on the next consecutive plane. From the bandwidth diagram, figure (5.7 (a)), it is clear how easily the signal can appear in the wrong place completely. Whilst different chemical species can be selectively removed prior to image acquisition, Main field inhomogeneity poses further problems.

Expressed in parts per million (p.p.m.) the z-direction voxel bandwidth for the above experimental configuration is about 0.4 p.p.m. For a 100 ms experiment this value increases to 0.5 p.p.m and for a 64 ms experiment it

is 0.7 p.p.m. Considering the 100 ms case, it is clear that in order to avoid the unwanted spread of signal between transaxial image planes, due to main field inhomogeneities alone, the homogeneity along the z-direction, over the volume of interest, needs to be better than 0.5 p.p.m. Magnetic susceptibility of the sample, however, only serves to worsen this problem.

### 5.11.2 $T_2$ and Point Spread Function (PSF) Limitations

The ultimate limit to experimental duration is the $T_2$ of the sample. A long experiment heavily weights the image so that only long $T_2$ components are retained. In addition to this, the field inhomogeneity component of $T_2^*$ dominates over long $T_2$ values. Short $T_2$ values, on the other hand, lead to large linewidths and broadening of the image PSF. When the PSF is wider than the voxel bandwidth then signal spread occurs between adjacent voxels resulting in lower intrinsic resolution. Many of these problems can be overcome by shortening the experiment thereby increasing the voxel bandwidth. A more practical approach, which is less technically demanding, would be to intersperse data acquisition with 180° RF pulses to refocus inhomogeneity induced dephasing. SE-EVI is a very basic form of this kind of experiment. If more RF pulses were included, gradient blips and a more complex scan of k-space would be required.

## 5.12 Applications

There are many areas of imaging in which EVI could be applied to provide dynamic 3D images. Coupled with a zoom technique, 3D visualization of a tumour could be performed in real time during the introduction of a contrast agent, thereby providing the clinician with a wealth of extra structural information relating to the vascularity of the tumour.

The application to cardiovascular imaging would provide instantaneous 3D visualization of the heart throughout the cardiac cycle, being of particular use in cases where non-periodic motion is present.

Gastro-Intestinal (GI) tract motility studies constitute another area where EVI would provide an excellent way of observing much of the non-periodic motion present.

## 5.13 General Discussion - Future Requirements

The results presented here, although not of clinical quality, demonstrate the basic feasibility of EVI. Being such a technically demanding technique, the present hardware limits of the Nottingham imaging system were reached. Improvements in gradient technology are required to enable much faster switching at much higher amplitudes. At time of writing this particular problem has been addressed and forms the basis of the work presented in chapter 6.

Another concern connected with rapid gradient modulation is its potential to cause peripheral nerve stimulation. This reason alone may put a limit on the eventual allowable matrix sizes. Peripheral nerve stimulation forms the basis of the work presented in chapter 7.

Main field inhomogeneity is a potential problem, and at high fields, magnetic susceptibility of the sample also becomes worse. To overcome these problems much shorter data acquisition is required which, for large matrix sizes, increases technical demands enormously. The use of $180^o$ pulses overcomes, to a certain extent, the main field inhomogeneity problems with the added concern that, for a modulus experiment, the $T_2$ components of interest in the body have usually decayed away before data acquisition begins. Fast flowing blood also tends to disappear from the image. A reduction in acquisition time is required in this case also.

A further option exists. Combining spin echo EVI with half-Fourier data acquisition would mean that the $180^o$ RF pulse could be positioned immediately after the $90^o$ RF pulse. The signal peak (k-space origin) would occur almost immediately following the $180^o$ pulse and data acquisition could begin here. Many of the short $T_2$ components, still being present at this time, would contribute more signal to the final image. Flowing blood, unless very fast, would also register in the image. The disadvantage with half-Fourier acquisition however is the loss of S/N incurred and the requirement for a complex phase correction scheme in order to realize useful resolution.

# Chapter 6: Multi-Mode Resonant Gradient Coil Drive Circuit

## 6.1 Introduction

Ultra high speed imaging techniques like EPI and EVI require at least one gradient which is modulated in either a sinusoidal, cosinusoidal or preferably trapezoidal manner. Sinusoidal or cosinusoidal modulation is straightforward to achieve in practice by using a series or parallel resonant circuit in which the gradient coil assembly forms the inductance. Data acquisition in such an imaging arrangement can be achieved by varying the data sampling rate in order to get equal spin phase increments between sampling points (non-linear sampling). A disadvantage of this method is the fact that the peak gradient amplitude is $\pi/2$ greater than the amplitude of an equivalent square wave modulation. This means that the gradient driver amplifier must be capable of supplying $\pi/2$ more current than in the square or trapezoidal modulation case.

Another factor which militates against using sinusoidal modulation is patient safety. Induced current within the body due to rapidly varying magnetic field gradients present a potential hazard if the induced current levels approach the neural stimulation threshold level. Neurone models suggest that the important factors determining neural stimulation are concerned with the charging and discharging of nodal capacitance in the process of achieving the neurone firing potential. This leads to a formula which involves the product of the rate of change of magnetic field throughout the body multiplied by the duration over which this time varying gradient is applied. When this function is suitably integrated, it has been shown [63] that the critical factor in calculating stimulation threshold levels for gradient switching is not the rate of change of magnetic field but the maximum field excursion experienced by the tissue. Indeed, neurone stimulation turns out to be independent of the rate of change of the gradient field. In this circumstance it is therefore more efficient, and in general safer, to consider fast rise trapezoidal or square wave modulation of currents rather than sinusoidal gradients since for a given imaging time square wave gradients are $\pi/2$ lower than those with an equivalent sinusoidal modulation.

The practical problem is how to generate a fast rise square wave for use in a whole-body imaging machine. It is clear that for the most efficient square wave modulation system, the circuit arrangement must be energy conserving. Such energy conserving non-linear switches have been developed and are described elsewhere [64]. A difficulty with non-linear circuitry is that the switch is an active device and will have a maximum current carrying

capacity and at the same time be required to have a high inverse voltage requirement. Desirable current levels for future advances of EPI and EVI are around 1000 Amps. High power switches capable of carrying 500 to 1000 Amps are not available with the requisite peak voltage requirements of up to 10 kV. Such devices may be developed in the future but are likely to be very expensive and temperamental.

In this chapter an entirely passive approach to the generation of trapezoidal and square wave modulated gradients is described. The circuit arrangement exploits energy conserving principles and operates in a series drive arrangement which is eminently suitable for high power low voltage audio amplifiers available commercially. A parallel multi-modal circuit has been described [65], but is not as valuable because high voltage driver amplifiers are required.

## 6.2 Theoretical Basis

The repeated bipolar square wave of unit amplitude shown in figure (6.1 (a)) may be represented by the Fourier series

$$f(t) = \frac{4}{\pi}\left[sin\ \omega t + \left(\frac{1}{3}\right) sin\ 3\omega t + \left(\frac{1}{5}\right) sin\ 5\omega t\right] \qquad (6.1)$$

where $f(t)$ is the square wave function with period $T = 2\pi/\omega$. Equation (6.1) represents an odd harmonic expansion in which $\omega$ is the fundamental frequency, $3\omega$, $5\omega$ the third and fifth harmonics etc. in a slowly converging series. Figure (6.1 (c)) shows an ideal square wave and its synthesis from a truncated series of harmonics. Although the series is slowly converging, it is shown that using the first and third harmonic gives a recognizable approximation to a continuous square wave. Adding the fifth harmonic gives an even better approximation but more importantly brings the maximum waveform excursion down from $\pi/2$ in the case of the first harmonic to 1.2. Adding further harmonics like the seventh and the ninth may not be worthwhile experimentally because of slow convergence. Also their contribution will not significantly affect the safety questions referred to earlier and in chapter 7.

The approach taken was to construct a multi-resonant circuit capable of responding to a specified number of harmonics.

## 6.3 Circuit Design Procedure

Figure (6.2) shows a simple series resonant circuit in which $L$ represents the inductance of the gradient coil assembly. Also shown in this circuit is the amplifier drive arrangement here represented as a voltage generator. In such a series arrangement it is clear that the total generator current $I$ passes through $L$ and thus represents the most efficient arrangement for producing high magnetic field gradients. Present day high current commercial audio amplifiers are capable of delivering their full current capacity into what is effectively a short circuit, i.e. a series resonant circuit. These amplifiers can be

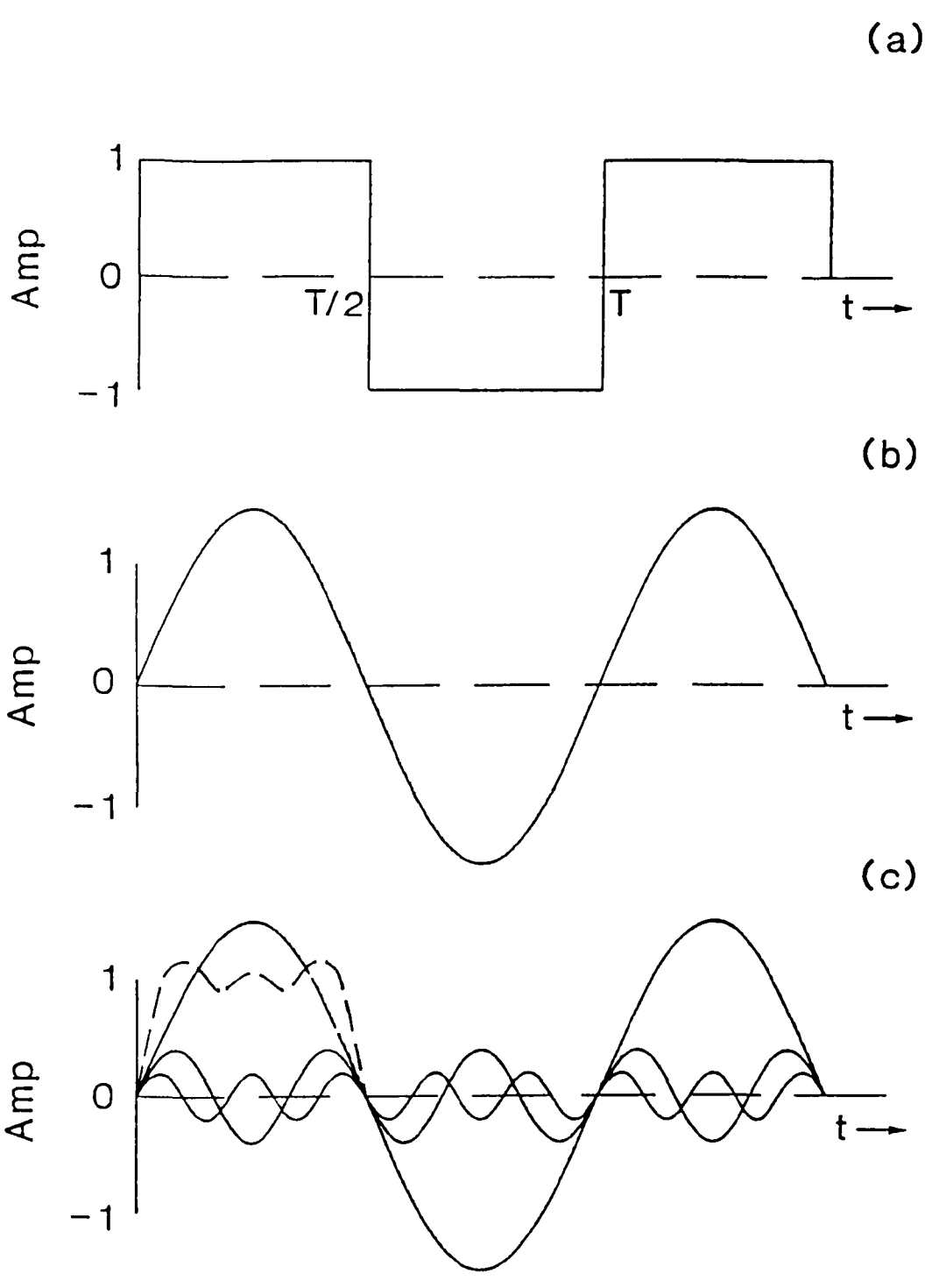


Figure 6.1: (a) Sketch of bipolar square waveform with period $T$ and unit amplitude. (b) The simple sine wave approximation to (a) above in which the areas under the curves in a half period are equal. (c) Partial synthesis of the square waveform of (a) above from the first three Fourier harmonics.

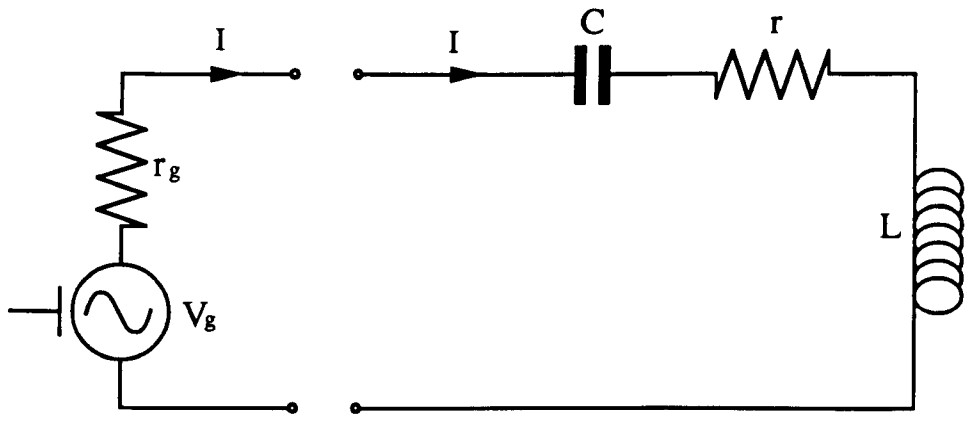


Figure 6.2: Simple series resonant circuit and generator drive.

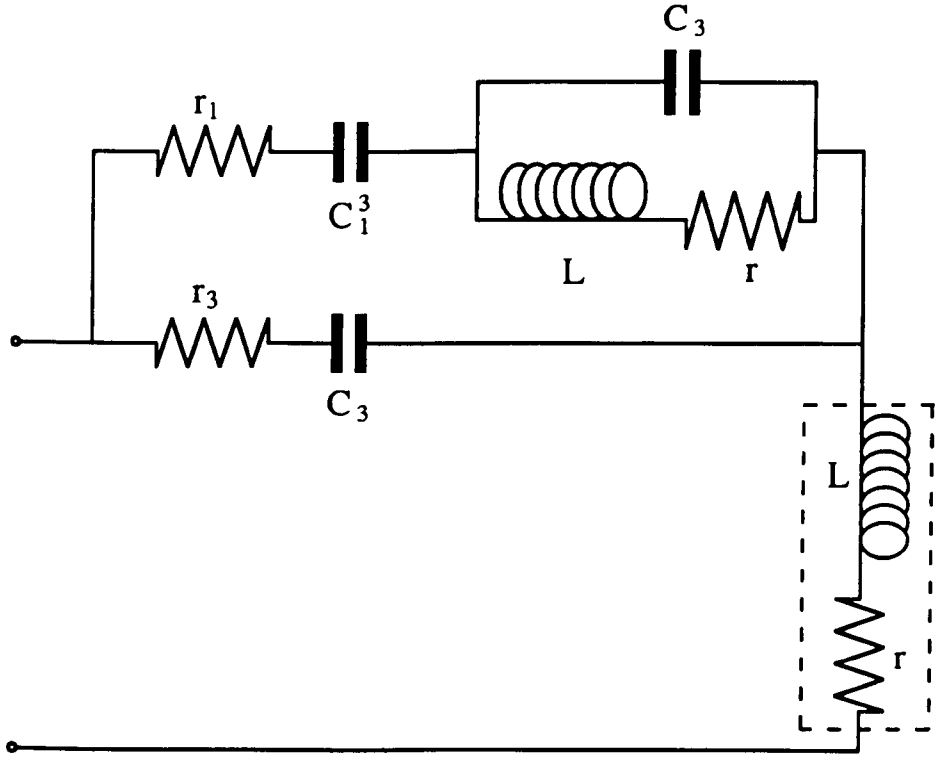


Figure 6.3: Bimodal series resonant circuit of order l = 3.

operated either as voltage generators or alternatively as current generators. In the current generator mode, it is possible to control more accurately the response time when driving a series tuned circuit. In general the rise time for a series tuned circuit as in figure (6.2) with $V_g = 0$ is determined by the quality factor $Q$ given by

$$Q = \frac{\omega L}{r} \tag{6.2}$$

The current for this circuit will rise to $(1 - e^{-1})$ of its final current in $Q/\pi$ cycles when driven in the voltage mode. In current mode the rise time can be significantly shorter so that the equilibrium situation can often be achieved in just one cycle.

In order to accommodate the necessary higher harmonics to form an approximate square wave requires the introduction of additional components in such a way that all the harmonic current components pass through $L$.

Figure (6.3) shows a modified circuit which accommodates the fundamental and third harmonic only. In calculating the requisite component values of this third order circuit, all resistors are taken to be effectively zero in the first instance. It is also helpful but not absolutely necessary to make all inductors equal to $L$. The design process then reduces to calculating the component values starting with the highest harmonic, in this case the third harmonic, at which $C_3$ and L are resonant, i.e. $C_3 = 1/9\omega^2 L$. The parallel resonant circuit shunting $C_3$ via $C_1^3$ passes no current at $3\omega$ and can, therefore, be ignored to first approximation in calculating the resonant features of the main third harmonic current pathway. At the fundamental harmonic resonance the parallel circuit behaves as an inductor at frequency $\omega$. This effective inductor given by

$$L_{eff} = \left(\frac{9}{8}\right) L \tag{6.3}$$

is combined with the series capacitance $C_1^3$ to produce an effective capacitance given by

$$C_{1eff}^3 = C_1^3/(1 - \omega^2 C_1^3 L_{eff}) \tag{6.4}$$

This is combined in parallel with $C_3$ to resonate with $L$ at frequency $\omega$. Solution of the resonant circuit equations gives

$$C_1^3 = \frac{4}{9\omega^2 L} = 4C_3 \tag{6.5}$$

If resistance is reintroduced into the circuits, the resonance conditions will be changed slightly so that the two resonant frequencies may not be exactly a factor of three different. Trimming of $C_1^3$ would then be necessary in order to get the exact frequency, and phase relationship between the two harmonics.

The principles may be straightforwardly extended to include the first three or more resonant harmonics. Figure (6.4) shows the basic principle extended to cover a fifth order circuit with resonant modes up to and including $5\omega$. The design process is similar to that outlined above, namely that the additional two shunt circuits are arranged to reject current at $5\omega$ in which case $C_5$ and

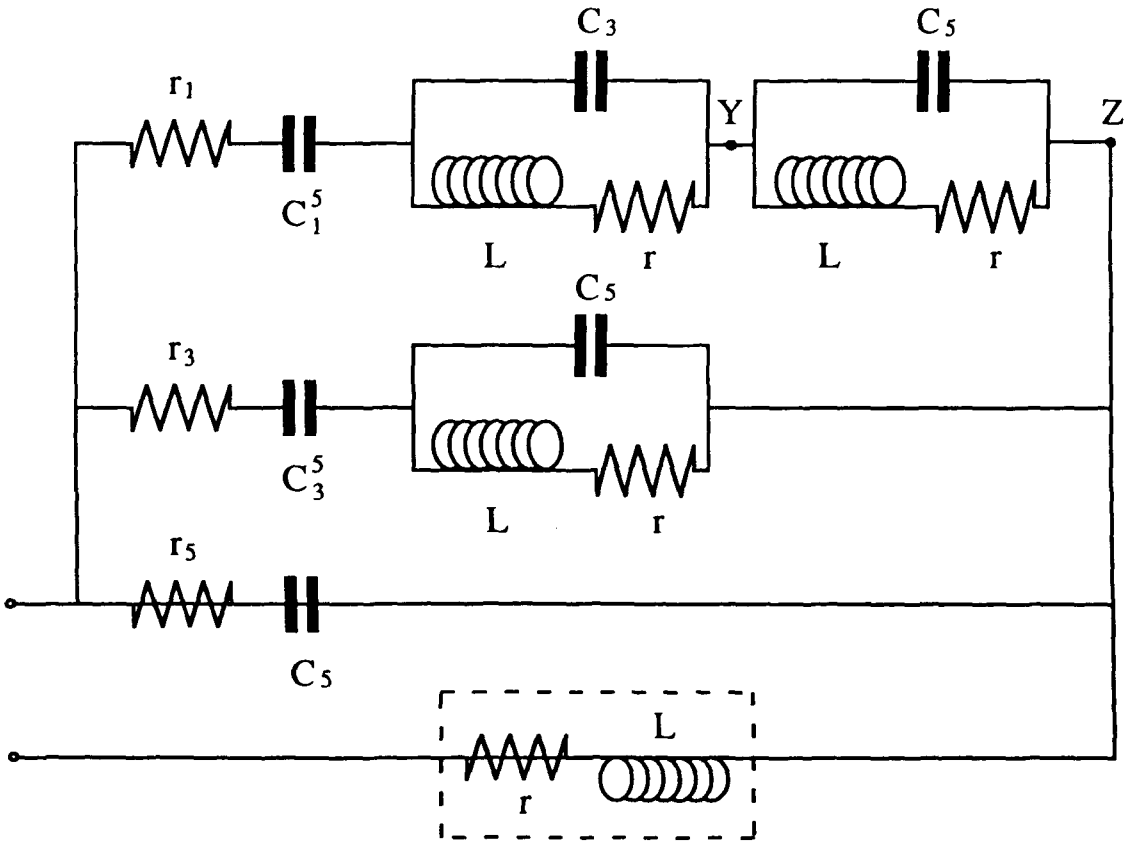


Figure 6.4: Trimodal series resonant circuit of order l = 5.

$L$ form a simple series resonant circuit tuned to $5\omega$. Again all the inductors are chosen to be the same value $L$ and for the initial design zero resistance is again assumed. Resistance is reintroduced at the next step when phase and frequency are adjusted by varying $C_3^5$ and $C_1^5$ in an iterative cycle.

When all resistors are zero, for the circuit in figure (6.4)

$$C_3^5 = \left(\frac{9}{8}\right) C_5 \tag{6.6}$$

and

$$C_1^5 = \left(\frac{100}{13}\right) C_5 \tag{6.7}$$

For an $l$th order multi-modal resonant circuit like figure (6.3) and (6.4) with $l$ modes, in which all inductors have the same value $L$, the resonant capacitors for the $n$th mode, $1 < n \leq l$, are given by

$$C_n = \frac{1}{n^2\omega^2 L} \tag{6.8}$$

The series capacitors $C_n^l$ may be represented by the expression

$$C_n^l = l^2 C_l K_n^l \tag{6.9}$$

$K_n^l$ is a calculable constant for the $l$th order filter.

For the 3rd order filter of figure (6.3)

- $K_1^3 = 4/9$

For the 5th order filter of figure (6.4)

- $K_1^5 = 4/13$
- $K_3^5 = 8/(9 \times 25)$

For a 7th order filter

- $K_1^7 = 2.362275 \times 10^{-1}$
- $K_3^7 = 1.34029 \times 10^{-2}$
- $K_5^7 = 9.7959 \times 10^{-3}$

## 6.4 Circuit Redundancy

The 5th order circuit of figure (6.4) comprises two tuned rejection circuits or traps resonant at $5\omega_0$ and one tuned circuit resonant at $3\omega_0$. Higher order filters would include more duplication of the rejection circuits. However if, in figure (6.4), the rejection filter between points Y and Z is removed, the same purpose is served, namely, that each rejection filter isolates all circuitry above it from currents at or above its resonance frequency. This removes circuit redundancy, thereby making the filter easier and cheaper to construct. Fewer circuit components also reduces the resistance thereby making the overall $Q$ higher.

With this modification, the higher order filters simply require additional L-sections. Also the response of such a circuit is straightforward to calculate using the product of individual transfer matrices for each section. Figure (6.5) shows a 7th order filter network. The transfer matrix for this circuit is given by

$$M^7 = A^7 A_5^7 A_3^7 A_1^7 \tag{6.10}$$

where for $L_n = L'_n = L$ and $C'_n = C_n$ and for $r = r_n = 0$

$$A_n = \begin{bmatrix} 1 - \frac{\beta^2}{7^2} & j\omega L \\ j\omega C_7 & 1 \end{bmatrix} \tag{6.11}$$

and

$$A_n^7 = \begin{bmatrix} 1 - \frac{\beta^2 C_{n-2}^7 / 7^2 C^7}{1 - \beta^2/n^2} & j\omega L \\ j\omega C_{n-2}^7 & 1 - \beta/n^2 \end{bmatrix} \tag{6.12}$$

where

$$\beta = \frac{\omega}{\omega_0} \tag{6.13}$$

and $n = 1, 3$ and 5.

The input and output voltages and currents are respectively $v_1$, $i_1$ and $v_2$, $i_2$. When $i_2 = 0$, the input impedance $Z_1$ is given in terms of the transfer matrix elements by

$$Z_1 = \frac{M_{1\,1}^7}{M_{2\,1}^7} \tag{6.14}$$

At the nodal resonances $Z_1 = 0$ so that equations (6.10) and (6.14) can be used to evaluate the capacitor values. Because of the action of the traps, evaluation of the capacitors can be carried out in tandem starting with the highest mode and ignoring all other circuit sections of equal and lower frequency. Adopting this approach it is found for the 7th order filter that

- $K_1^7 = 1.78 \times 10^{-2}$
- $K_3^7 = 2.37037 \times 10^{-2}$
- $K_5^7 = 9.7959 \times 10^{-3}$

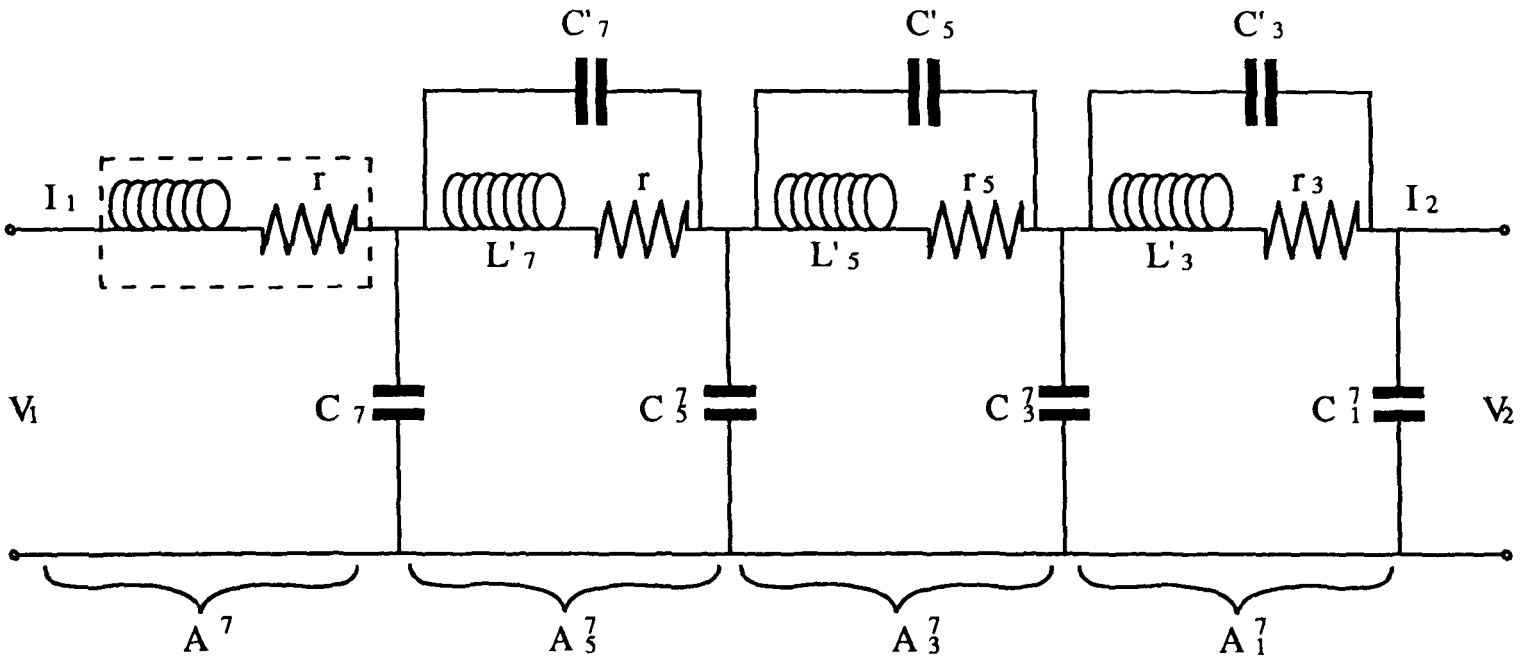


Figure 6.5: Alternative 7th order circuit based on a ladder network.

As expected, the ratio for $K_5^7$ agrees with the previous result but the other values differ by virtue of the removed circuit redundancy.

An alternative arrangement in which the capacitors $C_n' = 0$ is also possible. In this case $L_n \neq L_n' \neq L$.

The approach developed above is readily extended to any order including selective odd and even frequency modes. This latter feature is useful in cases where frequency modes are not present in a required waveform (see later).

## 6.5 Energy Conservation and Q values

An important feature of this discrete filter circuit is that all resistors when introduced to the parallel tuned circuits are made equal. This means that the $Q$ values of the various harmonics are given by

$$Q_n = \frac{n\omega L}{r} \tag{6.15}$$

The rise time $t_R$ of all parallel circuits is given by

$$\begin{aligned} t_{Rn} = \frac{T_n Q_n}{\pi} &= \left(\frac{2\pi}{n\omega}\right)\left(\frac{n\omega L}{r\pi}\right) \\ &= \frac{2L}{r} = t_R \end{aligned} \tag{6.16}$$

where $T_n$ is the period of oscillation. This ensures that all harmonics stay in phase. If the rise time for all harmonics is not constant the initial response of this circuit will not maintain the correct phase relationships between all harmonics during establishment of the steady state. The correct phase relationships can be established by introducing resistance $r_n$ into the circuit arms as indicated in figure (6.4).

Once the equilibrium waveform is established, energy is exchanged between $L$ and the capacitors in the discrete filter. Only the small energy losses arising from the finite $Q_n$ values have to be supplied from the driver amplifier in order to sustain the waveform. In this case the transitions between waveform extrema can in principle be infinitely fast. In practice it means that the bandwidth of the amplifier limits the waveform rise time rather than the coil inductance and power output.

For a non-energy conserving arrangement comprising a loss-less inductor $L$ driven directly by an amplifier the square wave rise time or step response time $\Delta t$ achievable is given by

$$\Delta t = \frac{LI}{E} \tag{6.17}$$

where $I$ and $E$ are respectively the peak current and voltage outputs of the driver amplifier. For the linear Techron driver amplifier $I = 360$ and $E = 300$. Using a typical gradient coil inductance of 110 $\mu$H gives $\Delta t = 132$

$\mu$s. In 131 ms MBEST the slew rate presently used is lower corresponding to $\Delta t = 150$ $\mu$s in a non-energy conserving mode. It will be shown later that trapezoidal rise times much shorter than 160 $\mu$s can be readily achieved experimentally using the same amplifiers.

## 6.6 Trapezoidal Waveform Synthesis

In practice the generation of a perfectly square waveform is not easily possible. A large number of harmonics would be required using the resonant approach, requiring a prohibitively large number of filter components. In general using linear amplifiers a trapezoidal waveform suffices. It is therefore interesting to note that trapezoidal waveforms may themselves be simulated by Fourier series and can often be more convergent than generation of direct square wave functions. The difference between the peak currents required in a trapezoidal waveform versus a square wave is proportional to the ratio of the areas contained within or under the waveform half-period. In the case of the rather severe trapezoidal waveform given in figure (6.6) the Fourier series is given by

$$\begin{aligned} f(t) &= \left(\frac{6\sqrt{3}}{\pi^2}\right)\left[sin\ \omega t - \left(\frac{1}{5^2}\right) sin\ 5\omega t\right. \\ &+ \left.\left(\frac{1}{7^2}\right) sin\ 7\omega t - \left(\frac{1}{11^2}\right) sin\ 11\omega t \ldots\right] \end{aligned} \tag{6.18}$$

The amplitudes of the third, ninth and fifteenth harmonics are missing and it is worth noting that the amplitude of the harmonics varies as $1/n^2$ making the series more rapidly convergent. Figure (6.7) shows the first two harmonics of equation (6.18) and the fit to the trapezoidal waveform of figure (6.6). The Fourier harmonic amplitudes are given by

$$A_n = \frac{4}{T}\int_{-T/2}^{T/2} f(t) sin\ n\omega t\ dt \tag{6.19}$$

where $T$ is the waveform period.

It is instructive to evaluate $A_n$ for the general trapezoidal waveform shown in figure (6.8) in which the linear ramp rises to 1.0 in time $T/2p$ where $p$ is an integer. The function f(t) is defined over the half period as

$$f(t) = \begin{cases} t(2p/T) & \text{for } 0 < t < T/2p \\ 1 & \text{for } T/2p < t < T(p-1)/2p \\ p - t(2p/t) & \text{for } T(p-1)/2p < t < T/2 \end{cases}$$

These functions may be used to evaluate $A_n$, equation (6.19). This gives

$$\begin{aligned} A_n &= \left(\frac{4p}{\pi^2 n^2}\right)\left\{sin\left(\frac{n\pi}{2}\right) cos\left[\frac{n\pi(p-2)}{2p}\right]\right\} \\ &= \left(\frac{4}{\pi^2}\right) B_n(p) \end{aligned} \tag{6.20}$$

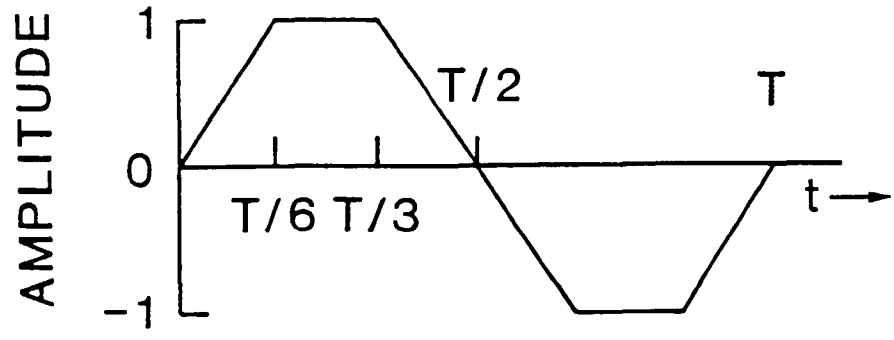


Figure 6.6: Trapezoidal waveform in which the rise time to full unit amplitude takes 1/6th of the period.

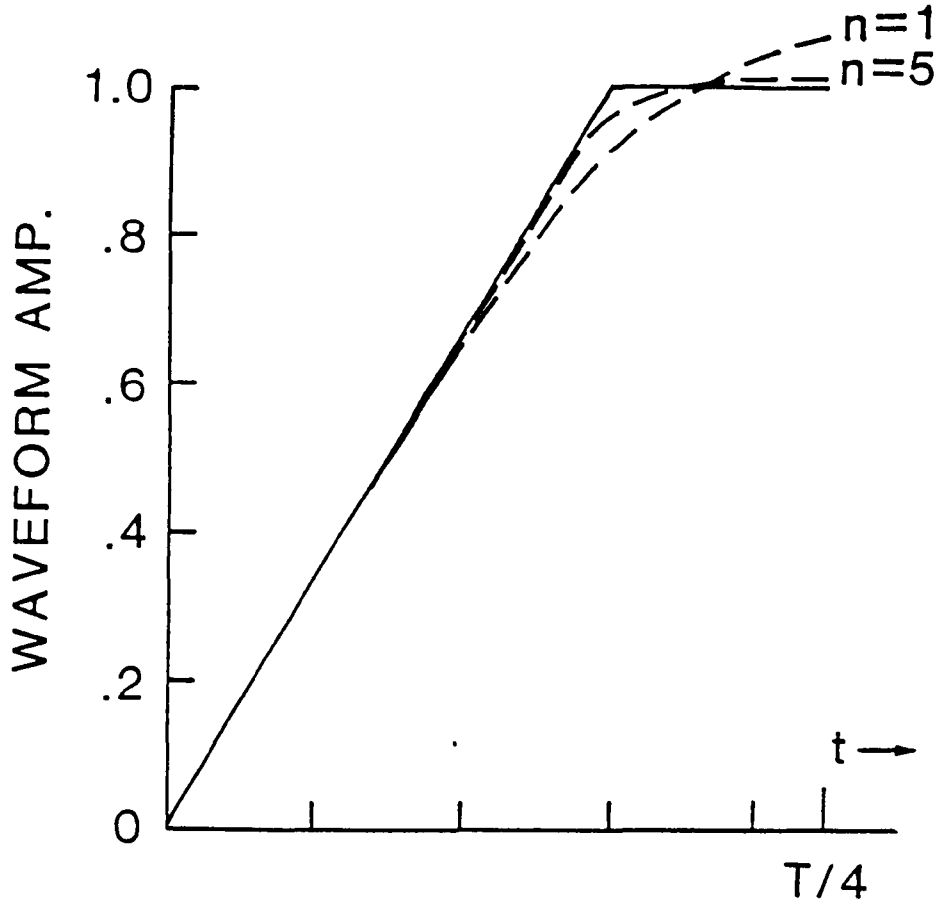


Figure 6.7: Trapezoidal waveform as in figure (6.6) plotted over a quarter period together with a first and fifth harmonic fit.

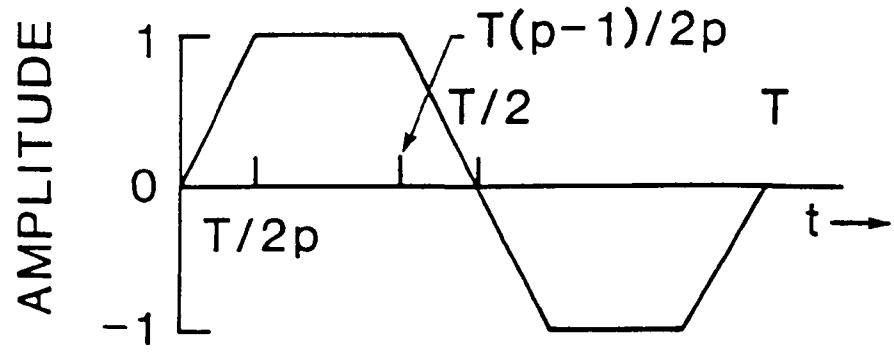


Figure 6.8: General trapezoidal waveform in which the rise time to the full unit amplitude is $T/2p$ where $T$ is the period of the waveform and $p$ is an integer.

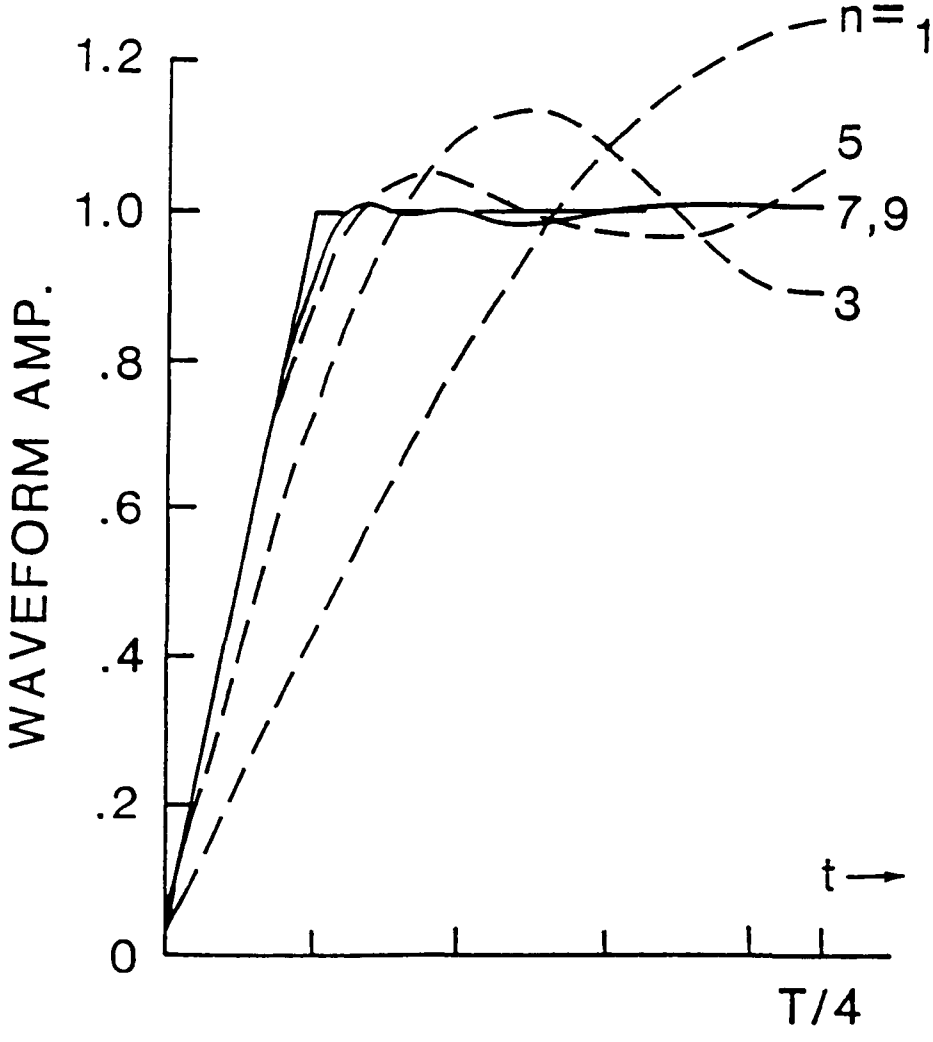


Figure 6.9: Plot over a quarter period of a trapezoidal waveform of the type in figure (6.8) with $p = 9$. Also plotted is the waveform synthesis up to and including the order $n$. Note that the amplitudes of all even orders vanish.

Equation (6.20) shows that convergence to a given waveform approximation can be achieved by choosing $p$ to remove particular harmonics in the series. For example when $p$ is odd, certain odd harmonics starting with $n = p$ are removed. When $p$ is even, all lower odd harmonics remain.

The synthesis to various orders in $n$ over a quarter cycle is shown in figure (6.9) for a trapezoidal waveform with $p = 9$. Since the 9th order vanishes the solid curve $n = 7$ is accurate up to 11th order.

Using equations (6.1) and (6.20), the waveform amplitude at time $T/4$ synthesized up to and including $n = 11$ is plotted in figure (6.10) for the square wave and various trapezoidal waveforms. By choosing the trapezoidal ramp time as described above it will be seen that the number of resonant modes required in the discrete filter circuit may be reduced.

The more general trapezoidal waveform of figure (6.11 (a)) may also be produced with relatively few odd harmonics. This function is represented by the expression

$$f(\beta) = 4\sum_n \frac{(sin\ nB - sin\ nb)sin\ n\beta}{\pi(B-b)n^2} \tag{6.21}$$

with $n = 1, 3, 5, \ldots$ and where $\beta = (2\pi/T)t$ and T is the period. The delay $2b$ represents a useful window for the application of other gradients and/or RF pulses in EPI and EVI experiments.

## 6.7 Circuit Drive

The discrete frequency filter approach developed above assumes that the output phase relationship of all harmonics is equal to that of the driving waveform. In an ideal circuit that would be the case. In practice there may be slight differences in phase between the harmonic components introduced by inequalities in inductance and resistance among the components and also through the effects of stray capacitance within the inductors which has been entirely ignored in this analysis. Of course, stray interturn resistance within the inductances will only become important at very high frequencies, i.e. very high harmonics, and so may not constitute a problem. Nevertheless, the other factors mentioned can introduce undesirable phase shifts which could be tedious to eliminate. An alternative approach therefore is to tailor the input drive waveform by synthesizing the desired Fourier components, but at the same time adding in a phase term to each Fourier component which may be varied in order to generate the correct output phase relationship in the circuit. In this case the driver waveform for trapezoidal wave modulation becomes

$$f(t) = (i.p.)\sum_n A_n e^{i(n\omega t + \theta_n)} \tag{6.22}$$

with $n = 1, 3, 5, \ldots$, where $\theta_n$ is the introduced phase shift for the nth mode and the coefficient $A_n$ is given by equation (6.20).

With DC and a sufficient number of harmonic modes, the circuit is capable of generating other waveforms including a series of positive or negative short

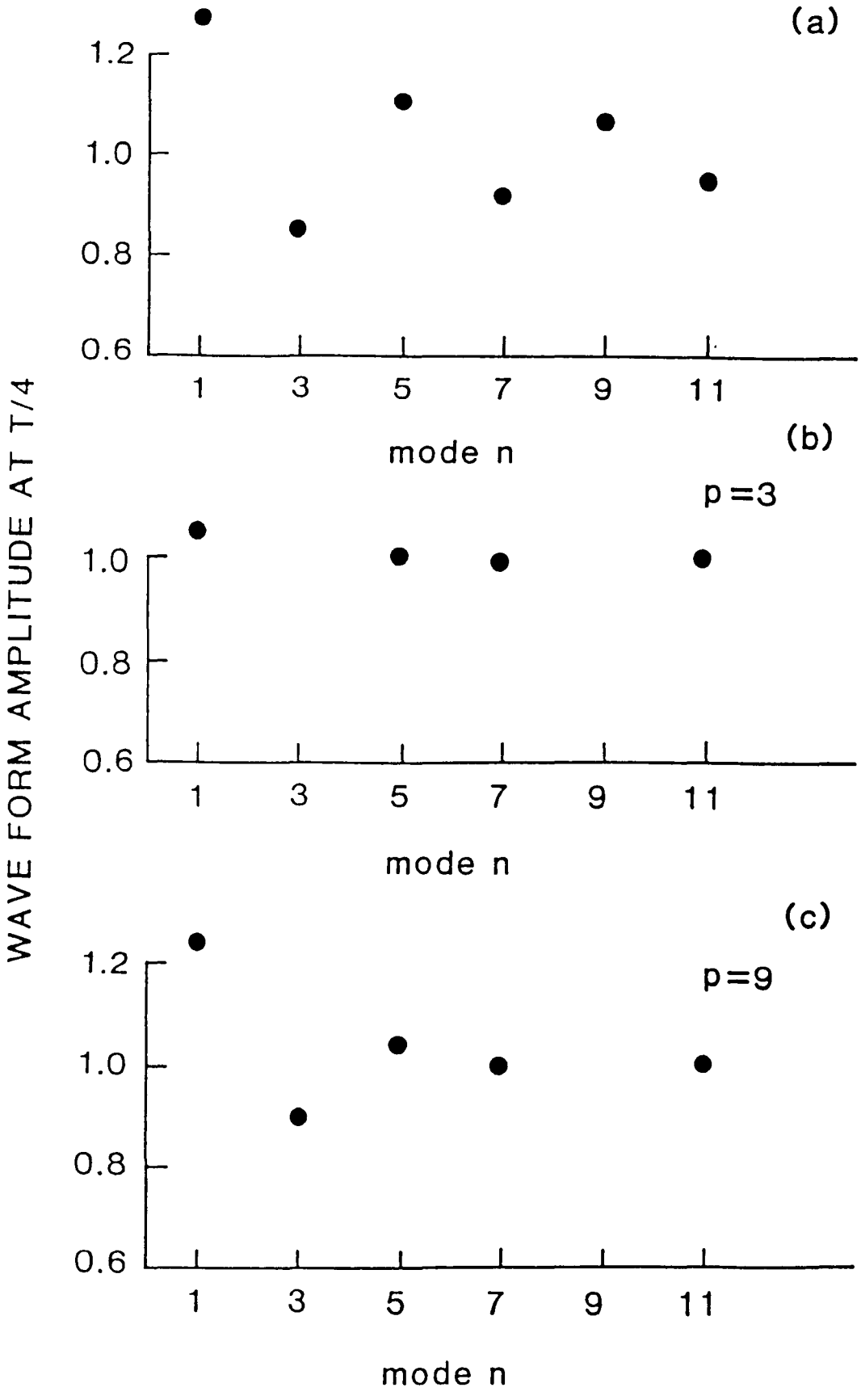


Figure 6.10: Comparison of the waveform convergence at $T/4$ for (a) a square wave, and trapezoidal waveforms with (b) $p = 3$ and (c) $p = 9$.

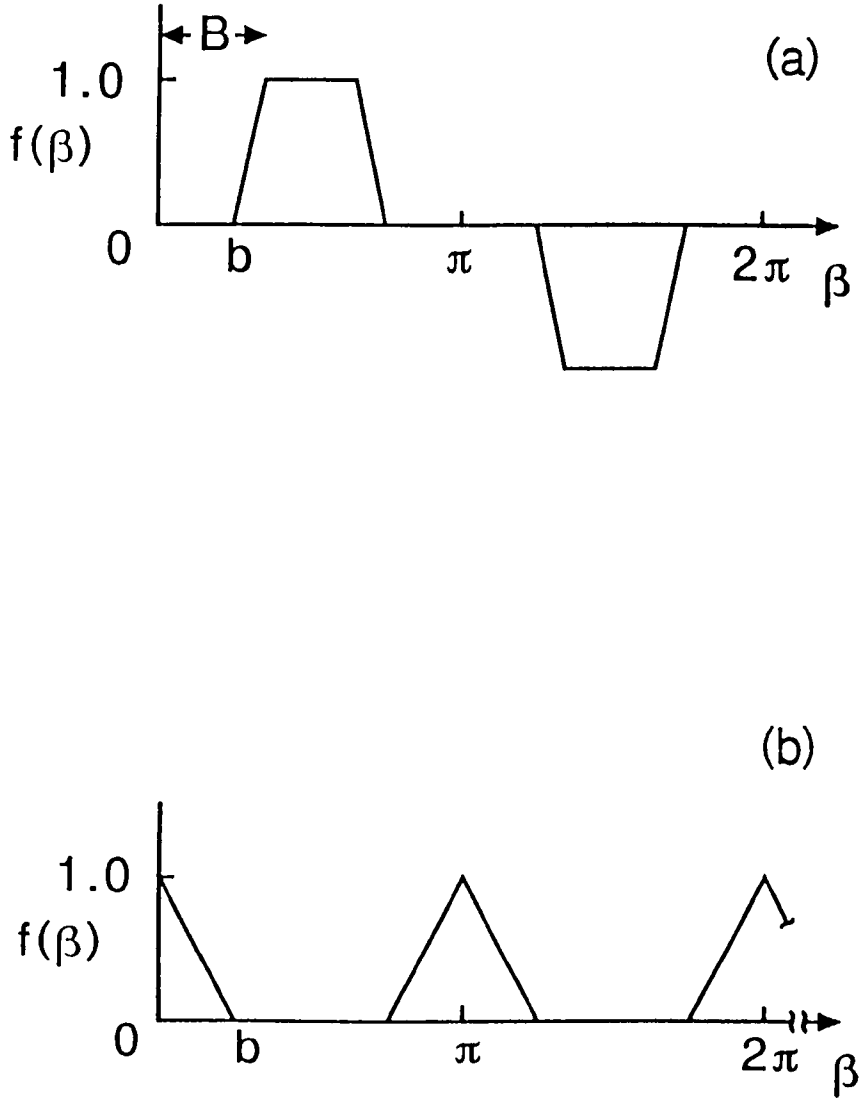


Figure 6.11: (a) Sketch of general trapezoidal waveform $f(\beta)$ with $2b$ windows. (b) Sequence of triangular blips $f(\beta)$ useful for echo-planar or echo-volumar imaging.

duration current blips, also useful in echo-planar and echo-volumar imaging methods. A sequence of triangular blips is sketched in figure (6.11 (b)) and is represented by the convergent series

$$f(\beta) = \frac{b}{2\pi} + 2\sum_{n} \frac{(1 - cos\ nb)cos\ n\beta}{\pi b n^2} \tag{6.23}$$

where $n = 1, 2, 3, \ldots$ and in which $\beta = (2\pi/T)t$.

## 6.8 Circuit and Waveform Simulation

Simulation of the following resonant circuit configurations was based around a two port network analysis BASIC program and the BBC "Microspice" circuit simulation program.

In the two port network analysis each portion of the circuit is separated into series or parallel component impedance matrices and written into the simulation program in the format dictated by the custom designed functions (see appendix A). The program was adapted from an earlier version written by Coxon and Glover.

Starting with the harmonic traps on the arm which passes the lowest frequency, their complex parallel impedances are added in series with the single capacitor impedance on that arm. In this way the impedance for the whole arm is reduced to representation by a single matrix. Repeating this procedure for the other arms and combining the results yields the complex impedance of the circuit at any specific frequency. The program performs a sweep through the frequency range of interest and the impedance and phase versus frequency plotted to the screen. Appendix A is a printout of the BASIC program RES7 which plots the impedance/phase characteristics for a 7th order filter circuit.

In the "Microspice" program, component values are entered and their position in the circuit specified by numbered nodes between which they are connected. A choice of AC or DC, voltage or current source is available and a sweep through any desired frequency range can be specified. Voltage and phase can be monitored across any component during circuit operation, and the values printed to screen or printer as the frequency sweep is performed. Appendix B is an example of the input format and results obtained for a 5th order filter circuit similar to that shown in figure (6.4).

### 6.8.1 Fifth Order Discrete Filter Network

For simulation purposes an inductance value of $L = 120\ \mu$H was chosen. The capacitance values required for the 5th order circuit were calculated using equations (6.8) and (6.9) assuming a fundamental frequency for resonance of 1 kHz. The circuit subroutine was entered into the two port network program and executed. The output is shown in figure (6.12). The points of low impedance correspond to the series resonances of the circuit at 1, 3 and 5 kHz demonstrating that the circuit is working correctly. Changing the values

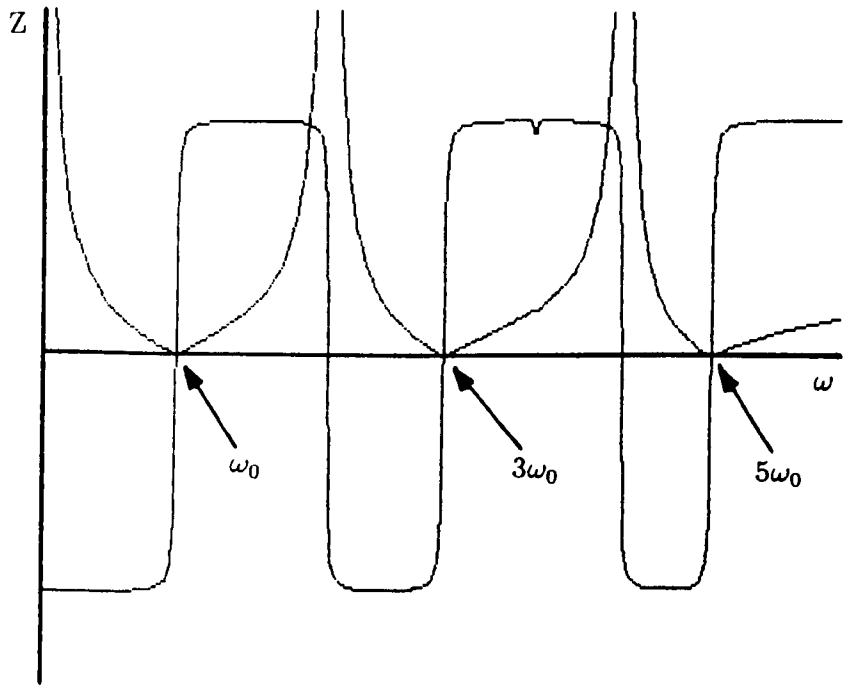


Figure 6.12: Simulated impedance/frequency plot for 5th order filter circuit. Series resonances at $\omega_0$, $3\omega_0$ and $5\omega_0$.

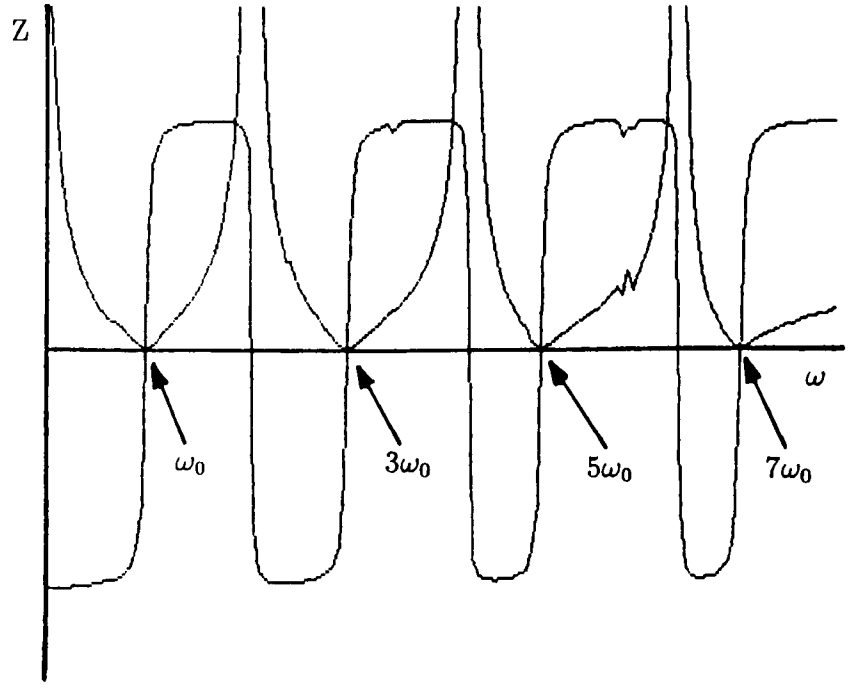


Figure 6.14: Simulated impedance/frequency plot for 7th order filter circuit. Series resonances at $\omega_0$, $3\omega_0$, $5\omega_0$ and $7\omega_0$.

of resistance around the circuit was found to affect the width of the Q for each resonance. For realistic values of resistance the Q is low enough to produce a plateau of almost constant low impedance in the regions around each resonance. This, as will be seen, allows a certain amount of flexibility in the driving waveform since it is not required to contain harmonics corresponding to exact circuit resonances in order to achieve maximum efficiency.

### 6.8.2 Seventh Order Discrete Filter Network

The diagram for a 7th order filter circuit is shown in figure (6.13). The number of inductors required has doubled over the 5th order circuit. The impedance/frequency response is shown in figure (6.14). All component values were calculated using equations (6.8) and (6.9) assuming this time, an inductance closer to the measured inductances of the field coils on the imaging system i.e. $L = 107\ \mu$H. The frequency response shows series resonances at four frequencies correspond to the fundamental, the third, fifth and seventh harmonics. The fundamental frequency in this simulation was 1 kHz.

### 6.8.3 Trapezoidal Waveform Simulation

Figure (6.15 (a)) shows the trapezoidal waveform plotted using equations (6.1) and (6.20) for $p = 7$ and $l = 5$. Such a waveform could be produced using a fifth order circuit since $p$ is chosen such that the 7th harmonic vanishes. The synthesized waveform is then accurate to 7th order with a corresponding rise time given by

$$\Delta t_{multi} = \frac{T}{2p} \tag{6.24}$$

where $T$ is the period of the fundamental. In effect, the circuit achieves 7th order performance with only 5th order components.

### 6.8.4 Windowed Trapezoidal Simulation

Figure (6.15 (b)) shows the waveform synthesized using equation (6.21) and specifying $b = B/3$. In this way the window is equal in width to the rise time of the trapezoidal lobe leaving a very narrow gap for the inclusion of RF pulses or gradient blips, as could be used in an imaging application. Simulation shows that the narrower the window the more harmonics that are required. Harmonics up to and including the 13th are required in the waveform shown and the rise time is specified as a 36th of the period. It is somewhat intuitive, as in all Fourier applications, that smaller and sharper details require higher frequencies for their synthesis resulting in a slowly converging series.

### 6.8.5 Blip Generation

The waveform in figure (6.15 (c)) was synthesized using equation (6.23). The same problem arises in that narrow blips require higher harmonics. For the example shown, all the harmonics, including the even ones, up to the 50th

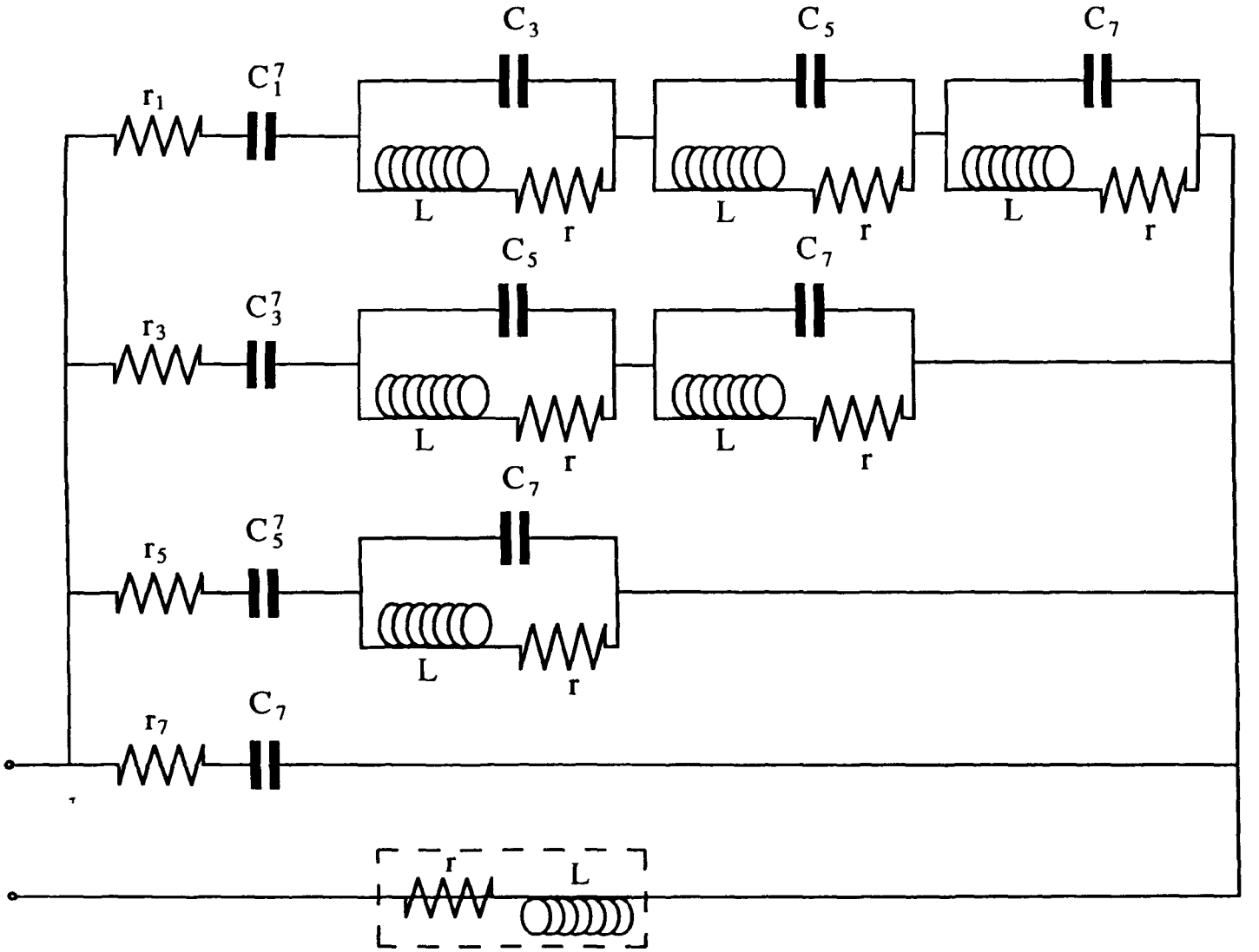


Figure 6.13: 7th order series resonant circuit

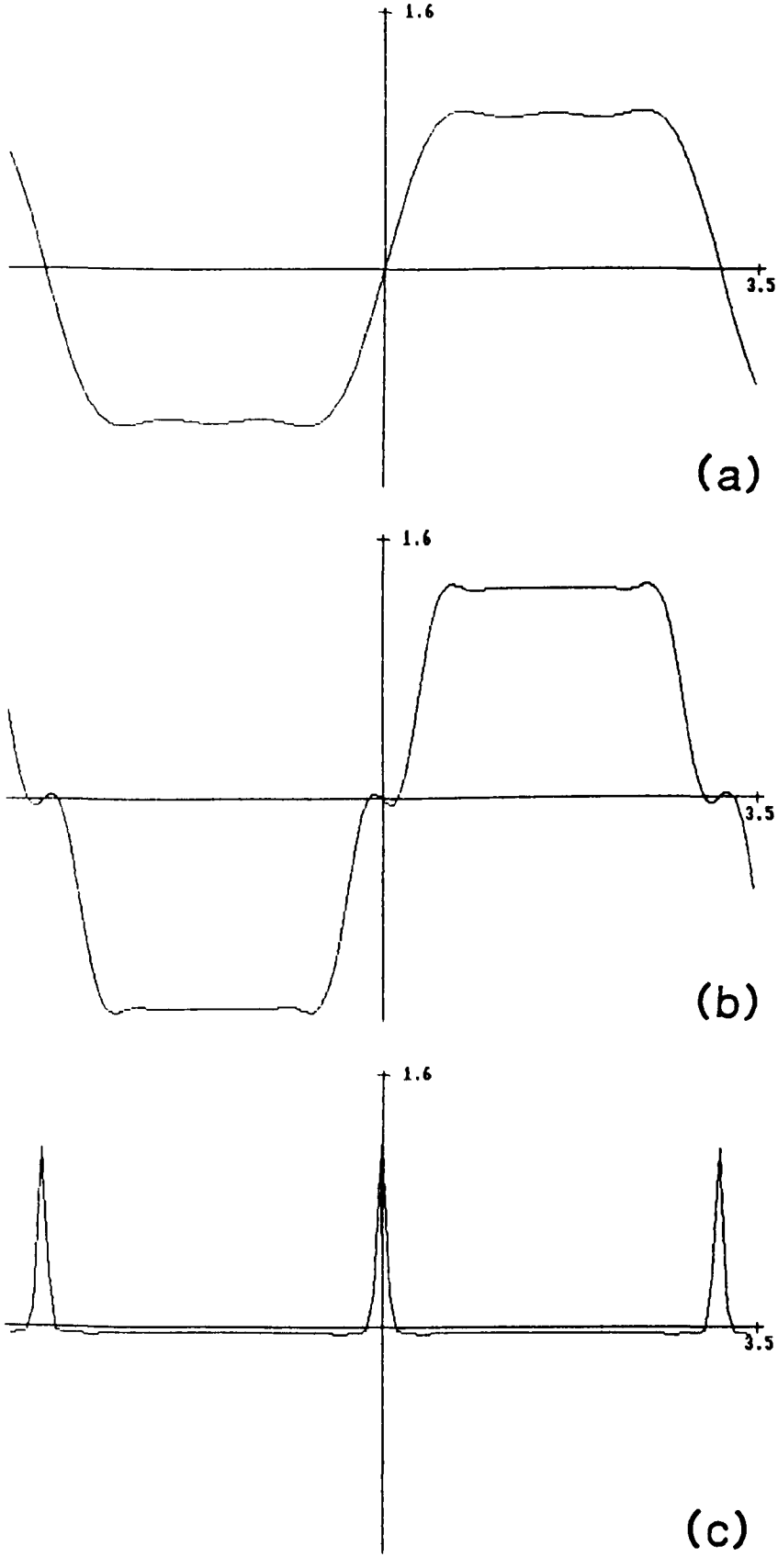


Figure 6.15: (a) Trapezoidal waveform synthesized using equations (6.1) and (6.20) for $p = 7$ and $l = 5$. (b) Windowed trapezoidal waveform synthesized from harmonics up to and including the 13th using equation (6.21). (c) Triangular blip generation using equation (6.23). Harmonics up to and including the 50th are used in this synthesis.

harmonic were used. Practical realization of this waveform would be difficult due to the number of components required in the filter circuit.

### 6.8.6 Alternative Circuit Simulation

Figure (6.16) shows the simulated response of the 7th order circuit shown in figure (6.5) using an inductance $L = 107\ \mu$H. At time of writing this circuit has not been tested practically. However, the impedance characteristics indicate a similar sort of response as for the other circuits discussed so far.

## 6.9 Experimental Results

### 6.9.1 Small Scale Test Circuit

Using the principles described above a small scale 5th order discrete filter network, as illustrated in figure (6.4), was constructed in which the dummy gradient coil inductance $L_G = L = 130\ \mu$H. The fundamental frequency was 1 kHz with harmonics at 3 kHz and 5 kHz. The driver used in these experiments was a Techron amplifier which could run in either constant voltage or constant current mode.

Waveform generation for sinusoidal input was provided by a Philips PM 5132 function generator. For trapezoidal and controlled harmonic input, a home built waveform controller (WC), interfaced to the SUN workstation, was used.

The WC was designed and built by Glover [66] and works on a similar principle to that used for the imaging system (chapter 4). Trapezoidal waveforms were synthesized via equations (6.1) and (6.20) in software using a program, SQRES, written in the language C. The generated waveforms were then downloaded to the WC where they could be executed under control of WCtool.

WCtool is a program written by Coxon which allows on-screen interaction with the WC. The frequency of the synthesized waveform was specified in SQRES. The number of cycles input to the amplifier at any one time is specified by WCtool which also allows a variable delay between executions. In this way a fixed number of cycles of the synthesized waveform could be executed once every few seconds (in a similar manner to an EPI experiment). This keeps the duty cycle, and hence power deposition, low thus preventing damage to the circuit or amplifier.

Input to the amplifier was via the direct input of an opto-isolated control box (chapter 4). The control box also allowed independent zero adjustment and gain control. A digital storage oscilloscope (DSO) was used to monitor the current through the dummy gradient coil via the voltage drop across a 0.1 $\Omega$ resistor placed in series with it. Normally the current monitor facility on the front of the control box would have been used to directly monitor the current that the amplifier is supplying. For these preliminary experiments,

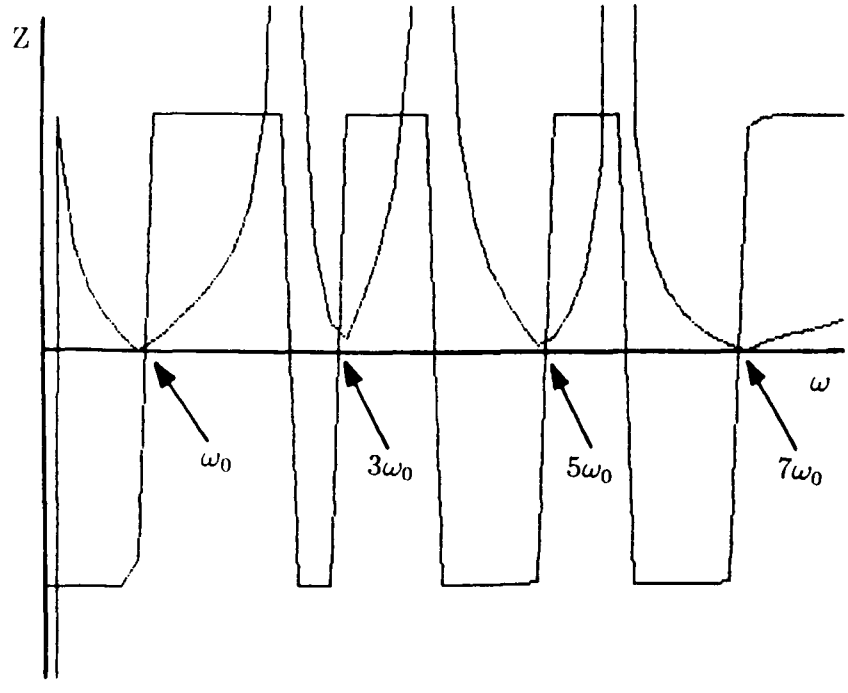


Figure 6.16: Simulated impedance/frequency plot for alternative 7th order filter circuit.

however, this was not connected. The "test" circuit set up is shown in figure (6.17).

Capacitance Requirements

The values of capacitance used were

- $C_5 = 7.8\ \mu F$
- $C_3^5 = 6.9\ \mu F$
- $C_1^5 = 60.0\ \mu F$
- $C_3 = 21.6\ \mu F$

All capacitors were low power polyester components from RS with a tolerance of $5 - 20$ %.

Inductance Requirements

The 5th order circuit required a total of 4 inductors of inductance $L = 130$ $\mu$H. One of which was to act as the dummy gradient coil.

Each inductor was wound in a solenoid fashion on a cardboard former of diameter 5.5 cm. To keep the physical size down and reduce the amount of wire required, two layers were wound, one on top of the other. The bottom layer contained 36 turns and the top layer, 28 turns. The wire used was enamelled 14 SWG copper wire. Each inductor was terminated with 5 Amp screw terminals and flexible wire connections were made between the components in the circuit. The windings were tightly bound with PVC tape to prevent any movement which could result in a change in inductance.

Voltage Comparisons - Theoretical and Practical

To check that the circuit was operating correctly, the amplifier was set into constant voltage mode and a continuous sinusoidal waveform of fixed amplitude input using the PM 5132 function generator. The frequency was swept until the fundamental resonance was excited at about 1 kHz. This was easily determined by the sudden amplitude increase of the gradient coil current at the resonant frequency. Alternatively, the amplifier voltage, when measured across the output, showed sudden decrease at the circuit resonances.

Voltages across various components in the circuit were measured, using a FLUKE multimeter, for a number of fixed current amplitudes through the dummy gradient coil. The results were then compared to values acquired using the BBC "Microspice" circuit simulation program. Table (6.1) shows the comparison obtained. The comparison is very favourable. The $V_{IN}$ required as calculated by "Microspice" is higher than the measured value and is possibly due to an over estimation of the DC resistance values of the circuit components.

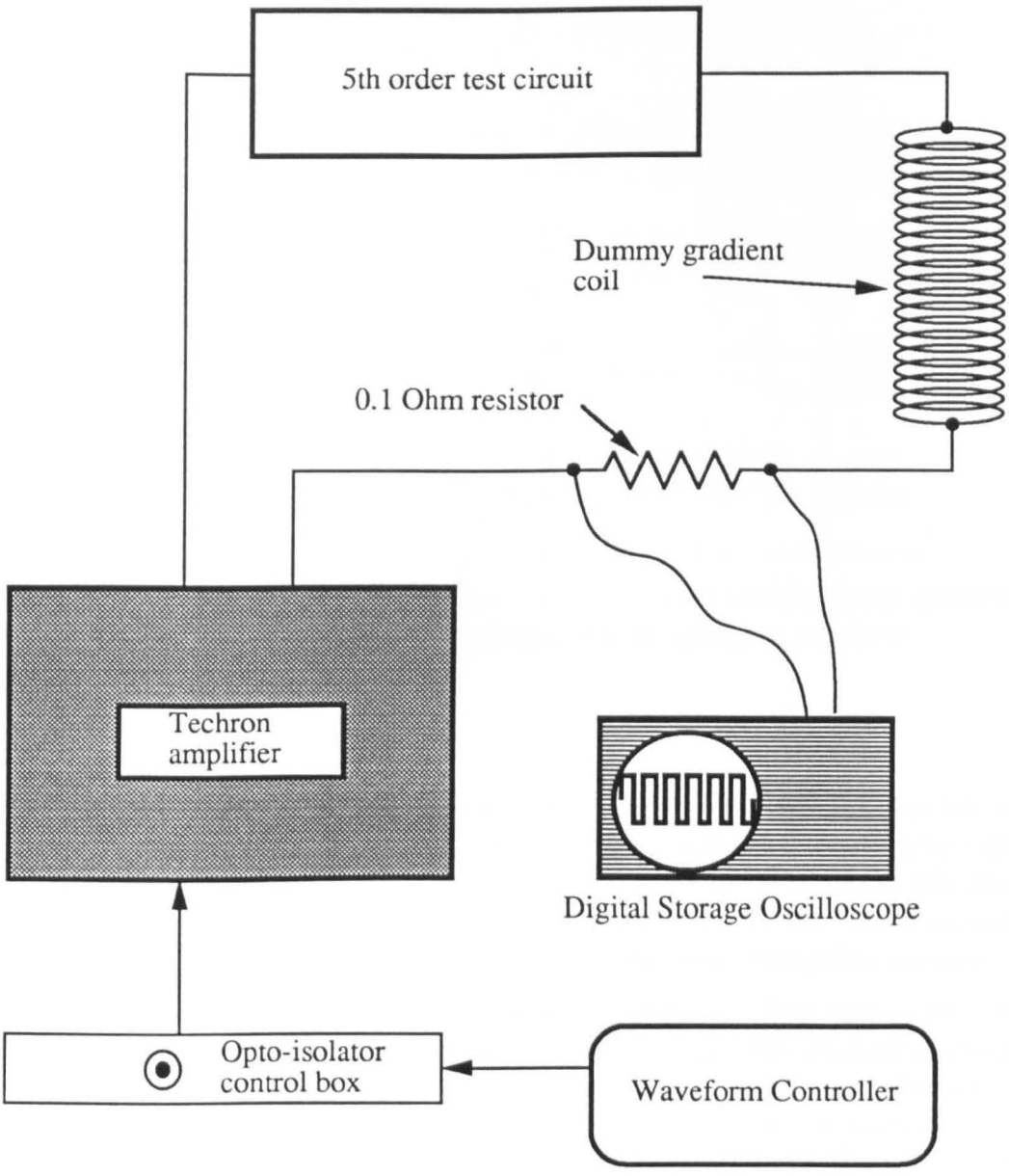


Figure 6.17: Test circuit layout.

| Gradient Coil Current (RMS Amps) | RMS Voltage | | | |
|---|---|---|---|---|
| | $V_{C_5}$ | $V_{C_3^5}$ | $V_{C_1^5}$ | $V_{IN}$ |
| 2.73 | 2.55 (2.54) | 2.65 (2.64) | 6.88 (6.70) | 1.07 (1.64) |
| 4.50 | 4.26 (4.18) | 4.45 (4.34) | 11.30 (11.00) | 1.77 (2.70) |
| 7.34 | 7.01 (6.83) | 7.30 (7.09) | 18.52 (17.94) | 2.93 (4.40) |
| 10.00 | 9.50 (9.30) | 9.90 (9.65) | 25.03 (24.45) | 4.10 (6.00) |

Table 6.1: Voltages measured around 5th order filter circuit versus gradient coil current for 1 kHz sinusoid. Simulated values shown in brackets.

Constant Voltage Mode Operation

Having determined correct operation of the circuit, the amplifier was left in constant voltage mode and a synthesized square waveform containing only the 1st, 3rd and 5th harmonics introduced. For this application the WC and SUN computer were used. The fundamental frequency of the waveform was 1 kHz and WCtool was programmed to pulse 32 cycles every few seconds.

Figure (6.18 (a)) shows the input waveform from the WC and (6.18 (b)) shows the corresponding current waveform through $L_G$, the dummy gradient coil. Due to the capacitor tolerances and inaccuracies in the manufacture of the inductors, the resonant harmonics of the circuit do not match exactly the harmonics in the input waveform. This mismatch produces the observable phase errors in the gradient current waveform.

Figure (6.19 (a)) shows the input waveform when the phase errors have been taken into account and represents the phase compensated input. The corresponding current through $L_G$, figure (6.19 (b)), now resembles more closely the desired waveform.

Figure (6.20 (b)) shows the overall rise time $t_R$ of the waveform in response, this time, to a trapezoidal phase compensated input as determined by equations (6.1), (6.20) and (6.22). $t_R$ is determined by equation (6.16) and indicates in this case that the individual rise times, $t_{Rn}$, for each harmonic component are equal, thus preserving the trapezoidal waveform shape during establishment of equilibrium. The peak current shown in all figures is approximately 10 Amps.

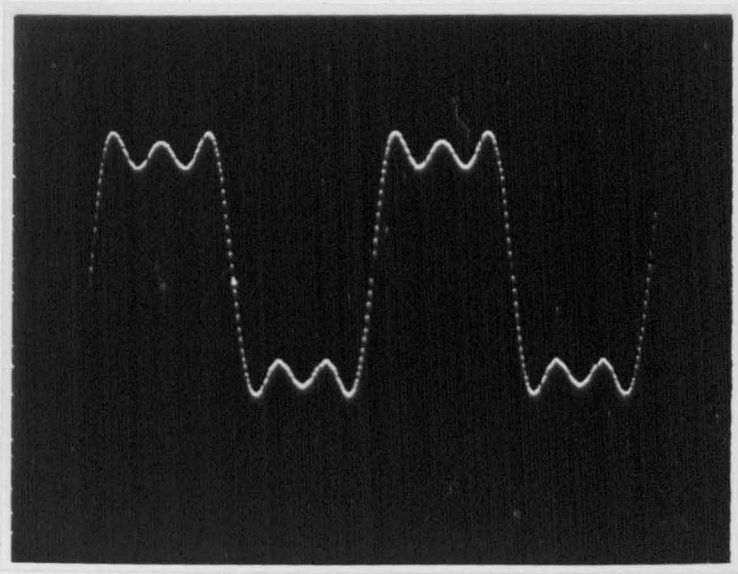

Figure 6.18 (a): Squarewave input to amplifier (small scale test circuit).

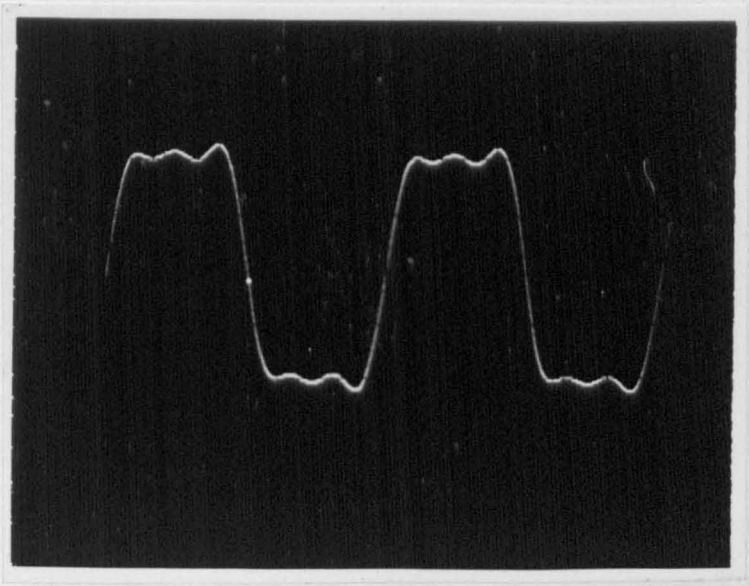

Figure 6.18 (b): Current waveform through dummy gradient coil in response to input of figure (6.18(a)) (amplifier in constant voltage mode).

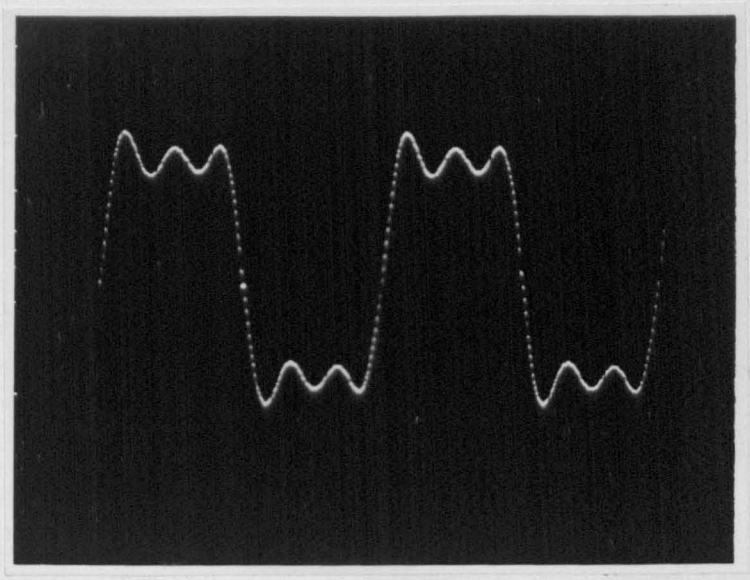

Figure 6.19 (a): Phase-compensated squarewave input to amplifier (small scale test circuit).

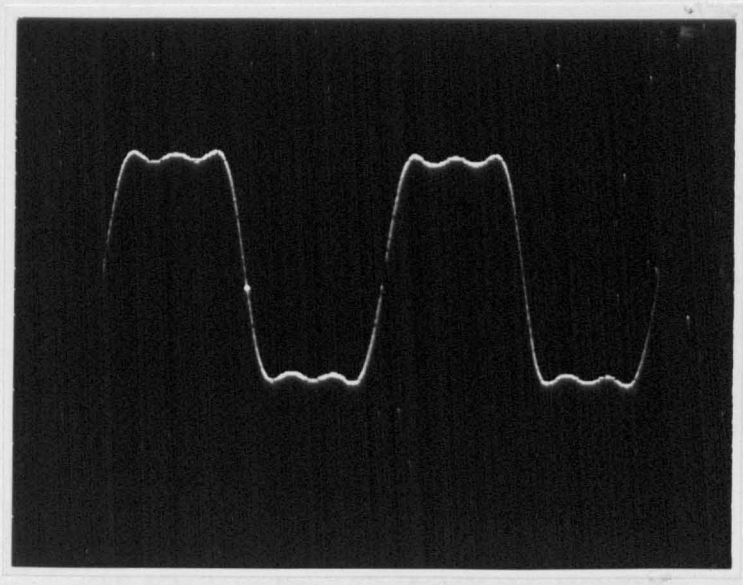

Figure 6.19 (b): Current waveform through dummy gradient coil in response to input of figure (6.19(a)) (amplifier in constant voltage mode).

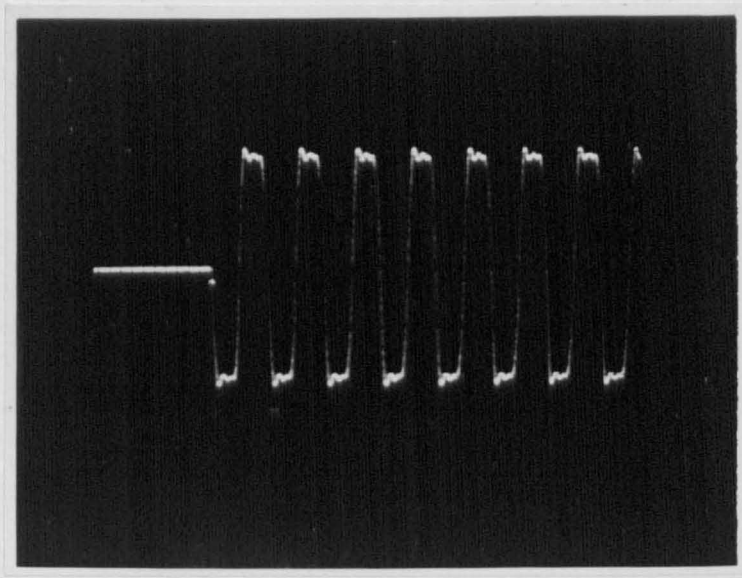

Figure 6.20 (a): Phase-compensated trapezoidal input to amplifier (small scale test circuit).

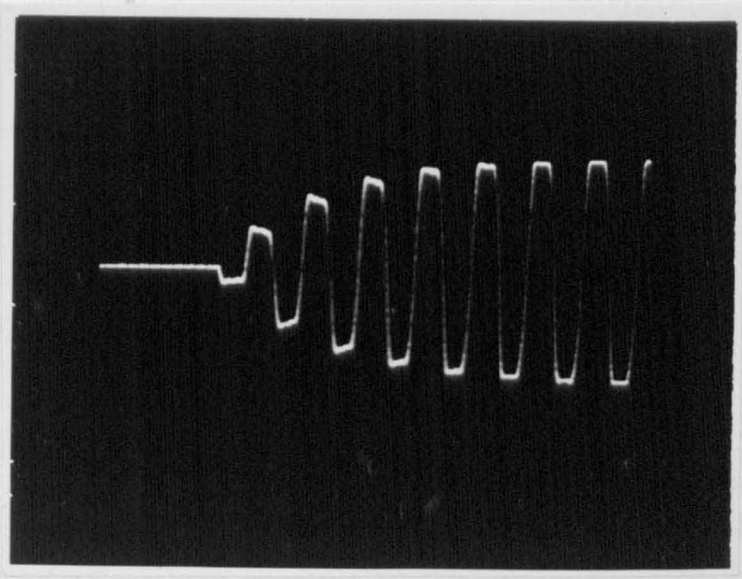

Figure 6.20 (b): Current waveform through dummy gradient coil in response to input of figure (6.20(a)) (amplifier in constant voltage mode).

Constant Current Mode Operation

With the Techron switched to constant current mode, a non-phase compensated trapezoidal waveform was input to the circuit. Figure (6.21) shows the current waveform through $L_G$ on start up. Here the initial response is much speeded up as compared to figure (6.20 (b)), establishing equilibrium conditions in approximately half a cycle. It is also interesting to note the absence of phase errors.

Figure (6.22 (a)) shows the input waveform on an expanded time base of 200 $\mu$s per large division. The current through $L_G$ once again indicates that the phase errors are compensated for automatically by the amplifier since, in constant current mode, the voltage supplied is constantly adjusting in order that the current waveform follows the input waveform exactly. The value of $p = 7$ used in the defining the trapezoid specifies a rise time, $\Delta t_{multi}$ of 71.4 $\mu$s at a fundamental frequency of 1 kHz. The experimentally observed value is in good agreement with this.

### 6.9.2 Large Scale Application

In order to perform whole-body imaging experiments using the multi-mode resonant filter circuit to drive the $G_x$ coil, a scaling up of the 5th order circuit was undertaken requiring the design of more robust inductors and the use of high power, water cooled, capacitors to facilitate the larger currents (in the region of 600 Amps (Pk - Pk)) required in an imaging experiment.

Suitable capacitors were available from a previous attempt to perform sinusoidal resonance. The inductance of the imaging gradient assembly and the available capacitors therefore determined the fundamental frequency of operation. The eventual operating frequency of 786 Hz corresponds to a $128^2$ MBEST experiment with data acquisition performed in approximately 80 ms and is 200 Hz higher than that used in conventional gradient drive for the standard 131 ms MBEST experiment. The peak current through $G_x$ required for 3 mm isotropic image resolution in an 80 ms experiment is approximately 1.6 times that required for the 131 ms experiment.

Capacitor Requirements

The capacitors were manufactured by Asea Brown Boveri (ABB) Capacitors Ltd. and supplied in four separate aluminium cases with in/outlets for water cooling. Each case contains eight capacitors, all with a common point such that different combinations can be connected in parallel, within a box, to give a range of capacitance. Two boxes each contain $8 \times 6.25$ $\mu$F capacitors and are rated at 2000 Volts RMS. The other two boxes each contain $8 \times 15.28$ $\mu$F capacitors and are rated at 1250 Volts RMS. Measurement of each individual capacitance, however, showed that the values quoted were only approximate. All four boxes were bolted into a Schroff 19 inch eurorack and their water inlets and outlets plumbed together.

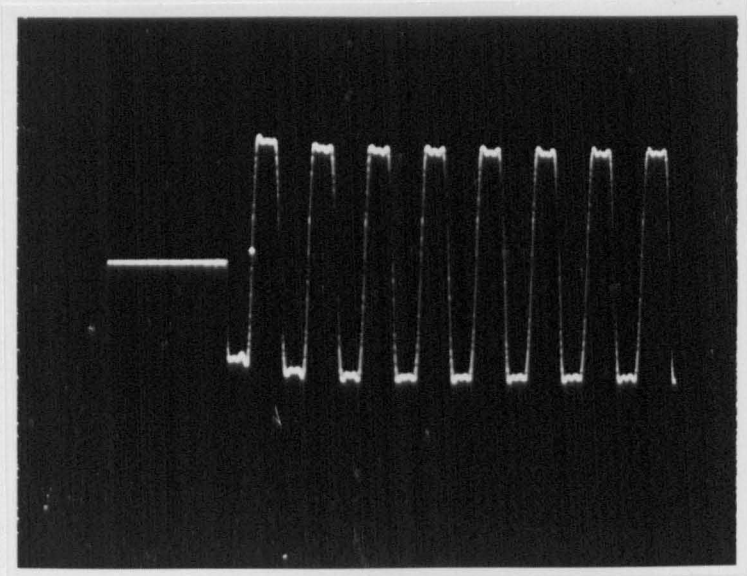

Figure 6.21: Current waveform through dummy gradient coil in response to input of figure (6.20 (a)) with amplifier in constant current mode. Note: Initial response much speeded up.

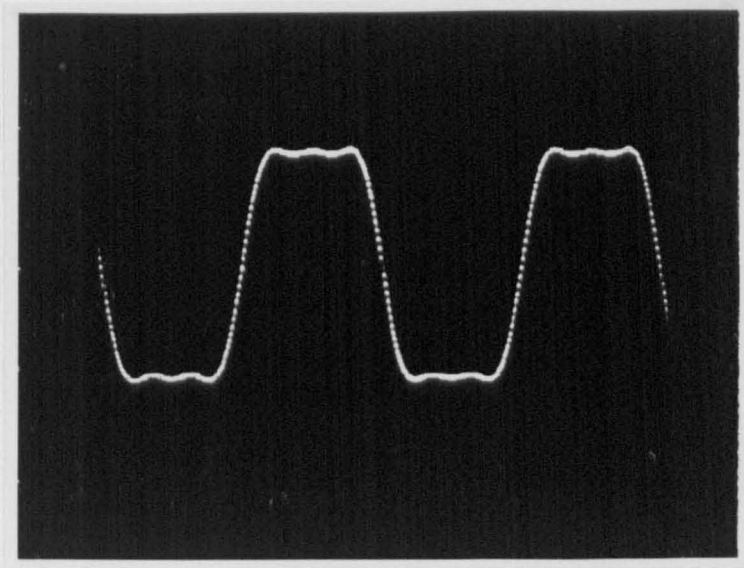

Figure 6.22 (a): Input trapezoidal waveform on expanded timebase.

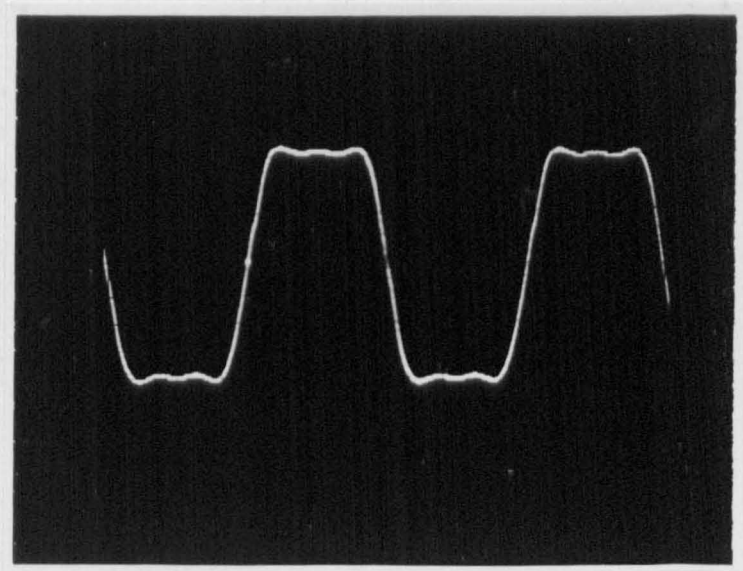

Figure 6.22 (b): Current response through dummy gradient coil with amplifier in constant current mode. Risetime approx. 71 $\mu$s.

| Capacitor | Required $\mu$F | Actual $\mu$F |
|---|---|---|
| $C_3$ | 41.66 | 39.70 |
| $C_5$ | 15.00 | 15.00 |
| $C_1^5$ | 115.38 | 115.31 |
| $C_3^5$ | 13.33 | 13.32 |

Table 6.2: Capacitor values required in 5th order filter circuit for fundamental resonance at 794 Hz with inductance $L_G = L = 107$ $\mu$H.

Taking a gradient assembly inductance $L_G = 107$ $\mu$H (the average value for $G_x$ and $G_y$ see chapter 4), the values of capacitance required were calculated in the usual way with the added constraint that the highest harmonic corresponds to resonance with $C_5 = 15$ $\mu$F resulting in a theoretical fundamental resonance at 794 Hz. The calculated values for the 5th order circuit and the actual values achieved using the combinations of capacitors available are shown in table (6.2). Suitable combinations of capacitors within each box were wired together in the manner shown in figure (6.23). One box supplied the capacitors for all three arms of the circuit requiring careful attention to the positions of the common points for each box in relation to the circuit, see figure (6.24). In addition, the largest capacitance value was split between two boxes. All connections between capacitor boxes were made with heavy duty PVC insulated wire cut to length and crimp terminated.

Inductance Requirements

The inductors were designed using an empirical formula by Grover [67]. In all, eight units were manufactured to an inductance of approximately 107 $\mu$H each. Of these eight only three were required for the 5th order circuit, the fourth being the $G_x$ coil assembly.

For a solenoidal inductor Grovers formula states

$$\gamma = \frac{1000L}{d_1^3 n_1^2} \tag{6.25}$$

where $L$ is the required inductance in micro-Henries, $d_1$ is the average diameter, in cm, of the solenoid including wire thickness and $n_1$ is the number of turns/cm of wire. The value $\gamma$ is then compared with tables in Grovers book from which a value of $R$ can be found. $R$ is related to the length of the solenoid, $b_1$ by

$$b_1 = d_1 R \tag{6.26}$$

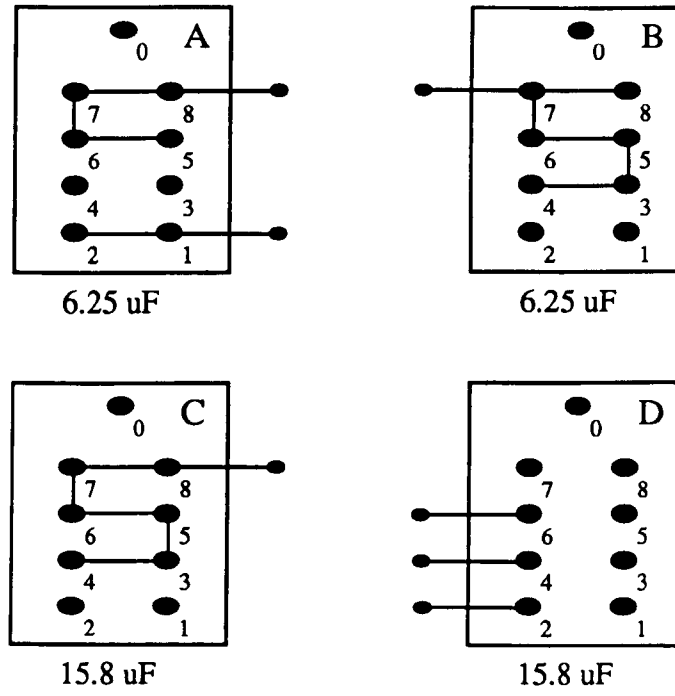


Figure 6.23: Wiring arrangements for each capacitor box. Combinations give values in table (6.2).

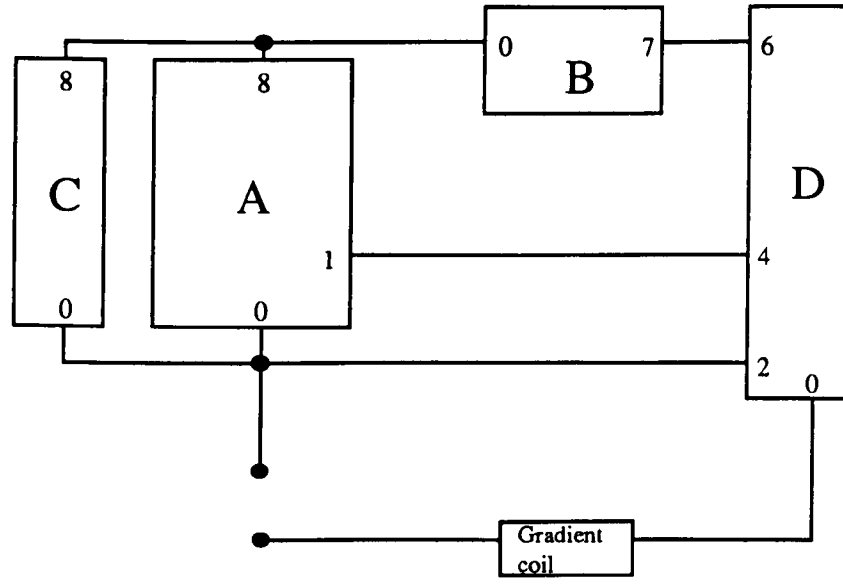


Figure 6.24: Common point connections for capacitor boxes as wired in figure (6.23).

Here, $b_1$ is also measured in cm.

The total number of turns at $n_1$ turns/cm required on a cylindrical former of approximate diameter $d_1$ and length $b_1$ to achieve an inductance $L$ micro-Henries is given by

$$N = b_1 n_1 \tag{6.27}$$

For the large scale application, the diameter of wire used was 4 mm. Combining this with the diameter of the former (chosen to be as small as possible, whilst allowing adequate surface area for heat dissipation) gave a value for $d_1$ of 16.2 cm. The corresponding value of $\gamma$ is 6.47 giving an $R$ value of 0.965. From equation (6.26) $b_1$ is also approximately 16 cm and the total number of turns, $N$, at 2 turns/cm is 32. This particular pitch was chosen to allow for air gaps between the turns on the inductors. At high currents the inductors in the main arm of the circuit would be required to dissipate a large amount of heat. This can be done more efficiently if as much of the surface area of the wire is open to the air as possible.

The inductor formers were manufactured out of wood with a shallow thread of pitch 2 turns/cm milled along each length. 16 m of 4 mm diameter enamelled copper wire was used to wind each solenoid and was held in place by braising each end to a heavy duty screw terminal which was, in turn, bolted to the wooden former. Three of the inductors were mounted in the eurorack in close proximity to the capacitors by means of aluminium angle supports. Connections to the appropriate points in the filter circuit were made using heavy duty, multi strand, insulated cable, doubled up and crimp terminated.

Simulated Constant Current Mode Operation

Using the component values previously calculated in table (6.1), the 5th order circuit was analysed, using "Microspice", to pinpoint the resonances and determine the voltages that might occur around the circuit at a peak operating current of 320 Amps (the sort of level required in an imaging experiment).

The simulation showed resonances at 794 Hz, 2403 Hz and 3980 Hz. The two upper resonances were not exact harmonics of the fundamental, being 21 and 15 Hz out respectively. However, the resonances were broad enough that the impedance 15 or 21 Hz off resonance at each harmonic was not too different from the on-resonance impedance. For practical purposes this represents a convenient advantage since, in constant current mode operation, the filter circuit would be forced to resonate at the harmonics specified by the input waveform. The amplifiers would see no real difference in the circuit impedance, as described above, and would not need to supply any extra voltage. Being effectively, a current controlled voltage source, the amplifiers would also compensate for the slight phase errors resulting from the resonance/drive mismatch.

At 794 Hz the amplifier voltage $V_{IN}$ required to resonate the gradient coil in a 5th order trapezoidal configuration at a peak current of 320 Amps was

deduced from the simulation to be 70 Amps (Pk). This represents a circuit DC resistance of 0.22 Ω. The voltage developed across the gradient coil would be approximately 103 Volts (Pk) and the largest voltage around the circuit would be 512 Volts (Pk) across $C_1^5$. All values lie well within the power ratings of the filter components.

Full Scale Circuit Operation

Having performed the simulation, the full scale filter network was wired in series with the $G_x$ coils of the imaging system and connected to a bank of eight Techron amplifiers, configured for balanced drive as described in chapter 4. Figure (6.25) shows the circuit layout. To minimize the possibility of introducing extra inductance and capacitance, wires to and from the gradient assembly were made as short as possible and large loops avoided. This required placing the filter circuit in relatively close proximity to the magnet. Input to the amplifier bank was via the direct input of the usual opto-isolated control box.

For preliminary tests the amplifiers were switched into constant voltage mode and the PM 5132 function generator used to input a continuous sinusoidal waveform. Current levels through the gradient coil were monitored via the socket on the amplifier control box which, for eight Techrons, scales at 80 Amps/Volt. Monitoring the amplifier voltage was achieved directly across a sense resistor in the front control board of the master amplifier. Both current and voltage waveforms were displayed on the DSO.

The resonant frequencies of the circuit were found by setting the current level to a low value and performing a frequency sweep of the sinusoidal input whilst looking for input voltage minima. The fundamental frequency was found at 786 Hz with the higher harmonics occurring at 2413 Hz and 4028 Hz respectively. These values are different to the simulated predictions due to differences in the inductance values of both the gradient coil and the inductors used in the filter circuit.

Having found the fundamental frequency of operation, The function generator was replaced by the WC and SUN workstation. Using the program SQRES in conjunction with WCtool, the 5th order trapezoidal waveform was input to the amplifiers at 786 Hz. WCtool was adjusted to provide bursts of 32 cycles with an interval of 3 seconds between each. At this stage each of the amplifiers was balanced so that all eight gave as uniform response as possible. In an unbalanced state the amplifiers are prone to driving each other, resulting in damage.

The input gain was increased until 320 Amps (Pk) current flowed through the gradient coil. The measured amplifier voltage, $V_{IN}$, was 51 Volts (Pk), 20 Volts less than predicted by the simulation. The circuit DC resistance is thus 0.16 Ω, only 0.03 Ω higher than the measured gradient coil resistance. These values indicate that the circuit is working better than expected.

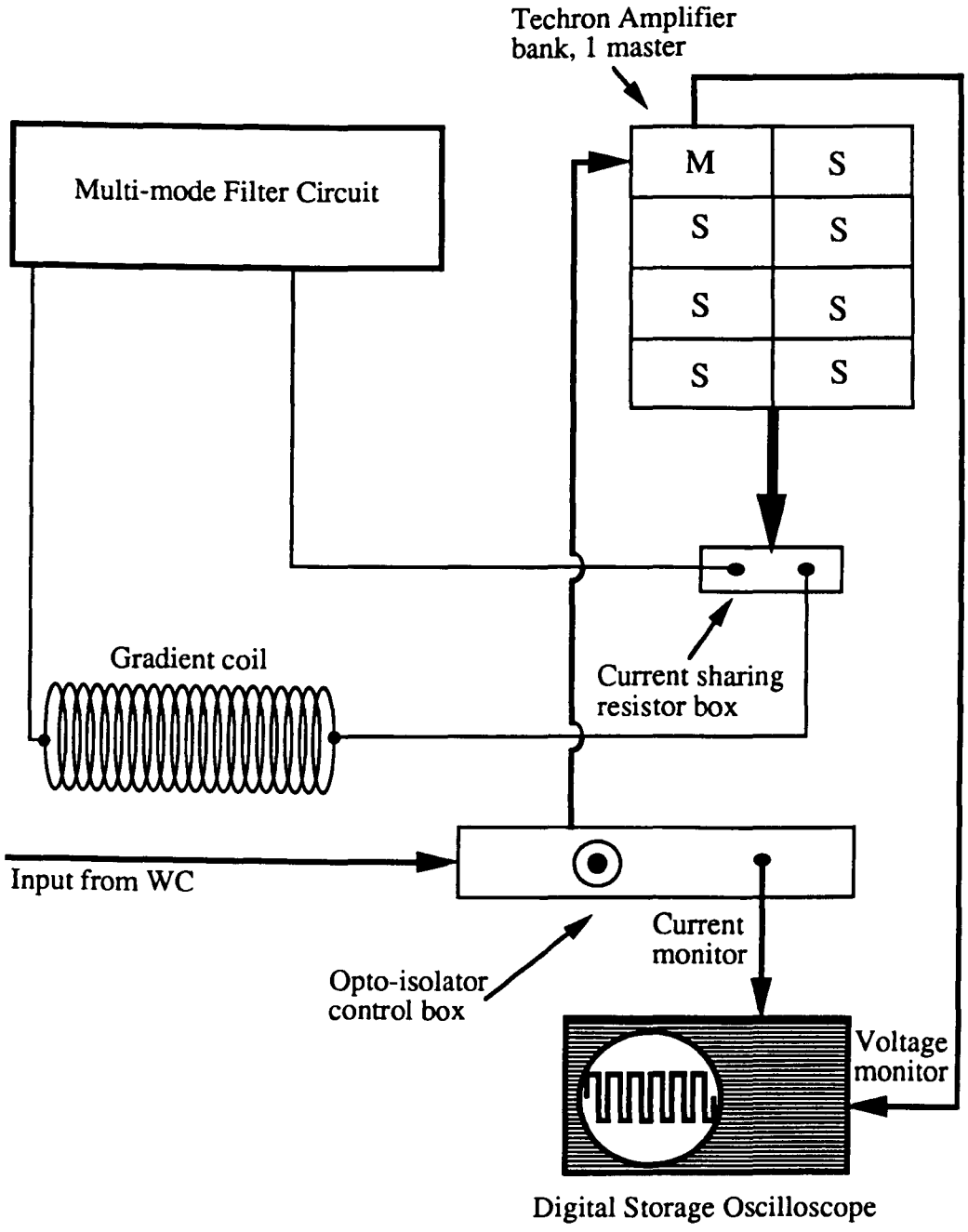


Figure 6.25: Full scale circuit drive layout.

The current and voltage waveforms for the full scale circuit are shown in figure (6.26). The peak to peak current is 640 Amps and is identical, in shape, to the input waveform. The peak to peak voltage is approximately 100 Volts, the shape is only slight distorted illustrating the inherent phase compensation of constant current mode operation. The rise time in these waveforms is approximately 90 $\mu$s corresponding well with the theoretical value at this frequency. For the level of current and frequency of operation this rise time represents a considerable improvement in performance over direct, non-energy conserving, gradient drive.

The low amplifier voltage requirement of only 50 Volts (Pk) for 320 Amps (Pk) means that the number of Techrons required for an imaging experiment can be reduced by a half. Using just four Techrons in parallel it should be possible to to drive the gradient coil, in a trapezoidal fashion, at peak currents of up to 600 Amps. The maximum voltage available from a single Techron is $\pm$ 150 Volts (Pk) which, for this application, puts an upper limit on the current amplitude of 960 Amps (Pk). This level of current would require six Techrons connected in parallel.

At levels of 960 Amps (Pk), however, the voltages around the circuit are likely to exceed the power capabilities of the filter components. The audible noise level and stand-off voltage of the gradient assembly is a further potential source of problems.

## 6.10 80 ms MBEST Using 5th Order Multi-Mode Resonant Gradient Drive

Having engineered correct operation of the large scale filter circuit, it was used in conjunction with the SUN workstation to perform 80 ms MBEST.

For this application experimental control was switched from the Data General Eclipse (DG) and associated WC, to the SUN workstation and its associated hardware. This was done by means of a purpose built patchboard which switches control of gradient drivers, RF electronics and data acquisition between the two systems.

Under SUN control the same RF electronics are used. However, the AP500 array processor and 16 bit ADC's are replaced by the AT & T pixel machine and 14 bit ADC's respectively. All gradient and RF waveforms are issued from the WC attached to the SUN. Further details of the exact control architecture are outside the scope of this project.

In the experiments detailed below, conventional amplifier drive was used on both $G_y$ (blipped gradient) and $G_z$ (slice selection) requiring no WC connection changes. The multi-resonant drive, on $G_x$ was incorporated into the imaging program by simply swapping the WC x-channel output from the bank of amplifiers (now disconnected from $G_x$) used for conventional drive to the amplifiers used in the 5th order filter circuit (now connected to $G_x$).

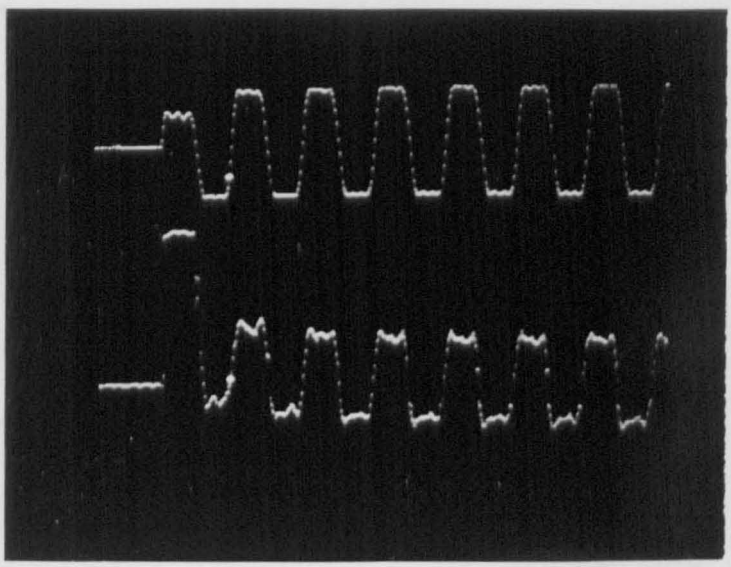

Figure 6.26: Full scale application. Top trace: Current waveform through gradient coil approx. 640 Amps Pk-Pk. Bottom trace: Amplifier voltage waveform approx. 100 Volts Pk-Pk.

### 6.10.1 EPItool

EPItool is a general experimental control program written for the SUN by Coxon. It allows on-screen control of all imaging parameters and can perform processing, Fourier transformation and interpolation on the fly, at a rate of 10 frames per second. Facilities exist for variable gradient waveforms enabling non-linear sample patterns to be calculated exactly using the waveform algorithm. For the 5th order trapezoidal waveform, a half-period of 636 $\mu$s (786 Hz) was specified and the number of points used to define a half cycle set to 159 giving exactly 4 $\mu$s per point. The appropriate non-linear sample pattern was calculated on the same basis.

### 6.10.2 MBEST Pulse Sequence Modifications

The gradient and RF pulse sequence employed on the SUN was similar to that used for MBEST on the DG. It differed in that it was shorter in duration, corresponding to 80 ms acquisition. No fat suppression was available and the normally square waveform on $G_x$ was replaced with the 5th order trapezoidal waveform for the multi-resonant application.

The pre-$G_x$ blip (sometimes referred to as FQUAD) was expected to pose a problem in the multi-resonant application. Normally both its amplitude and duration could be adjusted to correctly centre echo peaks. In the multi-resonant application the nature of the circuit means that it is difficult to introduce pulses which do not correspond in duration (frequency) to the harmonic components of the circuit. In practice, however, it was found that such a pre-pulse could be introduced at low amplitude by virtue of the constant current mode operation of the driver amplifiers. The resonant waveform, as mentioned earlier, took approximately 1.5 cycles to reach equilibrium and data acquisition was set to begin on the second full cycle. During this rise to equilibrium, the combination of the low amplitude pre-blip and the successive amplitudes of the first 1.5 cycles resulted in correct centring of the echoes. An alternative to the pre-blip would be a variable amplitude adjustment to the first half cycle of the resonant waveform.

### 6.10.3 Running EPItool

With all hardware connected and checked, EPItool was configured to acquire $128^2$ MBEST image in 80 ms. With a bottle phantom in the magnet, shimming and RF coil matching were performed in the usual manner. With slice selection and $G_x$ on, EPItool was set into "free run" mode.

A convenient facility of EPItool is that it enables the user to view the sampled diffraction pattern (k-space map) directly. Errors in setting up are much easier to asses in this way. With just $G_x$ on the k-map appears, when FQUAD is set correctly, as a white vertical central line on a black background. This line corresponds to the peaks of the correctly centred echos after being stacked into a 2D array. An advantage of resonant gradient drive is that $+ve$ and $-ve$

amplitudes of the gradient waveform balance each other exactly requiring no fine adjustment in an imaging situation.

With both $G_x$ and $G_y$ on, the k-map appears as a diffraction pattern with a central white spot (k-space origin) which can be positioned easily by adjusting the appropriate parameters. Once the diffraction pattern has been refined, the Fourier transform can be applied and PSD adjusted to remove ghosting artefacts from the image.

With the 14 bit ADC it was found necessary to precisely adjust the RF receiver attenuation in order to utilize the full dynamic range. Failure to do this resulted in a large central point artefact and low image S/N ratio.

Having achieved a clean image, of the bottle, the gradient amplitudes were increased until image resolution was 3 mm by 3 mm. This was assessed by comparing the diameter of the bottle in the image to its actual dimensions.

For 80 ms acquisition the pixel bandwidth is increased from 7.6 Hz (131 ms acquisition) to 12.5 Hz. The total image bandwidth is thus 205 kHz. For the experiments performed here, the receiver bandwidth was restricted to 256 kHz. This was not deemed to be too much of a problem since non-linear sampling requires a higher bandwidth.

### 6.10.4 Imaging Results

All the images presented here were acquired using the experiment detailed above, utilizing 5th order, trapezoidal, multi-mode resonant gradient drive on $G_x$.

Swirling Water Phantom

Figure (6.27) shows a series of $128^2$, 80 ms, MBEST images of a swirling water phantom. These images were acquired and displayed at a rate of 5 frames/second. The in-plane resolution is 3 mm by 3 mm. Because of the shorter acquisition time, however, the S/N ratio is slightly reduced. The images appear slightly sharper than 131 ms MBEST possibly due to the higher pixel bandwidth. Much detail can be seen in the turbulent flow patterns which arise partly from spin refreshment and partly from velocity induced signal dephasing in the plane. The peak current measured in $G_x$ for 3 mm resolution was 288 Amps (in the sinusoidal case this would be required to be closer to 450 Amps (Pk)). The amplifier voltage at this level was measured at $< 50$ Volts (Pk) indicating excellent performance of the multi-resonant $G_x$ driver configuration.

Tube Array

The image in figure (6.28) shows an array of test tubes positioned within the imaging plane. Each tube is approximately 20 mm in diameter. The in-plane resolution is once again 3 mm by 3 mm. The full field of view is utilized with excellent image clarity.

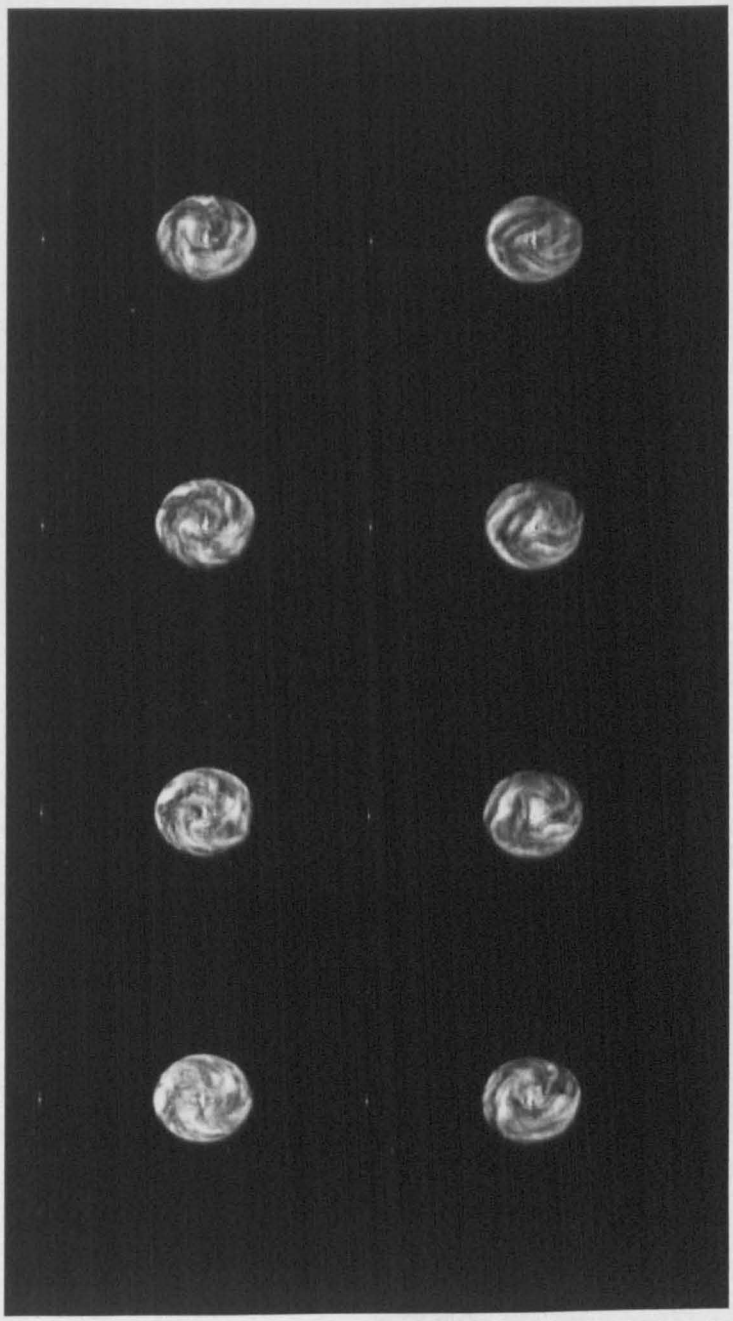

Figure 6.27: Images of a swirling water phantom acquired using 5th order multi-mode resonant gradient driver circuit and MBEST imaging sequence. Acquisition time for these images was 80 ms. In-plane resolution is 3 mm by 3 mm.

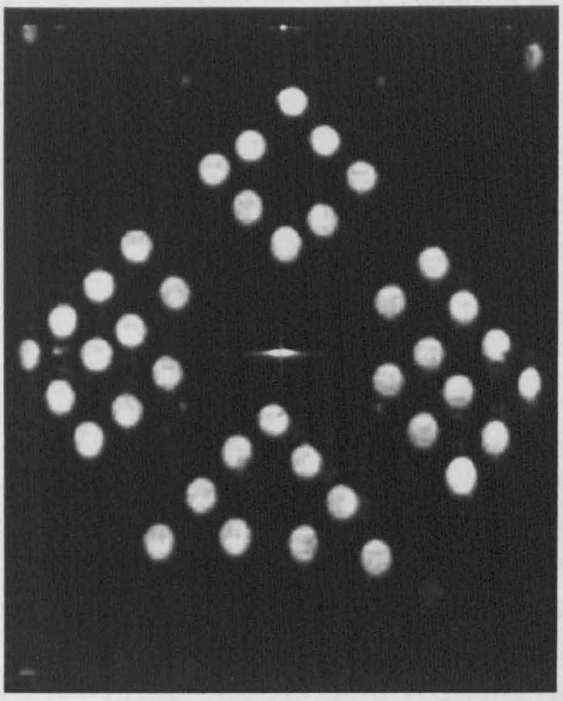

Figure 6.28: Image of test-tube phantom. Diameter of tubes approx. 2 cm. In-plane resolution is 3 mm by 3 mm.

Figure (6.29) shows a collection of whole-body images depicting the thorax, liver and kidneys of a healthy volunteer. No fat suppression was used and the k-space origin occurred approximately 25 ms into data acquisition. The shift of the origin was required in order to improve upon the S/N ratio and capture some of the signal from tissue with short $T_2$ components (i.e. myocardium). Unfortunately, without suitable phase correction, shifting the k-space origin too far results in blurring and phase errors across the image.

## 6.11 Conclusions On Multi-Resonant Gradient Drive

A systematic way of designing a discrete filter circuit which has a multi-mode series response useful for driving a series resonant gradient coil for use in ultra high speed MRI has been described. Detailed circuits are explained which respond to a truncated Fourier series comprising two, three and four harmonics respectively. However, the principles described may be extended to higher harmonics and to the generation of waveforms other than square wave, where the Fourier series is more convergent and where the amplitude of particular harmonics may be designed to be zero, thus reducing the circuit complexity necessary to generate the waveform. In all cases the approach exploits the energy conserving principle so that current waveform rise times for a given gradient coil and driver amplifier can be considerably faster than can be achieved by direct drive through the coil. The circuits described for this application are entirely passive arrangements and therefore have a considerable advantage over switched non-linear circuits where expensive components are required.

The technology developed here has been applied in this laboratory to provide usable waveforms for EPI. MBEST images have been acquired in 80 ms, employing gradient rise times and amplitudes in excess of those achievable by direct drive under the same experimental conditions. In addition, the gradient amplitude for the given image resolution is much less than would have been required had simple sinusoidal resonant drive been used. The more significant point of this work is underlined by the fact that only three Techron amplifiers need be used where previously eight were required. This represents quite a significant financial saving.

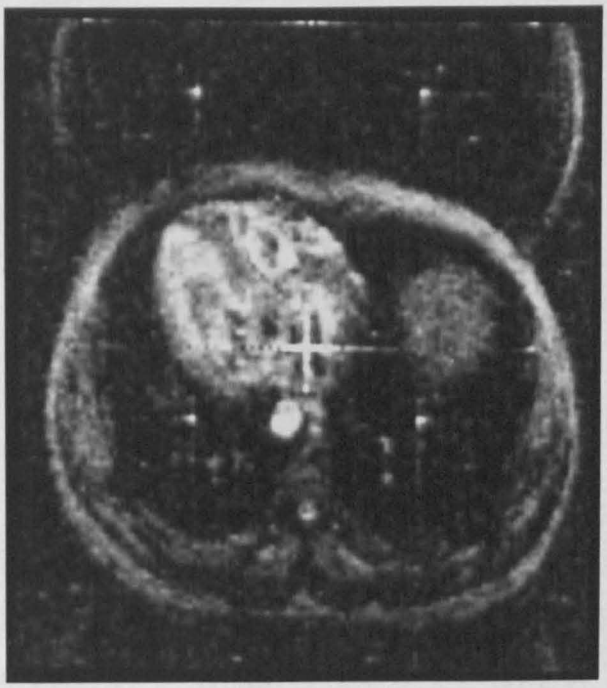

Figure 6.29 (a): Whole-body images taken on a volunteer using 80 ms MBEST and multi-mode resonant gradient drive. Thorax.

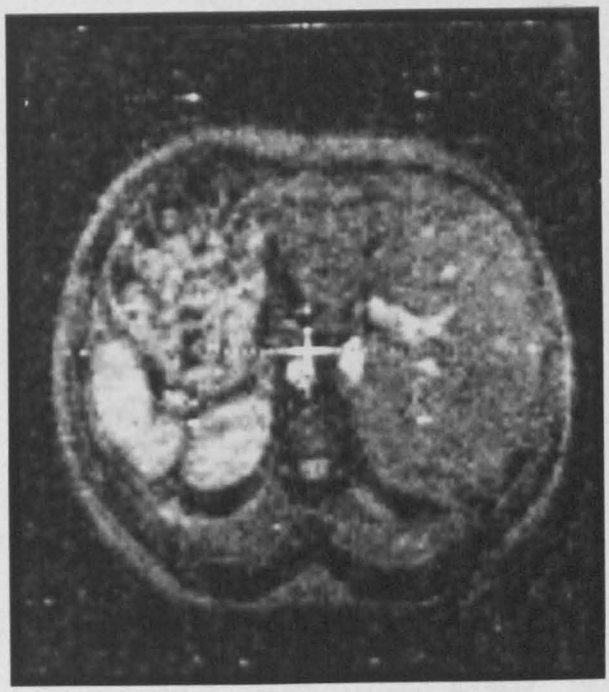

Figure 6.29 (b): Liver region.

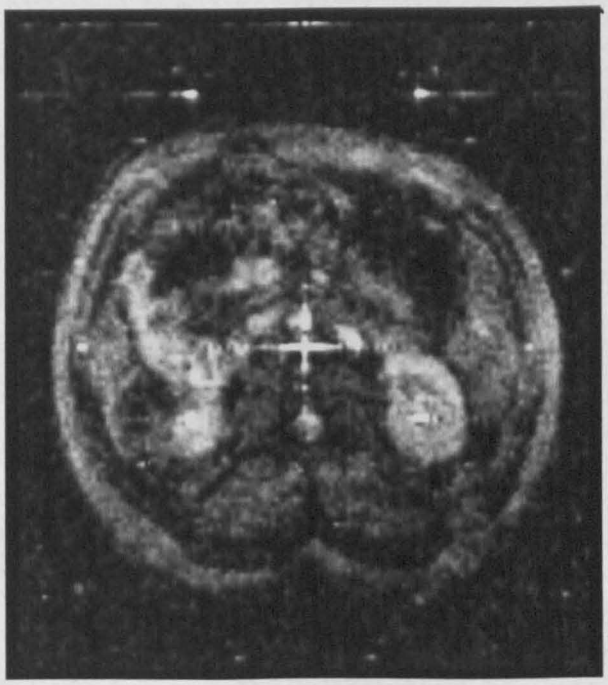

Figure 6.29 (c): Kidneys.

# Chapter 7: Limits to Neural Stimulation in Echo Planar Imaging

## 7.1 Introduction

Echo planar imaging together with other ultra-high speed imaging methods requires large rapidly switched magnetic field gradients to be applied to the patient as part of the spatial encoding process. In exploring the limits of whole-body EPI, magnetically induced tingling sensations in peripheral body regions have been reported recently [26, 27, 68]. At very high gradient strengths, peripheral nerve stimulation is, of course, not unexpected. Indeed, there is considerable literature on the effects of magnetic and electric neural stimulation [28, 69, 70]. This forms the basis of the guidelines suggested by the British NRPB [71] and others. However, there is wide disparity among the safety authorities not only with the levels recommended but also with the formulae used to define the gradient switching problem. For example, NRPB currently use the expression

$$\left(\frac{dB}{dt}\right)^2 t < 4 \ T^2 s \tag{7.1}$$

to define the maximum permissible $dB/dt$ in $\mathrm{Ts}^{-1}$. The German authorities use an expression based on the product $(dB/dt)t$. In all cases and no doubt for historical reasons, there is a preoccupation with the switching rate $dB/dt$.

In this chapter, the basic stimulation model which lies behind the $(dB/dt)t$ formula is re-examined and shown to be incorrect. Experimental results confirm this. Using a new approach it is possible to deduce that trapezoidal gradient waveforms with very high switching rates may actually be safer than the equivalent sine modulation in EPI of a given image array size and imaging time.

## 7.2 The Theory of Peripheral Nerve Stimulation

The following model is based on myelinated neurones but similar results are expected for other electrically excitable tissue. Breaks in the myelin sheath form nodes comprising a selectively permeable membrane through which external currents may be introduced. In the resting state the membrane takes up a negative potential $E$ of about $-70$ mV due to a preponderance of potassium ions in the axoplasm [73]. During neural propagation the axon potential rises to about $+50$ mV as a result of the flow of sodium ions through the membrane. The difference of these two voltages, the transmembrane potential reaches 120 mV and is called the nerve action potential $V_m$. The

neurone can be triggered by de-polarizing the transmembrane potential by an amount $\Delta V = fV_m$, where $f$ is the threshold fraction with a value in the range $0 < f < 1$. During conduction the nodal membrane behaves like the linear electrical circuit of figure (7.1) with a membrane resistance-area product $r_m$ and a membrane capacitance/area $C_m$. In the analysis presented here it is considered that magnetic stimulation of the nervous tissue is equivalent to applying a current generator to a node.

Let the source generator produce a current density $j$. From the circuit

$$j = j_1 + j_2 \tag{7.2}$$

Before the source generator is switched on, the nodal capacitor sits at a potential of $-E$. Since no currents flow, then for $t \leq 0$, $j = j_2 = j_1 = 0$. Following turn-on of $j$, the capacitor potential will change depending on the amount of charge that enters or leaves $C_m$. For $t \geq 0$, therefore, the capacitor potential is given by

$$V_c(t) = \frac{1}{C_m} \int j_1 dt - E = j_2 r_m - E \tag{7.3}$$

Combining equations (7.2) and (7.3) gives

$$j r_m = j_1 r_m + \frac{1}{C_m} \int j_1 dt \tag{7.4}$$

Equation (7.4) can be solved for $j_1$ using the Laplace transform method (see Appendix C) to obtain the integral equation [72]

$$j_1(t) = j(t) - \frac{e^{-t/\tau_m}}{\tau_m} \int_0^t e^{t'/\tau_m} j(t') dt' \tag{7.5}$$

which from equation(7.2) gives

$$j_2(t) = \frac{e^{-t/\tau_m}}{\tau_m} \int_0^t e^{t'/\tau_m} j(t') dt' \tag{7.6}$$

where the nodal membrane time constant is

$$\tau_m = r_m C_m \tag{7.7}$$

From the measured membrane characteristics [73], $\tau_m = 150\ \mu s$. When $j(t)$ is constant equation (7.6) can be integrated to yield the expression given by Hodgkin for the induced nodal current density $j_s$

$$j_s = j_2 = j[1 - e^{-t/\tau_m}] \tag{7.8}$$

If the value of the current density necessary to fire the nerve is $j_{s0}$, then for $t/\tau_m < 1$, equation (7.8) may be approximated [28] by

$$j_{s0} \tau_m \simeq jt = q \tag{7.9}$$

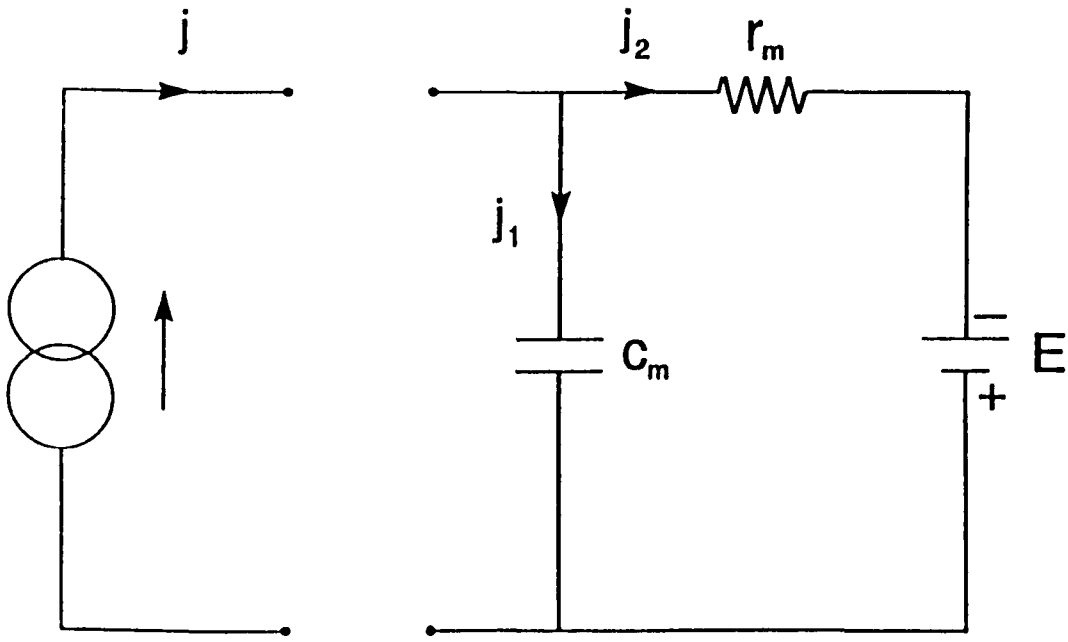


Figure 7.1: Equivalent electrical circuit of a neural node shown here driven by a current generator.

where $q$ is the nodal membrane surface charge density.

For a homogeneous tissue cylinder the magnetically induced current density is usually given by

$$j(t) = \frac{\alpha\sigma r}{2}\left[\frac{dB}{dt}\right] = K\left[\frac{dB}{dt}\right] \tag{7.10}$$

where

$$K = \frac{\alpha\sigma r}{2} \tag{7.11}$$

in which $\sigma$ is the tissue conductivity typically in the range $0.25 - 0.5\ \Omega^{-1}m^{-1}$, $r$ is the radius of the circular induced current path when the magnetic field $B$ lies along the cylinder axis. The constant $\alpha$ is introduced to account for induced current anisotropy and lies in the range $0 \rightarrow 1$.

The problem with the above approach is that it does not take account of the dispersive nature of tissue which, as will be shown later, can introduce frequency dependent phase shifts into the induced current density. These phase shifts are best introduced by using a sinusoidal version of equation (7.10) rather than $dB/dt$ directly. This means that even in the case of a linear ramp, the current density, though temptingly simple to evaluate, in fact must be Fourier analysed into its frequency components first, phase dispersion applied, then inverse Fourier transformed to obtain the total induced current density. Only when phase dispersion is absent can the simple expression, equation (7.10), be applied.

## 7.3 Tissue Phase Dispersion

Using a more sophisticated theory presented elsewhere [28], it can be shown that when frequency effects are included the induced current density in response to a time varying magnetic field input function of the form $B(t) = B_m e^{i(\omega t)}$ may be approximated by the complex expression

$$\begin{aligned} j(t,k) &= j'(t,k) + ij''(t,k) \\ &= T(k)B(t) \\ &= i\omega K B_m e^{i(\omega t - \theta)} \end{aligned} \tag{7.12}$$

where the transfer function $T(k)$ is

$$T(k) = i\omega K e^{-i\theta} \tag{7.13}$$

in which for small phase angles, $\theta$ is given by

$$tan\ \theta = \frac{k}{\omega\tau_m} \tag{7.14}$$

The constant $k$ is given by

$$k = \frac{\tau_m}{\tau_0} \tag{7.15}$$

The intrinsic tissue time constant $\tau_0$ is given by

$$\tau_0 = \frac{a^2 \mu \mu_0 \sigma}{4} \tag{7.16}$$

in which $\mu_0$ is the free space permeability, $\mu$ the relative permeability and $a$ the tissue cylinder radius. The tissue characteristics therefore introduce a phase dependence into the induced current $j(t,k)$. In this approximate theory $\sigma$ and $\mu$ are taken as frequency independent. In practice this is not true so that phase shifts larger than those predicted by equations (7.12) to (7.15) may occur (see later).

Substitution of equation (7.10) into (7.6) gives the general solution for $j_s$ namely

$$j_s = \frac{K}{\tau_m} e^{-t/\tau_m} \int_0^t e^{t'/\tau_m} \left[\frac{dB}{dt'}\right] dt' \tag{7.17}$$

When $t/\tau_m \ll 1$ and if $dB/dt$ does not change significantly over the period $t$ and there are no phase shifts, equation (7.17) reduces to

$$j_s = \frac{K}{\tau_m} \int_0^{B_m} dB = \frac{KB_m}{\tau_m} \tag{7.18}$$

where $B_m$ is the maximum excursion of $B$. This result is generally true for any waveform variation of $dB/dt$. The result stated in a slightly different way says that $j_s$ is proportional to the maximum magnetic field variation $B_m$. In this case $B$ behaves like a potential function so that $B_m$ is independent of the waveform or path taken in $B$, t-space to achieve $B_m$. This result is easily verified for a number of $B$ field pathways as illustrated in figure (7.2 (a)), i.e. case (A) and (B), $j = j_0$; $B = (j_0/K)t = B_m(t/t_{max})$, case (C), $j_0 = at$; $B = at^2/2K = B_m(t/t_{max})^2$. In each case the induced current waveforms are shown in figure (7.2 (b)). The accumulated electrical charge $q$ is proportional to the areas under these curves (shaded case (A)). In all three examples $q$ is constant.

As mentioned earlier, when phase dispersion is present it is necessary to examine the frequency components of $dB/dt$. The simplest case is when $B(t)$ has a sinusoidal variation with time.

## 7.4 Sinusoidal Gradient Modulation

Equation (7.17) can of course be evaluated for any general waveform variation of $dB/dt$. The results can then be used to study the approach to the case when either the inequality $t/\tau_m \ll 1$ (the time domain) or an equivalent inequality in the frequency domain ($\omega\tau_m > 1$) is satisfied. Let the magnetic field

$$B = B_m sin\ \omega t \tag{7.19}$$

Combining equations (7.12), (7.13), (7.14) and (7.19) yields

$$j''(t,k) = \omega K B_m cos(\omega t - \theta) \tag{7.20}$$

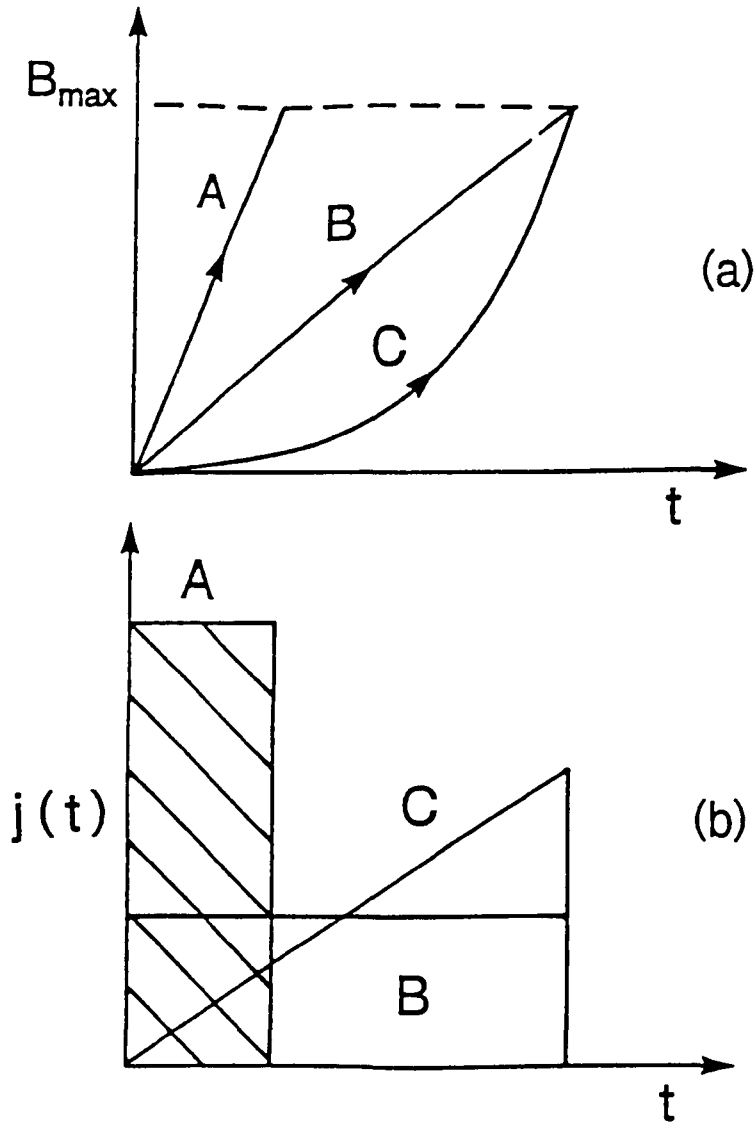


Figure 7.2: Sketches showing (a) various $B$ field waveforms taken to reach $B_m$, and (b) the corresponding induced current density for the $B$ field waveforms in (a). Note that the areas under the current curves are all equal and correspond to constant charge $q$.

where $j''(t,k)$ is the imaginary current component. Substituting $j''(t,k)$, equation (7.20) into equation (7.6) and integrating gives, for $j_2 = j_s$

$$\begin{aligned} j_s &= \frac{KB_m}{\tau_m}\left\{a(\omega)[cos(\omega t-\theta)-e^{-t/\tau_m}cos\theta]\right. \\ &+ \left. b(\omega)[sin(\omega t-\theta)+e^{-t/\tau_m}sin\theta]\right\} \end{aligned} \tag{7.21}$$

in which

$$a(\omega) = \frac{\omega\tau_m}{1+\omega^2\tau_m^2} \tag{7.22}$$

and

$$b(\omega) = \frac{\omega^2\tau_m^2}{1+\omega^2\tau_m^2} \tag{7.23}$$

In the special case when $\omega t = \pi/2$, $\theta = 0$ (corresponding to $k = 0$) and for $\omega\tau_m \gg 1$, $j_s \rightarrow KB_m/\tau_m$. However, when these conditions are not met, sinusoidal modulation can produce a de-sensitization so that higher fields are required in order to reach $j_s$. These effects occur at lower frequencies, i.e. when $\omega\tau_m \leq 1$.

Equation (7.21) may be written in a more compact form as

$$j_s = K\left[\frac{B_m}{\tau_m}\right] f(\omega) \tag{7.24}$$

where

$$\begin{aligned} f(\omega) &= a(\omega)[cos(\omega t-\theta)-e^{-t/\tau_m}cos\theta] \\ &+ b(\omega)[sin(\omega t-\theta)+e^{-t/\tau_m}sin\theta] \end{aligned} \tag{7.25}$$

Equation (7.25) may be contracted to the expression

$$f(\omega) = f_m(\omega)[cos(\omega t-\theta-\phi)-cos(\theta+\phi)e^{-t/\tau_m}] \tag{7.26}$$

in which

$$f_m(\omega) = \frac{\omega\tau_m}{(1+\omega^2\tau_m^2)^{\frac{1}{2}}} \tag{7.27}$$

and where

$$tan\ \phi = \omega\tau_m \tag{7.28}$$

For long times ($t/\tau_m \ll 1$) the exponential term in equation (7.26) reduces to zero giving the steady state solution. This has a maximum value $f_m(\omega)$ when $\omega t = \theta + \phi$. For short times $f(\omega) \rightarrow 0$ for $\omega \leq \pi/2\tau_m$. For frequencies higher than this, and depending on the size of the phase $\theta + \phi$, the initial transient term can effectively add to the steady state solution but the magnitude of $f(\omega)$ is always less than or equal to $f_m(\omega)$ for the conditions and frequencies considered here. Also worth noting is that when $k = 1$, $\theta + \phi = 90°$. By deduction from equations (7.24) to (7.28), the magnetic field excursion $B_s$ required to produce neural stimulation is given by

$$B_s = B_m = \frac{\tau_m j_{s0}}{Kf_m(\omega)} = \frac{1}{f_m(\omega)} \quad \text{(normalized)} \tag{7.29}$$

Phase effects, though present, do not explicitly enter in equation (7.29) because $j_{s0}$ depends on the magnitude of $B_s$. However, for more complicated waveforms synthesized from many Fourier-components, phase shifts cannot be neglected.

## 7.5 Trapezoidal Gradient Modulation

In chapter 6 it was shown that trapezoidal gradient waveforms of a given rise time can be generated effectively from a finite and small number of Fourier components. That is to say, for odd $n$

$$B^T(t) = B_m^T F \sum A_n sin\ n\omega t \tag{7.30}$$

and

$$\frac{dB^T(t)}{dt} = B_m^T F \sum n\omega A_n cos\ n\omega t \tag{7.31}$$

where $A_n$ is the amplitude of the $n$th harmonic, $F$ is a normalization factor which allows for truncation of the Fourier series, and the attributes $T$ and $S$ (used later) refer respectively to trapezoidal and sinusoidal waveforms. For $n = 5$ the rise time is $\pi/7\omega$ with $A_1 = 1$; $A_3 \simeq 1/4$; $A_5 \simeq 1/14$. Equation (7.30) is, of course a generalization of equation (7.19) and produces an induced current response counterpart of equation (7.20), namely

$$j''(t,k) = KB_m^T F \sum n\omega A_n cos(n\omega t - \theta_n) \tag{7.32}$$

and gives a nodal current $j_2 = j_s$, equation (7.6) of

$$j_s = K\frac{B_m^T}{\tau_m} F \sum A_n f_m(n\omega) cos[n\omega t - (\theta_n + \phi_n)] \tag{7.33}$$

Generalizing the steady-state current solution, equation (7.24) and inverting gives, for $j_s = j_{s0}$, the expression

$$B_m^T = \frac{\tau_m j_{s0}}{KF \sum A_n f_m(n\omega) cos[n\omega t - (\theta_n + \phi_n)]} \tag{7.34}$$

in which

$$tan\ \theta_n = \frac{k}{n\omega\tau_m} \tag{7.35}$$

where $k$ is defined by equation (7.15) and

$$tan\ \phi_n = n\omega\tau_m \tag{7.36}$$

For the examples used in this chapter, $A_1 = 1$, $A_3 = 0.2493$, $A_5 = 0.0723$ and $F = 1.215$.

## 7.6 Comparison of Trapezoidal and Sinusoidal Gradient Modulation

It is useful to compare the magnetic field levels $B^S$ and $B^T$ necessary to elicit neural stimulation with a current density $j_{s0}$. For the pure sinusoidal field

$$B^S(t) = B^S_m sin\ \omega t \tag{7.37}$$

Combining equations (7.33) and (7.37) gives

$$\frac{B^S_m}{B^T_m} = R = \frac{F \sum A_n f_m(n\omega) cos[n\omega t - (\theta_n + \phi_n)]}{f_m(\omega)} \tag{7.38}$$

In this expression the numerator and denominator are maximized separately. In this case explicit phase dependence vanishes in the denominator so that $B^S(t)$ may be replaced by $B^S_m$.

A perfect trapezoidal waveform would require an infinite series of Fourier harmonics to describe it. The simpler approach of equations (7.10) and (7.8) can only be used if $k = \infty$, i.e. $\theta_n = 90^o$. In this case the limiting value of the field ratio, $R_l$ is

$$R_l = \left[\frac{p\omega\tau_m}{f_m(\omega)\pi}\right]\left(1 - e^{-2\pi/p\omega\tau_m}\right)\left(1 + e^{2\pi(1-p)/\omega\tau_m p}\right) \tag{7.39}$$

where the trapezoidal ramp time is $T/2p$ ($p = n + 2$, integer) and the waveform period $T = 2\pi/\omega$. For the synthesized trapezoidal waveforms referred to later $p = 7$.

## 7.7 Experimental Results

### 7.7.1 Surface Stimulator Coils - Manufacture and Calibration

For the purpose of investigating the theory, local surface coil magnetic stimulators were used which, when applied to the palmar surface of the wrist, create a mild tingling sensation at the neural stimulation threshold.

Two stimulator coils were constructed to operate, using resonant drive, at two different fundamental frequencies, i.e. 800 Hz and 1.3 kHz. Figure (7.3 (a)) is a sketch of the stimulator coil arrangement for a particular coil which is fixed within a PVC box for good electrical insulation. Each coil had a mean diameter of 48 mm. Other details are summarized in table (7.1). Both the coils were designed to operate under multi-mode resonance (see chapter 6) to facilitate the application of trapezoidal as well as sinusoidal magnetic fields. Due to the extra harmonics required in the trapezoidal waveforms each coil was able to operate under resonance at three pure sinusoidal frequencies. 800 Hz, 2.4 kHz and 4 kHz in the case of the 112 $\mu$H coil and 1.3 kHz, 3.9 kHz and 6.5 kHz in the case of the 39 $\mu$H coil.

For the 112 $\mu$H coil the arrangement described in chapter 6 was used for both sinusoidal and trapezoidal waveforms. For the 39 $\mu$H coil the inductors in

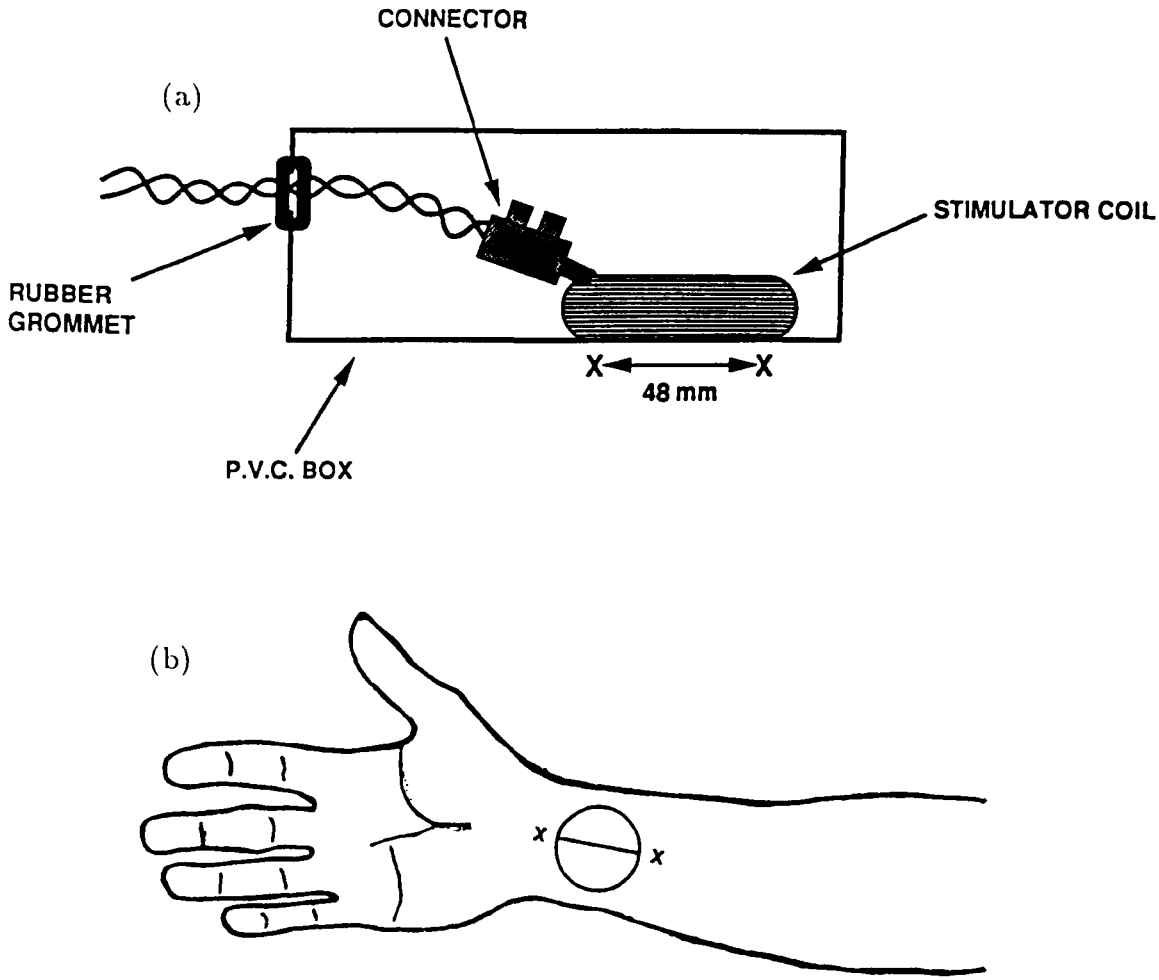


Figure 7.3: (a) sketch of stimulator coil and insulating enclosure. The mean coil diameter is 48 mm and 10 mm thick. See table (7.1) for more coil details. (b) Position of stimulator coil on the palmar surface of the wrist.

| Freq. Hz | Inductance $\mu$H | Effective Diameter (mm) | Height mm | Wire dia. mm | No. Turns Approx. |
|---|---|---|---|---|---|
| 800 | 112 | 48 | 20 | 1.6 | 42 |
| 1300 | 39 | 48 | 16 | 1.6 | 26 |

Table 7.1: Stimulator coil details.

the multi-mode filter circuit had to be changed from $L = 107$ $\mu$H to $L = 39$ $\mu$H in order for the circuit to work correctly for the trapezoidal waveform. Changing the inductances of the individual inductors was achieved by simply bridging approximately 13 of the 32 windings with thick copper wire.

Each of the coils was calibrated using a WALKER Scientific inc. model MG-5D gaussmeter to provide the current-magnetic field conversion factor. Measurements of the axial field profile for each coil were also made. Figure (7.3 (c)) shows them to be very similar. The current-magnetic field conversion factor for the 112 $\mu$H (800 Hz) coil is

$$B_{800}\,(\mathrm{mT}) = (1.2759 \pm 8 \times 10^{-4})I \text{ Amps } + 0.461 \pm 4 \times 10^{-3} \qquad (7.40)$$

and for the 39 $\mu$H (1.3 kHz) coil

$$B_{1300}\,(\mathrm{mT}) = (0.8338 \pm 6 \times 10^{-4})I \text{ Amps } + 0.250 \pm 3 \times 10^{-3} \qquad (7.41)$$

Figure (7.3 (b)) shows the coil position when in place on the wrist. The whole probe was strapped in position using adhesive tape. The current through each coil was monitored using the DSO via the current monitor facility on the opto-isolator control box connected to the amplifiers. The conversion factor in this case was 80 Amps/Volt.

### 7.7.2 Volunteer Stimulation Experiments

Sinusoidal Stimulus Only

As a test of the theory sinusoidal stimulus was applied to the volunteers at three different frequencies in 20 ms bursts. The three frequencies used were; 800 Hz, 2.4 kHz and 4 kHz. The volunteers were unaware of the level of stimulus applied. In each case the lowest magnetic field strength $B_s$ required to produce peripheral neural stimulation in the wrist region was recorded. Eight measurements were made on each volunteer at each frequency. Four of these approached the stimulation threshold point from below using an increasing magnetic field strength while the other four measurements involved decreasing the field strength from above the stimulation threshold until stimulation ceased. In the former case the volunteer was asked to identify the

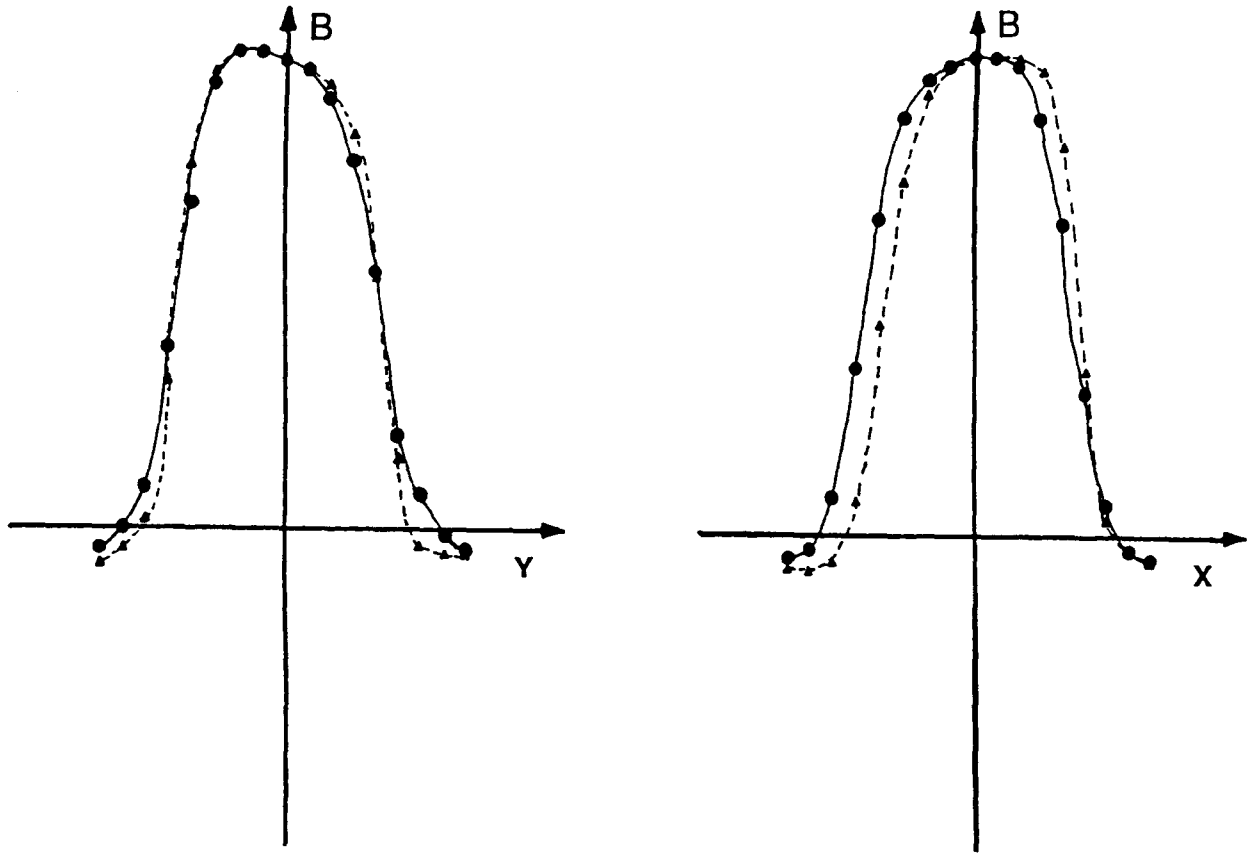


Figure 7.3 (c): Normalized magnetic field profile for stimulator coils. ● = 800 Hz coil and ▲ = 1300 Hz coil.

point at which stimulation could just be felt and in the latter case, the point at which stimulation could no longer be felt. The perception of stimulation was sensory at low levels and at higher levels both sensory and motor, the latter effect producing considerable finger twitch. Particular care was taken not to disturb the probe which was taped to the wrist. The standard deviation on all sets of readings was within 3%. The magnetic field strength when approached from above the stimulation threshold was on average 8% lower than when approached from below. The normalized results when approached from below the stimulation threshold are plotted in figure (7.4) together with the theoretical expression $B_s = 1/f_m(\omega)$, equation (7.29). The results for four subjects are shown separately. In all cases the following fitting procedure was used. The three frequency results for each subject were simultaneously fitted to the curve by normalizing to the lowest frequency point and by an initial choice of $\tau_m = 150$ $\mu$s. This assumes implicitly that the same nerves are excited at the three frequencies and that $\tau_m$ is independent of frequency over the frequency range used. This gives a first pass fit which can be improved for overall best fit of all three points by varying $\tau_m$. Following this procedure it is found that the $\tau_m$ values for the four volunteers, ■, ▲, ⬬ and ● are given by $\tau_m = 134$ $\mu$s, 139 $\mu$s, 149 $\mu$s and 159 $\mu$s respectively and could reflect a genuine variation in the nerve fibre characteristics among the volunteers. The average value of $\tau_m = 145.25$ $\mu$s. The fitting procedure gives rise to the horizontal shifts in the data points. The vertical error arises from experimental uncertainties in the measurement of $B_s$.

R Value Measurements

As a further test of the theory the magnetic field ratio $R$ was measured for sinusoidally modulated magnetic field stimuli at fundamental frequencies of 800 Hz and 1.3 kHz to those for trapezoidal stimuli at the same fundamental frequencies and with rise times of 89 $\mu$s and 55 $\mu$s respectively. The stimuli were applied for 20 ms in all cases. The same four volunteer subjects were tested at 800 Hz and three of these four tested again at 1.3 kHz. The results are the average of a number of individual measurements per subject, four at 800 Hz and eight at 1.3 kHz. Again the standard deviations for each subject data set were within 3% and as previously the stimulation threshold magnetic field when approached from above the threshold level was found to be 8% lower than when the threshold was approached from below. The results when approached from below the stimulation threshold are plotted in figure (7.5) together with the theoretical curve $R$ versus $\omega\tau_m$, equation (7.38), for different values of the parameter $k$. The horizontal displacements arise from the variation in $\tau_m$. The same values of $\tau_m$ are used for a given subject deduced from the results of figure (7.4). The data give a reasonable fit to the $k = 1.3$ curve.

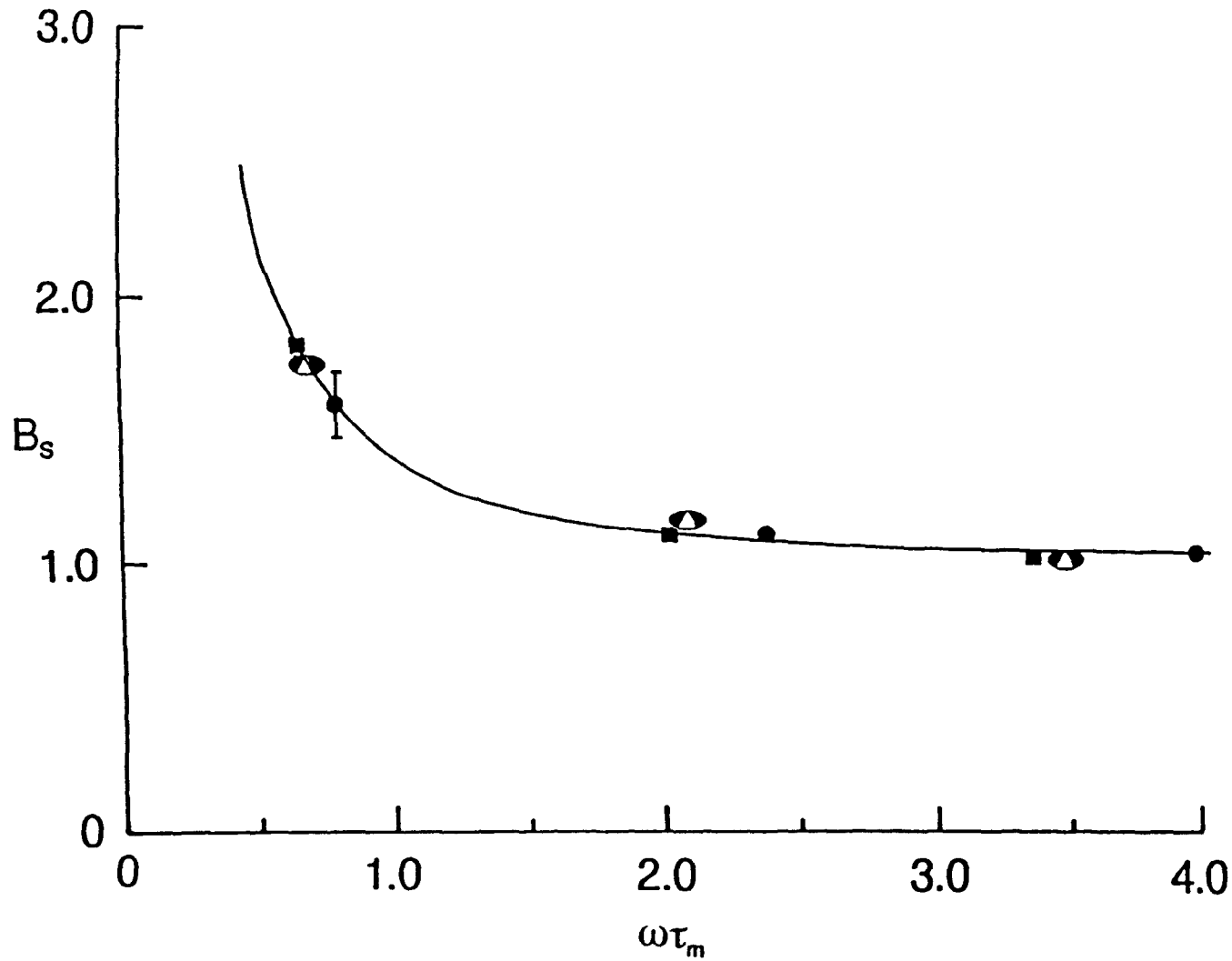


Figure 7.4: Graph of $B_s$ versus $\omega\tau_m$, equation (7.29) theoretical and measured.

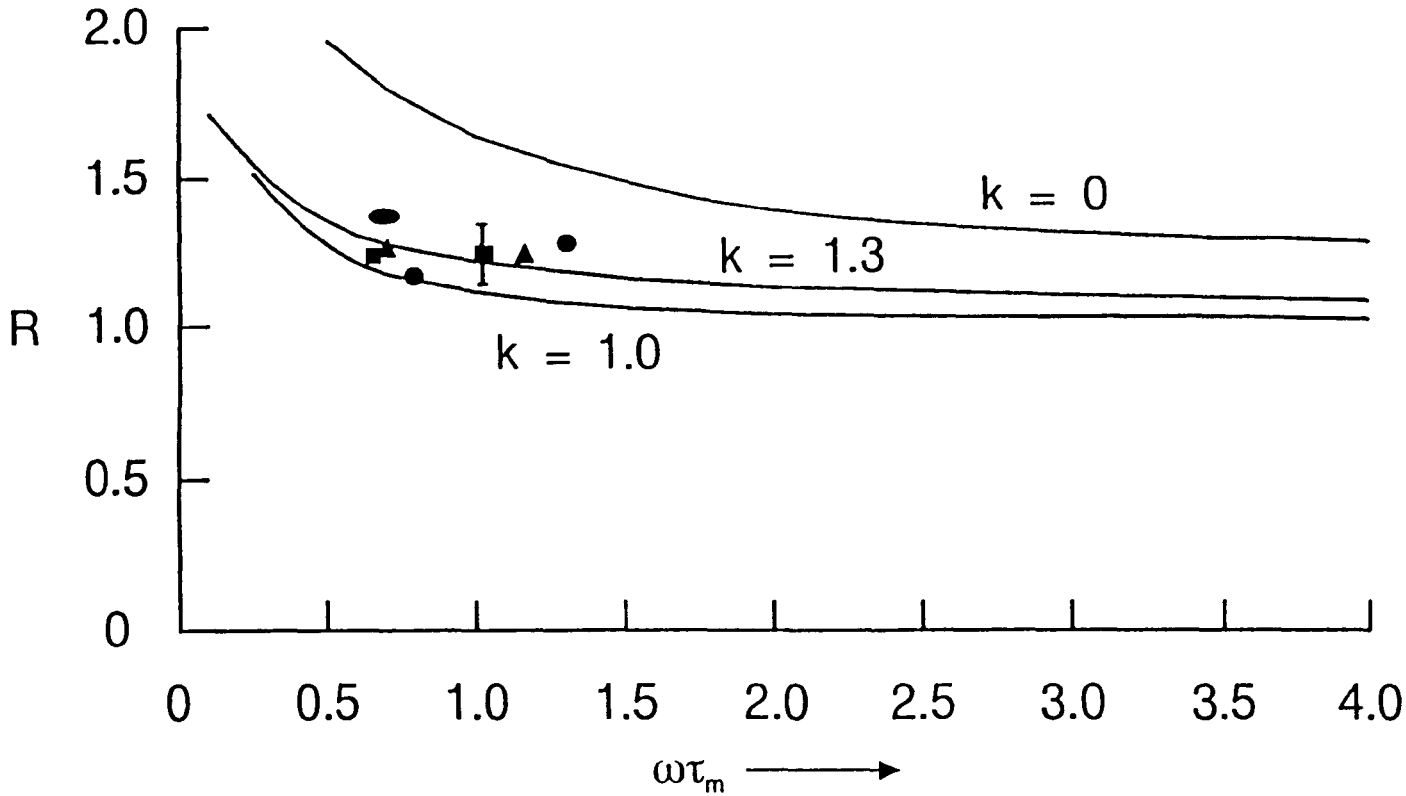


Figure 7.5: Graphs showing $R$ versus $\omega\tau_m$, for various values of the parameter $k$. Also plotted are the measured values of $R$ for the four subjects together with an estimate of the experimental accuracy.

## 7.8 The Empirical Value of $k$

Interestingly a value of $k = 0.76$ gives the same curve as $k = 1.3$. In both cases these values are many orders of magnitude smaller than would be predicted by substituting physical values into equations (7.15) and (7.16).

Clearly, further refinement of the theory is required with respect to this fact and at this point $k$ is used only to provide an empirical fit of theory to experimental data.

If $k$ is excluded all together i.e. $k = 0$ then the theory as it stands shows only a very slight advantage in using square wave modulation over sine wave modulation. This obtains only at very high frequencies. Experimental results however show that the advantage occurs at much lower frequencies than predicted. This is advantageous in imaging and choosing the value of $k = 1.3$ or $k = 0.76$ brings the theory into line with the experimental observations made so far.

As mentioned earlier the relative permeability and the conductivity of the sample are assumed to be frequency independent. If this is not the case then the value of $k$ will vary with frequency which will result in a much more complicated variation of the theory. Quantifying exactly what has been called the dispersive nature of the tissue is a very difficult process, dependent on many variables such as temperature, geometry, internal tissue/fat interfaces to name but a few.

The theory as it stands predicts the sinusoidal stimulus results with excellent correlation. The frequency dependence of the trapezoidal results, few as they are, are also well predicted. The problem comes when the two are compared to give the ratio $R$. In this case the "scaling effect" performed by $k$ must be used to bring the theory into line with the results. The difference between single sinusoidal stimulus and trapezoidal stimulus is that phase relationships, in the latter case, between components in the current waveform in the tissue are affected in some complex manner which as yet can only be partially explained by the theory developed so far.

## 7.9 Magnetic Field Rates

The values of peak $dB/dt$ used to elicit neural stimulation in these experiments are listed in table (7.2) and correspond to approach from below the stimulation threshold level. The data in table (7.2), although covering only two frequencies, show that the safety regulations based on either $t(dB/dt)$ or $t(dB/dt)^2$ do not seem to work.

The $dB/dt$ ratio for sine/trap has an average value of 0.56 for both 800 Hz and 1.3 kHz, and clearly illustrates that trapezoidal waveforms with higher $dB/dt$ values (almost double) produce the same stimulation threshold as does a much lower $dB/dt$ sinusoidal stimulation. Conversely, this means that when sinusoidal and trapezoidal waveforms have the same $dB/dt$, and

| Subject | $dB/dt$ (Pk) $Ts^{-1}$ | | $dB/dt$ Ratio | Area ratio | |
|---|---|---|---|---|---|
| | Sine | Trap | Sine/Trap | Sine/Trap | R |
| Fundamental Frequency 800 Hz | | | | | |
| ● | 1191 | 2255 | 0.53 | 0.87 | 1.18 |
| ▲ | 1114 | 1998 | 0.56 | 0.92 | 1.26 |
| ⬬ | 1076 | 1770 | 0.61 | 1.01 | 1.35 |
| ■ | 1025 | 1836 | 0.55 | 0.91 | 1.23 |
| Average | 1102 | 1970 | 0.56 | 0.93 | 1.25 |
| Fundamental Frequency 1.3 kHz | | | | | |
| ● | 1532 | 2641 | 0.58 | 0.96 | 1.29 |
| ▲ | 1525 | 2792 | 0.55 | 0.90 | 1.22 |
| ■ | 1369 | 2399 | 0.57 | 0.94 | 1.27 |
| Average | 1475 | 2611 | 0.56 | 0.93 | 1.26 |

Table 7.2: Recorded field rates of change necessary to reach the neural stimulation threshold in the wrist. Also listed are the magnetic field ratio $R$ and sine/trap area ratio under the half-period waveforms.

when the sinusoidal waveform just breaches the neural stimulation threshold, trapezoidal gradient modulation will always be roughly a factor of two below the threshold, thus making trapezoidal safer than sinewave gradient modulation. The question is can this fact be used to advantage in high speed imaging? Referring to table (7.2), the average area ratio for sinusoidal and trapezoidal waveforms is 0.93 at both 800 Hz and 1.3 kHz and is indicative of a small advantage for trapezoidal modulation. The theory outlined above suggests that this advantage will increase at higher fundamental frequencies and especially for squarer trapezoidal waveforms.

## 7.10 Whole-body EPI

The theory developed so far may be used to establish the switched gradient field limits below which magnetic stimulation does not breach the neural stimulation threshold. However, the geometry and design features of the coil will influence matters.

### 7.10.1 Gradient Coils

Cylindrical $G_z$ coils with z-axis coincident with the long axis of the patient are commonly used in MRI. With this type of coil it is easy to see how induced currents may be produced in the body circumference. Transverse gradients $G_x$ and $G_y$ are more complicated. In cylindrical transverse gradients with saddle geometry $G_x$ is produced from a set of inner current arcs which in the simplest case corresponds to one arc per quadrant. The current return path for each inner arc creates current loops which produce large transverse magnetic fields $B_x$. The inner arcs, of course, produce a magnetic field along the z-axis $B_z(x, y)$. The transverse fields might therefore be expected to induce currents within the subject. In more complicated cylindrical transverse gradient designs, more than one arc per quadrant is often employed, and nowadays complete distributed arc designs are commonly used. With such gradient designs the induced current paths in a subject are expected to be quite complex and to some extent follow the current paths within the gradient coil arcs themselves. In some early transverse gradient coil designs [28, 75], the current return paths were arranged in such a way that there is very little transverse field interaction with the subject.

### 7.10.2 Neural Stimulation - General Considerations

The range of $B_s$ over which peripheral neural stimulation may be expected in whole-body imaging may be approximated using equation (7.29). The difficulty in performing this calculation arises in choosing reliable values for the parameters $j_{s0}$, $\tau_m$, $\alpha$ and $\sigma$. There is also the question of which value of $r$ is appropriate. Using frog axon preparations, Hodgkin [73] has reported a value of $j_{s0} = 15.0$ Am$^{-2}$. Others [69, 70, 71] have reported much lower values. These results are obtained by direct coupling of electrodes. In the work on magnetically induced peripheral nerve stimulation $j_{s0}$ cannot be

measured absolutely. This is because the surrounding tissue characteristics enter the expression, equation (7.29), used to deduce $j_{s0}$. The best that can be done is to evaluate $j_s/\sigma\alpha$ which can be reduced to $j_{s0}/\sigma\alpha$ using equation (7.29) together with a value of $\tau_m$ deduced from experiment.

In their experiments on the human forearm, McRobbie and Foster [76] have reported the value of $j_s/\sigma\alpha = 36.66$ A $\Omega$ m$^{-1}$ for the induced current present during neural stimulation. The stimulating waveform used was a damped sinusoid with a frequency of 3 kHz which produced a peak value of $dB/dt =$ 2100 T s$^{-1}$ at stimulation. Using these values in equation (7.29) with an assumed value of $\tau_m = 150$ $\mu$s produces a value for $j_{s0}/\sigma\alpha = 12.26$ A $\Omega$ m$^{-1}$. Results presented here for the cases of sinusoidal stimulus at frequencies of 800 Hz and 1.3 kHz predict values of $j_{s0}/\sigma\alpha$ of 10.5 A $\Omega$ m$^{-1}$ and 10.9 A $\Omega$ m$^{-1}$ respectively using the measured average value, $\tau_m = 145.25$ $\mu$s.

### 7.10.3 Comparison with Experiment

Two groups have reported whole-body neural stimulation effects when driving their gradients at $dB/dt$ rates of 84.85 T s$^{-1}$ and 63 T s$^{-1}$ [26, 27]. One approach is therefore to use the measured results of the average value of $j_{s0}/\sigma\alpha = 11.3$ A $\Omega$ m$^{-1}$ from the work in this chapter and that of McRobbie and Foster to evaluate the current density contour radius in equation (7.29) for a uniform tissue sample placed in a uniform fluctuating magnetic field of given strength. However, equation (7.29) assumes a spatially uniform field and a homogeneous tissue sample.

What really matters in inducing current density to flow is the total magnetic flux coupling the specimen. This can be represented by $\int B_z(y,z)dydz$ or $\int B_y(z,x)dzdx$ or $\int B_z(x,y)dxdy$ for the x, y and z axes respectively. If the field is uniform then the flux is simply $BA$ where $A$ is the area. However, if the field varies it is possible to crudely approximate the flux by $< B_z(x,y) > A$ or $< B_x(y,z) > A$, where $< B_z(x,y) >$, etc. are spatial averages.

A better approach, which avoids making statements about absolute values, is to form ratios of quantities to be compared. For example, stimulation conditions in the arm and body, referred to with subscripts $a$, $b$ respectively. From equation (7.29)

$$\frac{r_b}{r_a} = \left[\frac{j_{s0b}\alpha_a\sigma_a}{j_{s0b}\alpha_b\sigma b}\right]\left\{\frac{1+\omega_b^2\tau_{mb}^2}{1+\omega_a^2\tau_{ma}^2}\right\}^{1/2} \times \left[\frac{\omega_a < B_{sa} >}{\omega_b < B_{sb} >}\right] \qquad (7.42)$$

where $< B_{sa} >$ and $< B_{sb} >$ refer to the spatially averaged mean stimulation fields. Using this equation it is possible to calculate the expected current density contour radius $r_b$ under different conditions.

In the work of Cohen et al [26] performed at a frequency $\nu = 1.4$ kHz, a peak value of $dB/dt = 86$ T s$^{-1}$ is reported to have produced neural stimulation.

This gradient is applied typically for 20 ms and corresponds to a maximum transverse field $B_x(0,z) = 9.78$ mT = 97.8 G. This maximum field occurred at $z = 0.34$ metres from the mid-plane of the gradient set. Their work also shows that the z-axis variation of $B_x(0,z)$ varies pretty well linearly up to the maximum point. If it is assumed that an average transverse field $< B_x >= 4.9$ mT acts uniformly within a circular flux contour, then from equation (7.42) the contour radius

$$r_b = 0.87 \left[ \frac{j_{s0b}\alpha_a\sigma_a}{j_{s0a}\alpha_b\sigma_b} \right] \tag{7.43}$$

In the theory presented here, it is not possible to make predictions for the anisotropy factor $\alpha$ other than to assume $\alpha_a = \alpha_b$. If $(j_{s0b}\sigma_a/j_{s0a}\sigma_b) = 1$, $r_b = 0.87$ m which means the current density contour length must be 5.46 m in order to produce neural stimulation. It seems clear that the implied flux coupling area and current density contour are far too large, bearing in mind the typical gradient coil dimensions and, more particularly, the subject dimensions.

The work of Budinger et al [27] reports neural stimulation effects in a z-gradient coil driven at 1.27 kHz when $dB/dt = 63$ T s$^{-1}$. Using equation (7.42) and a value of $< B_z >= 7.89$ mT deduced from [27], together with the measured average value of $\tau_m = 145.25$ $\mu$s, the induced current density contour radius in their experiments should be

$$r_b = 0.58 \left[ \frac{j_{s0b}\alpha_a\sigma_b}{j_{s0a}\alpha_b\sigma_b} \right] \tag{7.44}$$

for neural stimulation.

Since a z-gradient was used, $r_b$ must be of the order of 0.18 m. Taking this value and assuming $\alpha_a = \alpha_b$ gives the ratio $(j_{s0a}\sigma_b/j_{s0b}\sigma_a) = 3.2$. This in turn leads to a revised and more acceptable value of $r_b = 0.27$ m for the transverse field current density in the work of Cohen et al [26].

In both of the above cases , it seems clear that without making special assumptions about neural stimulation threshold values and tissue characteristics for the thighs and torso, relative to those of the arm, the expected current density contour paths cannot be sustained within the subject for the values of the gradient field parameters disclosed in these publications. Furthermore, in the paper by Bourland et al [68] which is also concerned with peripheral nerve stimulation in z-gradients in a whole-body coil, similar conclusions are drawn, namely that the quoted gradient strengths are simply not large enough to evoke neural stimulation in the body without making the additional assumption that $(j_{s0a}\sigma_b/j_{s0b}\sigma_a) > 1$. These results lead one to consider alternative explanations of the results reported in references [26, 27, 68].

### 7.10.4 Coil-Subject Capacitive Coupling

The change in capacitance across a spare transverse gradient assembly was measured when an adult subject was placed between its coils. The magni-

tude of this change was approximately 10 pF. The coil design is a single inner arc per quadrant arrangement. For a distributed arc system the capacitance between the coil system and patient could be as much as 100 pF. For gradient coils with an inductance of 1 mH operating in a resonant mode at 1.4 kHz which pass a current of 300 A, the peak voltage across the coils is 2.64 kV. This means that between the two halves of the gradient set displacement currents of up to 2.3 mA could flow through the body of a patient. such currents would be most likely to be concentrated in those parts of the anatomy closest to the gradient coil conductors and in protuberances like the nose and feet where the electric fields might be strongest. The description of reported whole-body stimulation effects and the localized nature of the reported effects could be consistent with electric field rather than magnetic field neural stimulation. Indeed, in the paper by Bourland et al [68], stimulation effects were experienced in the heel of the foot in some subjects, a result hardly consistent with magnetic neural stimulation bearing in mind the cross-sectional area of the foot. If electric fields are responsible for the reported neural stimulation sensations, it will be a straightforward matter to introduce an earthed Faraday screen between patient and gradient coil, thereby completely obviating displacement currents within the subject.

### 7.10.5 EPI Parameters

In EPI the relationship between gradient $G$ and maximum imaging field $B'_m$ is given by

$$B'_m = Gx_m = \frac{M^2}{2\gamma T_r} \tag{7.45}$$

where $M$ is the total pixel array size, $\gamma$ is the magnetogyric ratio and $T_r$ the imaging or exposure (acquisition) time. Equation (7.45), $B'_m$ or $G$ versus $M$, is plotted in figure (7.6) for various values of $T_r$. The maximum object field dimension is 192 mm along both the frequency and phase encoding directions, $x_m$, $y_m$. For a square array of 256 x 256 pixels this gives a spatial resolution $\Delta x = 1.5$ mm. It is emphasized that equation (7.45) applies for squarewave gradient modulation. For sinusoidal modulation $B_m$ must be multiplied by $\pi/2$.

The uncertainties in currently available whole-body magnetic stimulation results make it difficult to place unequivocal limits on gradient parameters for EPI. In addition, the average stimulation field, $< B_s >$ can be greater than $B'_m$ and depends on gradient coil design, and also on whether $B_s$ is transverse or axial. In general

$$< B_s >= SB'_m \tag{7.46}$$

where $S$ is a scaling factor with a value which is typically 0.5 but could be as low as 0.1 for some transverse gradient designs [75], and as high as 2.0 for typical z-gradient coils.

In view of the uncertainties referred to above it is best to take the quotient $(j_{s0b}\alpha_a\sigma_a/j_{s0a}\alpha_a\sigma_a) = 1$ rather than 3.2. Using the arm stimulation results

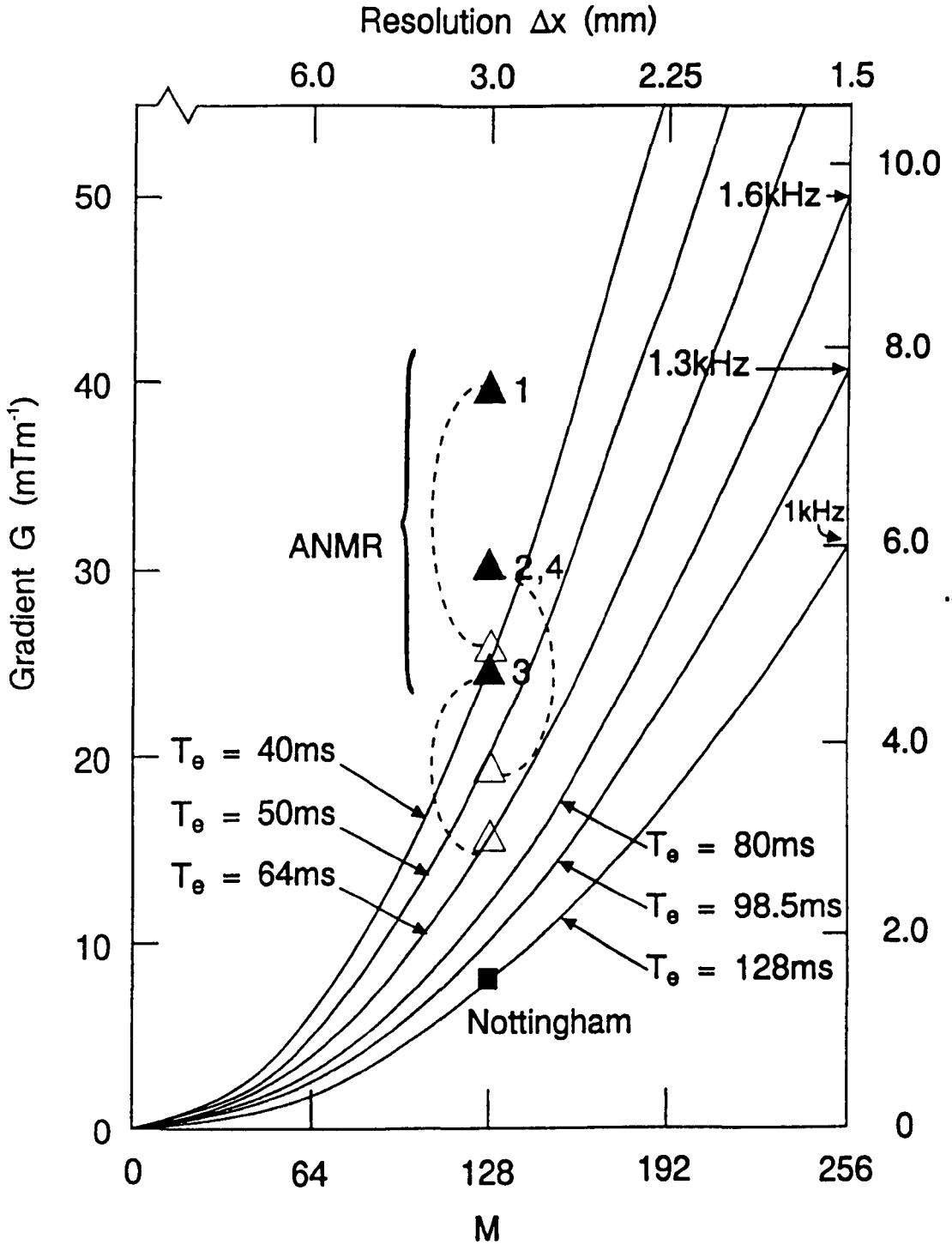


Figure 7.6: Parametric graphs of equation (7.45) showing the required peak squarewave gradient amplitudes for echo-planar imaging with an array of $M^2$ pixels spanning an object field 38.4 × 38.4 cm$^2$. The snapshot imaging time $T_e$ is varied from 40 – 128 ms. The experimental conditions currently used for EPI at Nottingham are also shown (solid square). The trapezoidally modulated experiments were performed with a frequency of 0.50 kHz. ANMR (refs. [55, 77, 78, 79]) (closed triangles) refer to sinusoidal experiments covering a range of frequencies, resolutions and imaging times. The coupled open triangles are the values of $B_m$ which would obtain if square wave modulation were used.

at 800 Hz and assuming that $\tau_{ma} = \tau_{mb}$ in equation (7.42) it is found for $r_a = 0.024$ m and $r_{sb} = 0.18$ m that at a frequency $\nu_b = 1.6$ kHz $< B_{sb} >= 22$ mT = 220 G, whereas for $\nu_b = \infty$, the threshold drops to $< B_{sb} >= 18.3$ mT = 183 G. Thus for $\nu_b = 1.6$ kHz and in the worst case that $S = 2$, $B_m^i = 11$ mT = 110 G which is just above the 9.8 mT = 98 G required for image arrays of 256 × 256 pixels acquired in an exposure time, $T_e = 80$ ms using square wave gradient modulation. A quotient value of 3.2 reduces $B_m^i$ to 3.4 mT = 34 G which would limit the array size to $M \leq 192$ depending on $T_e$.

Interestingly, for both examples, the corresponding sinusoidal EPI experiment would take $B_m$ over the stimulation threshold, thus rendering it unworkable for patient imaging. Of course, as $T_e$ is shortened it will in general be necessary to increase the gradient modulation frequency in order to maintain the image array size. This will result in a lowering of $B_s$. However, using equations (7.42) to (7.46) it is possible to optimize EPI experiments for array size and spatial resolution without transgressing the stimulation threshold.

All recent EPI work performed at Nottingham follows the $T_e = 128$ ms curve which for a $128^2$ pixel array requires $B_m^i = 1.6$ mT = 16 G, which is well below the worst case threshold discussed above.

Also included in figure (7.6) are experimental conditions published by others [77, 55, 78, 79] for sinusoidally modulated EPI. Their data (closed triangles numbered 1−4) are for 3 mm spatial resolution in all cases. The coupled open triangles are the values of $B_m^i$ which would obtain if square wave modulation had been used.

## 7.11 Conclusions on Experimental and Theoretical Findings

Using a linear electrical model of a neural node, it has been shown that the critical factor in considering the neural stimulation threshold under magnetic stimulation is the maximum change in the time varying field $B_m$ rather than the product $(dB/dt)_{max}t$. This situation obtains at frequencies of around 1.6 − 2.0 kHz or above. At these frequencies, therefore, the stimulation field $B_s$ is substantially independent of frequency. This means that the threshold stimulation current density, which is proportional to the time integral over the time derivative of the modulation gradient waveform, is independent of $dB/dt$. It therefore follows that square waveforms with very fast rise times can be used in imaging without sacrificing gradient strength. This confers a considerable advantage on trapezoidal modulation over sinusoidal modulation, since for equivalent imaging regimes, the area under the half-period sine and trapezoid must be equal. This in turn means that ideally $B_m^S/B_m^T = \pi/2$ so that when a trapezoidal EPI experiment is operating at just below the stimulation threshold, the equivalent sine experiment will always exceed the threshold limit, thereby rendering it unsuitable for clinical imaging. This situation is expected to obtain for single shot EPI when the image matrix size is given by $128 \leq M \leq 256$. The precise value of $M$ attainable without

transgressing the neural stimulation threshold will depend on a number of factors including the value of $T_e$, the gradient coil design and configuration and especially the relevant value of the quotient $j_{s0b}\alpha_a\sigma_a/j_{s0a}\alpha_b\sigma_b$.

## 7.12 Future Investigation

It is clear, due to the unusual value of the constant $k$, that certain non-linearities are present which cannot be accounted for at this stage. To verify the theory more completely, more information is required on the physical nature and behaviour of the current density induced within the tissue.

The current may flow by ionic conduction for which a conducting medium is required. Values quoted for conductivity of tissue vary widely and usually assume a homogeneous tissue sample. In the body there are different layers consisting of skin, fat, muscle fibre etc. Ionic flow may be restricted preferentially to one layer which could induce current flow in an adjacent layer by induction again.

Another way in which current may flow in the tissue is by polarization transfer. In this process individual cells or compartments of muscle fibre behave like small capacitors with the current flow being effected by the transfer of charge between fibres. This property of the tissue would show low resistance to AC current but may show a much higher resistance to DC current. The current density would then depend on the size of each compartment and the frequency of the stimulus. It may be that the current density in the tissue by magnetic induction has a maximum value in this case.

It has also been assumed that the same nerve fibres have been excited at each frequency. The sizes of nerve fibres present in the body vary and it is not unlikely that the frequency response and $\tau_m$ values of these may also vary. Since the nerve impulse is either an "on" or "off" process (in some ways almost digital) it follows that different nerve fibres or combinations of nerve fibres firing together or in systematic response to external stimulus, could be responsible for the range of sensations encountered.

Clearly many unknowns are present which the simple theoretical approach outlined in this chapter cannot accommodate. Empirically, however, the theory works well to a reasonable approximation. For further verification, measurements of the ratio $R$ at higher values of $\omega\tau_m$ are essential. In addition, the experimental comparisons of sinusoidal stimulus to trapezoidal stimulus need to be investigated in a whole-body application. These measurements were not possible within the time scale allowed for this project.

# Chapter 8: Conclusions

The work presented in this thesis outlines the further progress made towards faster and more efficient imaging of the human body using MRI.

In chapter 5 are described the improvements made in EVI which have resulted in larger image matrix sizes and the first ever "snapshot" EVI images of the human torso. The amount of data acquired in an EVI experiment, during the acquisition times used, puts the technique into the hyper-fast bracket of imaging modalities.

Using a single-pass modulus technique the feasibility of spin echo EVI (SE-EVI) and zoomed EVI (ZEVI) have also been demonstrated. Technical restraints and future hardware requirements have also been addressed. The ultimate limit to EVI however may be determined by the physiological effects, on the patient, of the rapidly modulated gradients used. This does not rule out the possibility of using EVI in the study of non-biological systems such as porous rock samples where gradient strength and RF power deposition are not a concern. In all the experiments performed on volunteers up to this point, no sensory stimulation effects have been observed.

Of the technical limitations reached in the EVI experiments, rapid modulation of high amplitude imaging gradients has been addressed in more detail. The solution described in chapter 6 is a multi-mode resonant gradient driver circuit which uses a filter network, coupled in series with the gradient coil, and allows simultaneous resonance of the coil at the harmonics required to synthesize a trapezoidal current/magnetic field gradient waveform. The net effect of this, in application to whole body imaging, is a reduction in the number of gradient amplifiers required and a reduction in the peak gradient field experienced by the patient as compared to the equivalent resonant sinusoidal gradient modulation. The design procedure employed theoretical treatment and simulation to show that trapezoidal waveforms can be synthesized using relatively few harmonics.

The filter design was tested on a small scale circuit and applied in full scale to the whole-body gradient assembly to provide 3 mm by 3 mm resolution images of the body of a volunteer. The data acquisition time was just 80 ms and the number of gradient amplifiers required was reduced by a half.

The multi-mode resonant gradient driver circuit was then used to investigate the stimulatory effects of rapidly modulated magnetic fields on the human forearm. In chapter 7 the theory of stimulation is described and used in conjunction with experimental data taken at modulation frequencies of 800 Hz and 1.3 kHz for both sine and trapezoidal waveforms. It is shown that the neural stimulation threshold on the forearm, under magnetic stimulation,

is more dependent on $B_m$, the maximum change in the time varying field, rather than the product $(dB/dt)_{max}t$. This indicates an advantage to using square gradient waveforms with very fast risetimes in imaging instead of sinusoidally modulated gradients.

The results obtained on the forearm correlate well with other published results. When compared with results obtained on the whole-body by other workers, problems arise over geometry and tissue characteristics. In order to make comparisons, therefore, certain assumptions were required making it difficult to unequivocally state whole-body thresholds for the waveforms discussed.

Further research is required in this area to determine whether the results measured on the forearm (particularly in the case of the trapezoidal measurements) can be achieved or improved upon in the whole-body case. Measurements at higher frequencies using faster risetime trapezoidal waveforms are also required in order to fully test the outlined theory. Due to the empirical value of $k$ required to compare theory and experimental results, it is clear that non-linearities and, as yet, unforseen conduction mechanisms are present in the tissue surrounding the nerve fibre itself.

Alternative mechanisms for the reported whole-body stimulation levels have also been presented.

# Appendix A: RES7

```
  10 DIM Z(4,1),ANS(1000,1),TMP(2,1),ARM1(2,1),ARM2(2,1),ARM3(2,1),LL(2,1),LL1(
2,1),LL2(2,1)
  20 DIM IMP(2,1)
  30 *KEY 0 "L.20,139!M"
  40 L0=107*10^-6
  50 L1=107*10^-6
  60 CA=2.32*10^-6
  70 CB=6.17*10^-6
  80 CC=55.91*10^-6
  90 C3=26.30*10^-6
 100 C5=9.47*10^-6
 110 C7=4.83*10^-6
 120 R0=0.01
 130 R1=0.10
 140 r3=10000
 150 R=50
 160 FMIN=1
 170 FMAX=8000
 180 STPS=100
 190 YSCAL=20
 200 G=0
 210 FOR F=FMIN TO FMAX STEP (FMAX-FMIN)/STPS
 220   W=2*PI*F
 230   PROCUNITZ:PROCLL(R0,L0,C7):ARM1(1,0)=IMP(1,0):ARM1(1,1)=IMP(1,1)
 240   PROCUNITZ:PROCLL(R0,L0,C5):ARM2(1,0)=IMP(1,0):ARM2(1,1)=IMP(1,1)
 250   PROCUNITZ:PROCLL(R0,L0,C3):ARM3(1,0)=IMP(1,0):ARM3(1,1)=IMP(1,1)
 260   TMP(1,0)=ARM1(1,0)+ARM2(1,0)+ARM3(1,0)
 270   TMP(1,1)=ARM1(1,1)+ARM2(1,1)+ARM3(1,1)
 280   PROCUNITZ:PROCSERIES(0,-1/(W*CC)):PROCPARLL(TMP(1,0),TMP(1,1))
 290   PROCIMP:ARM1(1,0)=IMP(1,0):ARM1(1,1)=IMP(1,1)
 300   REM*************************************************************
 310   PROCUNITZ:PROCLL(R0,L0,C7):ARM2(1,0)=IMP(1,0):ARM2(1,1)=IMP(1,1)
 320   PROCUNITZ:PROCLL(R0,L0,C5):ARM3(1,0)=IMP(1,0):ARM3(1,1)=IMP(1,1)
 330   TMP(1,0)=ARM2(1,0)+ARM3(1,0)
 340   TMP(1,1)=ARM2(1,1)+ARM3(1,1)
 350   PROCUNITZ:PROCSERIES(0,-1/(W*CB)):PROCPARLL(TMP(1,0),TMP(1,1))
 360   PROCIMP:ARM2(1,0)=IMP(1,0):ARM2(1,1)=IMP(1,1)
 370   REM*************************************************************
 380   PROCARMIMP(R0,L0,C7,CA)
 390   ARM3(1,0)=IMP(1,0):ARM3(1,1)=IMP(1,1)
 400   REM*************************************************************
 410   PROCUNITZ
 420   PROCPARLL(ARM1(1,0),ARM1(1,1))
 430   PROCPARLL(ARM2(1,0),ARM2(1,1))
 440   PROCPARLL(ARM3(1,0),ARM3(1,1))
 450   PROCPARLL(0,-1/(W*C7))
 460   PROCIMP
 470   ANS(G,0)=IMP(1,0)+R1
 480   ANS(G,1)=IMP(1,1)+(W*L1)
 490   G=G+1
 500 NEXT
 510 MODE0:MOVE 0,500:DRAW 1000,500:MOVE 0,500
 520 FOR J=0 TO 1000 STEP 1000/STPS
 530   K=J*STPS/1000
 540   PLOT 5,J,SQR(ANS(K,0)^2+ANS(K,1)^2)*500/YSCAL+500
 550 NEXT
 560 MOVE 0,500
 570 FOR J=0 TO 1000 STEP 1000/STPS
 580   K=J*STPS/1000
 590   PLOT 5,J,DEG(ATN(ANS(K,1)/ANS(K,0)))*4+500
```

```
600 NEXT
610 PROCCURSOR
620 END
630 DEFPROCSERIES(Z0,Z1)
640 Z(2,0)=Z0*Z(1,0)-Z1*Z(1,1)+Z(2,0)
650 Z(2,1)=Z0*Z(1,1)+Z1*Z(1,0)+Z(2,1)
660 Z(4,0)=Z0*Z(3,0)-Z1*Z(3,1)+Z(4,0)
670 Z(4,1)=Z0*Z(3,1)+Z1*Z(3,0)+Z(4,1)
680 ENDPROC
690 DEFPROCPARLL(A,B)
700 Z0=A/(A^2+B^2):Z1=-B/(A^2+B^2)
710 Z(1,0)=Z(1,0)+Z0*Z(2,0)-Z1*Z(2,1)
720 Z(1,1)=Z(1,1)+Z0*Z(2,1)+Z1*Z(2,0)
730 Z(3,0)=Z(3,0)+Z0*Z(4,0)-Z1*Z(4,1)
740 Z(3,1)=Z(3,1)+Z0*Z(4,1)+Z1*Z(4,0)
750 ENDPROC
760 DEF PROCCURSOR
770 MOVE500,0:PLOT 6,500,1000:X=500
780 S$=INKEY$(10)
790 IF S$="X" PROCSTP(1)
800 IF S$="Z" PROCSTP(-1)
810 IF S$="E" END
820 IF S$="P" PROCVALS
830 IF S$="G" PROCGDUMP
840 GOTO 780
850 ENDPROC
860 DEF PROCSTP(A)
870 MOVE X,0:PLOT 6,X,1000
880 X=X+A*2:IF X=1000 X=999
890 MOVE X,0:PLOT 6,X,1000
900 ENDPROC
910 DEF PROCVALS
920 FREQ=(X*(FMAX-FMIN)/1000)+FMIN
930 GPOS=STPS*X/1000
940 PRINTTAB(0,25)"FREQ = ";FREQ
950 PRINT"IMP = ";SQR(ANS(GPOS,1)^2+ANS(GPOS,0)^2)
960 PRINT"PHASE = ";DEG(ATN(ANS(GPOS,1)/ANS(GPOS,0)))
970 ENDPROC
980 DEF FNMDL =(Z(3,0)^2+Z(3,1)^2)
990 DEF PROCIMP :REM CALC. IMPEDANCE &STORE IN IMP(1,0)&(1,1)
1000 IMP(1,0)=(Z(1,0)*Z(3,0)+Z(1,1)*Z(3,1))/FNMDL
1010 IMP(1,1)=(Z(3,0)*Z(1,1)-Z(1,0)*Z(3,1))/FNMDL
1020 ENDPROC
1030 DEF PROCLL(RP,LP,CP):REM PARLL. RES CCT
1040 PROCUNITZ
1050 PROCPARLL(0,-1/(W*CP))
1060 PROCPARLL(RP,W*LP)
1070 PROCIMP
1080 ENDPROC
1090 DEF PROCARMIMP(RP,CP,LP,CS):REM ARM IMP.
1100 PROCLL(RP,CP,LP)
1110 TMP(1,0)=IMP(1,0):TMP(1,1)=IMP(1,1)
1120 PROCUNITZ
1130 PROCSERIES(TMP(1,0),TMP(1,1))
1140 PROCPARLL(0,-1/(W*CS))
1150 PROCIMP
1160 ENDPROC
1170 DEF PROCUNITZ
1180 FOR I=1TO4:Z(I,0)=0:Z(I,1)=0:NEXT
1190 Z(1,0)=1:Z(4,0)=1
1200 ENDPROC
1210 DEF PROCGDUMP
1220 *FX5,1
1230 *GDUMP 0 0 1 1
1240 *FX5,0
1250 ENDPROC
```

# Appendix B: Microspice Simulation For 5th Order Filter Network

```
 ++ Microspice 1.6 ++

User: Dept Physics, Univ Nottingham

C 1 2 7.8U
C 1 4 6.9U
C 4 2 7.8U
L 4 5 130U
R 5 2 0.2
C 1 6 60U
C 6 8 21.6U
L 6 7 130U
R 7 8 0.2
C 8 2 7.8U
L 8 9 130U
R 9 2 0.2
L 2 3 130U
R 3 0 0.2
I 1 0 AC 10
AC 1000 5000 LIN 5
PRINT AC VM(1,2) VM(1,4) VM(1,6) VM(1,0)
```

| Freq. | VM1,2 | VM1,4 | VM1,6 | VM1,0 |
|---|---|---|---|---|
| 1000 | 9.299 | 9.654 | 24.45 | 5.998 |
| 2000 | 100.8 | 121.1 | 37.08 | 113.7 |
| 3000 | 24.72 | 48.6 | 0.7131 | 5.942 |
| 4000 | 29.3 | 48.19 | 4.333 | 59.02 |
| 5000 | 40.2 | 2.212 | 0.2547 | 5.892 |

```
run complete   49.5 secs
```

# Appendix C: Laplace Transformation

$$
\begin{aligned}
j(t)r_m &= j_1(t)r_m + \frac{1}{C_m}\int j_1(t)\,dt \\
j(t) &= j_1(t) + \frac{1}{r_m C_m}\int j_1(t)\,dt \\
J(p) &= J_1(p) + \left(\frac{1}{r_m C_m}\right)\frac{1}{p}J_1(p) \\
\frac{1}{r_m C_m} &= \tau_m^{-1} \\
J_1(p) &= J(p)\left[1 + \frac{(\tau_m^{-1})}{p}\right]^{-1} \\
&= J(p)\left[\frac{1}{1 + (\tau_m^{-1})/p}\right] \\
&= J(p)\left[\frac{p}{(\tau_m^{-1}) + p}\right] \\
&= J(p)\left[1 - \frac{(\tau_m^{-1})}{(\tau_m^{-1}) + p}\right] \\
&= J(p) - \left[\frac{(\tau_m^{-1})}{(\tau_m^{-1}) + p}\right] J(p) \\
&= J(p) - (\tau_m^{-1})\int_0^\infty \frac{e^{-pt}}{(\tau_m^{-1}) + p} j(t)\,dt \\
&= J(p) - (\tau_m^{-1})\int_0^\infty \frac{e^{-(p+(\tau_m^{-1}))t'}}{(\tau_m^{-1}) + p} e^{(\tau_m^{-1})t'} j(t')\,dt' \\
&= J(p) - (\tau_m^{-1})\int_0^\infty \int_{t'}^\infty e^{-((\tau_m^{-1})+p)t} e^{(\tau_m^{-1})t'} j(t')\,dt\,dt' \\
&= J(p) - (\tau_m^{-1})\int_0^\infty \int_0^t e^{-((\tau_m^{-1})+p)t} e^{(\tau_m^{-1})t'} j(t')\,dt'\,dt \\
&= J(p) - (\tau_m^{-1})\int_0^\infty \int_0^t e^{-(\tau_m^{-1})t} e^{(\tau_m^{-1})t'} e^{-pt} j(t')\,dt'\,dt \\
&= J(p) - (\tau_m^{-1})\int_0^\infty \int_0^t e^{-(\tau_m^{-1})t} e^{(\tau_m^{-1})t'} j(t')\,dt'\,e^{-pt}\,dt \\
&= \int_0^\infty \left[j(t) - (\tau_m^{-1})e^{-(\tau_m^{-1})t}\int_0^t e^{(\tau_m^{-1})t'} j(t')\,dt'\right] e^{-pt}\,dt \\
\int_0^\infty j_1(t)e^{-pt}\,dt &= \int_0^\infty \left[j(t) - (\tau_m^{-1})e^{-(\tau_m^{-1})t}\int_0^t e^{(\tau_m^{-1})t'} j(t')\,dt'\right] e^{-pt}\,dt \\
j_1(t) &= j(t) - (\tau_m^{-1})e^{-(\tau_m^{-1})t}\int_0^t e^{(\tau_m^{-1})t'} j(t')\,dt'
\end{aligned}
$$

# Bibliography


[1] Bloch F., Hansen W.W., Packard M.E.,
Phys. Rev. **69**, 127 (1946)

[2] Purcell E.M., Torrey H.C., Pound R.V.,
Phys. Rev. **69**, 37 (1946)

[3] Knight W.D.,
Phys. Rev. **76**, 1259 (1949)

[4] Dickinson W.C.,
Phys. Rev. **77**, 736 (1950)

[5] Proctor W.G., Yu F.C.,
Phys. Rev. **77**, 717 (1950)

[6] Hahn E.,
Phys. Rev. **80**, 580 (1950)

[7] Gabillard R.,
Phys. Rev. **85**, 694 (1952)

[8] Damadian R.,
Science **171**, 1151 (1971)

[9] Bowman R.L., Kudravcev V.,
IRE Trans. Med. Electron. **ME6**, 267 (1959)

[10] Lauterbur P.C.,
Nature **242**, 190 (1973)

[11] Mansfield P., Grannell P.K.,
J. Phys. C **6**, L422 (1973)

[12] Mansfield P., Maudsley A.A.,
J. Phys. C **9**, L409 (1976)

[13] Damadian R., Goldsmith M., Minkoff L.,
Physiol. Chem. Phys. **10**, 285 (1978)

[14] Garroway A.N., Grannell P.K., Mansfield P.,
J. Phys. C **7**, L457 (1974)

[15] Kumar A., Welti D., Ernst R.R.,
J. Mag. Res. **18**, 69 (1975)

[16] Edelstein W.A., Hutchison J.M.S., Johnson G., Redpath T., Phys. Med. Biol. **25**, 751 (1980)

[17] Mansfield P., J. Phys. C: Solid State Phys. **10**, L55 (1977)

[18] Hasse A., Frahm J., Matthaei D., Hanicke W., Merboldt K.D., J. Mag. Res. **67**, 256 (1986)

[19] Turner R., J. Phys. D: Appl. Phys. **19**, L147 (1986)

[20] Mansfield P., Chapman B., J. Mag. Res. **72**, 211 (1986)

[21] Turner R., J. Phys. E: Sci. Instrum. **21**, 948 (1988)

[22] Aldeman D.W., Grant D.M., J. Mag. Res. **36**, 447 (1979)

[23] Hayes C.E., Edelstein W.A., Schenck J.F., Mueller D.M., Eash M., J. Mag. Res. **63**, 622 (1983)

[24] Mansfield P., McJury M.J., Glover P., Meas. Sci. Technol. **1**, 1052 (1990)

[25] Mansfield P., McJury M.J., Glover P., Clemence M., Mag. Res. Med. **17**, 10 (1991)

[26] Cohen M.S., Weisskoff R.M., Rzedzian R.R., Kantor M.L., Mag. Res. Med. **14**, 409 (1990)

[27] Budinger T.F., Fischer H., Hentschel D., Reinfelder H.E., Schmitt F., Proc. 9th Ann. Mtg. SMRM, New York **1**, 276 (1990)

[28] Mansfield P., Morris P.G., "NMR Imaging in Biomedicine", Academic Press, New York (1982)

[29] Slichter C.P., "Principles of Magnetic Resonance", Harper and Row, New York and London (1963)

[30] Abragam A., "The Principles of Nuclear Magnetism", Oxford Univ. Press, London (1961)

[31] Farrar T.C., Becker E.D.,
"Pulse and Fourier Transform NMR; Introduction to Theory and Methods", Academic Press, New York and London (1971)

[32] Chen C.N., Hoult D.I.,
"Biomedical Magnetic Resonance Technology", Adam Hilger, Bristol and New York (1989)

[33] Morris P.G.,
"Magnetic Resonance Imaging in Medicine and Biology", Oxford Univ. Press (1986)

[34] Turner R.,
J. Phys. E: Sci. Instrum. **18**, 875 (1985)

[35] Morris P.G., McIntyre D.J.O., Rourke D.E.,
Conference on "Spatially Determined NMR", University of Cambridge, December (1989)

[36] Ljunggren S.,
J. Mag. Res. **54**, 338 (1983)

[37] Banwell C.N.,
"Fundamentals of Molecular Spectroscopy", McGraw-Hill (1983)

[38] Bracewell R.N.,
"The Fourier Transform and its Applications", McGraw-Hill, (1978)

[39] Hinshaw W.S.,
Phys. Lett. A **48**, 87 (1974)

[40] Margosian P., Schmitt F., Purdy D.,
Health Care Instrum. **1**, 195 (1986)

[41] Ernst R.R., Morgan R.E.,
Mol. Phys. **26**, 49 (1973)

[42] Guilfoyle D.N., Blamire A.M., Gibbs P., Mansfield P.,
7th Ann. Congress, Euro Soc. Mag. Res. Med. & Biol., Strasbourg, May 2-5 (1990) p 436

[43] Chapman B., Turner R., Ordidge R.J., Doyle M., Cawley M., Coxon R., Glover P., Mansfield P.,
Mag. Res. Med **5**, 246 (1987)

[44] Howseman A.M., et al.,
Brit J. Radiol. **61**, 822 (1988)

[45] Mansfield P.,
"Principles of NMR Imaging", Review Article (1988)

[46] Mansfield P.,
J. Phys. E: Sci. Instrum. **21** (1988)

[47] Ordidge R.J., et al.,
Mag. Res. Med. **8**, 110 (1988)

[48] Ordidge R.J., et al.,
Mag. Res. Med. **10**, 227 (1989)

[49] Stehling M.K., et al.,
Radiology **170**, 257 (1989)

[50] Ordidge R.J., Mansfield P.,
U.S. Patent 4,509,015 (1985)

[51] Howseman A.M.,
Thesis, University of Nottingham (1988)

[52] Faranzeh F., Riederer S.J., Pelc N.J.,
Mag. Res. Med. **14**, 123 (1990)

[53] Johnson G., Hutchison J.M.S.,
J. Mag. Res. **63**, 14 (1990)

[54] Stehling M.K., Ordidge R.J., Coxon R., Mansfield P.,
Mag. Res. Med. **13** 514 (1990)

[55] Pykett I.L., Rzedzian R.R.,
Mag. Res. Med. **5**, 563 (1987)

[56] Mansfield P., Ordidge R.J., Coxon R.,
J. Phys. E: Sci. Instrum. **21**, 275 (1988)

[57] Blamire A.M.,
Thesis, University of Nottingham (1990)

[58] Mansfield P., Howseman A.M., Ordidge R.J.,
J. Phys. E: Sci. Instrum. **22**, 324 (1989)

[59] Stehling M.K.,
Thesis, University of Nottingham (1989)

[60] Coxon R.,
"Programmable Waveform Controller Users Reference Manual", Internal Document: Physics Department, University of Nottingham (1982)

[61] Guilfoyle D.N., Mansfield P.,
Mag. Res. Med **2**, 479 (1985)

[62] Coxon R., Mansfield P.,
Proc. 8th Ann. Mtg. SMRM, Abstract 361 (1989)

[63] Mansfield P., Harvey P.R.,
Proc. 8th Ann. Congress, Euro Soc. Mag. Res. in Med. & Biol., Zurich, April 18-21 (1991) p. 264

[64] Mansfield P., Coxon R.,
U.K. Patent GB 2184625B (1989)

[65] Macovski A., Meyer C.,
Proc. 6th Ann. Mtg. SMRM, New York, 1 499 (1987)

[66] Paul Glover et al,
To be published

[67] Grover F.W.,
"Inductance Calculations", D. Van Nostrand Company Inc. (1946)

[68] Bourland J.D., Nyenhuis J.A., Mouchowar G.A., Geddes L.A.,
Proc. 9th Ann. Mtg. SMRM, New York WIP, 1157, (1990)

[69] Reilly J.P.,
Med. Biol. Eng. Comput. **27**, 101 (1989)

[70] Reilly J.P.,
"Peripheral Nerve Stimulation and Cardiac Excitation by Time Varying Magnetic Fields: A comparison Of Thresholds".
The office of Science and Technology, Centre for Devices and Radiological Health, US Food and Drug Administration (1990)

[71] NRPB Revised Guidlines,
Brit. J. Radiol. **56**, 974 (1983)

[72] Mansfield P., Blamire A.M., Coxon R., Gibbs P., Guilfoyle D.N., Harvey P.R., Symms M.,
Phil. Trans. Roy. Soc. **A 33**, 495 (1990)

[73] Hodgkin A.L.,
"The Conduction of the Nervous Impulse", Liverpool Univ. Press (1967)

[74] Mansfield P., Harvey P.R., Coxon R.,
Meas. Sci. Technol. (1991)

[75] Bangert V., Mansfield P.,
J. Phys. E. **15**, 235 (1982)

[76] McRobbie D., Foster M.A.,
Clin. Phys. Physiol. Meas. **5**, 67 (1984)

[77] Weisskoff R.M., Crawley A.P., Wedeen V.,
Proc. 9th Ann. Mtg. SMRM, New York **1**, 398 (1990)

[78] Weisskoff R.M., Dalcanton J.J., Rzedzian R.R.,
Proc. 9th Ann. Mtg. SMRM, New York **1**, 123 (1990)

[79] Cohen M.S., Dalcanton J.J., Weisskoff R.M., Roman M.L.,
Proc. 9th Ann. Mtg. SMRM, New York **1**, 189 (1990)